Cost-effective and novel seismic methods for mineral and coal exploration: Examples from Witwatersrand goldfields and Bushveld Complex

Mpofana Sihoyiya

A dissertation submitted in fulfilment of the requirements for the degree of

Doctor of Philosophy

School of Geosciences

University of the Witwatersrand

Johannesburg



November, 2023

DECLARATION

I declare that this thesis is my own, unaided work. It is being submitted for the Degree of Doctor of Philosophy at the University of the Witwatersrand, Johannesburg. It has not been submitted before for any degree or examination in any other University.

_____

Mpofana Sihoyiya

Student Number: 1284606

ABSTRACT

The reflection seismic method has its origin from oil and gas exploration in the land and offshore sedimentary soft rock environment. Since the inception of the reflection seismic technology in hardrock environment, more advanced processing methods such as migration algorithms have been established to revamp the quality of hardrock seismic data for deep mineral targeting. This study shows the value of recovering and reprocessing legacy reflection seismic data using advanced processing techniques that were not available at the time of acquisition. This is achieved through different novel processing workflows that incorporate iterative static corrections, Kirchhoff pre-stack depth migration (KPreSDM), Kirchhoff pre-stack time migration (KPreSTM), and the newly developed Fresnel-volume (FV) and coherency migration (CM) techniques. This research also shows the value of novel processing of the seismic data acquired in-mine challenging environments.

The legacy data from the Kaapvaal Craton in South Africa have been processed to improve the delineation of the deep-seated mineral deposits such as the gold-bearing horizons (termed reefs) in the Witwatersrand Basin and Platinum Group Element (PGE) horizons in the Bushveld Complex. Furthermore, the shallow coal seams and associated geological structures of the Karoo Supergroup in the Evander Basin, an arcuate basin characterized by the Witwatersrand Basin towards the south and the Bushveld Complex towards the north, have been delineated for future mine planning and designs.

To better image and understand the geometry of the gold-bearing reefs and crosscutting geological structures in the South Rand goldfield, an 18 km long legacy two-dimensional (2D) reflection seismic line was reprocessed using today's standard processing workflow which employed iterative static corrections. Improved structural imaging of the steeply dipping faults (mostly normal and reverse), as well as dolerite intrusions, was mostly achieved by using KPreSTM and KPreSDM, with KPreSDM providing better structural imaging than other techniques. Moreover, reprocessing of this profile using an improved velocity model and numerical simulations assisted in delineating near surface stratigraphic units and deep-seated (> 1 km depth) geological structures that are associated with the gold-bearing reef but missed by the legacy post-stack time migrated section.

In the Bushveld Complex, the PGE deposits (known as platinum reefs) are delineated using a newly developed depth migration technique called coherency migration. Imaging through CM workflow shows evidence of the complex structural architecture that controls the platinum deposits in the study area. The 50 km long legacy 2D profile traverses towards the center of the complex and provides a better understanding of the tectonic evolution in the region. Additionally, magnetic data were utilised to constrain seismic interpretation and delineate the highly magnetic major geological structures such as the Chaneng structure and strongly magnetized rocks of the Rustenburg Layered Suite. The Chaneng structure, in particular, was poorly defined by the seismic data due to its steeply dipping nature.

In 2020, in-mine seismic experiments were conducted to delineate the PGE-bearing horizons such as the Upper Group-2 (UG2) and Merensky Reef. Three reflection seismic profiles from these experiments were cautiously processed to attenuate the infrastructure-generated noise. The experiments were successful and delineated the Merensky Reef and UG2 mineralisations at depths between 55 m and 124 m beneath the developmental tunnel (~550 m below the surface).

Six legacy 2D reflection seismic profiles acquired for gold exploration in 1986 in the Evander Basin are processed for imaging both the Witwatersrand Basin and the Bushveld Complex, as well as the coal seams of the Highveld and Witbank coalfields. The profiles were acquired perpendicular to each other providing pseudo-three-dimensional (3D) imaging of the subsurface and better delineation of the geological structures. The degree of faulting and folding that affect the mineralisation observed on the processed profiles in all sites would not have been achieved if advanced processing workflows were not implemented. Processing of the legacy data provides a more cost-effective way to explore the mineral deposits than reacquiring new data, which could be costly and limited by surface conditions. The processing approaches used in this thesis can be used in other brownfield mining regions where the legacy data exist, and they can also be used to revamp the quality of the data acquired in noisy mining environments.

ACKNOWLEDGEMENTS

A number of people have played a major role in helping me throughout my PhD journey. Firstly, I would like to express my unwavering gratitude to my supervisor, Professor Musa S. D. Manzi for his patience, guidance, and mentorship throughout my career. He inspired and led me from my undergraduate through to the Doctoral level, which he did with patience and understanding. Not only did he help my academic career, but he has also helped in guiding my personal life and providing life mentorship. I have learnt a lot from his enormous skills and experience in the mining industry, academic career space and his knowledge in reflection seismics. To Dr. Michael Westgate, thank you for your guidance and supervision. In particular, I am grateful for teaching me that I should always try things out myself before seeking assistance from the experts. This advice will forever stay with me.

I would like to thank Ian James from Southern Geoscience Consultants who vowed to never stop assisting until I become an expert in using Globe Claritas seismic processing software. My gratitude extends to Prof. Alireza Malehmir from Uppsala University for hosting us during a month visit to Sweden (made possible by Prof. Musa Manzi). Thank you to Dr. Felix Hloušek and Prof. Stefan Buske from TU Bergakademie Freiberg for their collaborative work, I am grateful for their contribution to my career. I would like to acknowledge my friends and colleagues at the University of the Witwatersrand, School of Geosciences. Thank you to the Wits Seismic Research Centre and the Geophysics department for providing a home for me at the University of the Witwatersrand. Particularly, Profs Raymond Durrheim, Gordon Cooper, Susan Webb, and Dr Stephanie Enslin for their support in scientific engagement and guidance. I am grateful for the edge from the University of the Witwatersrand, of which I am a proud student.

My further gratitude extends to the National Research Foundation (NRF) and the DSI-NRF Centre of Excellence (COE) for Integrated Mineral and Energy Resource Analysis (DSI-NRF CIMERA). The financial support from them and my supervisor Prof. Manzi has helped me a great deal in pursuing my academic career.

Opinions expressed and conclusions arrived at are those of the author and are not to be attributed to DSI-NRF CIMERA.

Table of Contents

LIST OF PAPERS viii

LIST OF FIGURES x

LIST OF ABBREVIATION xiii

1 INTRODUCTION 1

1.1 Aims and Objectives 2

1.2 Thesis Structure 3

1.3 Authorship Statement 5

2 GEOLOGICAL BACKGROUND 8

2.1 Kaapvaal Craton 8

2.2 Witwatersrand Supergroup 10

2.3 Bushveld Complex 13

2.4 Evander Basin 15

3 REFLECTION SEISMIC IMAGING 16

3.1 Seismic Design and Acquisition 17

3.2 Pre-stack Reflection Seismic Processing 20

3.2.1 Crooked Line Geometry 20

3.2.2 Static Correction 22

3.2.3 Frequency Filtering 29

3.2.4 Deconvolution 34

3.3 Migration 35

3.3.1 Migration Velocity Model 36

3.3.2 Kirchhoff Migration 38
3.3.3 Migration Strategies 40
3.3.4 Focusing Migration 42
3.4 Numerical Modelling 48
3.4.1 Finite-Difference Technique 48
4 References 51
5 Paper I: Seismic delineation of the gold-bearing structures in the South Rand Goldfield (South Africa) – a comparison of pre-stack time and depth migration approaches on legacy seismic data 63
5.1 Paper Summary 63
5.2 Manuscript 64
6 Paper II: Seismic imaging of the complex geological structures in the southwestern edge of the Western Limb, Bushveld Complex through focusing prestack depth migration of legacy 2D seismic data 90
6.1 Paper Summary 90
6.2 Manuscript 91
7 Paper III: Legacy seismic data processing for mineral and coal exploration in the Evander Basin 124
7.1 Paper Summary 124
7.2 Manuscript 125
8 Paper IV: Cost-effective in-mine seismic experiments to image platinum deposits and associated geological structures at Maseve platinum mine, South Africa 155
8.1 Paper Summary 155
8.2 Manuscript 156

9 DISCUSSION 196

10 CONCLUSIONS AND OUTLOOK 200

11 APPENDICES 202

Appendix A: Reprocessing Legacy Seismic Data for Imaging PGE Mineralisation: Case Studies from the Bushveld Complex, South Africa 202

Appendix B: Re-appraising legacy seismic data using modern processing algorithms: case studies from South African Goldfields 208

Appendix C: Seismic solutions utilizing existing in-mine infrastructure for mineral exploration: A case study from Maseve platinum mine, South Africa 214

Appendix D: Integrated geophysical methods for boulder delineation to improve mining. ... 238

LIST OF PAPERS

This thesis is based on the following papers, and they are referred to in the text by their numbering:

I. **Sihoyiya M**., Manzi M. S. D., James I., Rapetsoa M. K., Westgate M., Nwaila G., Linzer L., Durrheim R. J., and Staley P. (2022). Seismic delineation of the gold-bearing structures in the South Rand Goldfield (South Africa) – comparison of pre-stack time and depth migration approaches on legacy seismic data. *Near Surface Geophysics*. pp. 697 – 709.

II. **Sihoyiya M**., Hloušek F., Manzi M. S. D., Rapetsoa M. K., Buske S., and Khoza D. (under-review). Seismic imaging of the complex geological structures in the southwestern edge of the Western Limb, Bushveld Complex through focusing prestack depth migration of legacy 2D seismic data. *Geophysical Prospecting.*

III. **Sihoyiya M.**, Hloušek F., Manzi M. S. D., Rapetsoa M. K., Buske S., (In preparation). Legacy seismic data processing for mineral and coal exploration in the Evander Basin.

IV. Rapetsoa M. K., Manzi M. S. D., Westgate M., **Sihoyiya M**., James I., Onyebueke E., Kubeka P., Durrheim R. J., Kgarume T. (2022). Cost-effective in-mine seismic experiments to image platinum deposits and associated geological structures at Maseve platinum mine, South Africa. *Near Surface Geophysics.* pp. 572 – 589.

The candidate has additionally made the following contributions in the duration of the PhD that do not form part of this thesis:

Papers:

V. Gomo S., Rapetsoa M. K., Manzi M. S. D., Onyebueke E., Dildar J., **Sihoyiya M**., Mutshafa N., Harrison W., Bourdeau J E., Brovko O., James I., Cooper G. R. J., Scheiber S., Durrheim R. J. (2023). Integrated geophysical methods for boulder delineation to improve mining. *Geophysical Prospecting.*

VI. Rapetsoa M. K., Manzi M. S. D., **Sihoyiya M**., Westgate M., Kubeka P., Onyebueke E., Durrheim R. J. (2022). Seismic solutions utilizing existing in-mine infrastructure for mineral exploration: A case study from Maseve platinum mine, South Africa. *The Leading Edge.*

Peer-reviewed conference abstracts:

VII. **Sihoyiya M**., Manzi M. S. D., Westgate M., Rapetsoa M. K., James I. (2022). Reprocessing Legacy Seismic Data for Imaging PGE Mineralisation: Case Studies from the Bushveld Complex, South Africa. *NSG2022 4th Conference on Geophysics for Mineral Exploration and Mining.*

VIII. Berhanu R., Manzi M. S. D., Westgate M., **Sihoyiya M**., Rapetsoa M. K. (2022). Reprocessing of Legacy Seismic Profile for Shale Gas Exploration in the Karoo Basin (South Africa). *NSG2022 4th Conference on Geophysics for Mineral Exploration and Mining.*

IX. Dildar J., Manzi M. S. D., Abiye T., Gomo S., Rapetsoa M. K., **Sihoyiya M**. (2022). An Integrated Approach to Characterize the Subsurface Using Near Surface Geophysical Methods. *NSG2022 4th Conference on Geophysics for Mineral Exploration and Mining.*

X. Mkhomazi M. N., Rapetsoa M. K., Manzi M. S. D., Gomo S., **Sihoyiya M**. (2022). Delineation of Underground Tunnels Using Seismics and Magnetics at Golden Valley Mine, South Africa. *NSG2022 4th Conference on Geophysics for Mineral Exploration and Mining.*

XI. Rapetsoa M. K., Manzi M. S. D., Westgate M., Gomo S., **Sihoyiya M**., Dildar J. (2022). Multi-Geophysical Characterization of Water Conduits in an Open Pit Mine, Bushveld Complex, South Africa. *NSG2022 4th Conference on Geophysics for Mineral Exploration and Mining.*

XII. **Sihoyiya M**., Manzi M. S. D., Westgate M., James I., Durrheim R. J., Staley P. (2021). Re-appraising legacy seismic data using modern processing algorithms: case studies from South African Goldfields. *NSG2021 2nd Conference on Geophysics for Infrastructure Planning, Monitoring and BIM.*

LIST OF FIGURES

Figure 2.1: Image showing the localities of the Kaapvaal Craton, with the locations of the data used in **Papers** I to IV outlined by the black stars (Eglington and Armstrong, 2004).

Figure 2.2: The geological map of the Witwatersrand Basin (modified from Dankert and Hein, 2010).

Figure 2.3: A simplified stratigraphy of the Witwatersrand Supergroup (modified from Van der Heever et al., 2009).

Figure 2.4: The geological map of the Bushveld Complex, showing the 50 km long profile reprocessed on **Paper II** and the study area at Maseve mine where the data presented on **Paper IV** was acquired (modified from Cawthorn, 2015).

Figure 2.5: The geology of the Witwatersrand Basin (a) and the covered geology of the Evander Basin, showing the legacy seismic profiles processed on **Paper III** (b) (modified from Dankert and Hein, 2010).

Figure 3.1: Reflection seismic processing workflows applied to the legacy profiles reprocessed on **Papers I** (a), and **II** (b).

Figure 3.2: Schematic image illustrating the active seismic method principles, with the target wavefield events e.g., direct (green), surface (red), refracted (orange) and reflected (blue) waves colour coded in the shot gather example from **Paper I**.

Figure 3.3: Common depth point (CDP) fold coverage, CDP positions (cyan), shots (red), and receivers (blue) (a), and CDP fold histogram (b) for the 18 km long legacy profile reprocessed on **Paper I**.

Figure 3.4: Example of the topographic elevation and floating datum elevation from the 18 km long legacy profile reprocessed on **Paper I**.

Figure 3.5: (a) Refracted arrivals geometry, where, V_b = velocity of the bedrock, V_w = velocity of the weathering layer, t_i = intercept time at zero-offset, S_b = slowness of the bedrock, S_w = slowness of the weathering layer, X_c = critical distance, θ_c = critical angle, R = receivers, S = shot, and X_{ij} = distance between source (S_i) and receiver (R_j) (modified from Yilmaz,

2001). (b) Example of a shot gather from the profile reprocessed on **Paper I**, with first break pics shown in red.

Figure 3.6: Example of a shot gather before (a) and after (b) static correction from the profile reprocessed on **Paper I**. The white arrows show the effect of static correction on first arrivals and the blue arrows show the effect of static correction on reflections.

Figure 3.7: Example of the power spectrum (a) with band-pass (b), low-pass (c), high-pass (d), and band-stop (e) applied from shot 167 of the legacy profile reprocessed on **Paper I**.

Figure 3.8: Example of a shot gather before (a) and after (b) attenuating ground rolls (shaded blue) using an *f-k* filter and the frequency spectrum before (c) and after (d) removal of ground rolls (black arrows) from the profile reprocessed on **Paper I**.

Figure 3.9: Example of a shot gather before (a) and after (b) applying predictive deconvolution from the profile reprocessed on **Paper I**. The blue arrows show the attenuated multiples, and the white arrows represent the improved reflection.

Figure 3.10: Example of the migration velocity model used for Kirchhoff-based migration techniques in **Paper II**. (a) is the refraction tomography velocity model characterizing the very near surface geology. (b) is the 2D velocity model used for 2D migration and (c) is the stacked 2D velocity slices to create a 2.5D velocity model with identical y-values used for pseudo-3D migration of the 2D crooked line.

Figure 3.11: Representation of migration strategies depending on structural complexity and lateral velocity variation of the subsurface (Yilmaz, 2001).

Figure 3.12: Principle of Kirchhoff pre-stack depth migration (KPSDM) for a single point diffractor (D) in a homogeneous subsurface. (a) Imaging result for a single shot (asterisk) and a single receiver (red triangle). (b) Imaging results for multiple receivers (Hloušek et al., 2015b).

Figure 3.13: Principle of coherency migration for diffraction point D, source point S, and receiver point R in constant velocity medium (a). The time window around the two-way traveltime (TWT) for the main receiver and the TWT for the neighbouring comparison receivers are shown in (b). The weighting factor in the region of the TWT isochrone is shown in (c). The

raypaths through hypothetical diffraction point D_{hyp} along the TWT-isochrone is shown in (d), and the shifted time windows for comparison traces are shown in (e). The focused image of the true diffraction point is shown in (f) (Hloušek et al., 2015b).

Figure 3.14: Example of unmigrated (a) and Kirchhoff pre-stack depth migrated (KPreSDM) (b) data from **Paper I**. The unmigrated data has diffractions (green arrows), and the dipping reflections are moved in the up-dip direction (blue arrows).

Figure 3.15: Example of Kirchhoff pre-stack time (a) and depth (b) migrated data from **Paper I**. Kirchhoff pre-stack depth migration outperforms the Kirchhoff pre-stack time migration, especially on the near surface reflection continuity (U1 and U2) and outcrop is shown by the coloured rectangles.

Figure 3.16: Example of a synthetic (a) and real (b) shot gather from the data reprocessed on **Paper I**, with clear first breaks (FB) and reflections (green arrows) on both data sets. The direct waves are highlighted in blue.

Figure 3.17: (a) Geological model created by Antrobus (1986) parallel to the legacy profile reprocessed in **Paper I**. (b) Geological model used for finite-difference numerical modelling in **Paper I**.

LIST OF ABBREVIATION

AC	Alternating Current
ca.	Circa (approximately)
CM	Coherency Migration
CMP	Common Midpoint
FFT	Fast Fourier Transform
FVM	Fresnel Volume Migration
Ga	Giga annum (Billion years ago)
KPreSDM	Kirchhoff Pre-stack Depth Migration
LG	Lower Group
LGS	Lebowa Granite Suite
Ma	Mega annum (Million years ago)
MG	Middle Group
PGE	Platinum Group Element
RGS	Rashoop Granophyre Suite
RLS	Rustenburg Layered Suite
RMS	Root Mean Square
SRD	Seismic Reference Datum
TWT	Two-Way-Time
UG	Upper Group

1 INTRODUCTION

The reflection seismic method has its origins in sedimentary rocks for oil and gas exploration, with the first experiment conducted in Oklahoma City, in 1921 (Perez, 2011). Softrock commonly refers to sedimentary rocks while hardrock commonly refers to both igneous and metamorphic rocks (Hall, 1988; Ahmadi, 2015). In the past decades, the technology has been utilized in hardrock environment to delineate mineral deposits, especially the deep-seated gold- and platinum group element (PGE)-bearing horizons in South Africa (Manzi et al., 2012; Malehmir et al., 2012). Since its inception in hardrock terrane, the reflection seismic method has been faced with several key challenges. For example, the data often have low signal-to-noise ratio (SNR) and the reflections tend to have weak amplitudes because of low acoustic impedance contrasts between the target and the host rocks. Due to the structurally complex nature of the hardrock setting, the mineral deposits are often affected by steeply dipping structures that are hard to image with conventional seismic approaches. Moreover, the wave field propagation is complex owing to the presence of anisotropy introduced by fractures and layering, and the induced seismic energy is strongly scattered (Milkereit et al., 1998; Eaton et al., 2003; Salisbury et al., 2003; Malehmir et al., 2012; Greenhalgh and Manukyan, 2013; Schmelzbach et al., 2016; Scheiber-Enslin and Manzi; 2018). As a result, there has been a rapid increase in the number of seismic solutions, which employ advanced acquisition, processing, and imaging techniques to address these challenges (Manzi et al., 2018).

In the 1980s, Green and Mair (1983) and Pretorius et al. (1989) illustrated the advantages of using the reflection seismic method in hardrock environment for imaging fracture systems at radioactive waste disposal sites in the Laurentian Plateau (Canadian shield) and complex geological structures for mineral exploration and mining in the Witwatersrand Basin, South Africa. These, in conjunction with CORCOP (USA), LITHOPROBE (Canada), DEKORP (Germany), ECORS (France) and AGSO (Australia) are some of the successful implementations of the reflection seismic method in hardrock terrains (Eaton et al., 2003). In South Africa, between 1983 and 2000 over 36 000 km of two dimensions (2D) reflection seismic profiles were collected by the Gold Division of Anglo-American Corporation (nowadays called the AngloGold Ashanti Ltd.) targeting the gold-bearing horizons (locally termed reefs) of the Witwatersrand Basin (Pretorius et al., 1989; Malehmir et al., 2012). Following this, tens of 2D and three dimensions (3D) seismic datasets were

also acquired in the Bushveld Complex to map the PGE-bearing horizons (or platinum reefs) for mining planning and designs (Manzi et al., 2019a). To date, according to the author's knowledge, South Africa holds one of the largest legacy reflection seismic databases in the world of these pioneering applications of the reflection seismic method in hardrock environment, and it is available at the Wits Seismic Research Centre of the University of the Witwatersrand, Johannesburg.

In this research, some of these 2D legacy data are recovered and processed using contemporary state-of-the-art reflection seismic processing techniques for mineral and coal exploration in South Africa, focusing on the Witwatersrand Basin and Bushveld Complex. Successful re-appraisal and processing of legacy reflection seismic data have been demonstrated by several authors (e.g., Malehmir and Bellefleur, 2010; Manzi et al., 2019a, b; Donoso et al., 2020; Westgate et al., 2020 and references therein) for hardrock mineral exploration. Challenges presented by these datasets include but are not limited to bad storage, documentation, outdated tapes and hard copies. The legacy data also suffer from inaccurate coordinates and coordinate systems. Despite these challenges, the legacy data are still valuable, cost-effective, and have a potential to be revised and reworked, as demonstrated by several authors (e.g., Malehmir et al., 2019; Manzi et al., 2019a). Additionally, cost-effective and small-scale in-mine seismic experiments were conducted for the characterization of the reflectivity from PGE mineralisation in the Bushveld Complex.

1.1 Aims and Objectives

The aim of this study is to showcase the value of processing legacy data using recent reflection seismic processing methods for mineral exploration in the Kaapvaal craton, South Africa. This is demonstrated through three different case studies, while the last case study demonstrates the value of applying the same processing techniques on a new in-mine dataset acquired in a cost-effective manner:

- **Paper I**: This paper demonstrates the value of reprocessing a 2D legacy seismic profile collected in the South Rand Goldfield near Burnstone mine. Burnstone was placed under care in 2012 and Sibanye Stillwater is currently evaluating the viability of exploiting the gold-bearing reefs at depths ranges of 0.8 km to 1.5 km. The results from this study provide insight into the geometry of the reef and the geological structures cross-cutting it. The data

were processed using Kirchhoff pre-stack time and depth migration techniques, which improved the imaging of complex geological structures. Thus, showing the value of legacy seismic data in mineral exploration and research.

- **Paper II**: The main aim of this paper is to delineate the complex geological structures and the Platinum Group Elements (PGEs) in the Bushveld Complex, which hosts the world's largest platinum deposits. Moreover, the study contributes to the long-standing debate about the inter-limb connectivity in the centre of the Bushveld Complex. An approximately 50 km long 2D legacy seismic profile is reprocessed using a newly developed focusing migration technique (called coherency migration) based on the conventional Kirchhoff migration.
- **Paper III**: This study aims to image the PGE horizons of the Bushveld Complex, the gold-bearing reefs of the Witwatersrand Basin, and the coal seams in the Evander goldfield, South Africa. There are several 2D legacy reflection seismic profiles in the Evander goldfield covering both the Bushveld Complex and the Witwatersrand Basin. Six of these profiles collected perpendicular to each other are processed following a novel seismic processing workflow.
- **Paper IV**: This study was conducted for imaging of the PGE-bearing Upper Group 2 (UG2) and Merensky horizons of the Bushveld Complex and the geological structures crosscutting them. Several in-mine seismic experiments were performed on the auxiliary tunnel approximately 550 m below the surface. Three reflection seismic profiles from these experiments with a total length of ~300 m were merged and processed for imaging of the mineralisation using cost-effective seismic techniques.

1.2 Thesis Structure

This thesis is separated into ten chapters based on four published papers and focuses mainly on 2D legacy reflection seismic data reprocessing using several migration approaches. The first four chapters provide a summary of the aims and objectives of the thesis and the relevant geophysics theoretical background, and the papers are presented in the last three chapters.

Chapter 1 introduces the study and provides the aims and objectives, as well as the thesis structure. Chapter 2 is a summary of the geological background of the Kaapvaal craton with an overview of the target areas of the three papers. Firstly, the South Rand goldfield geology is outlined. Secondly,

the western Bushveld Complex geology overview is given in the region covered by the 2D legacy seismic profile. Finally, the geology of Evander goldfield is discussed where the Witwatersrand Basin meets the Bushveld Complex.

Chapter 3 describes the reflection seismic processing workflow followed when reprocessing the 2D legacy seismic profiles. This chapter gives a theoretical background and methodology of the pre-stack processing steps, migration techniques, and numerical modelling steps used to enhance the imaging of the geological structures and mineralisation in the Kaapvaal craton. Chapter 4 is a reference list for Chapters 1 – 3.

In Chapter 5, **Paper I** reports on imaging of the complex geological structures that host the gold-bearing reefs in the South Rand goldfield near Burnstone mine through reprocessing of a 2D legacy reflection seismic data. Static corrections and cautious pre-stack denoising played a major role in improving the continuity of reflection events. Kirchhoff pre-stack depth migration performed better than pre-stack time migration in improving structural imaging. Additionally, 2D finite-difference modelling was conducted to study the source of reflectivity found on the reprocessed shot gathers.

In Chapter 6, **Paper II** demonstrates an application of a focusing depth migration technique called coherency migration, an extension of the conventional Kirchhoff migration algorithm. This algorithm is applied to a 50 km long 2D legacy reflection seismic profile from the western Bushveld Complex for imaging the PGE deposits and the associated complex geological structures. The profile runs towards the centre of the complex and improved imaging of the subsurface geology on the southern edge of the centre of the complex. It does not show evidence of the PGE mineralization. This is interpreted to be due to the presence of a Transvaal inlier in this region covered by the profile.

In Chapter 7, **Paper III** presents the value of processing multiple 2D reflection seismic profiles using a ray-based migration technique. The six legacy profiles were collected in the Evander Basin, where the gold-bearing rocks of the Witwatersrand basin meet the Bushveld complex as well as the economic coal seams. Exploration in the Evander goldfield commenced with gold mining in the 1950s, and it is currently dominated by shallow coal mining operations. Novel migration processing workflows provide insight into the structural complexity that complicates the coal seams mining in the region.

In Chapter 8, **Paper IV** demonstrates the value of in-mine seismic investigation in mineral exploration. The experiments consisted of seven 2D reflection seismic profiles acquired at a depth of approximately 550 m and three of these profiles with a total length of ~300 m were merged and processed for characterization of the PGE bearing Merensky reef and UG2 horizons reflectivity. The profiles were acquired on the developmental tunnel at Maseve mine on the Western Limb of the Bushveld Complex.

Chapter 9 is the discussion and Chapter 10 provides conclusive remarks and potential future research.

1.3 Authorship Statement

The supervisor (Musa S. D. Manzi) was responsible for setting the aims and objectives of the project, providing the data, and assisting in preparing the papers. The contribution of the candidate to the papers is outlined below. The candidate is the primary author of chapters 5 – 7 and a secondary author of appendices C – E.

Chapter 5**:** **Sihoyiya M.**, Manzi M. S. D., James I., Rapetsoa M. K., Westgate M., Nwaila G., Linzer L., Durrheim R. J., and Staley P. (2022). Seismic delineation of the gold-bearing structures in the South Rand Goldfield (South Africa) – comparison of pre-stack time and depth migration approaches on legacy seismic data. *Near Surface Geophysics*. pp. 697 – 709. https://doi.org/10.1002/nsg.12209

The candidate was responsible for recovering and reprocessing the 1993 2D legacy reflection seismic profile using processing software, as well as conducting a numerical model using the Tesseral Pro. Modelling software. Additionally, the candidate created the images and carried out the interpretation of the final migrated section with the assistance of co-authors.

Chapter 6**:** **Sihoyiya M.**, Hloušek F., Manzi M. S. D., Rapetsoa M. K., Buske S., and Khoza D. (under-review). Seismic imaging of the complex geological structures in the southwestern edge of the Western Limb, Bushveld Complex through focusing pre-stack depth migration of legacy 2D seismic data. *Geophysical Prospecting.*

As the primary author, the candidate recovered the raw legacy data from the Council for Geosciences (CGS) database and was responsible for the pre-stack reprocessing of the legacy data.

The coherence migration was applied by the candidate and was assisted by the second author Felix Hloušek from the Technische Universität Bergakademie Freiberg, Germany. Co-authors assisted with reviewing the manuscript.

Chapter 7**:** **Sihoyiya M.**, Hloušek F., Manzi M. S. D., Rapetsoa M. K., Buske S., (In preparation). Legacy seismic data processing for mineral and coal exploration in the Evander Basin.

The candidate recovered and processed the legacy seismic profiles, and the processing workflows are outlined in **paper III**. The candidate also prepared the manuscript.

Chapter 8: Rapetsoa M. K., Manzi M. S. D., Westgate M., **Sihoyiya M**., James I., Onyebueke E., Kubeka P., Durrheim R. J., Kgarume T. (2022). Cost-effective in-mine seismic experiments to image platinum deposits and associated geological structures at Maseve platinum mine, South Africa. *Near Surface Geophysics*. pp. 572-589. https://doi.org/10.1002/nsg.12216

The candidate was part of the team that collected the data and was responsible for survey design. The candidate contributed in reflection seismic data processing and reviewing the manuscript.

Supplementary Peer Reviewed Abstract:

Appendix A**:** **Sihoyiya M**., Manzi M. S. D., Westgate M., Rapetsoa M. K., James I. (2022). Reprocessing Legacy Seismic Data for Imaging PGE Mineralisation: Case Studies from the Bushveld Complex, South Africa. *NSG2022 4th Conference on Geophysics for Mineral Exploration and Mining.*

The candidate recovered and reprocessed the legacy reflection seismic data and prepared the abstract. The secondary authors were responsible for editing and reviewing the abstract.

Appendix B**:** **Sihoyiya M**., Manzi M. S. D., Westgate M., James I., Durrheim R. J., Staley P. (2021). Re-appraising legacy seismic data using modern processing algorithms: case studies from South African Goldfields. *NSG2021 2nd Conference on Geophysics for Infrastructure Planning, Monitoring and BIM.*

The candidate recovered and reprocessed the legacy reflection seismic data and prepared the abstract. The secondary authors were responsible for editing and reviewing the abstract.

Supplementary manuscript:

Appendix C**:** Rapetsoa M. K., Manzi M. S. D., **Sihoyiya M**., Westgate M., Kubeka P., Onyebueke E., Durrheim R. J. (2022). Seismic solutions utilizing existing in-mine infrastructure for mineral exploration: A case study from Maseve platinum mine, South Africa. *The Leading Edge.* pp. 54 – 61. https://doi.org/10.1190/tle41010054.1

The candidate was part of the team that collected the data and was responsible for survey design. The candidate contributed to reflection seismic data processing and reviewing the manuscript.

Appendix D**:** Gomo S., Rapetsoa M. K., Manzi M. S. D., Onyebueke E., Dildar J., **Sihoyiya M**., Mutshafa N., Harrison W., Bourdeau J E., Brovko O., James I., Cooper G. R. J., Scheiber S., Durrheim R. J. (2023). Integrated geophysical methods for boulder delineation to improve mining. *Geophysical Prospecting.* https://doi.org/10.1111/1365-2478.13322

The candidate was part of the team that collected the data. The candidate contributed to reflection seismic data processing and reviewing the manuscript.

2 GEOLOGICAL BACKGROUND

The papers (chapters 5 - 8) outline a more comprehensive description of the geological background of the study areas. In summary, the study was conducted in the Bushveld Complex and the Witwatersrand Basin, which are both located at the centre of the Kaapvaal Craton in South Africa.

Paper I presents a study of a 6s 2D legacy reflection seismic line collected near Burnstone mine, which is currently exploiting the gold-bearing reef (known as UK9) in the eastern margin of the Witwatersrand Basin. **Papers I** and **III** investigate the seismic imaging of the UK9 reef and geological structures that crosscut it in the eastern margin of Witwatersrand Basin. **Paper II** investigates the continuity of the PGE mineralisation in the Western Limb of the Bushveld Complex. This is done by reprocessing a 50 km long 2D legacy reflection seismic profile using coherency migration. The geological structures and stratigraphic units delineated include the Transvaal Supergroup, Rustenburg Layered Suite, Lebowa granites, Rashoop granophyre, and the overlying Karoo sediments. **Paper IV** images the PGE bearing Merensky and UG2 horizons in the Western Limb of the Bushveld Complex at Maseve mine. The seismic lines were acquired inside the developmental tunnels approximately 550 m below the surface in 2020.

2.1 Kaapvaal Craton

The Kaapvaal Craton (Figure 2.1), covering South Africa and neighboring countries is one of the oldest (3.6 – 2.5 Ga) and better preserved Archean continental crusts on Earth with an estimated area of 1.2×10^6 Km^2 (Poujol et al., 2003; Good and De Wit, 1997). The majority of the Kaapvaal Craton is overlain by Neoarchaean-to-Palaeoproterozoic volcano-sedimentary rocks with few outcrops of the basement rocks (Poujol et al., 2003). The Kaapvaal Craton is subdivided into four domains according to the geological, structural and aeromagnetic lineaments as shown in Figure 2.1 for easy comparison of the timing of the tectonic events. The eastern Swaziland domain comprises the Barberton greenstone belt (BGB) and extends to the south into the Pongola Supergroup. The central Witwatersrand domain comprises the Vredefort impact structure, the Johannesburg dome and the Rand Anticline. The western Kimberley domain comprises the Madiba (MaGB), Kraaipan (KGB) and Amalia (AGB) greenstone belts. Finally, the northern Pietersburg domain consists of Pietersburg (PGB), Murchison (MGB) and Giyani (GGB) greenstone belts (Eglington and Armstrong, 2004; Poujol et al., 2003). In this study, data from the central

Witwatersrand domain, which comprises the Witwatersrand Basin and the Bushveld Complex is presented in **Papers I** to **IV** as shown by the black stars in Figure 2.1.

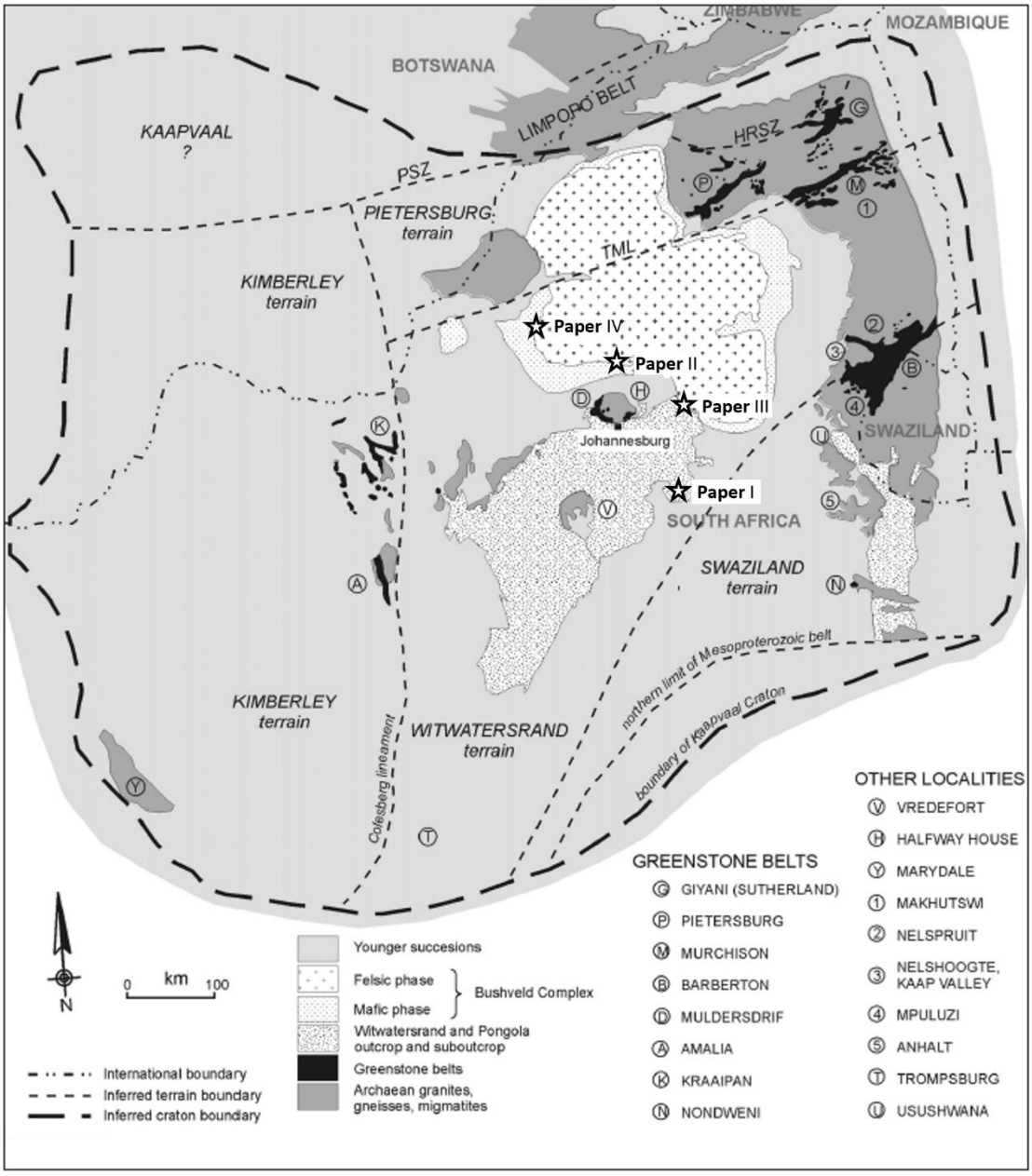


Figure 2.1: Image demonstrating the localities of the Kaapvaal Craton, with the locations of the data used in **Papers I** to **IV** outlined by the black stars (Eglington and Armstrong, 2004).

2.2 Witwatersrand Supergroup

The Witwatersrand Supergroup (Figure 2.2) is one of the world's premier Mesoarchaean (ca. 2.985 – 2.849 Ga) gold provinces deposited on the central Kaapvaal Craton (Kositcin and Krapež, 2004). It comprises 10 goldfields with only 8 actively producing gold, namely: Central Rand, Evander, East Rand, Klerksdorp, South Rand, West Rand, Welkom Free State and West Wits Line goldfields (Dankert and Hein, 2010). Multiple researchers have studied the stratigraphy and geology of these goldfields, including Kositcin and Krapež (2004), Dankert and Hein (2010), Manzi et al. (2013a, b), and Tucker et al. (2016).

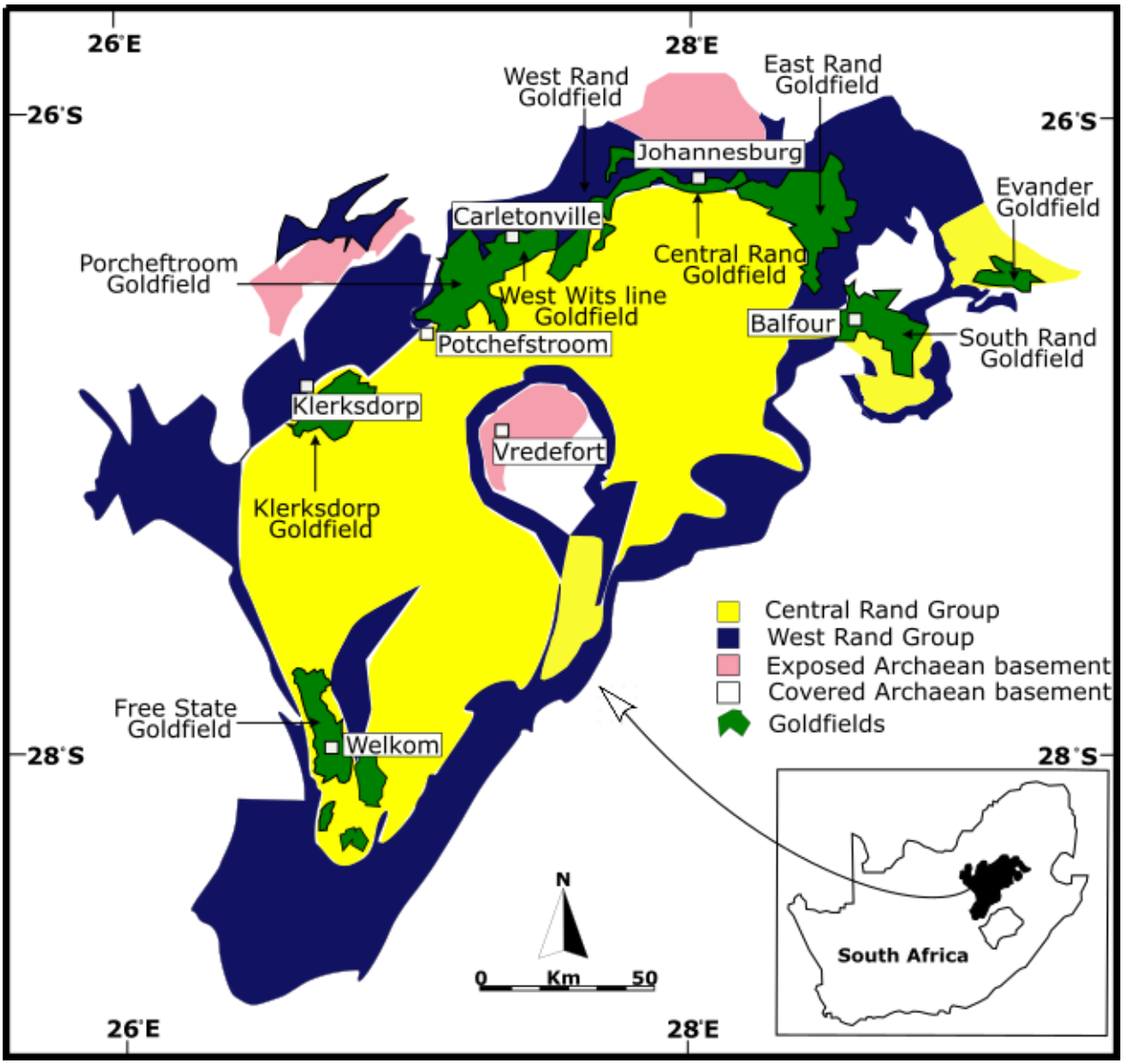


Figure 2.2: The geological map of the Witwatersrand Basin (after Dankert and Hein, 2010).

This study is focused on the lithostratigraphy of the South Rand and Evander goldfields on the eastern margin of the Witwatersrand Basin where the legacy reflection seismic profiles processed in **Papers I** and **III** were collected. The Witwatersrand Supergroup is divided into upper Central Rand Group and lower West Rand Group. The West Rand Group (ca. 2.985 – 2.902 Ga), with mostly marine and clastic sedimentary rocks unconformably overlies the volcano-sedimentary stratigraphy of the Dominion Group (Kositcin and Krapež, 2004). It comprises Discovery, Crown and Jeppestown formations. The Central Rand Group (ca. 2.902 – 2.849 Ga), with sandstone, conglomerate and shale units, which hosts 93% of the gold deposits of the Witwatersrand Basin comprises the basal Johannesburg Subgroup and upper Turffontein Subgroup (Kositcin and Krapež, 2004; Tucker et al., 2016; Manzi et al., 2013). The Turffontein Subgroup hosts the only economically viable gold reef in South Rand and Evander goldfields, the Kimberly reef (UK9A) (Figure 2.3), which is the target reef for the 2D legacy reflection seismic profiles in **Papers I** and **III**. The Kimberly reef is a 2 m thick gold-bearing conglomerate band hosted by the conglomerates and quartzites of the Kimberly Formation. The reef is too thin to be directly imaged by the seismic method. However, the reef is interbedded between seismically reflective lower Kimberly shales and the upper basaltic rocks of the Ventersdorp Supergroup, which can be used as proxies to map the reef.

The Ventersdorp Supergroup (ca. 2.72 – 2.63 Ga) overlies the Ventersdorp Contact Reef (VCR) (ca. 2.729 Ga) of the Venterspost Formation (Kositcin and Krapež, 2004; Manzi et al., 2013). The Ventersdorp Supergroup comprises the Klipriviersberg Group ultramafic and mafic metavolcanic rocks at the base, overlain by the Platberg Group metasedimentary and bimodal metavolcanic rocks, and the Pniel Group on top (Van der Westhuizen et al., 1991; Manzi et al., 2013). The Ventersdorp Supergroup is unconformably overlain by the Black Reef Formation (BRF), which is a basal unit of the Transvaal Supergroup (ca. 2.588 Ga; Kositcin and Krapež, 2004). The Transvaal Supergroup comprises the basal Chuniespoort Group carbonate (dolomite), banded iron formation and lacustrine deposits and the Pretoria Group intercalated mudstone-sandstone, andesite and subordinate conglomerate, diamictite and carbonate units (Eriksson et al., 2007; Manzi et al., 2013). The youngest overlying rocks of the Karoo Supergroup cover the majority of the Kaapvaal Craton.

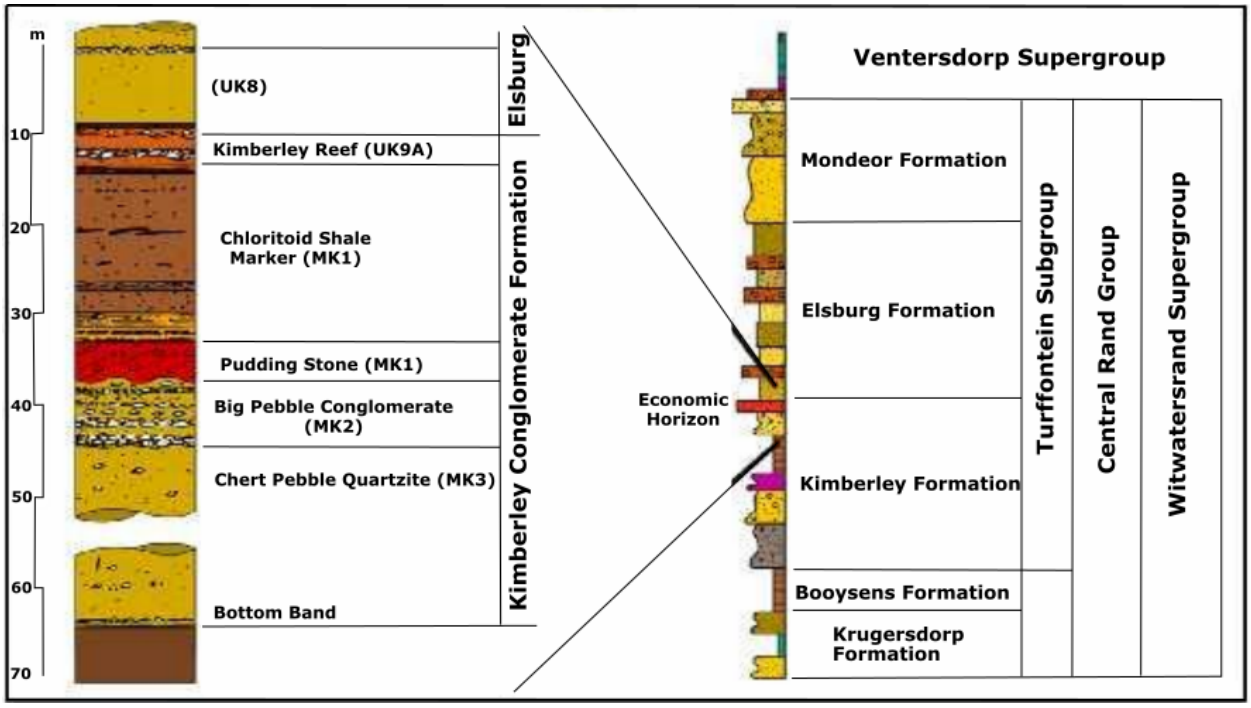


Figure 2.3: A simplified stratigraphy of the Witwatersrand Supergroup (modified from Van der Heever et al., 2009)

The Witwatersrand Basin tectonic history has been the subject of multiple studies including Coward et al. (1995), Beach and Smith (2007), Dankert and Hein (2010), Manzi et al. (2013) and references therein. However, according to Dankert and Hein (2010) after more than 100 years of gold mining and geological investigations in the basin, surprisingly little information is known about the regional-scale geometric and kinematic chronological detail of the Witwatersrand basin. Regardless, it is known that the basin encountered multiple episodes of deformation, including, inversion tectonics (from extension to compression) syn and post Central Rand Group quartzite and conglomerate deposition (Beach and Smith; 2007; Dankert and Hein; 2010; Manzi et al, 2013). The positive inversion tectonics called Umzawami event developed an easterly-verging fold-thrust belt traceable on the Witwatersrand goldfields ca. 2.90 – 2.72 Ga (Kositcin and Krapež, 2004; Dankert and Hein; 2010; Manzi et al, 2013).

Furthermore, prior to the emplacement of the Transvaal Basin, syn- and post-Ventersdorp Supergroup deposition, the Witwatersrand Basin experienced negative inversion tectonics (from compression to extension) (Dankert and Hein; 2010; Manzi et al, 2013). The Klipriviersberg Group deposition was accompanied by normal fault activity and extension, which culminated in Platberg

Group emplacement and graben formation (Manzi et al, 2013). Prior to and/or during the deposition of the upper Pretoria Group of the Transvaal Supergroup, the Ukubambana deformation event deformed the Witwatersrand supracrustal rocks forming faults and folds ca. 2.2 – 2.0 Ga (Dankert and Hein; 2010).

2.3 Bushveld Complex

The Bushveld Complex (Figure 2.4) is the world's largest igneous intrusion (~ 64 000 km^2) of the Paleoproterozoic age (2.06 Ga) and it is known for its large PGE deposits (Eriksson et al., 2001; Kruger, 2005; Cawthorn and Webb, 2001; Manzi et al., 2019a). The complex was intruded into the Transvaal Supergroup intracratonic sedimentary rocks from 2.55 – 2.06 Ga ago (Cawthorn and Webb, 2001). The mafic rocks of the complex have four lobes: Eastern, Western, Northern, and Southern (completely covered by younger sediments) Limbs. There is a long-standing debate over the connectivity of the Eastern and Western Limbs of the Bushveld Complex. Initially, a cross-section from east to west created by Hall (1932) suggested the connectivity in the form of a lopolith. Cousin's (1959) interpretation of regional gravity data proposed that the limbs were not connected, instead they originated from separate intrusions. Other studies (e.g., Biesheuvel, 1970; van der Merwe, 1976; Walraven and Darracott, 1976; and references therein) suggested that the limbs were discrete dipping sheet-like intrusions. Recent studies (e.g., Cawthorn et al., 1998, Cawthorn and Webb, 2001; Webb et al., 2004) reinstated the single lopolith model suggesting connectivity of the limbs.

In this study, the focus is on the geology of the Western and Southern Limbs where the reprocessed legacy reflection seismic profile presented in **Papers II** to **IV** was acquired (see Figure 2.4 black rectangle). The lithostratigraphy of the Southern Limb is imaged by the legacy profiles processed in **Paper III**. The main aim is to image the PGE-bearing Upper Group-2 (UG2) and Merensky horizons. The Merensky reef is a package of pyroxenite with up to 3 chromitite layers, with thickness ranging from as little as 0.5 m to 2.0 m (Hunt et al., 2018; Manzi et al., 2019). The UG2 is usually located between 15 and 400 m below the Merensky reef and is one of the richest platinum-bearing horizons in the Bushveld Complex (Hunt et al., 2018). The thinness of these horizons makes them seismically transparent, however, the conformable litho-marker horizons present nearby are used as proxies to constrain their geometry and indirectly delineate them (Campbell, 2011).

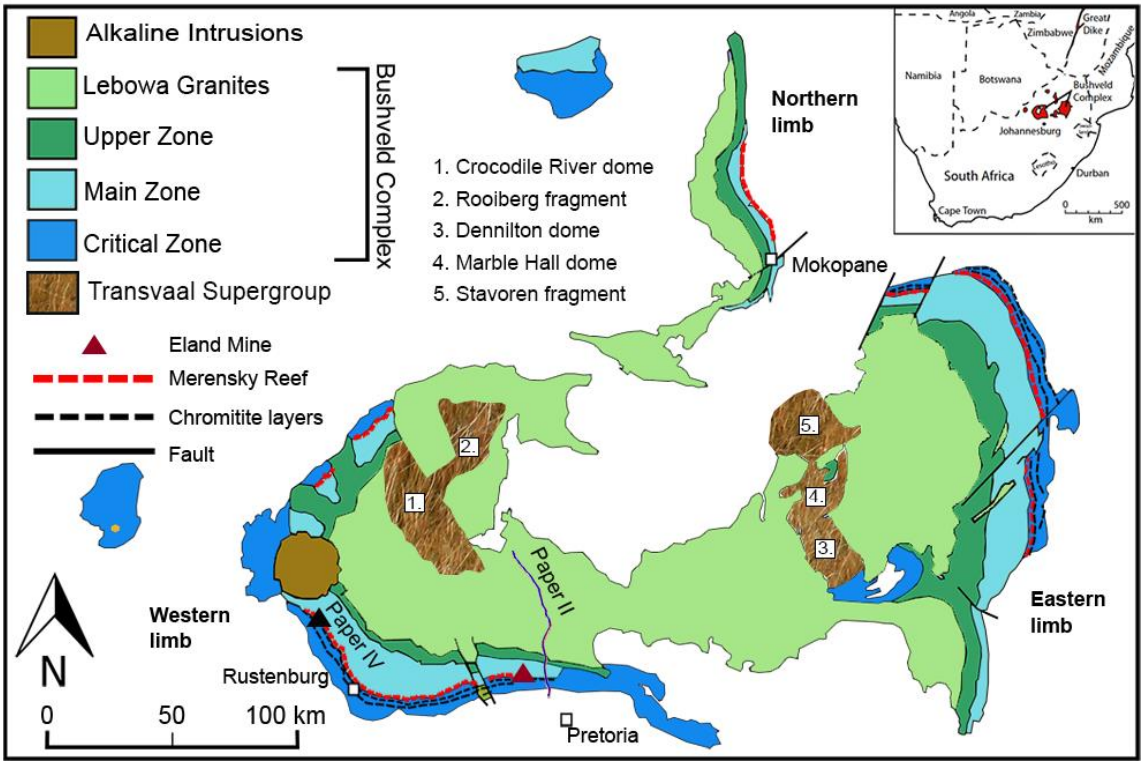


Figure 2.4: The geological map of the Bushveld Complex, showing the 50 km long profile reprocessed on **Paper II** and the study area at Maseve mine where the data presented on **Paper IV** was acquired (modified from Cawthorn, 2015).

The Bushveld Complex is subdivided into the upper granitic component, the Lebowa Granite Suite (LGS) and Rashoop Granophyre Suite (RGS) and the lower mafic component, the Rustenburg Layered Suite (RLS). Several authors (e.g., Eriksson et al., 2001; Kruger, 2005; Cawthorn, 2006; Scheiber-Enslin and Manzi, 2018; Basson, 2019 and references therein) have studied the Bushveld Complex, with most of the research concentrated on the Western Limb due to the extensive mining activities and a relatively flatter topography. The RLS, unconformably overlying the Transvaal Supergroup, is subdivided into five zones distinguishable by composition, namely the basal Marginal Zone comprising norite and metasediments approximately 250 m thick. The overlying Lower Zone, with varying thicknesses, consists of pyroxene and harzburgite. The Critical Zone, hosting the PGE mineralization is subdivided into the Upper Critical Zone and the Lower Critical Zone. The Lower Critical Zone consists of orthopyroxenite, harzburgite, and chromite layers, while the Upper Critical Zone consists of chromite, feldspathic orthopyroxenite, norite, and anorthosite/troctolite layers (Basson, 2019). The chromite layers are divided into three groups,

namely Lower (LG), Middle (MG), and Upper (UG) groups and they are overlain by Merensky reef pyroxenites near the top of the Critical zone (Scheiber-Enslin and Manzi, 2018). The overlying alternating layers of pyroxenite, anorthosite and norite/gabbronorite form the Main zone, which is overlain by the positively magnetized Upper Zone which comprises gabbronorite and anorthosite containing olivine, Fe-rich pyroxenes, magnetite and apatite (Basson, 2019).

2.4 Evander Basin

The Evander Basin (Figure 2.5) provides unique geology in the Kaapvaal Craton as it comprises the Witwatersrand Basin rocks, the Bushveld Complex rocks, as well as the Highveld and Witbank coalfields sequence. It is a northerly dipping subsidiary basin with potential for gold and PGE mineralisation as well as coal deposits. Exploration in the Evander goldfield commenced in the early 1950s with gold mineralisation at depths between 400 and 2 000 m below the ground as well as shallow coal mining operations (Witthuser et al., 2015).

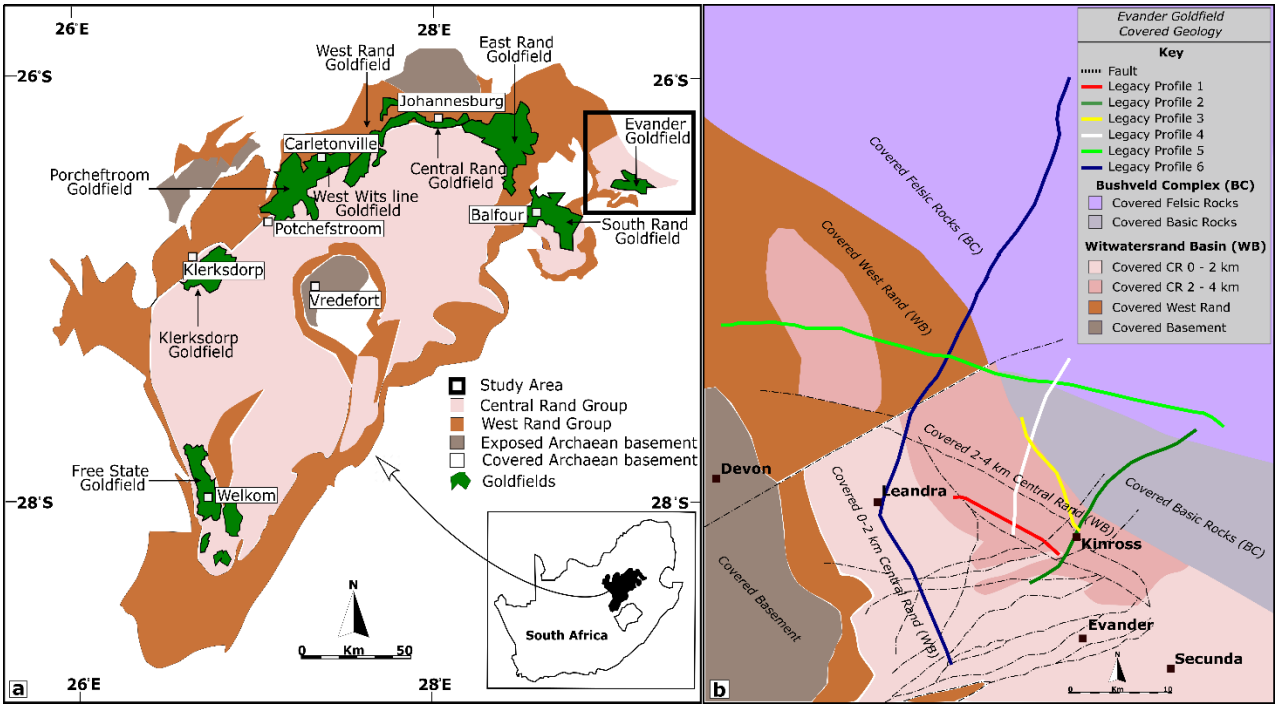


Figure 2.5: The geology of the Witwatersrand Basin (a) and the covered geology of the Evander Basin, showing the legacy seismic profiles processed on **Paper III** (b) (modified from Dankert and Hein, 2010).

3 REFLECTION SEISMIC IMAGING

Newly developed fast computers and computationally efficient algorithms have been the main driving force behind the evolution of reflection seismic processing techniques. Moreover, this provides noteworthy residual prospects in legacy reflection seismic data that were processed many decades ago using sub-optimal techniques due to the constraints introduced by the computational capabilities at the time (Van Buren et al., 2019). The use of computers to process geophysical data has its origins in the 1950s, from the Massachusetts Institute of Technology (MIT) in the Geophysical Analysis Group (GAG). This pioneering work on oil and gas exploration developed the predictive deconvolution algorithm (Treitel, 2005). Some of the early work includes the use of a matrix formalism to calculate the phase and group velocities of Rayleigh and Love waves on multilayered solid media (Haskell,1953). The reflection seismic method was well-developed and functional in a softrock environment before it was applied to a hardrock environment.

The early application of the reflection seismic method in hardrock environment includes imaging of crystalline basement by geophysical surveys (e.g., Moss and Jones, 1974; Mathur et al., 1977) and delineation of fault and fracture zones in nuclear-waste repository sites (Noponen et al., 1979; Mair and Green, 1981; Green and Mair, 1983; Juhlin et al., 1991; Juhlin, 1995; Cosma et al., 2001; Juhlin and Stephens, 2006). A comprehensive summary of the application of the reflection seismic method in hardrock environment for mineral exploration is provided by Malehmir et al. (2012). In South Africa, extensive 2D reflection seismic surveys started in the early 1980s to map deep crustal structures and search for gold- and platinum-bearing horizons (reefs) below the thick cover in the Kaapvaal Craton (Campbell and Peace, 1984; Durrheim, 1986; Pretorius et al., 1989). The reprocessed 2D legacy reflection seismic profiles presented in this thesis are part of the data catalogue from this extensive seismic programme in South Africa (Pretorius et al., 1989).

This chapter provides a theoretical background and methodology of the reflection seismic processing workflows applied in **Papers I** to **IV**. It outlines pre-stack processing steps and migration with examples from processing software and focusing migration codes. A summary of the processing workflow implemented in this thesis is shown in Figures 3.1 a, b.

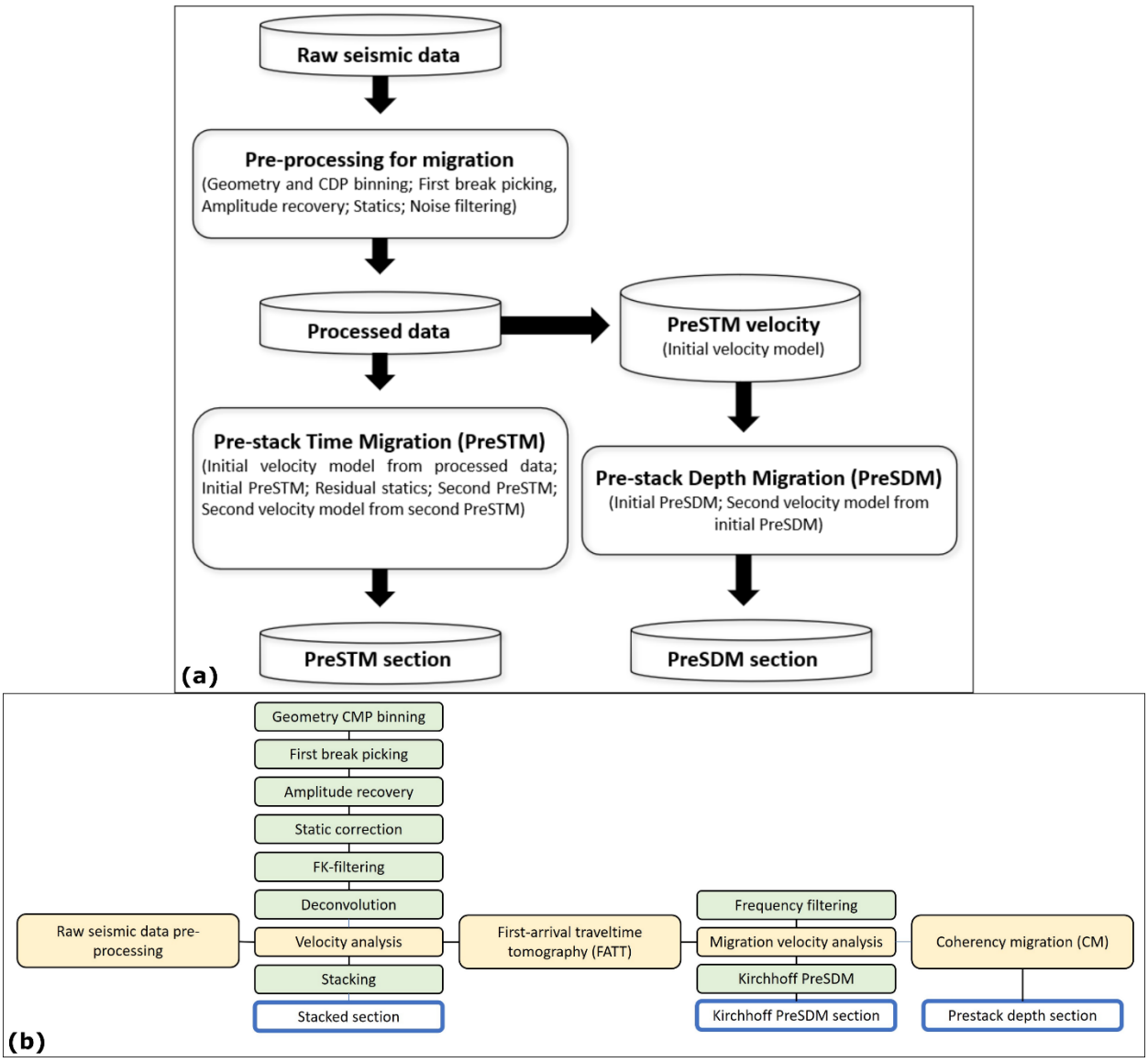


Figure 3.1: Reflection seismic reprocessing workflows applied to the legacy profiles presented in **Papers I** (a) and **II** (b).

3.1 Seismic Design and Acquisition

The active seismic method (Figure 3.2) images the Earth's subsurface by generating, recording, and analyzing the seismic waves that propagate through the Earth. These waves can be described as propagations of elastic disturbances through medium and are generated using an energy source (e.g., a vibroseis, impact, or dynamite source) into the subsurface (Sheriff, 2002). Depending on the physical properties (e.g., bulk density and seismic velocity) of the subsurface geological units, seismic waves can be refracted, reflected, or diffracted on a boundary between units. They can

traverse the subsurface as compressional (primary or P) or shear (secondary or S) waves. P-waves travel at higher velocities compared to the S-waves, and these waves are non-dispersive in nature. In addition to these waves, there are Rayleigh and Love waves which can travel between the elastic medium and the free space and are guided and dispersive in nature (Kearey et al., 2002).

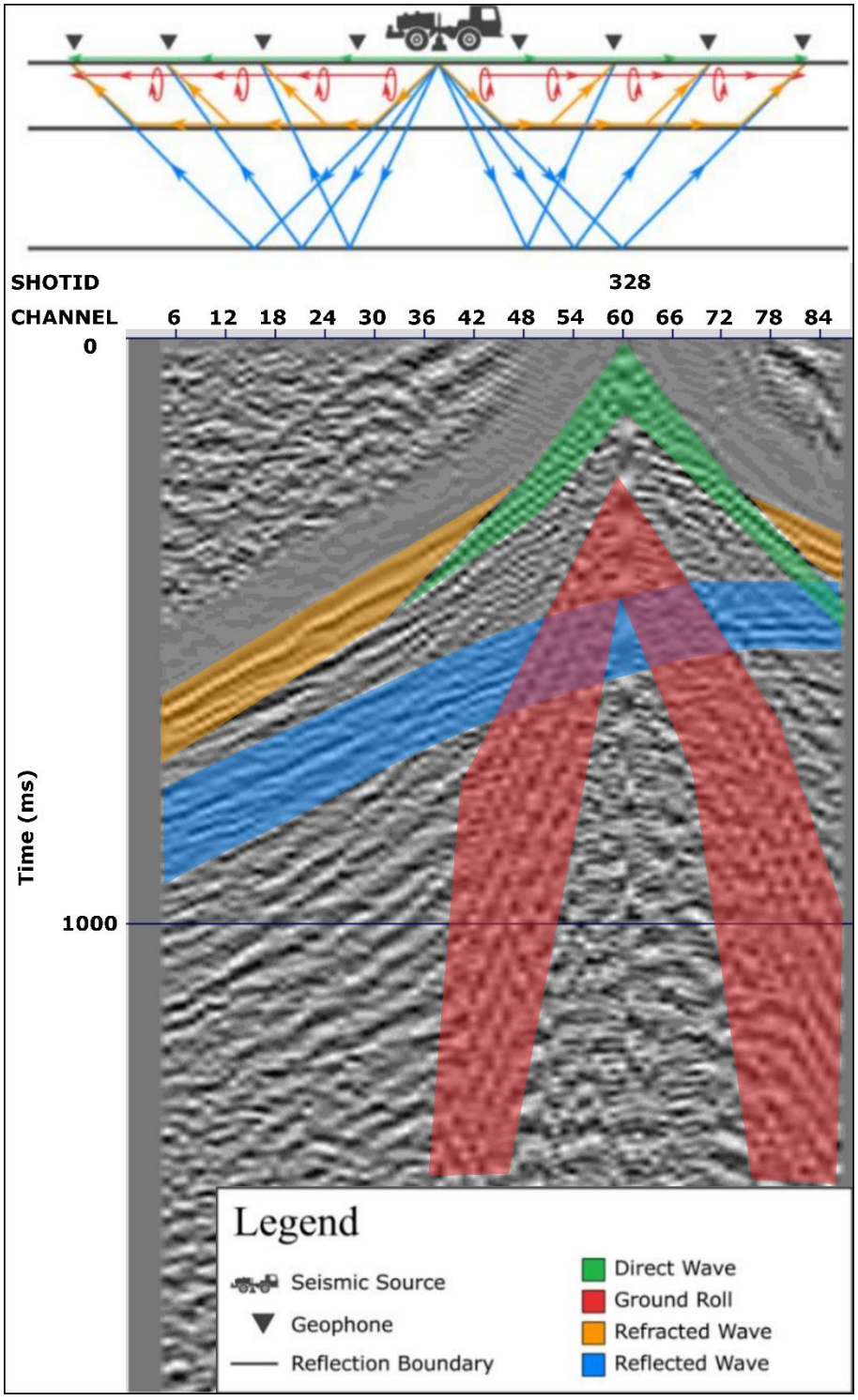


Figure 3.2: Schematic image illustrating the active seismic method principles, with the target wavefield events e.g., direct (green), surface or ground roll (red), refracted (orange) and reflected (blue) waves colour-coded in the common shot gather example from **Paper I,** together with the seismic source exciting the seismic energy and the receivers (geophones) detecting it.

Reflection seismic data acquired in hardrock environments are commonly dominated by the ground roll, which is a type of Rayleigh wave with low frequency, high amplitude, and low velocity. Ground roll is dispersive, commonly masks the shallow reflection signals, and is characterized as the main coherent noise in a seismic shot gather (Porsani et al., 2010).

The seismic waves are recorded using various recording devices (e.g., analog (coil-base geophones or accelerometers), and digital (microelectric-mechanical sensors (MEMS) or distributed acoustic sensing (DAS) systems)) placed on the surface following a 2D or 3D survey design geometry (Meunier, 2011; Willis, 2022). The multichannel seismic acquisition geometries most commonly used are split-spread, having receivers distributed on both sides of the central shot or single-ended spread with the receiver on one side of the shot (Yilmaz, 2001).

Sheriff (2002) defined a gather as a side-by-side display of seismic traces with common acquisition parameters (e.g., common shot, common receiver, common offset, common midpoint or depth point). Gathers are usually created to examine the dependency of amplitude, signal, noise, and frequency on neighbouring traces. The refracted, reflected, and diffracted seismic energy is distinguishable on a gather (see Figure 3.2). The reflected waves present as hyperbolic reflections on a shot gather. The refracted waves manifest as gently dipping linear first arrivals on a shot gather, while the diffracted waves appear as hyperbolic reflections on some zero-offset gathers (Decker et al., 2017). The surface waves dominate the central portion of the shot gather commonly known as the noise cone, and they are usually characterized by high amplitude steeply dipping linear features (Telford et al., 1990; Yilmaz, 2001). The legacy data from this thesis were acquired decades ago and the author was not involved in survey design and acquisition. However, the author was involved in 2D reflection seismic survey design and data acquisition of the in-mine seismic experiments presented in **Paper IV**.

3.2 Pre-stack Reflection Seismic Processing

Before any processing was carried out on the data, a number of preprocessing steps had to be carried out. Firstly, the header names had to be renumbered because the data were recovered in SEGY format which had header names that were stored in non-standard byte locations. Secondly, the data headers had no information about the geometry of the profiles, and it was extracted from handwritten observer's logs with shot positions extrapolated from the receiver coordinates. Finally, the data are commonly stored in vibroseis correlated shot gathers which only require editing out bad traces, and amplitude recovery. This chapter gives a summary of reflection seismic theory on processing steps applied to the legacy profiles presented in this thesis.

3.2.1 Crooked Line Geometry

The 2D legacy reflection seismic profiles processed on **Papers I**, **II**, and **III** were collected using a crooked line geometry along local roads in the centre of the Kaapvaal Craton. The acquisition parameters, examples from **Papers I**, and **II** of the legacy data, are summarized in Table 3.1.

Survey Parameters	**Paper I**	**Paper II**
Survey type	2D crooked line	2D crooked line
Year	1993	1986
Length	18 km	50 km
Direction	NE-SW	S-N
Spread	2975-25-X-25-2975	1200-112.5-X-112.5-1200
Nominal Fold	56	24
Recording System		
Recording Device	Sercel SN368	MDS-10, 96 channel
Sample Rate	2 ms	2 ms
Recording Length	6 s	21 s
Sweep Length	16 s	16 s
Sweep Frequency range	10 – 60 Hz	20 – 90 Hz
Source Information		
Source Device	Vibroseis	3 Vibroseis
Vibrator Controller	P II	P II

Source Spacing	50 m	50 m
Receiver Information		
Receiver Spacing	50 m	25 m
Geophone Type	SM4U (10 Hz)	SM4U (10 Hz)

Table 3.1: The acquisition parameters of the two legacy profiles processed on **Papers I**, and **II**.

The data are collected in shot-receiver geometry while processing is carried out in midpoint-offset coordinates. The coordinate transformation is achieved by fitting a crooked line to the seismic profile and sorting the data into common midpoint (CMP) gathers based on the field geometry assigning each trace to a midpoint between shot and receiver. The geometry is designed to maximize the fold of coverage for each CMP and the fold n_f is calculated using the following equation:

$$n_f = \frac{n_g \Delta g}{2\Delta s} \tag{3.1}$$

Where Δg is the receiver interval, Δs is the shot interval, and n_g is the number of recording channels (Yilmaz, 2001). Figure 3.3a shows the CMP fold coverage along the legacy profile reprocessed in **Paper I** with a crooked line geometry (Nedimovic and West, 2003), and Figure 3.3b is the CDP fold histogram for the same profile.

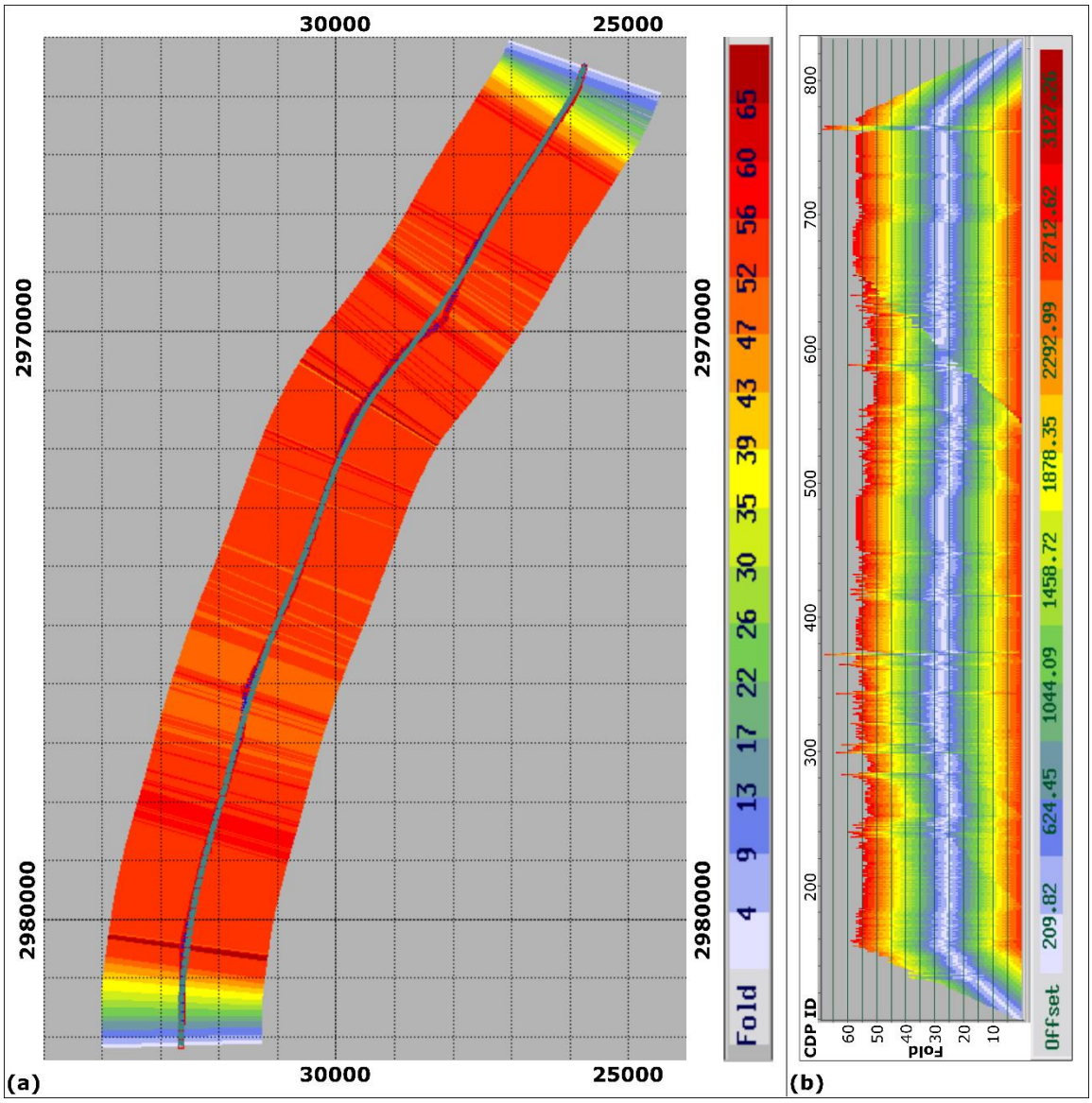


Figure 3.3: Common midpoint (CMP) fold coverage, CMP positions (cyan), shots (red), and receivers (blue) (a), and CMP fold histogram (b) for the 18 km long legacy profile reprocessed on **Paper I**.

3.2.2 Static Correction

The legacy seismic profiles were collected in terrains with varying topography, and the elevation changes led to discontinuities in the reflections due to travel time differences from trace to trace. This results in a dataset with low signal-to-noise-ratio (SNR) which can be rectified by shifting traces in time to a datum level that replaces the topographical elevation (Figure 3.4). Floating datum statics is the first static correction applied to the data to rectify these shifts on the reflection

hyperboles resulting from the topographic changes. Before calculating the static corrections, one assumes that the recorded wave field traveled vertically immediately below any shot or receiver. The correction on ray travel time is carried out for the time it takes for the ray to travel the vertical distance between the shot or receiver elevation and the survey datum. The survey may lie directly above the land surface or above the base of the weathered layer. Therefore, the corrections on travel times to the datum replace the height interval between the datum and the base of the weathered layer with material with subweathering velocity (Kearey et al., 2002).

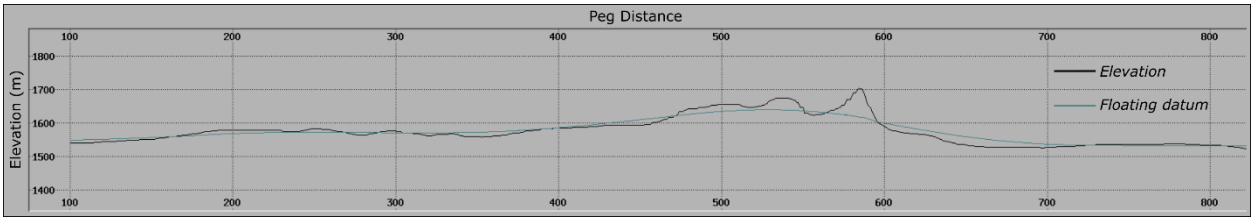


Figure 3.4: Example of the topographic elevation and floating datum elevation of the 18 km long legacy profile reprocessed on **Paper I**.

Firstly, the raw data are shifted from the source and receiver datum to the floating datum in pre-stack processing stages. Secondly, after normal moveout and stacking in post-stack processing stage, the data are shifted from floating datum to fixed datum (or seismic reference datum, SRD). The floating datum shift is calculated by selecting the replacement velocity which is equivalent to the velocity of the bedrock. The fixed datum is picked above the highest elevation of source-receiver pairs to avoid data losses during time-shifting given by the following equation:

$$\tau_D = \frac{E_D - E_S}{v_r} + \frac{E_D - E_R}{v_r} \quad (3.2)$$

Where τ_D is the floating datum shift, E_D is the fixed datum elevation, E_S is the shot elevation, E_R is a receiver elevation, and v_r is the replacement velocity measured from refracted rays (Yilmaz, 1987; Telford et al., 1990).

On the seismic processing software, the floating datum is applied as a set of time shifts which are a function of CDP, where each CDP is assigned one value stored in a shift file. It is created from the user-defined replacement velocity and fixed datum by calculating the elevation static shift for each trace using acquisition geometry. The time shifts are then grouped into a CDP gather and averaged for each CDP. Significant smoothing of the resultant time shifts is required to avoid

jumps or discontinuities, as they can affect the continuity of reflections, particularly post-stack. CDP-based floating datum is stored in the geometry file to include the CDP datum values on the CDP geometry information. These values are given by the following equation: CDP_datum = Fixed_datum + replacement_velocity*smoothed_time_shifts/2000.

Apart from the static correction, another crucial processing step in hardrock seismic data is the dynamic correction, more generally termed, the refraction static correction. This correction is based on analysis of P-wave first breaks. P-wave first breaks refer to the onset of the P-wave first arrivals in the shot gathers which are associated with the refracted waves propagating at the base of the weathering layer and direct waves (Telford et al., 1990). The quality of the first breaks comes in varying degree depending on the data's signal-to-noise ratio. Data collected in areas with varying elevation usually have nonlinear first breaks before shifting the shot gathers to floating datum. During reprocessing of the legacy seismic profiles, first break onset picking was carried out using the manual picking method. The refracted arrival times picked at the onset of first breaks were used in the least-squares inversion technique for near-surface model parameters (Yilmaz, 2001). The velocity model of the near-surface weathering layer is generally obtained using Layered-based refraction inversion (RI) which uses generalized linear inversion (GLI) and the Tomostatic methods which use tomography-based solutions. Both methods perturb the velocity model to minimize the difference between the picked and modelled first break traveltimes in a least-square sense (Woodward, 1992; Zhang and Toksöz, 1998). There are several alternatives (e.g., the plus-minus method, the generalized reciprocal method, and the least-squares method) to determine the velocity of the bedrock and weathering layer, and intercept time for modelling the weathering layer in hardrock environment for static correction. In this study, the least-squares inversion method was used for calculating the refraction statics for the data. The least-squares inversion method still requires picking of first breaks and estimates the velocity of the bedrock (V_b) and weathering layer (V_w), and the thickness of the weathering layer (Z_w) by modelling first arrivals.

Near-surface anomalies often affect the reflection times leading to reflections that do not exhibit hyperbolic moveout and the first breaks leading to nonlinear first breaks. These anomalies may be due to discordant weathering, glacial scouring or deposits, fluvial drainage system, and tectonic deformation. The effect of the anomalies on reflection seismic profile manifests by affecting the

arrival time of reflection hence leading to discontinuous reflections. Moreover, results in noisy stacked section and distorted amplitudes (Stein and Wysession, 2009).

To correct these distortions, the velocity and geometry of the weathering layer are modelled, and static corrections are calculated to counteract the travel time delays due to the weathering layer. Static refers to the constant time shift for the whole trace in a surface-consistent manner. The static corrections are carried out in two stages: with one compensating for long-wavelength component and another for short-wavelength component (Yilmaz, 2001). The long-wavelength component is associated with longer wavelength changes in the thickness and velocity of the weathering layer which affects the timing of reflection (expected hyperbolic moveout) events on shot gathers. Whereas the short-wavelength component is attributed to rapid fluctuations in the thickness and velocity of the near surface that affect the continuity of reflections on a stacked section (Stein and Wysession, 2009).

The long-wavelength distortions are due to the delay of the acoustic wave in the thicker parts of the weathered layer resulting in the deeper reflections taking the shape of the weathered layer. However, high velocity regions in the near surface layers lead to deeper reflections having a mirror image of the shallow layer. The short-wavelength errors are more consequential for a profile spread that spans weathered layer anomalies. The individual traces of a CMP gather exhibit different time shifts from the anomaly, and subsequently stacking these traces leads to destructive interference due to the relative time shifting. These time differences can also act as a high-cut frequency filter which destroys the resolution in the stacked section (Farrell and Euwema, 1984).

Figure 3.5a shows a straight-line curve fitting on first breaks assuming a horizontally stratified earth model, and Figure 3.5b shows an example of a shot gather from the profile reprocessed and presented in **Paper I**, showing manually picked first breaks. Refracted arrivals are those that have a source-receiver distance greater than the critical distance (X_c). They travel from the source to the subsurface interface between two layers at a critical angle (θ_c), along the interface at a velocity of the refracting layer (usually bedrock) and then back to the receiver (Farrell and Euwema, 1984). The direct arrivals are the rays with the source-receiver distance less than the critical distance (X_c) and they travel from source to receiver at a velocity of the overburden layer (weathering layer). The reciprocal of the velocity of the weathering layer (S_w) and bedrock (S_b) can be estimated by fitting a straight line on the first breaks and extending the straight line from refracted arrivals to

the zero-offset time (intercept time (t_i)). The depth to the bedrock is estimated by the following equation:

$$Z_w = \frac{V_b V_w t_i}{2\sqrt{V_b{}^2 - V_w{}^2}} \quad (3.3)$$

V_b is the velocity of the bedrock calculated from the slowness of the bedrock S_b and V_w is the velocity of the weathering layer calculated from the slowness of the weathering layer (S_w) (Yilmaz, 2001).

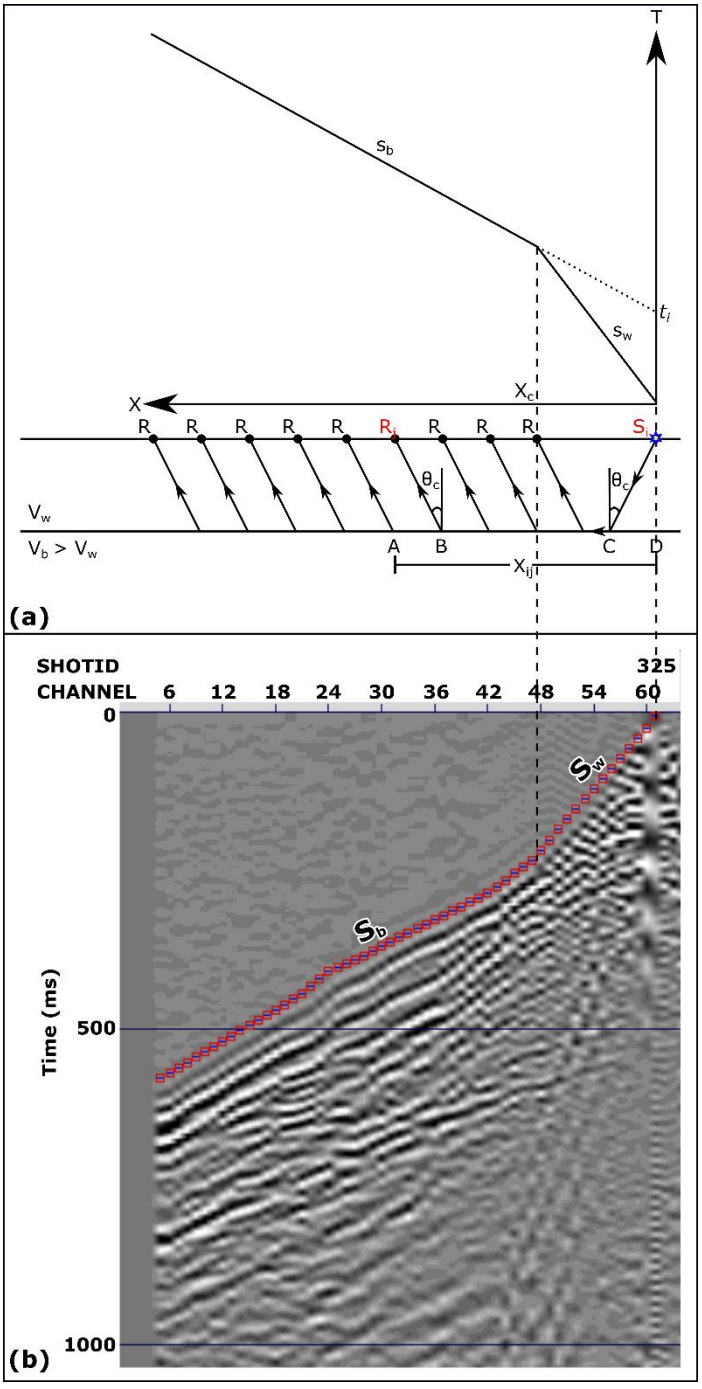


Figure 3.5: (a) Refracted arrivals geometry, where, V_b = velocity of the bedrock, V_w = velocity of the weathering layer, t_i = intercept time at zero-offset, S_b = slowness of the bedrock, S_w = slowness of the weathering layer, X_c = critical distance, θ_c = critical angle, R = receiver, S = shot, and X_{ij} = distance between source (S_i) and receiver (R_j) (modified from Yilmaz, 2001). (b) Example of a shot gather from the profile reprocessed on **Paper I**, with first break picks shown in red.

The depth to the bedrock can also be estimated by measuring the critical distance (X_c), which is the transition distance from direct arrivals to refracted arrivals using the following equation:

$$Z_w = \frac{1}{2}\sqrt{\frac{V_b - V_w}{V_b + V_w}}X_c \quad (3.4)$$

The total static correction, assuming clear first breaks and a horizontally stratified earth model for shifting the traces to a datum level below the weathering layer, is calculated using the following equation:

$$\Delta\tau_D = -\frac{2Z_w}{V_w} + \frac{2(E_D - E_s + Z_w)}{V_b} \quad (3.5)$$

Here, E_D is the datum elevation and E_s is the surface elevation (Yilmaz, 2001).

The process of refraction static correction starts with an initial near surface model to allow for parametrization of the equation that defines traveltimes. Assuming a horizontally stratified earth model, the modelled traveltimes for critically refracted raypaths from a source (S_i) to a receiver (R_j) is given by the following equation:

$$t_{ij} = \frac{S_i C}{V_w} + \frac{AD - AB - CD}{V_b} + \frac{BR_j}{V_w} \quad (3.6)$$

Simplifying equation 3.6 using the desired parameters (V_b, V_w, and Z_w) we get the following equation:

$$t_{ij} = T_i + T_j + S_b X_{ij} \quad (3.7)$$

Here, $T_i = \frac{Z_i\sqrt{V_b^2 - V_w^2}}{V_b V_w}$ and $T_j = \frac{Z_j\sqrt{V_b^2 - V_w^2}}{V_b V_w}$ are half intercept times at zero-offset for the source and receiver, respectively. Z_i and Z_j are depth to the bedrock beneath the source and receiver, respectively. S_b and X_{ij} are the bedrock slowness and offset (source-receiver distance), respectively. Since there are more source-receiver pairs compared to the unknowns in equation 3.7, the parameter vector contains more equations than the unknowns (Yilmaz, 2001).

In the case of the legacy data used in this study, most of the shot gathers did not have clear first breaks which made it difficult to measure the velocity of the weathering layer and bedrock from the picked arrivals by fitting a straight-line curve. In these data, also due to complex geology, the

bedrock and weathering layer interface is often undulating, with lateral variations in the weathering layer and the direct arrivals not clearly defined from the first breaks.

Figure 3.6 shows an example of a shot gather before (Figure 3.6a) and after (Figure 3.6b) static correction from the legacy seismic profile reprocessed on **Paper I**. The first arrivals become more linear as shown by the white arrows and the reflections become more hyperbolic as shown by the blue arrows after static correction. Detailed static correction parameters used on the profile are presented in **Paper I**.

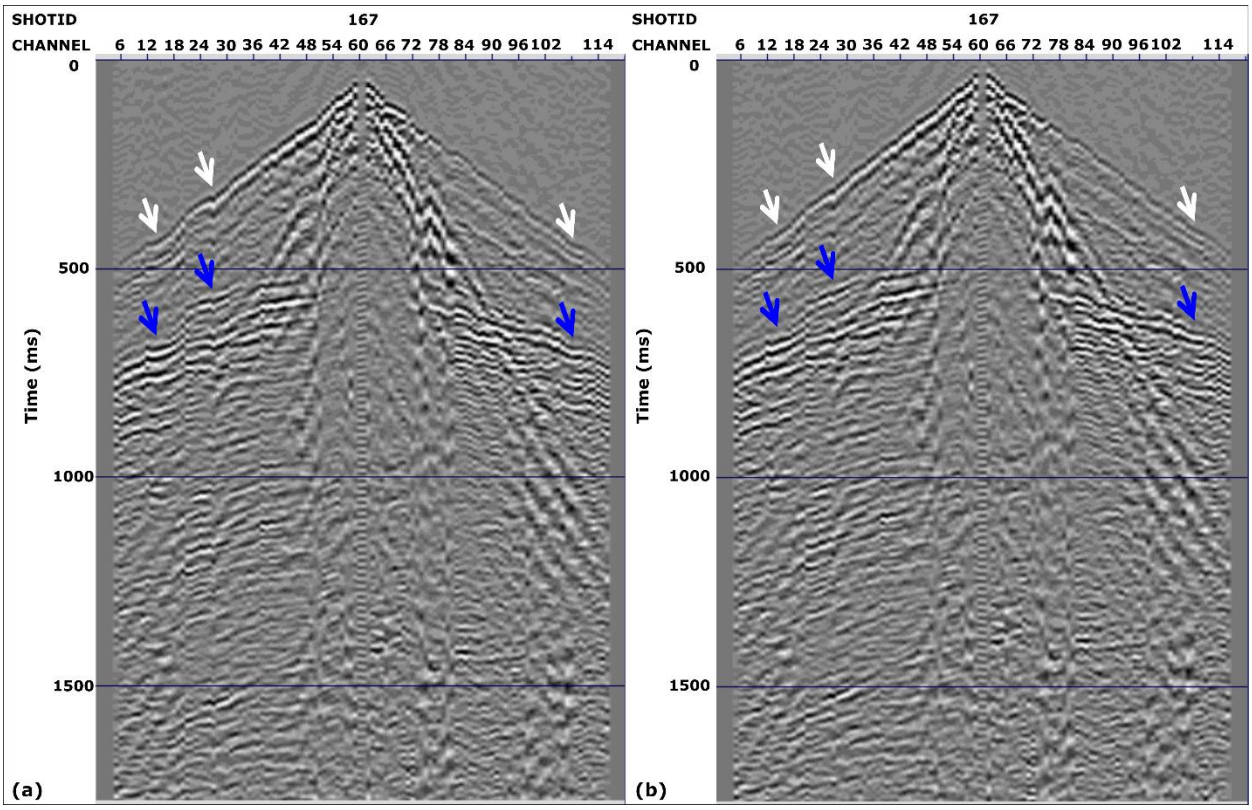


Figure 3.6: Example of a shot gather before (a) and after (b) static correction from the profile reprocessed on **Paper I**. The white arrows show the effect of static correction on first arrivals and the blue arrows show the effect of static correction on reflections.

3.2.3 Frequency Filtering

To suppress the noise and increase the useful signal bandwidth, seismic data are commonly filtered using different methods. The most common way is to convert seismic data from time to frequency domain where the data can be filtered using zero- or minimum-phase band-limited wavelets,

among others. Depending on the nature of the data and seismic source used (vibroseis - zero-phase, impact and explosive sources - minimum-phase), filter wavelet with appropriate phase response needs to be selected, to leave the original data phase information unchanged. This is carried out using a zero-phase frequency filtering technique where only the amplitude spectrum is band-limited while the phase spectrum remains unchanged. When carried out in the frequency domain it is equivalent to the product of the amplitude spectra and the filter operator. However, in time domain the filter operator and the time series are convolved for filtering, this is because convolution in time domain is equal to multiplication in frequency domain (Yilmaz, 2001).

Figure 3.7 shows the power spectrum example from shot 167 of the legacy profile reprocessed on **Paper I**. Frequency filtering is normally carried out as band-stop, band-pass, high-pass, low-pass or notch filters. Band-pass filtering is commonly applied in reflection seismic data processing as most noise in hardrock seismic data is characterized by low frequencies (e.g., ground roll) and high frequencies (e.g., ambient noise) (Yilmaz, 2001). This is particularly important in the legacy reflection seismic data presented in **Paper I** as they were collected with a sweep frequency of 10 to 90 Hz. A notch filter was applied to the data to remove the spiking electrical noise of 50 Hz from the AC on the national power grid.

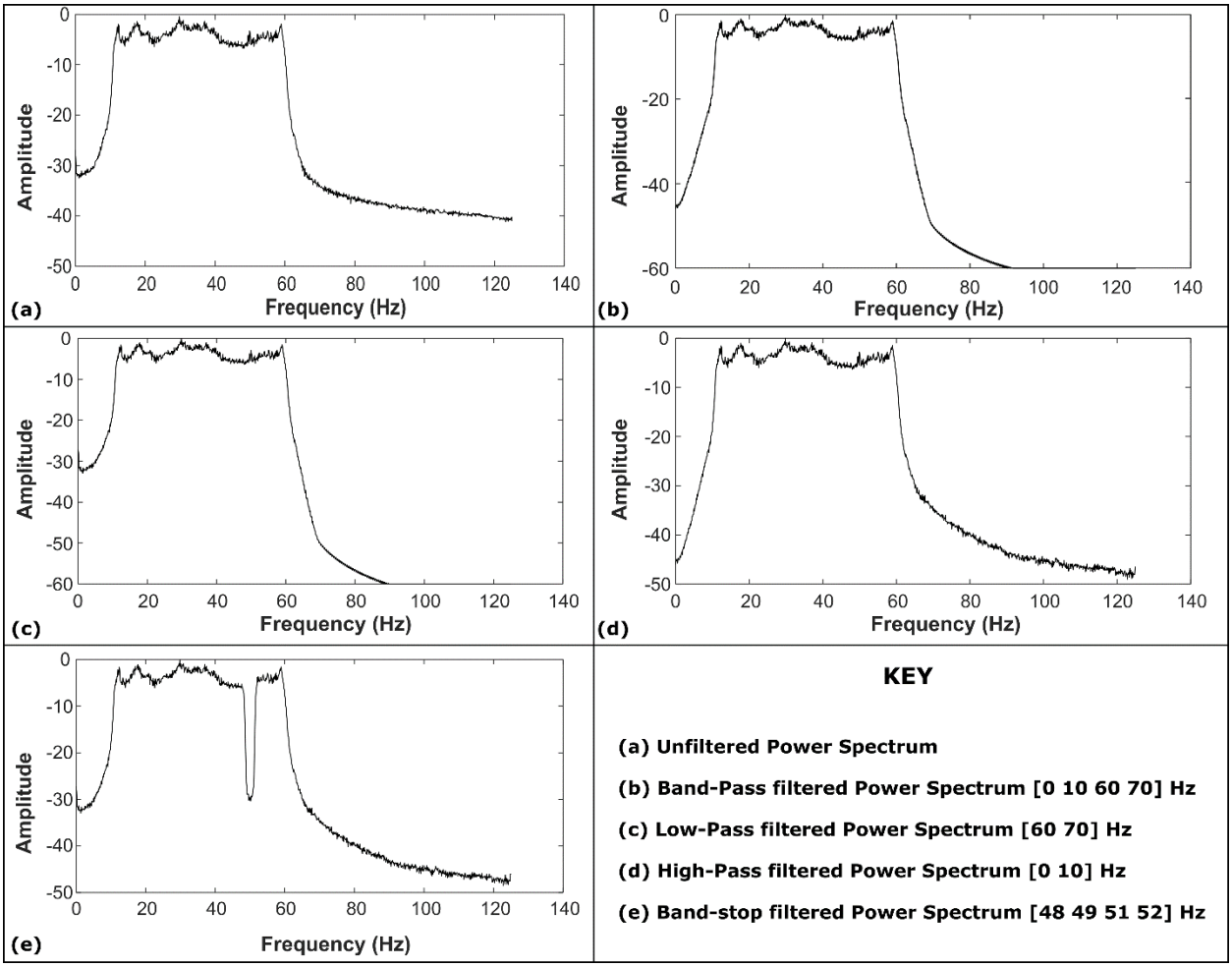


Figure 3.7: Example of the power spectrum (a) with band-pass (b), low-pass (c), high-pass (d), and band-stop (e) applied from shot 167 of the legacy profile reprocessed in **Paper I**.

In this thesis, the data were already acquired, and the frequency-wavenumber (*f-k*) filter was used to attenuate ground roll. *F-k* filtering relies on the 2D band-pass filtering in the frequency domain achieved by transforming a shot gather using 2D Fast Fourier transform (FFT). The 2D FFT in reflection seismics is used to identify signals that propagate at a specific velocity. According to the basic wave theory, a wave function whose FFT is a function of wavenumber and frequency (F(*k*, *f*)) propagates with velocity that is directly proportional to its frequency and inversely proportional to its wavenumber. Therefore, any signal with a characteristic velocity appears as linear features in the *f-k* domain. Refracted p- and s-waves as well as surface waves are signals that appear as linear features in the *f-k* domain because they propagate at a specific velocity (Telford et al., 1990; Keary et al., 2002). The coefficients of these signals are easily identifiable

and attenuated in the *f-k* domain. However, this requires careful execution as it can result in signal distortion if it is not well applied. For example, sometimes the ground roll signal in frequency domain overlaps with the reflection signal, and the designed filter can cut off some of the reflection signal resulting in distortions after transforming the data back to time domain. Moreover, designing a 2D band-pass filter that cuts off a lot of the area in the frequency domain can cause artificial lineaments in the shot gathers after inverse Fourier transform (Duncan and Beresford 1994).

Figure 3.8 shows an example of a shot gather before (Figure 3.8a) and after (Figure 3.8b) *f-k* filtering from the legacy seismic profile reprocessed in **Paper I**. The *f-k* filter successfully attenuated the ground roll (shaded blue in Figure 3.8a) from the data. It also shows the frequency spectra of the shot gather before (Figure 3.8c) and after (Figure 3.8d) attenuation of ground roll (indicated by the black arrows).

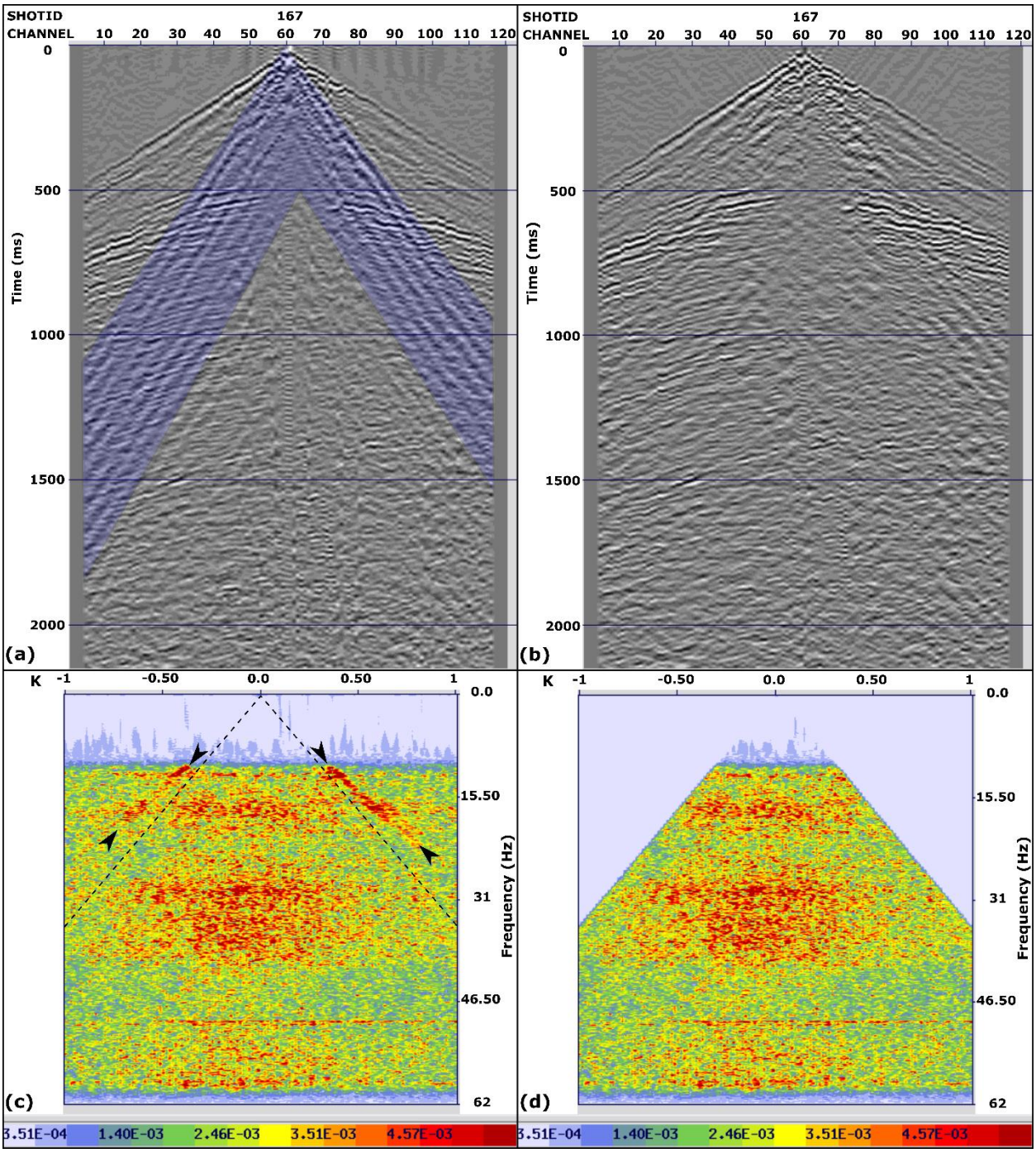


Figure 3.8: Example of a shot gather before (a) and after (b) attenuating ground rolls (shaded blue in (a)) using an *f-k* filter. The frequency spectra before (c) and after (d) removal of ground rolls (black arrows in (c)) from the profile reprocessed in **Paper I**.

3.2.4 Deconvolution

The deconvolution method is applied to achieve wavelet compression, reverberation attenuation, and multiple suppression to increase the temporal resolution of a reflection seismic shot gather (Yilmaz, 2001).

Theoretically, deconvolution is a process of extracting the earth's impulse response from a seismogram by convolving it with an inverse filter. In the case of this study, the Wiener filter is used as an inverse filter and many authors have detailed the mathematical computation of the filter (e.g., Wiener, 1949; Robinson and Treitel, 1967 and references therein). The Weiner filter is better regarded as a predictor of coherent energy in a seismogram than a filter that creates spikes. Deconvolution using the Weiner filter is documented by Peacock and Treitel (1969), and this chapter will only provide a summary.

Predictive or gap deconvolution is designed to set the desired output of the operation to be a time-advanced version of the input wavelet, with gap α according to the following equation:

$$\begin{bmatrix} T_0 & T_1 & T_2 & & T_{n-1} \\ T_1 & T_0 & T_1 & \cdots & T_{n-2} \\ T_2 & T_1 & T_0 & & T_{n-3} \\ \vdots & & & \ddots & \vdots \\ T_{n-1} & T_{n-2} & T_{n-3} & \cdots & T_0 \end{bmatrix} \begin{bmatrix} a_0 \\ a_1 \\ a_2 \\ \vdots \\ a_{n-1} \end{bmatrix} = \begin{bmatrix} T_\alpha \\ T_{\alpha+1} \\ T_{\alpha+2} \\ \vdots \\ T_{\alpha+n-1} \end{bmatrix} \tag{3.8}$$

Where the a_i is a prediction filter that generates the input wavelet at time $t + \alpha$ (desired output), from the input wavelet at time t. The above-mentioned filter produces the predictable component of the seismic trace (multiples). Subtracting the actual output from the desired output yields the prediction error filter, f_t, given by the following equation:

$$f_t = 1,0,0, \dots, -a_0, -a_0, -a_0, \dots, -a_n \tag{3.9}$$

Here $-a_0$ component occurs at a lagged time $t + \alpha$ and this error filter generates the unpredictable component of the seismic trace, which is the reflection coefficient series of the subsurface (Yilmaz, 2001).

Figure 3.9 demonstrates a shot gather before (Figure 3.9a) and after (Figure 3.9b) applying predictive deconvolution to the legacy profile reprocessed in **Paper I**. The blue arrows show a

note-worthy suppression of multiples, and the white arrows show an improved reflection after applying deconvolution.

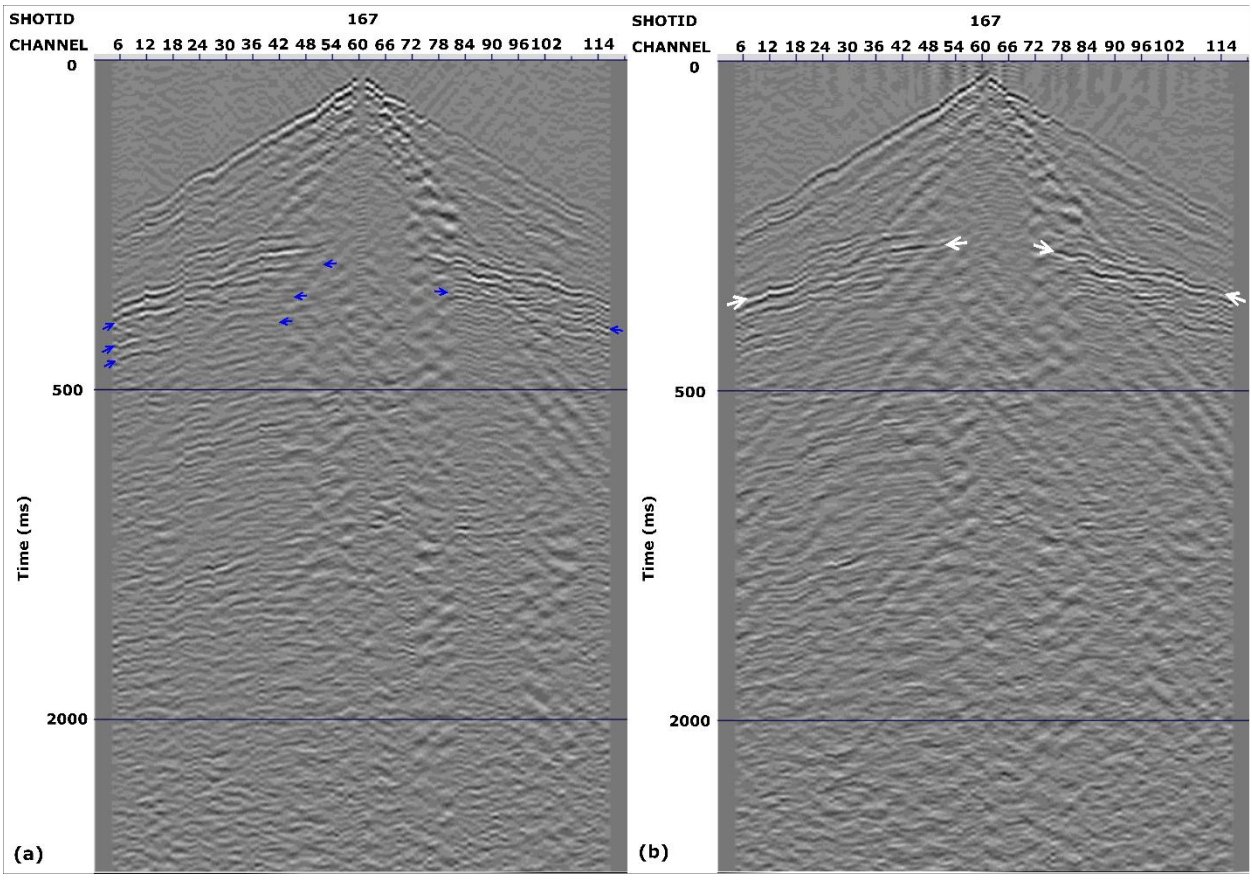


Figure 3.9: Example of a shot gather before (a) and after (b) applying predictive deconvolution from the profile reprocessed in **Paper I**. The blue arrows show the attenuated multiples, and the white arrows represent the improved reflection.

3.3 Migration

The computational implementation of migration in reflection seismic data processing dates back to the late 1960s. These programs carried out migration by summing stacked trace amplitudes along hyperbolic trajectories governed by root-mean-square (RMS) velocity field (Schneider, 1978). Migration is applied to reflection seismic data to create a high-resolution image of the Earth's subsurface by migrating dipping events to their true subsurface position, shortening the length of dipping reflections, moving reflections in the up-dip direction, and finally collapsing diffractions (Yilmaz, 1987). There has been a proliferation of migration techniques since the first

application of reflection seismic method in hardrock environment. These techniques can be categorized into three types, firstly, Kirchhoff migration, which is based on integral solutions to a wave equation; secondly, Finite-difference migration, which has origins from Stanford University, formulated by a finite-difference algorithm; and finally, frequency-wavenumber migration, which is carried out in a frequency-wavenumber domain (Yilmaz, 2001). Several authors (e.g., Chun and Jacewitz, 1978; Claerbout, 1985; Gardner et al., 1986; Yilmaz, 1987; 2001; Whitmore et al., 1988; Etgen et al., 2009; and references therein) have outlined the theoretical background of these migration algorithms, however, in this chapter Kirchhoff migration and newly developed Kirchhoff-based migration algorithms are discussed.

This study focuses on the application of Kirchhoff-based migration algorithms in the hardrock environment and implementation in pre-stack reprocessing of 2D legacy seismic data that was collected and processed before their inception. **Paper I** presents the contrast between pre-stack time and depth Kirchhoff migration through a case study near a gold mine in the Witwatersrand Basin. **Papers II** and **III** demonstrate the application of coherency migration through two case studies from the Bushveld Complex and Witwatersrand Basin, respectively.

3.3.1 Migration Velocity Model

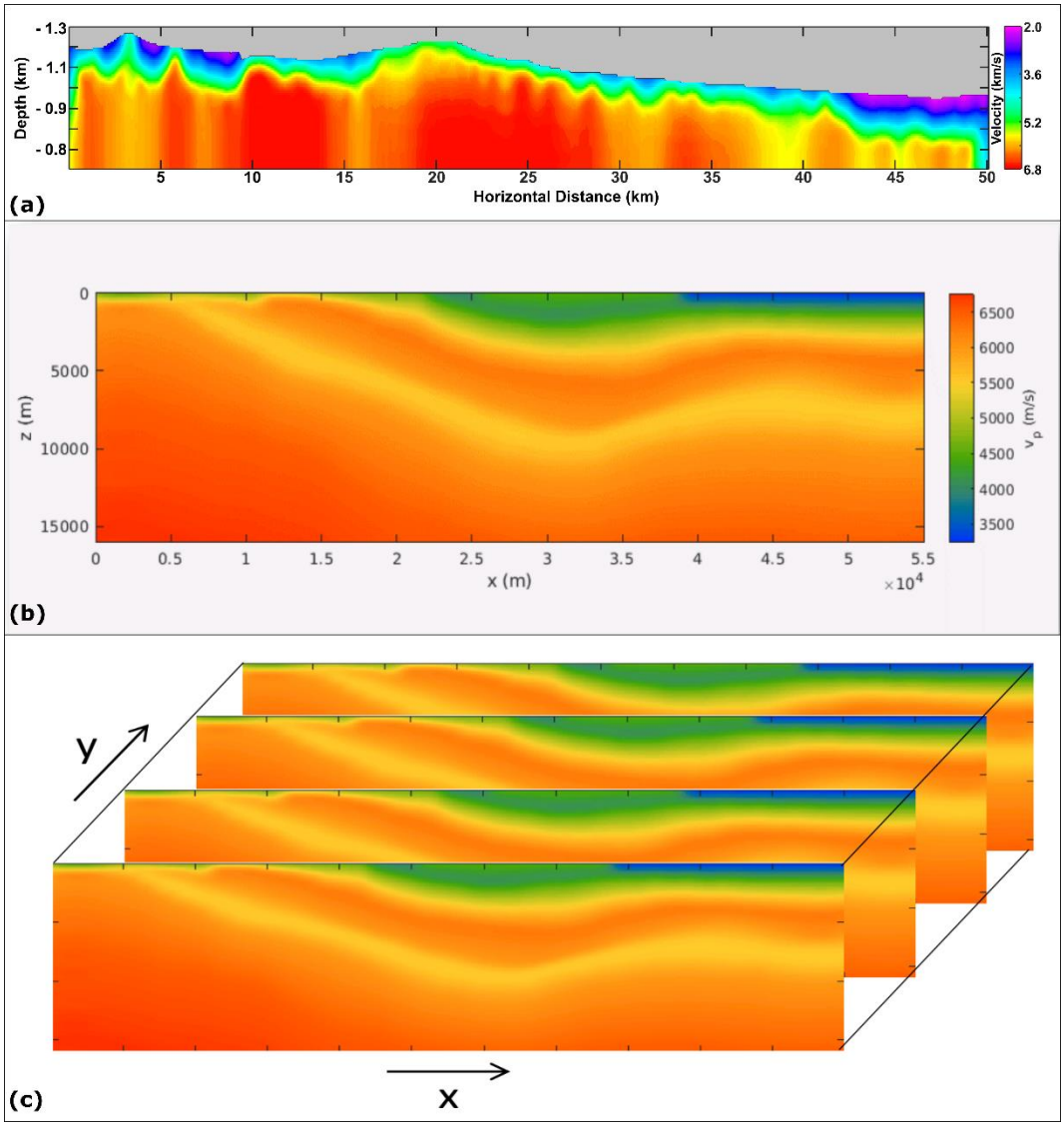
Pre-stack migration techniques require an accurate velocity model for structural imaging, however, in hardrock environment like the central Kaapvaal Craton, creating a good velocity model can be challenging. To date, a significant amount of effort has been invested in the measurements of the physical property (e.g., seismic velocities) of the lithostratigraphic units of the Kaapvaal Craton to constrain the seismic data processing and interpretation (e.g., Christensen, 1965; Castagna et al., 1985; Carlson and Miller, 2004; Punturo et al., 2005; Kern et al., 2009; Elbra et al., 2011; Malehmir et al., 2012; Nkosi et al., 2017, 2022; and references therein). During the processing stage, the velocity model is traditionally built using the information from common midpoint (CMP) gathers, the procedure involves picking the velocities via semblance analysis, constant velocity gathers or stacks, among others, where the velocity of a particular reflection is picked as the one where that reflection appears "flattest". The procedure is repeated for all reflections and CMP gathers and the final result is compiled into a unique normal moveout (NMO) velocity field. The reader is referred to Telford et al. (1990), Yilmaz (2001), and Eaton et al. (2003) for a detailed theoretical background on CMP stacking and NMO correction. In summary, NMO correction is a process of

eliminating the offset effect from gathers by creating zero-offset gathers while CMP stacking sums the zero-offset gathers to create a single trace. A good velocity model flattens the hyperbolic events resulting in continuous reflections that approximate the subsurface geology. Traditionally, velocity analysis involves stacking CMP gathers using different constant velocities and subsequently refining the stacking velocity model to generate the best reflection continuity. The NMO velocity can be approximately calculated from the hyperbolic traveltime equation:

$$t^2(h, V_{stk}) = t_{0stk}^2 + \frac{4h^2}{V_{stk}^2} \quad (3.10)$$

Here, V_{stk} is the stacking velocity and t is the two-way-time, t_0 is the zero-offset two-way-time, and h is the distance between the receiver and the source (Yilmaz, 2001). The velocity model can also be refined by information derived from the physical property studies of the borehole or field samples, inverted near-surface velocity models, and geological information.

Figure 3.10 shows an example of migration velocity models used in **Paper II**, and Figure 3.10a is the refraction tomography velocity model that characterizes the very near surface geology (top 500 m). Figure 3.10b is a 2D velocity model used for 2D Kirchhoff-based migration techniques, and Figure 3.10b is a 2.5D velocity model used for pseudo-3D Kirchhoff-based migration techniques. The velocity model was created from a 2D constant velocity stacked section, a refraction tomography velocity model, and previous physical property studies from the Bushveld Complex. The reader is referred to **Paper II** for detailed velocity model parameters.



716

717 **Figure 3.10:** Example of the migration velocity model used for Kirchhoff-based migration
718 techniques in **Paper II**. (a) The refraction tomography velocity model characterizing the very near
719 surface geology. (b) The 2D velocity model used for 2D migration, and (c)the stacked 2D velocity
720 slices to create a 2.5D velocity model with identical y-values used for pseudo-3D migration of the
721 2D crooked line.

722 ### 3.3.2 Kirchhoff Migration

723 Schneider (1978) describes the Kirchhoff migration algorithm from the first principles starting
724 from the following scalar wave equation:

725 $$\nabla^2 U - \frac{1}{c^2} U_{tt} = -4\pi q(r,t) \qquad (3.11)$$

Here, U is the measured wavefield, C is the P-wave velocity, U_{tt} is the second-order time derivative of the measured wavefield, and $q(r,t)$ is the source density function, where *r* and *t* are position and time vectors, respectively. The solution to the above-mentioned inhomogeneous wave equation in an arbitrary volume V_0 is calculated by a surface integral S_0 that encloses the volume. Assuming the initial values to be zero, the surface integral is given by:

$$U(r,t) = \frac{1}{4\pi}\int dt_0 \int dS_0 \left[G\frac{\partial}{\partial n}U(r_0,t_0) - U(r_0,t_0)\frac{\partial}{\partial n}G\right] \quad (3.12)$$

Here, n is a normal vector to the surface S_0 which includes the recording surface Z = 0, and the subsurface hemisphere spreading out to infinity. Using a suitable Green's function, ignoring contributions from the distant hemisphere, and setting boundary conditions reduces the integral. The input measured wavefield $U(r_0,t_0)$ requires G = 0 on the surface S_0 to make the gradient of U negligible. A suitable Green's function for image reconstruction of a point source r_0 and its negative image r'_0 in free surface is given by the following equation:

$$G(r,t|r_0,t_0) = \frac{\delta\left(t-t_0-\frac{R}{C}\right)}{R} - \frac{\delta\left(t-t_0-\frac{R'}{C}\right)}{R'} \quad (3.13)$$

Where,

$R = \sqrt{(z-z_0)^2 + (x-x_0)^2 + (y-y_0)^2}$, and $R' = \sqrt{(z+z_0)^2 + (x-x_0)^2 + (y-y_0)^2}$ (Kuhn and Alhilali, 1977). Substituting the above-mentioned Green's function on the integral representation of the wave field $U(r,t)$ in the image space in terms of the measured wavefield $U(r_0,t_0)$ yields the following equation called the Kirchhoff integral:

$$U(r,t) = \frac{1}{2\pi}\int dt_0 \int dA_0 \cdot U(r_0,t_0)\frac{\partial}{\partial z_0}\left[\frac{\delta\left(t-t_0-\frac{R}{C}\right)}{R}\right] \quad (3.14)$$

Evaluating the z_0 differentiation and t_0 integration yields the following equation:

$$U(r,t) = \frac{1}{2\pi}\int dA_0 \frac{\cos\theta}{RC}\left[U'(r_0,t_0) + \frac{C}{R}U(r_0,t_0)\right]_{t_0=t-(R/C)} \quad (3.15)$$

Here, $U'(r_0,t_0)$ is the time derivative of the recorded data, $U(r_0,t_0)$ is the recorded data, $\frac{C}{R}$ is the scaling factor, $t_0 = t - (R/C)$ is the "retarded" time used to evaluate these variables, and $\cos\theta$ is

the "obliquity" factor. Alternatively, replacing a z_0 derivative in equation 3.14 with a z derivative yields the following most compact form of the equation:

$$U(r,t) = -\frac{1}{2\pi}\frac{\partial}{\partial z}\int dA_0 \frac{U\left(r_0, t-\frac{R}{C}\right)}{R} \tag{3.16}$$

The 3D convolutional representation of the integral transformation in time domain is given by:

$$U(x,y,z,t) = U(x,y,z_0,t) * \frac{1}{2\pi}\frac{\partial}{\partial z_0}\left[\frac{\delta\left(t \pm \frac{r}{C}\right)}{r}\right] \tag{3.17}$$

Here, $r^2 = \Delta z^2 + x^2 + y^2$. In frequency wavenumber domain the operation becomes a complex multiplication given by:

$$\tilde{U}\left(k_x, k_y, z_0, \omega\right) = \tilde{U}\left(k_x, k_y, z_0, \omega\right) H\left(k_x, k_y, \Delta z, \omega\right) \tag{3.18}$$

Here, $H = e^{\pm i|\Delta z|}\sqrt{\left(\frac{\omega}{C}\right)^2 - k_x^2 - k_y^2}$, (Schneider, 1978).

In summary, the image value V at a random image point $m = m(x,y,z)$ below the Earth's surface is obtained by integrating the wavefield over the diffraction surface $(t_s + t_R)$:

$$V(m) = \frac{-1}{2\pi}\iint_A w(m,r)\dot{u}(r, t_s + t_R)dr \tag{3.19}$$

Here, t_s and t_R are the traveltimes from source S to the image point m and the receiver R to the image point m, respectively. The weighting function $w(m,r)$ accounts for the amplitude variation along the diffraction curve due to directivity and spherical divergence (Buske et al., 2009; Hloušek et al., 2015b).

3.3.3 Migration Strategies

Migration of reflection seismic data can be carried out using different strategies including 2D vs 3D, pre- vs post-stack, and time vs depth migration. 3D migration is favorable in a geological complex environment. However, in this study the legacy seismic profiles are in two dimensions, therefore this chapter focuses on 2D considerations of migration. Figure 3.11 shows the spectrum of migration strategies depending on the subsurface geological complexity and lateral velocity variation.

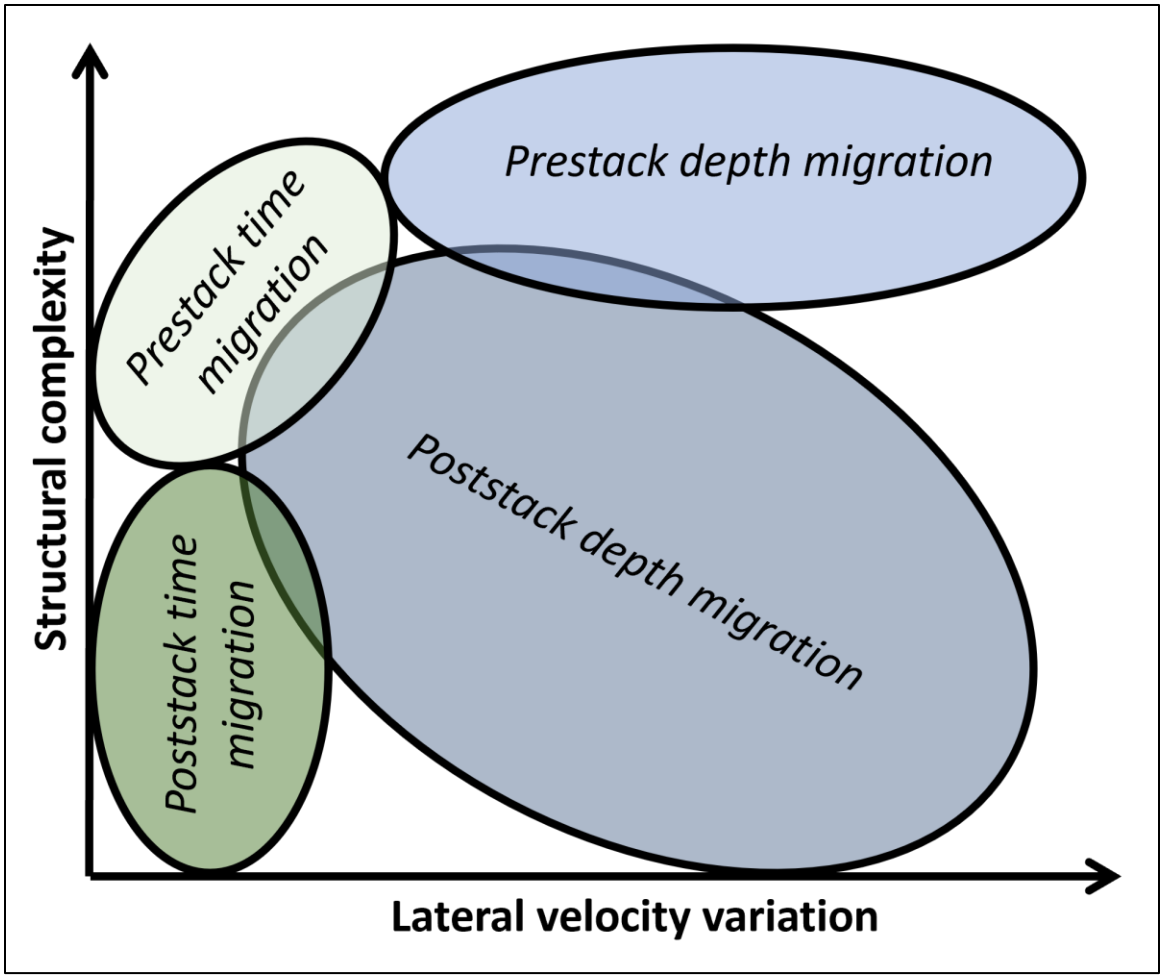


Figure 3.11: Representation of migration strategies depending on structural complexity and lateral velocity variation of the subsurface (Yilmaz, 2001).

The main difference between pre- and post-stack migration is in the names, with the former evaluated on unstacked gathers and the latter on stacked data. Time and depth migration differences are rooted in the way each uses the migration velocity model and are usually evaluated in their respective domains. Time migration treats the velocity model as a root mean square (RMS) velocity field, while depth migration treats the velocity model as the interval velocity field. Moreover, time migration creates local one-dimensional velocity models for each trace and this unphysical approach leads to sensitivity to lateral velocity variation (Etgen and Kumar, 2012). Post-stack time migration is the least mathematically complex and computationally intensive strategy, however, it is most sensitive to lateral velocity variations and structurally complex geology.

3.3.4 Focusing Migration

Figure 3.12 shows an example of a homogeneous medium with a single receiver (marked red in Figure 3.12a) that recorded a wavefield from a single shot (asterisk) diffracted by a single diffraction point (D). The resulting image using the Kirchhoff pre-stack depth migration (KPreSDM) technique for the above-mentioned receiver is created by smearing the amplitudes along the two-way-time (TWT) isochrone (dashed line in Figure 3.12a). For multiple receivers with high spatial coverage, constructive interference results in an image of the diffraction point D and destructive interference of noise (Figure 3.12b) (Hloušek et al., 2015b).

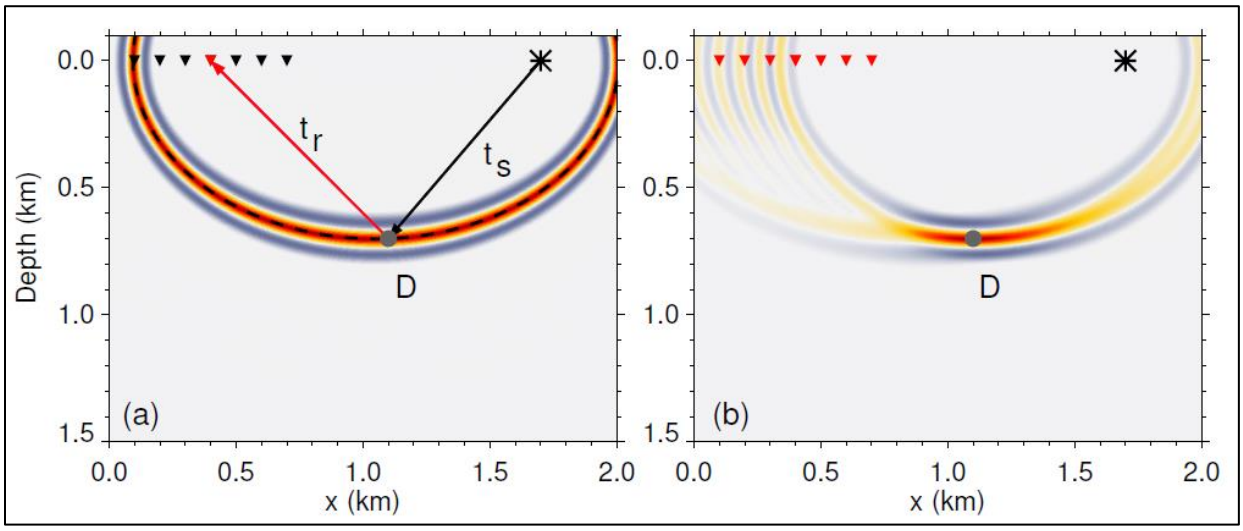


Figure 3.12: Principle of Kirchhoff pre-stack depth migration (KPSDM) for a single point diffractor (D) in a homogeneous subsurface. (a) Imaging result for a single shot (asterisk) and a single receiver (red triangle). (b) Imaging results for multiple receivers (Hloušek et al., 2015b).

In cases where the spatial coverage of receivers is limited depending on the acquisition geometry (aperture), KPreSDM results in migration artefacts which appear as migration smiles. In such cases, the resolution of the migrated section can be improved by extending KPreSDM to a focusing migration technique by adding an extra weighting factor $f(m,r)$ in the integral solution (equation 3.19) as follows:

$$V(m) = \frac{-1}{2\pi} \iint_A f(m,r) \cdot w(m,r) \dot{u}(r, t_s + t_R) \cdot dr \qquad (3.20)$$

There are numerous focusing migration techniques, for example, Fresnel-volume migration (FVM), coherency migration (CM), and coherency-based Fresnel-volume migration (cbFVM).

These techniques differ with the computation of the weighting factor $f(m,r)$, including the special case of KPreSDM with $f(m,r) = 1$ (Hloušek et al., 2015b). In this study, the mathematical computation of coherency migration as applied in **Papers II and III** is covered.

CM weighting factor $f(m,r) = C_c$ is computed using analysis of semblance coefficient on neighbouring receivers directly from input data. Neidell and Taner (1971) defined the semblance coefficient to be the normalized input/output energy ratio, where the sum of input traces is the output trace. Mathematically, the ratio of the total energy and the coherent energy within a time window is given by the following equation:

$$f = C_c^p(m,r) = \left(\frac{\int_{-\frac{T}{2}}^{\frac{T}{2}} \left| \sum_{j=0}^{N-1} u_j\left(t_s + t_{R_j} + t\right) \right|^2 dt}{N \int_{-\frac{T}{2}}^{\frac{T}{2}} \sum_{j=0}^{N-1} \left| u_j\left(t_s + t_{R_j} + t\right) \right|^2 dt} \right)^p \tag{3.21}$$

Here, p is an exponent factor used to enhance coherent signal and too high values of p can lead to enhanced migration artefacts, therefore careful consideration of values of p is needed. T is the window length which ranges from 1 to 3 times the period of the reflected signal, and N is the number of traces used for comparison. The resultant semblance coefficient can be utilized without modification on the migration integral since it is normalized (i.e., ranging from 0 to 1). This technique suppresses noise and calculates the incidence direction of the wavefield using traveltimes of the wavefield from the source to the image point and back to the receivers (Hloušek et al., 2015a; 2015b).

The most critical step in CM is choosing comparison traces because the results are not only dependent on the number of traces (N) but they also depend on the aperture spanned by these traces. Consequently, the boundary condition for the number of traces is set using the maximum offset from the actual trace location. Additionally, the source, image point, and receiver geometries are taken into consideration using the projected Fresnel zone as follows:

$$r_{F_{pro}} = \sqrt{dx^2 + dy^2 + dz^2} \cdot \sqrt{2 \cdot \frac{t_{dom}}{t_0}} \cdot \sqrt{\frac{dx^2 + dy^2}{dz^2} + 1} \tag{3.22}$$

Here, the first term is the image point – receiver distance, and the combination of the first and the second term approximates the first Fresnel zone radius on a constant velocity subsurface. t_{dom} represents the dominant period of the source signal, and $t_0 = 2 \cdot t_R$, where t_R is the travel time

between the image point and receiver. t_0 can alternatively be calculated using the finite difference eikonal solver (Vidale, 1988; 1990; Podvin and Lecomte, 1991). The last term represents the paraxial Fresnel zone projected to the surface at the receiver location. Therefore, this equation provides an additional boundary condition for the comparison traces (N) used in computing the semblance coefficient. The minimum value for the third term is 1, where the image point lies beyond the receiver location since $dx^2 + dy^2 \geq 0$. Therefore, the approximation is equivalent to the projected Fresnel zone and $r_{F_{pro}}$ is small for an image point that is located near the receiver and increases with increased lateral distance between the receiver and the image point (Hloušek et al., 2015b).

Figure 3.13 illustrates the principle of CM for the source point S, true diffraction point D, and receiver point R. The time windows at comparison traces for the true diffraction point match the diffracted signal (Figure 3.13b) resulting in the imaging condition represented in Figure 3.13c. However, for any other hypothetical diffraction point (D_{hyp} in Figure 3.13d) along the two-way-time isochrone, the time windows exhibit relative shift (Figure 3.13e). The final result is the construction of the focused image of the true diffraction point (Figure 3.13f) (Hloušek et al., 2015b).

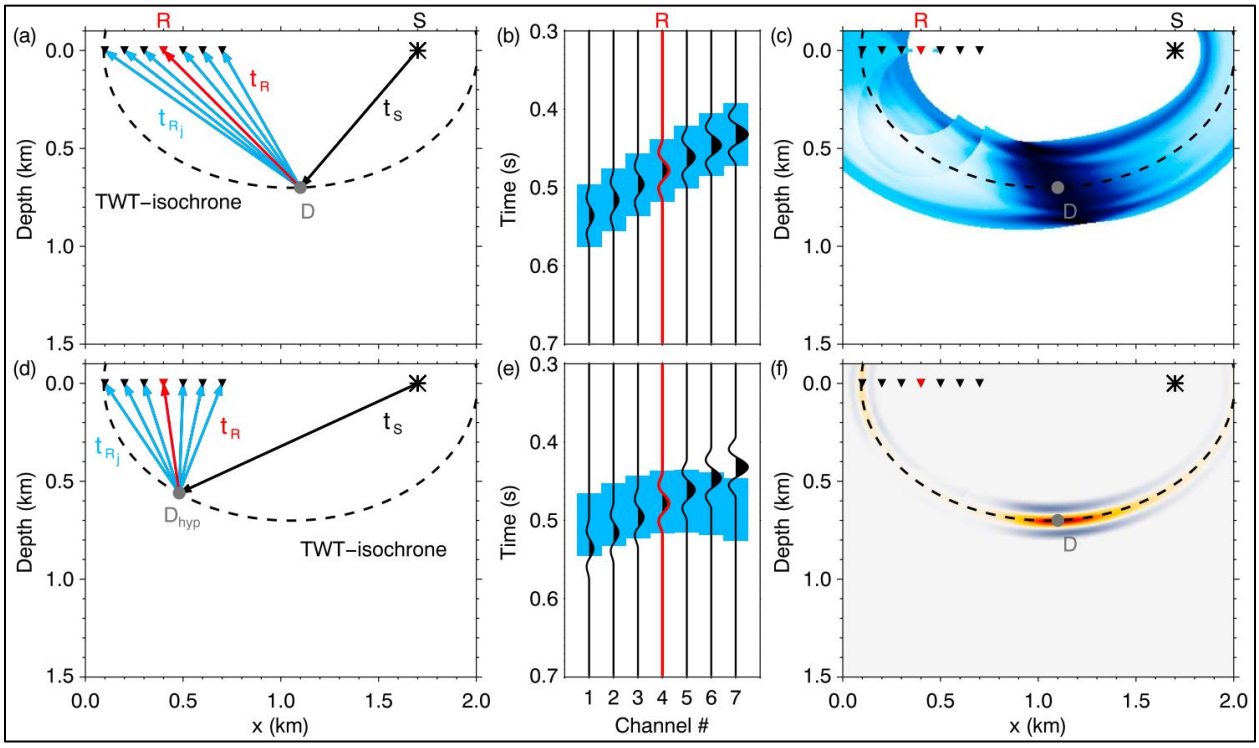


Figure 3.13: Principle of coherency migration for diffraction point D, source point S, and receiver point R in constant velocity medium (a). The time window around the two-way traveltime (TWT) for the main receiver and the TWT for the neighbouring comparison receivers are shown in (b). The weighting factor in the region of the TWT isochrone is shown in (c). The raypaths through hypothetical diffraction point D_{hyp} along the TWT-isochrone is shown in (d), and the shifted time windows for comparison traces are shown in (e). The focused image of the true diffraction point is shown in (f) (Hloušek et al., 2015b).

Figure 3.14 shows an example of unmigrated (Figure 3.14a) and Kirchhoff pre-stack depth migrated (KPreSDM) (Figure 3.14b) data from **Paper I**. The diffractions (green arrows) on the unmigrated data were successfully collapsed and the dipping reflections (blue arrows) are moved in the up-dip direction. The resolution of the section was significantly improved by the Kirchhoff migration.

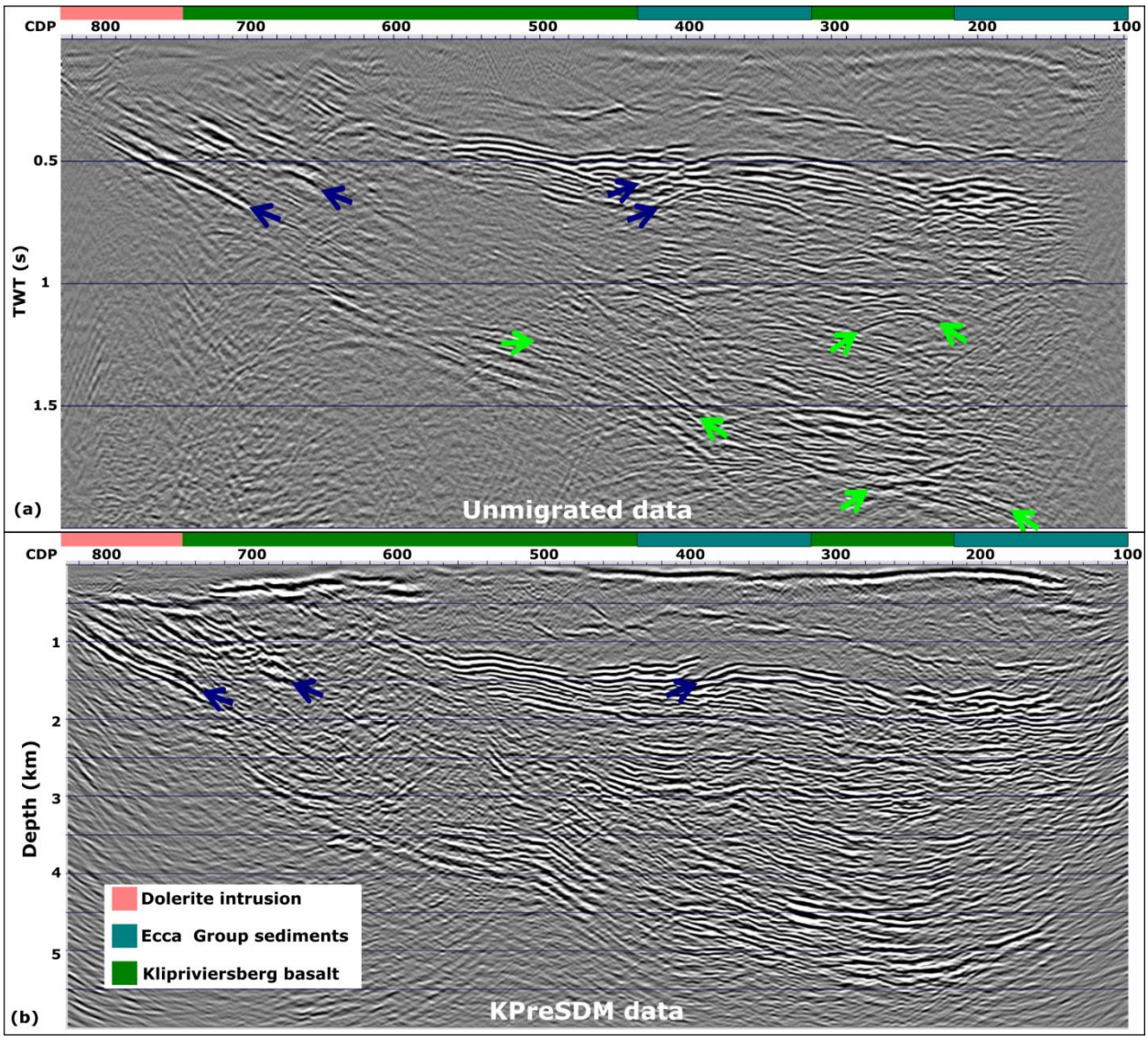


Figure 3.14: Example of unmigrated (a) and Kirchhoff pre-stack depth migrated (KPreSDM) (b) data from **Paper I**. The unmigrated data have diffractions (green arrows), and the dipping reflections are moved in the up-dip direction (blue arrows).

Pre-stack time migration (Figure 3.15a) can handle dipping reflections with minimal lateral velocity variation. Post-stack depth migration is the most commonly applied migration strategy in hardrock reflection seismic imaging, while pre-stack depth migration (Figure 3.15b) is most suited algorithm in a structurally complex environment with high lateral velocity gradients.

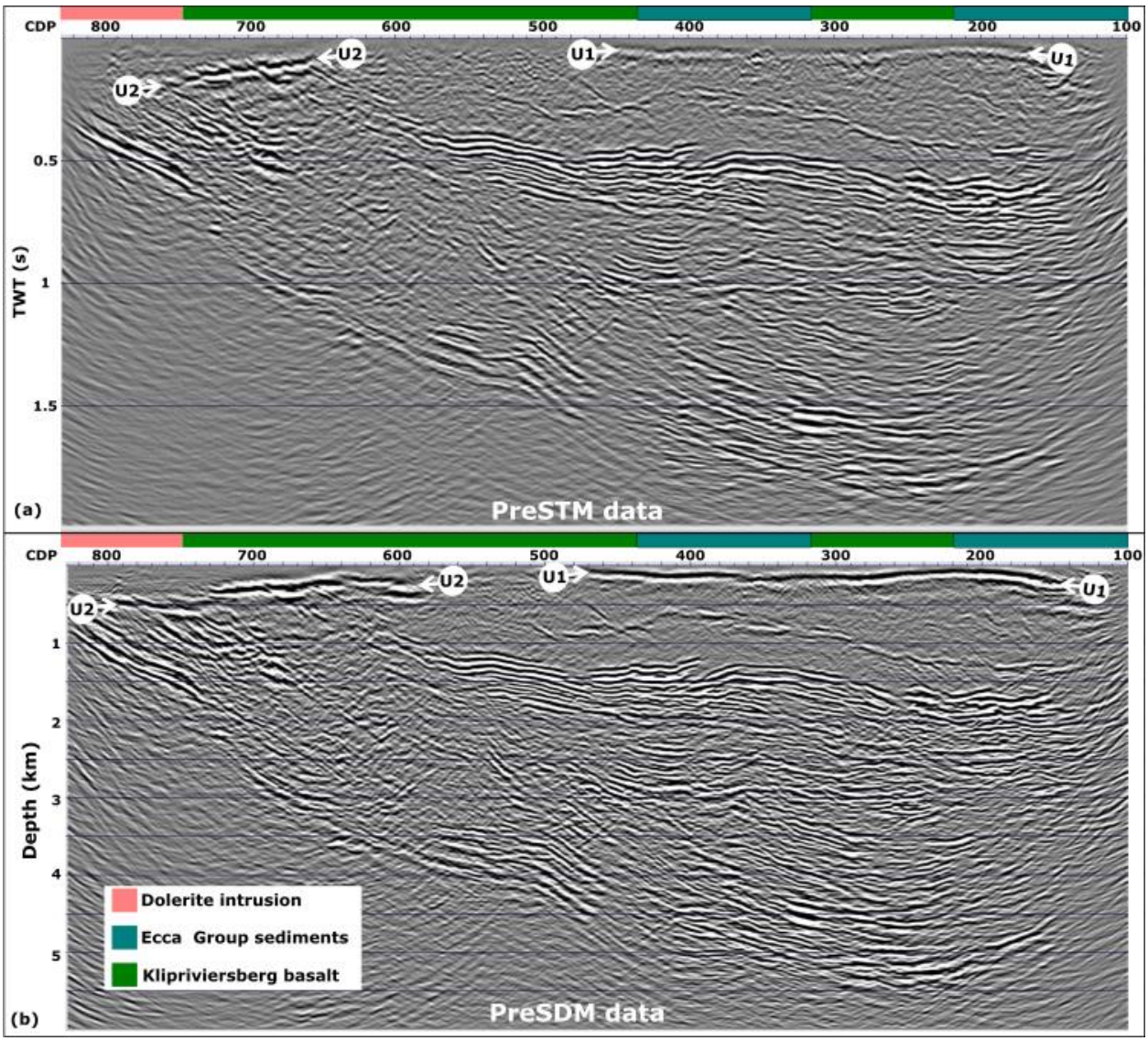


Figure 3.15: Example of Kirchhoff pre-stack time (a) and depth (b) migrated data from **Paper I**. KPreSDM outperforms the KPreSTM, especially on providing clear continuity in the near surface reflections (U1 and U2). The outcrop is shown by the coloured rectangles.

Figure 3.15 shows an example of the data from **Paper I** where the Kirchhoff pre-stack time (Figure 3.15a) is compared with the depth migration (Figure 3.15b). The comparison shows that the KPreSDM outperforms the KPreSTM, especially on the near surface geology where the reflection continuity is enhanced (e.g., U1 and U2). The lateral velocity variation is shown by varying outcrop indicated by the coloured rectangles in Figure 3.15.

3.4 Numerical Modelling

In order to find the possible source of reflectivity in seismic data one must perform reflection seismic forward modelling. There are numerous forward modelling techniques, for example, seismic ray tracing, and finite-difference methods (Juhlin, 1995; Ayarza et al., 2000; Bohlen et al., 2015). In this study, 2D acoustic finite-difference algorithm is used to generate synthetic shot gathers that were analyzed to provide some insight into the source of seismic reflectivity observed on the reprocessed legacy data. The results from numerical modelling play an important role in constraining interpretation of reflection seismic data. Synthetic data can be generated using the acquisition geometry of the real data, consequently making a comparison between synthetic and real data possible.

3.4.1 Finite-Difference Technique

In reflection seismic processing, finite-difference method is commonly used for modelling the propagation of seismic waves. It has been used in several studies in hardrock environment (e.g., Cheraghi et al., 2011; Bellefleur et al., 2012; Ahmadi, 2015) since it provides a good approximation to the solution of the wave equation (Ahmadi, 2015). According to the theory of wave propagation, the wave equation has two modes, namely the acoustic and elastic wave equation. The earth's subsurface is an elastic medium, therefore the elastic or visco-elastic wave equations simulate the propagation of the wavefield through the subsurface better. However, the acoustic wave equation has been used extensively in active seismic modelling. This is because the acoustic wave theory assumes negligible shear effects on the medium and dominant compressional effects. This is only truly valid with fluid media where the shear modulus is zero, and the use of acoustic wave equation on solid earth medium is only justifiable for P-wave first arrival processing with an active source that produces minimal S-waves. Moreover, the acoustic wave equation is less computationally intensive compared to the elastic and numerous reflection seismic processing algorithms assume an acoustic earth model (Fichtner, 2011).

Acoustic wave propagation through inhomogeneous media is expressed by the following equation in 2-dimensional space:

$$\nabla^2 \emptyset(x,z,t) = \frac{1}{c^2(x,z)} \frac{\partial^2}{\partial t^2} \emptyset(x,z,t) \qquad (3.23)$$

Here, $\emptyset(x,z,t)$ is the 2D wavefield and c is the velocity. Using the second-order finite-difference approximation equation (3.19) becomes:

$$\nabla^2\emptyset(x,z,t) = \frac{1}{\Delta t^2 c^2(x,z)}[\emptyset(x,z,t+\Delta t) - 2\emptyset(x,z,t) + \emptyset(x,z,t-\Delta t)] \quad (3.24)$$

Then:

$$\emptyset(x,z,t+\Delta t) = [2 + \Delta t^2 c^2(x,z)\nabla^2]\emptyset(x,z,t) - \emptyset(x,z,t-\Delta t) \quad (3.25)$$

Results from equation (3.21) give the wavefield at time $t + \Delta t$ calculated from two earlier times t and $t - \Delta t$ (Margrave, 2003; Ahmadi, 2015).

To achieve a stable and accurate numerical simulation, careful consideration of the grid spacing h is needed which satisfies the following equation to avoid grid dispersion:

$$h < \frac{\lambda_{min}}{n} \quad (3.26)$$

Here, λ_{min} is the minimum wavelength and n is the sum of the order in space and length in time of the finite-difference operator (Bohlen et al., 2015). Time-stepping Δt is required for amplitudes that grow without bounds to ensure stable simulations as follows:

$$\Delta t < const\,\frac{h_{min}}{c_{max}} \quad (3.27)$$

Here, h_{min} is the minimum grid spacing and c_{max} represents the maximum velocity in the model. The scaling constant coefficient is calculated from space and time discretization (Fichtner, 2011).

Figure 3.16 shows an example of the synthetic shot gather (Figure 3.16a) and the real unprocessed shot gather (Figure 3.16b) from the data reprocessed on **Paper I**. The synthetic shot gather was created using the acoustic finite-difference modelling with acquisition parameters similar to real acquisition parameters to enable comparison. The geological model and subsurface parameters were created from the previous physical property and geological studies (Pretorius, 1964; Antrobus, 1986; Manzi et al., 2013) conducted in the Witwatersrand Basin in the past. Both synthetic and real data sets show clear first breaks (FB) and reflections (green arrows). Figure 3.17a shows the geological model of the subsurface produced by Antrobus (1986) parallel to the legacy profile reprocessed in **Paper I** and Figure 3.17b shows an image of the geological model used for finite-difference numerical modelling in **Paper I**.

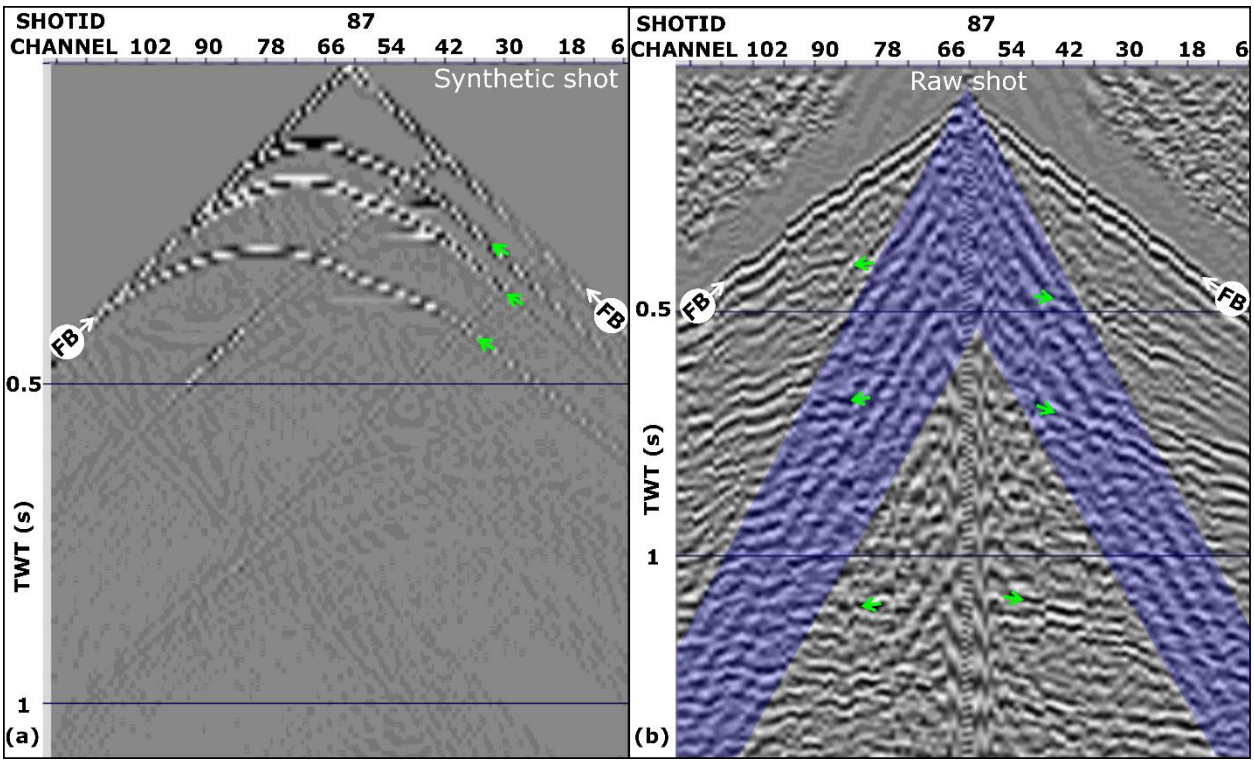


Figure 3.16: Example of a synthetic (a) and real (b) shot gather from the data reprocessed on **Paper I**, with clear first breaks (FB) and reflections (green arrows) on both data sets. The direct waves are highlighted in blue.

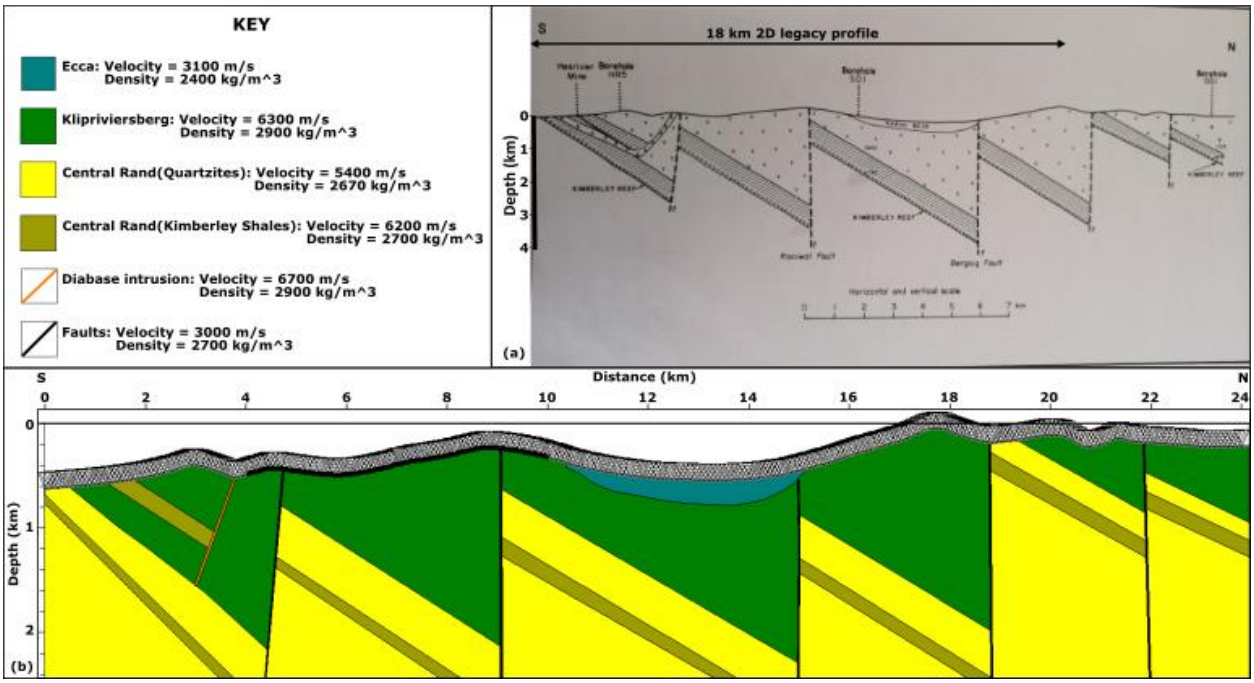


Figure 3.17: (a) Geological model created by Antrobus (1986) parallel to the legacy profile

reprocessed in **Paper I**. (b) Geological model used for finite-difference numerical modelling in **Paper I**.

4 References

Ahmadi O. 2015. Application of the Seismic Reflection Method in Mineral Exploration and Crustal Imaging. Unpub. PhD. Thesis. Uppsala Universitet, Uppsala, Sweden.

Antrobus E.S.A. 1986. The South Rand goldfield. In: Anhaeusser, C.R., Maske, S. (Eds.). Mineral Deposits of Southern Africa, vol. 1. Geological Society of South Africa, Johannesburg, 689–703.

Ayarza P., Juhlin C., Brown D., Beckholmen M., Kimbell G., Pechnig R., Pevzner L., Pevzner R., Ayala C., Bliznetsov M. and Glushkov A. 2000. Integrated geological and geophysical studies in the SG4 borehole area, Tagil Volcanic Arc, Middle Urals: Location of seismic reflectors and source of the reflectivity. *Journal of Geophysical Research: Solid Earth*, **105**(B9), 21333-21352.

Basson I. J. 2019. Cumulative deformation and original geometry of the Bushveld Complex. *Tectonophysics* **750**, 177-202. https://doi.org/10.1016/j.tecto.2018.11.004

Beach, A. and Smith, R., 2007. Structural geometry and development of the Witwatersrand Basin, South Africa. *Geological Society, London, Special Publications* **272**(1), pp.533-542. https://doi.org/10.1144/GSL.SP.2007.272.01.27

Bellefleur G., Malehmir A., Müller C. 2012. Elastic finite-difference modeling of volcanic-hosted massive sulfide deposits: A case study from Half Mile Lake, New Brunswick, Canada. *Geophysics* **77**(5), WC25–WC36. https://doi.org/10.1190/geo2011-0445.1

Biesheuvel K. 1970. An interpretation of a gravimetric survey in the area west of the Pilanesberg in the Western Transvaal. *Geological Society of South Africa, Special Publication* **1**, pp.266-282.

Bohlen T., Nil D. D., Köhen D., Jetschny S. 2015. SOFI3D - Seismic Modeling with Finite differences, 3D-acoustic and viscoelastic version- User Guide.

Buske S., Gutjahr S. and Sick C. 2009. Fresnel volume migration of single-component seismic data. *Geophysics* **74**(6), WCA47-WCA55. https://doi.org/10.1190/1.3223187

Campbell G., 2011. Exploration geophysics of the Bushveld complex in South Africa. *The Leading Edge* **30**(6), pp.622-638. https://doi.org/10.1190/1.3599148

967 Campbell G. and Peace D. G. 1984. Seismic reflection experiments for gold exploration, Wits
968 Basin, Republic of South Africa. In *6th Meeting and Technical Exhibition. European*
969 *Association of Exploration Geophysicists, London (June 19–22)*.
970 Castagna J. P., Batzle M. L. and Eastwood R. L. 1985. Relationships between compressional-
971 wave and shear-wave velocities in clastic silicate rocks. *Geophysics* **50**(4), 571-581.
972 https://doi.org/10.1190/1.1441933
973 Carlson R. L. and Jay Miller D. 2004. Influence of pressure and mineralogy on seismic velocities
974 in oceanic gabbros: Implications for the composition and state of the lower oceanic crust.
975 *Journal of Geophysical Research: Solid Earth* **109**(B9).
976 https://doi.org/10.1029/2003JB002699
977 Cawthorn R. G. 2015. The Bushveld Complex, South Africa. In B. Charlier, O. Namur, R.
978 Latypov, & C. Tegner (Eds.), *Layered Intrusions* (pp. 517–587). Dordrecht: Springer
979 Netherlands. https://doi.org/10.1007/978-94-017-9652-1_12
980 Cawthorn R. G. 2006. Centenary of the Discovery of Platinum in the Bushveld Complex.
981 *Platinum Metals Review* **50**(3), 30-133.
982 Cawthorn R.G. and Webb S.J. 2001. Connectivity between the western and eastern limbs of the
983 Bushveld Complex. *Tectonophysics* **330**(3-4), 195-209.
984 https://doi.org/10.1016/S0040-1951(00)00227-4
985 Cawthorn, R.G., 1998. Geometrical relations between the Transvaal Supergroup, the Rooiberg
986 Group, and the mafic rocks of the Bushveld Complex. *South African Journal of Geology*
987 **101**(4), pp.275-279. https://hdl.handle.net/10520/EJC-1ac397cef9
988 Cheraghi S., Malehmir A. and Bellefleur G. 2011. Crustal-scale reflection seismic investigations
989 in the Bathurst Mining Camp, New Brunswick, Canada. *Tectonophysics* **506**(1-4), 55-72.
990 https://doi.org/10.1016/j.tecto.2011.04.011
991 Chun J. H. and Jacewitz C. A. 1978. A fast multi-velocity function frequency domain migration,
992 presented at 48th Ann. *Mtg of SEG, San Francisco*.
993 Christensen N. I. 1965. Compressional wave velocities in metamorphic rocks at pressures to 10
994 kilobars. *Journal of Geophysical Research* **70**(24), 6147-6164.
995 https://doi.org/10.1029/JZ070i024p06147
996 Claerbout J. F. 1985. Imaging the earth's interior (Vol. 1). *Oxford: Blackwell scientific*
997 *publications*.

998 Cosma C., Olsson O., Keskinen J. and Heikkinen P. 2001. Seismic characterization of
999 fracturing at the Äspö Hardrock Laboratory, Sweden, from the kilometer scale to the meter
1000 scale. *International Journal of Rock Mechanics and Mining Sciences* **38**(6), 859-865.
1001 https://doi.org/10.1016/S1365-1609(01)00051-X
1002 Cousins C. A. 1959. The structure of the mafic portion of the Bushveld Igneous Complex.
1003 *Transactions of the Geological Society of South Africa* **62**, 79-189.
1004 Dankert B. T. and Hein K. A. A. 2010. Evaluating the structural character and tectonic
1005 history of the Witwatersrand Basin. *Precambrian Research* **177**(1-2), 1–22.
1006 https://doi.org/10.1016/j.precamres.2009.10.007
1007 Decker L., Merzlikin D. and Fomel S. 2017. Diffraction imaging and time-migration velocity
1008 analysis using oriented velocity continuation. *Geophysics* **82**(2), U25-U35.
1009 Donoso G. A., Malehmir A., Pacheco N., Araujo V., Penney M., Carvalho J., Spicer B. and
1010 Beach S. 2020. Potential of legacy 2D seismic data for deep targeting and structural
1011 imaging at the Neves–Corvo massive sulphide-bearing deposit, Portugal. *Geophysical*
1012 *Prospecting* **68**(1), 44-61. https://doi.org/10.1111/1365-2478.12861
1013 Duncan G. and Beresford G. 1994. Slowness adaptive fk filtering of prestack seismic data.
1014 *Geophysics* **59**(1), 140-147. https://doi.org/10.1190/1.1443525
1015 Du Plessis A. and Levitt J. G. 1987. On the structure of the Rustenburg layered suite—insight
1016 from seismic reflection data. *Indaba on the tectonic setting of layered intrusives*.
1017 Durrheim R. J. 1986. Recent reflection seismic developments in the Witwatersrand basin.
1018 *Reflection seismology: A global perspective* **13**, 77-83.
1019 https://doi.org/10.1029/GD013p0077
1020 Eaton D., Milkereit B. and Salisbury M. 2003. Hardrock seismic exploration: Mature
1021 technologies adapted to new exploration targets, Foreword to hardrock seismic
1022 exploration: *SEG Geophysical Developments* **10**, 1– 6.
1023 Eglington B. M. and Armstrong R. A. 2004. The Kaapvaal Craton and adjacent orogens,
1024 southern Africa: a geochronological database and overview of the geological
1025 development of the craton. *South African Journal of Geology* **107**(1-2), pp.13-32.
1026 https://doi.org/10.2113/107.1-2.13
1027 Elbra T., Karlqvist R., Lassila I., Hæggström E. and Pesonen L. J. 2011. Laboratory

measurements of the seismic velocities and other petrophysical properties of the Outokumpu deep drill core samples, eastern Finland. *Geophysical Journal International* **184**(1), 405-415. https://doi.org/10.1111/j.1365-246X.2010.04845.x

Eriksson P. G., Altermann W., Hartzer F. J., 2007. The Transvaal Supergroup and its precursors. In: Johnson M. R., Anhaeusser C. R., Thomas R. J. (Eds.), The Geology of South Africa. Geological Society of South Africa, Johannesburg/Council for Geoscience, Pretoria, pp. 237–260.

Eriksson P. G., Altermann W., Catuneanu O., Van der Merwe R. and Bumby A. J. 2001. Major influences on the evolution of the 2.67–2.1 Ga Transvaal basin, Kaapvaal craton. *Sedimentary Geology* **141**, 205-231. https://doi.org/10.1016/S0037-0738(01)00075-6

Etgen J., Gray S. and Zhang Y. 2009. An overview of depth imaging in exploration geophysics: *Geophysics* **74**, WCA5-WCA1.

Etgen J. T. and Kumar C. 2012. November. What really is the difference between Time and Depth Migration? A tutorial. In *2012 SEG Annual Meeting*. OnePetro.

Farrell R. C. and Euwema R. N. 1984. Refraction statics. *Proceedings of the IEEE* **72**(10), 1316 1329. Doi: 10.1109/PROC.1984.13020

Fichtner A. 2011. Full seismic waveform modelling and inversion. *Springer Science & Business Media.*

Gardner J. N., Goff F., Garcia S. and Hagan R. C. 1986. Stratigraphic relations and lithologic variations in the Jemez volcanic field, New Mexico. *Journal of Geophysical Research: Solid Earth* **91**(B2), 1763-1778. https://doi.org/10.1029/JB091iB02p01763

Good N. and De Wit M. J. 1997. The Thabazimbi-Murchison lineament of the Kaapvaal craton, South Africa: 2700 Ma of episodic deformation. *Journal of the Geological Society* **154**(1), pp.93-97. https://doi.org/10.1144/gsjgs.154.1.0093

Green A. G. and Mair J. A. 1983. Subhorizontal fractures in a granitic pluton; their detection and implications for radioactive waste disposal. *Geophysics* **48**(11), 1428-1449. https://doi.org/10.1190/1.1441428

Greenhalgh S. and Manukyan E. 2013. Seismic Reflection for Hardrock Mineral Exploration: Lessons from Numerical Modeling Seismic Reflection in Mineral Exploration. *Journal of Environmental and Engineering Geophysics* **18**(4), 281-296. https://doi.org/10.2113/JEEG18.4.281

Hall A. L. 1932. The Bushveld Igneous Complex of the central Transvaal. South African Geological Survey Memoir, 28, Pretoria, 560 pp.

Hall R. B. 1988. Hardrock versus softrock geology. *General Geology. Encyclopedia of Earth Science. Springer, Boston, MA.* 9, 1960-1963. https://doi. org/10.1007/0-387-30844-X_55

Haskell N. A. 1953. Dispersion of surface waves on multilayered media, *Bull. Seism. Soc. Am*. **43**, 17-34.

Hloušek F. and Buske S. 2016. Fresnel Volume Migration of the ISO89-3D data set. *Geophysical Supplements to the Monthly Notices of the Royal Astronomical Society* **207**(2), pp.1273-1285. https://doi.org/10.1093/gji/ggw336

Hloušek F., Hellwig O. and Buske S. 2015a. Three-dimensional focused seismic imaging for geothermal exploration in crystalline rock near Schneeberg, Germany. *Geophysical Prospecting* **63**(4), 999-1014. https://doi.org/10.1111/1365-2478.12239

Hloušek F., Hellwig O. and Buske S. 2015b. Improved structural characterization of the Earth's crust at the German Continental Deep Drilling Site using advanced seismic imaging techniques. *Journal of Geophysical Research: Solid Earth* **120**(10), 6943-6959. https://doi.org/10.1002/2015JB012330

Hunt, E.J., Latypov, R. and Horvath, P., 2018. The Merensky cyclic unit, Bushveld complex, South Africa: reality or myth?. *Minerals* **8**(4), p.144. https://doi.org/10.3390/min8040144

Juhlin C. and Stephens M. B. 2006. Gently dipping fracture zones in Paleoproterozoic metagranite, Sweden: Evidence from reflection seismic and cored borehole data and implications for the disposal of nuclear waste. *Journal of Geophysical Research: Solid Earth* **111**(B9). https://doi.org/10.1029/2005JB003887

Juhlin C. 1995. Imaging of fracture zones in the Finnsjon area, central Sweden, using the seismic reflection method. *Geophysics* **60**(1), 66-75. https://doi.org/10.1190/1.1443764

Juhlin C., Lindgren J. and Collini B. 1991. Interpretation of seismic reflection and borehole data from Precambrian rocks in the Dala Sandstone area, central Sweden. *First Break* **9**(1). https://doi.org/10.3997/1365-2397.1991002

Kearey P., Brooks M. and Hill I. 2002. An introduction to geophysical exploration (3rd ed). *Malden, MA: Blackwell Science*.

Kern H., Mengel K., Strauss K. W., Ivankina T. I., Nikitin A. N. and Kukkonen I.T. 2009. Elastic wave velocities, chemistry and modal mineralogy of crustal rocks sampled by the Outokumpu scientific drill hole: Evidence from lab measurements and modeling. *Physics of the Earth and Planetary Interiors* **175**(3-4), pp.151-166. https://doi.org/10.1016/j.pepi.2009.03.009

Kositcin N. and Krapež B. 2004. Relationship between detrital zircon age-spectra and the tectonic evolution of the Late Archaean Witwatersrand Basin, South Africa. *Precambrian Research* **129**(1-2), 141-168. https://doi.org/10.1016/j.precamres.2003.10.011

Kruger F. J. 2005. Filling the Bushveld Complex magma chamber: lateral expansion, roof and floor interaction, magmatic unconformities, and the formation of giant chromitite, PGE and Ti-V-magnetitite deposits. *Mineralium Deposita* **40**, 451-472. https://doi.org/10.1007/s00126-005-0016-8

Kuhn M. J. and Alhilali K. A. 1977. Weighting factors in the construction and reconstruction of acoustical wave fields. *Geophysics* **42**(6), 1183-1198. https://doi.org/10.1190/1.1440783

Larner K., Gibson B. R., Chambers R. and Wiggins R. A. 1979. Simultaneous estimation of residual static and crossdip corrections. *Geophysics* **44**(7), pp.1175-1192. https://doi.org/10.1190/1.1441001

Mair J. A. and Green A.G. 1981. High-resolution seismic reflection profiles reveal fracture zones within a 'homogeneous' granite batholith. *Nature* **294**(5840), 439-442.

Malehmir A., Donoso G., Markovic M., Maries G., Dynesius L., Brodic B., Pecheco N., Marsden P., Bäckström E., Penney M. and Araujo V. 2019. Smart Exploration: from legacy data to state-of-the-art data acquisition and imaging. *First Break* **37**(8), 71-74. https://doi.org/10.3997/1365-2397.n0049

Malehmir A., Bellefleur G., Koivista E. and Juhlin C. 2017. Pros and cons of 2D vs 3D seismic mineral exploration surveys. *First Break* **35**(8). https://doi.org/10.3997/1365-2397.35.8.89805

Malehmir A., Durrheim R. J., Bellefleur G., Urosevic M., Juhlin C., White D. J., Milkereit B. and Campbell G. 2012. Seismic methods in mineral exploration and mine planning: A general overview of past and present case histories and a look into the future. *Geophysics* **77**(5), WC173–WC190. https://doi.org/10.1190/geo2012-0028.1

Malehmir A. and Bellefleur G. 2010. Reflection seismic imaging and physical properties of

base-metal and associated iron deposits in the Bathurst Mining Camp, New Brunswick, Canada. *Ore Geology Reviews* **38**(4), 319-333. https://doi.org/10.1016/j.oregeorev.2010.08.002

Manzi M. S. D., Hunt E. J. and Durrheim R. J. 2019a. 3D Reflection Seismic Imaging for Gold and Platinum Exploration, Mine Development, and Safety: Case Studies from the Witwatersrand Basin and Bushveld Complex (South Africa). *Ore Deposits: Origin, Exploration, and Exploitation* 237-256. https://doi.org/10.1002/9781119290544.ch11

Manzi M. S. D., Malehmir A. and Durrheim R. J. 2019b. Giving the legacy seismic data the attention they deserve. *First Break* **37**(8), 89-96. https://doi.org/10.3997/1365-2397.n0050

Manzi M. S. D., Malehmir A. and Durrheim R. J. 2018. September. Improved Subsurface Imaging through Re-processing of Legacy 2D Seismic Data-A Case Study from a Deep South African Gold Mine. In *2nd Conference on Geophysics for Mineral Exploration and Mining* **2018**(1), 1-5. EAGE Publications BV. https://doi.org/10.3997/2214-4609.201802705

Manzi M., Cooper G., Malehmir A., Durrheim R. J. and Nkosi Z. 2015. Integrated interpretation of 3D seismic data to enhance the detection of the gold-bearing reef: Mponeng Gold mine, Witwatersrand Basin (South Africa). *Geophysical Prospecting* **63**(4-Hard Rock Seismic imaging), pp.881-902. https://doi.org/10.1111/1365-2478.12273

Manzi M. S. D., Hein K. A. A., King N. and Durrheim R. J. 2013a. Neoarchaean tectonic history of the Witwatersrand Basin and Ventersdorp Supergroup: New constraints from high-resolution 3D seismic reflection data. *Tectonophysics* **590**, 94-105. https://doi.org/10.1016/j.tecto.2013.01.014

Manzi M. S. D., Hein K. A. A., Durrheim R. J. and King N. 2013b. Seismic attribute analysis to enhance detection of thin gold-bearing reefs: South Deep gold mine, Witwatersrand basin, South Africa. *Journal of Applied Geophysics* **98**, 212-228. https://doi.org/10.1016/j.jappgeo.2013.08.017

Manzi M. S. D. 2013. Application of 3D seismic analysis techniques to evaluate ore resources on Kloof, South Deeps and Driefontein gold mines, Witwatersrand Basin, South Africa. Unpub. PhD. Thesis. University of the Witwatersrand, Johannesburg, South Africa.

Manzi M. S., Gibson M. A., Hein K. A., King N. and Durrheim R. J. 2012. Application of 3D

seismic techniques to evaluate ore resources in the West Wits Line goldfield and portions of the West Rand goldfield, South Africa. *Geophysics* **77**(5), pp. WC163-WC171. https://doi.org/10.1190/geo2012-0133.1

Margrave G. F. 2003. Numerical Methods of Exploration Seismology with algorithms in MATLAB. CREWES, Department of Geology and Geophysics, University of Calgary.

Mathur S. P., Moss F. J. and Branson J. C. 1977. Seismic and gravity investigations along the geotraverse, western Australia. *Bur. Miner. Resour. Aust. Bull.* **191,** 1-63.

Meunier J. 2011. Seismic Acquisition from Yesterday to Tomorrow. *Society of Exploration Geophysicists*.

Milkereit B. and Eaton D. 1998. Imaging and interpreting the shallow crust: *Tectonophysics* **286**(4), 5–18. https://doi.org/10.1016/S0040-1951(97)00251-5

Moss F. J. and Jones P. 1974. Ngalia basin seismic survey, Northern Territory, 1967-1969: Bur. *Mineral Res. Australia, Records* **49**.

Nedimović M. R. and West G. F. 2003. Crooked-line 2D seismic reflection imaging in crystalline terrains: Part 2, migration. *Geophysics* **68**(1), pp.286-296. https://doi.org/10.1190/1.1543214

Neidell N. S. and Taner M. T. 1971. Semblance and other coherency measures for multichannel data. *Geophysics* **36**(3), 482-497. https://doi.org/10.1190/1.1440186

Nkosi N. Z., Manzi M. S. D., Westgate M., Roberts D., Durrheim R. J., Ogasawara H., Ziegler M., Rickenbacher M., Liebenberg B., Onstott T. C. and Team D. 2022. Physical property studies to elucidate the source of seismic reflectivity within the ICDP DSeis seismogenic zone: Klerksdorp goldfield, South Africa. *International Journal of Rock Mechanics and Mining Sciences* **155**, 105082. https://doi.org/10.1016/j.ijrmms.2022.105082

Nkosi N. Z., Manzi M. S. D., Drennan G. R. and Yilmaz H. 2017. Experimental measurements of seismic velocities on core samples and their dependence on mineralogy and stress; Witwatersrand Basin (South Africa). *Studia Geophysica et Geodaetica* **61**, 115-144.

Noponen I., Heikkinen P. and Mehrotra S. 1979. Applicability of seismic reflection sounding in regions of Precambrian geology. *Geoexploration* **17**(1), 1-9. https://doi.org/10.1016/0016-7142(79)90002-4

Odgers A. T. R, Hinds R. C. and von Gruenewaldt, G. 1993. Interpretation of a seismic reflection

survey across the southern Bushveld Complex. *South African journal of geology* **96**(4), pp.205-212.

Peacock K. L. and Treitel S. 1969. Predictive deconvolution: theory and practice. *Geophysics* **34** (2), 155–169. https://doi.org/10.1190/1.1440003

Perez R., 2010. Seismic Reflection Method Made in Oklahoma. *2010 International Symposium, Lafayette, Louisiana.*

Podvin P. and Lecomte I. 1991. Finite difference computation of traveltimes in very contrasted velocity models: a massively parallel approach and its associated tools. *Geophysical Journal International* **105**(1), 271-284. https://doi.org/10.1111/j.1365-246X.1991.tb03461.x

Porsani M. J., Silva M. G., Melo P. E. and Ursin B. 2010. SVD filtering applied to ground-roll attenuation. *Journal of Geophysics and Engineering* **7**(3), pp.284-289. https://doi.org/10.1088/1742-2132/7/3/007

Poujol M., Robb L. J., Anhaeusser C. R. and Gericke B., 2003. A review of the geochronological constraints on the evolution of the Kaapvaal Craton, South Africa. *Precambrian research* **127**(1-3), pp.181-213. https://doi.org/10.1016/S0301-9268(03)00187-6

Pretorius C. C., Jamison A. A. and Irons C. 1989. Seismic exploration in the Witwatersrand Basin, Republic of South Africa: *Proceedings Exploration* **87**, Third Decennial International Conference on Geophysics and Geochemical Exploration for Minerals and Groundwater: Special Publication, *Ontario Geologic Survey* **3**, 241–253.

Pretorius D.A. 1964b. The geology of the South Rand Goldfield. In: Haughton, S.H. (Ed.). The Geology of Some Ore Deposits in Southern Africa. Geological Society of South Africa, Johannesburg, 219–282.

Pritchett W. C. 1991. System design for better seismic data. *The Leading Edge* **10**(11), 30-35. https://doi.org/10.1190/1.1436789

Punturo R., Kern H., Cirrincione R., Mazzoleni P. and Pezzino A. 2005. P- and S-wave velocities and densities in silicate and calcite rocks from the Peloritani Mountains, Sicily (Italy): The effect of pressure, temperature and the direction of wave propagation. *Tectonophysics* **409**(1-4), 55-72. https://doi.org/10.1016/j.tecto.2005.08.006

Robinson E. A. and Treitel S. 1967. Principles of digital Wiener filtering. *Geophysical prospecting* **15**(3), 311-332. https://doi.org/10.1111/j.1365-2478.1967.tb01793.x

Salisbury M. H., Harvey C. W., Matthews L., Eaton D. W. and Milkereit B. 2003. The acoustic properties of ores and host rocks in hardrock terranes. *Hardrock seismic exploration: SEG*, 9-19.

Scheiber-Enslin S.E. and Manzi M. S. D. 2018. Integration of 3D reflection seismics and magnetic data for deep platinum mine planning and risk mitigation: a case study from Bushveld Complex, South Africa. *Exploration Geophysics* **49**(6), 928-939. https://doi.org/10.1071/EG17083

Schmelzbach C., Greenhalgh S., Reiser F., Girard J.F., Bretaudeau F., Capar L. and Bitri A. 2016. Advanced seismic processing/imaging techniques and their potential for geothermal exploration. *Interpretation* **4**(4), SR1-SR18. https://doi.org/10.1190/INT-2016-0017.1

Schneider W. A. 1978. Integral formulation for migration in two and three dimensions. *Geophysics* **43**(1), 49-76. https://doi.org/10.1190/1.1440828

Sheriff R. E. 2002. Encyclopedic dictionary of applied geophysics. *Society of exploration geophysicists.*

Stein S. and Wysession M. 2009. An introduction to seismology, earthquakes, and earth structure. *John Wiley & Sons*.

Spencer R. M. 1992. Late Archaean Tectonics and Sedimentation of the South Rand Area, Witwatersrand Basin. PhD Thesis, University of the Witwatersrand, Johannesburg.

Telford W. M., Geldart L. P. and Sheriff R. E. 1990. Applied geophysics. *Cambridge university press.*

Tucker R. F., Viljoen R. P. and Viljoen M. J. 2016. A Review of the Witwatersrand Basin-The World's greatest goldfield. *Episodes Journal of International Geoscience* **39**(2), 104-133. https://doi.org/10.18814/epiiugs/2016/v39i2/95771

Treitel S. 2005. The MIT geophysical analysis group (GAG): 1954 and beyond. *Geophysics* **70**(4), 31JA-35JA. https://doi.org/10.1190/1.1993707

Van Buren R., Turner G. and Hird G. 2019. June. Modern seismic is illuminating the depths. In *Deep Mining 2019: Proceedings of the Ninth International Conference on Deep and High Stress Mining*, 363-374. The Southern African Institute of Mining and Metallurgy. https://doi.org/10.36487/ACG_rep/1952_27_van_Buren

Van der Heever D., Oelofse J. and Bentle P. 2009. Revised Technical Report Update of

the June 21, 2007, Technical Report (Optimized Feasibility Study), Inclusive of Updated. Mineral Resource and Reserve Estimates for the Burnstone Gold Project. Unpublished Company Report to Great Basin Gold Limited.

Van der Merwe M. J. 1976. The layered sequence of the Potgietersrus limb of the Bushveld Complex. *Economic Geology* **71**(7), pp.1337-1351. https://doi.org/10.2113/gsecongeo.71.7.1337

Van der Westhuizen W. A., De Bruiyn H. and Meintjes P. G. 1991. The Ventersdorp supergroup: an overview. *Journal of African Earth Sciences (and the Middle East)* **13**(1), pp.83-105. https://doi.org/10.1016/0899-5362(91)90045-Z

Vidale J.E. 1990. Finite-difference calculation of traveltimes in three dimensions. *Geophysics* **55**(5), 521-526. https://doi.org/10.1190/1.1442863

Vidale J. 1988. Finite-difference calculation of travel times. *Bulletin of the Seismological Society of America* **78**(6), 2062-2076. https://doi.org/10.1785/BSSA0780062062

Walraven F. and Darracott B. W. 1976. Quantitative interpretation of a gravity profile across the western Bushveld Complex. *South African Journal of Geology* **79**(1), pp.22-26.

Webb S. J., Cawthorn R. G., Nguuri T. and James D. 2004. Gravity modeling of Bushveld Complex connectivity supported by Southern African seismic experiment results. *South African Journal of Geology* **107**(1-2), pp.207-218. https://doi.org/10.2113/107.1-2.207

Westgate M., Manzi M. S. D., James I. and Harrison W. 2020. New insights from legacy seismic data: reprocessing of legacy 2D seismic data for imaging of iron-oxide mineralization near Sishen Mine, South Africa. *Geophysical Prospecting* **68**(7), 2119–2140. https://doi.org/10.1111/1365-2478.12996

Whitmore N. D., Gray S. H. and Gersztenkorn A. 1988. Two-dimensional post-stack depth migration: a survey of methods. *First Break* **6**(6). https://doi.org/10.3997/1365-2397.1988010

Wiener N. 1949. Extrapolation, Interpolation, and Smoothing of Stationary Time Series. Report of the Services 19, Research Project DIC-6037 MIT.

Willis M. 2022. Distributed Acoustic Sensing for Seismic Measurements ? What Geophysicists and Engineers Need to Know, Distinguished Instructor Series. *Society of Exploration Geophysicists*.

Witthüser K. T., Holland M., Seidel T. and König C. M. 2015. Numerical modelling of mine

dewatering and flooding in the Evander gold basin, South Africa. *South African Journal of Geology* **118**(1), pp.71-82. https://doi.org/10.2113/gssajg.118.1.71

Woodward M. J. 1992. Wave-equation tomography. *Geophysics*, **57**(1), 15-26.

Yilmaz Ö. 2001. Seismic data analysis: Processing, inversion, and interpretation of seismic data. *Society of exploration geophysicists*.

Yilmaz O. 1987. Seismic deta processing. *Investigation in geophysics* **2**, 526.

Zhang J. and Toksöz M. N. 1998. Nonlinear refraction traveltime tomography. *Geophysics*, **63**(5), 1726-1737.

5 **Paper I:** Seismic delineation of the gold-bearing structures in the South Rand Goldfield (South Africa) – a comparison of pre-stack time and depth migration approaches on legacy seismic data

5.1 Paper Summary

The legacy seismic profile reprocessed in this paper is 18 km long and it was collected near Burnstone mine on the eastern margin of the Witwatersrand Basin approximately 100 km southeast of Johannesburg. The profile was collected over Ventersdorp metabasalts outcrop and Karoo sediments in the South Rand goldfield. The profile was acquired in 1993 by the Gold Division of Anglo-American Corporation as part of their gold exploration programme. To delineate the geometry of gold-bearing horizons and complex geological structures near Burnstone mine, this legacy reflection seismic profile was reprocessed using today's reflection seismic processing algorithms.

Burnstone mine is a newly developed mine operating in the South Rand goldfield, which started gold production under Great Basin Gold in 2011 until it was placed under care two years later because the production team was extracting increased volumes of mine waste. They encountered unexpected geological structures, and in 2014 Sibanye Stillwater acquired the mine in hopes to extend exploration to greater depth. To date, the mine is under developmental stages and reprocessing of the legacy profile near the mine aims to delineate the target gold- reef and these geological structures that complicate mining. We envision that results from this study will aid in mine development and resource evaluation at Burnstone mine.

Since the acquisition of this data, there have been numerous processing algorithms developed to improve reflection seismic imaging in hardrock environment. Pre-stack migration techniques were not commonly applied in hardrock environment and the physical properties studies of the Witwatersrand lithostratigraphy have been improved. Consequently, these improvements and the experience gained in hardrock seismic imaging since its inception played a major role improving the imaging of the target geological structures and the gold reef. Reprocessing this data imaged reflections associated with the gold reef, For example, the footwall Kimberley shales and the hanging wall contact between the Central Rand quartzites and the Ventersdorp metabasalts. Additionally, the unconformity between the Ventersdorp and Karoo Supergroups was illuminated

and dolerite sill intrusion in the Karoo Supergroup was clearly delineated. However, all these reflections were missed by the legacy stack, consequently, all the geological structures mapped from the discontinuities of these reflections were not identifiable on the legacy stack.

The study shows that Kirchhoff pre-stack depth migration (KPreSDM) performs superior over Kirchhoff pre-stack time migration (KPreSTM) in hardrock environment, especially in regions with intrusions that introduce high lateral velocity gradients. KPreSDM clearly delineated the dolerite sill intrusion on the near surface Karoo sediments. The results from reprocessing the profile improved the continuity of the reflections that were clearly missed by the initial processing of the data.

5.2 Manuscript

Seismic delineation of the gold-bearing structures in the South Rand Goldfield (South Africa) – a comparison of pre-stack time and depth migration approaches on legacy seismic data

Mpofana Sihoyiya[1*], Musa S.D. Manzi[1], Ian James[2], Moyagabo K. Rapetsoa[1], Michael Westgate[1], Glen Nwaila[1], Linzer Linsay[3], Raymond Durrheim[1], Philip Staley[4]

[1]School of Geosciences, University of the Witwatersrand Johannesburg, PBag 3, Wits, 2050, Republic of South Africa, [2]Terraspect, 42a Grosvenor Road, Bayswater Western Australia 6053,[3]SRK House, 265 Oxford Rd, Illovo, Johannesburg, 2196, Republic of South Africa, and [4]Sibanye-Stillwater, Waltevredenpark, Roodepoort, 1709, Republic of South Africa.

ABSTRACT

To better image complex geological structures and explore for the gold-bearing quartz pebble conglomerate (locally termed Kimberley Reef) near Burnstone mine in the South Rand goldfield (South Africa), we reprocessed legacy 2D reflection seismic data using up-to-date seismic processing algorithms. The mining region is dominated by steeply dipping normal and reverse faults, as well as dolerite intrusions that crosscut the tabular gold mineralisation and complicate the extraction of the ore. The legacy seismic data were acquired in 1993 in the South Rand goldfield as part of the gold exploration programme by the Gold Division of Anglo-American Corporation. The pre-stack data quality was improved by cautiously removing noise and applying

static corrections to enhance the continuity of the reflection events. Improved structural imaging was then achieved using pre-stack time migration (PreSTM) and pre-stack depth migration (PreSDM) through careful velocity analysis. In particular, PreSDM provided better imaging of near-surface stratigraphic units and deep-seated complex structures, relative to older post-stack migrated images produced in 1993. Other re-processing improvements include accurate imaging of key seismic reflective interfaces that can be used as proxies to 2D map gold deposit, its dip variations, and geological structures (faults/dykes) crosscutting it. Synthetic shot gathers data computed using 2D finite-difference algorithm provided some insight into the source of seismic reflections observed on the reprocessed seismic data. The new structural information from reprocessing is essential for enhancing ore resource evaluation and guiding future exploration projects in the region.

Keywords: Seismics; processing, exploration, imaging

INTRODUCTION

The Mesoarchaean Witwatersrand Basin in South Africa hosts some of the world's largest gold deposits and has produced more than one-third of the gold ever mined (Coward *et al.* 1995; Manzi *et al.* 2013; Frimmel 2019). The gently dipping tabular gold orebodies mainly occur in pebble-conglomerate beds (known as reefs). The majority of these deposits are concealed beneath cover rocks and mining takes place more than a kilometre below the surface (Durrheim 1986; Manzi *et al.* 2012a,b). During the 1930s, exploration drilling and potential field methods (mainly magnetics and gravity) were successfully used to map the extent of the Witwatersrand Basin. However, these methods were unable to adequately and accurately delineate the deeply buried gold-bearing strata. In the 1980s, the reflection seismic method was introduced in the Witwatersrand Basin for brownfields and greenfields exploration (Durrheim 1986). By the late 1990s, the Gold Division of Anglo-American Corporation had already acquired more than 16,000 km line of 2D reflection seismic data in the Witwatersrand Basin. The 2D seismic surveys provided information about the down-dip extensions of the orebody below thick cover rocks and delineated complex structural styles such as folds and faults that might have controlled gold mineralization and brought the reefs to mineable depths. These surveys represented the first reflection seismic surveys to be acquired for mineral exploration in hard rock environment worldwide. Following these successes, 2D and 3D reflection seismic surveys have been conducted for gold exploration and mine planning in the

Witwatersrand Basin and contributed to the discovery of new Witwatersrand goldfields (Manzi *et al.* 2018; Pretorius *et al.* 2003).

Generally, the gold-bearing conglomerate units of the Witwatersrand Basin are interbedded with other metasedimentary rocks such as shales and quartzites of which some have similar seismic velocities and densities, making direct imaging of these deposits with reflection seismics difficult. However, previous studies (e.g., Durrheim 1986; Manzi *et al.* 2012a,b) have shown that these gold deposits can be targeted using seismic methods because they are overlain by basaltic rocks and underlain by shale units, thus providing strongly reflective interfaces that can be used as proxies to map these reefs.

Decades after the processing of the legacy seismic in Witwatersrand Basin, computational power has increased and understanding of the hard rock seismic imaging has improved; new advanced approaches of seismic signal processing and depth imaging have been introduced. Moreover, a better understanding of the velocity fields from hard rock environment has shown significant improvement in depth imaging of complex geological structures. The objective of this study is to reprocess the 18 km long, 6 s TWT, legacy 2D reflection seismic profile acquired in 1993 near Burnstone mine in the South Rand goldfield of the Witwatersrand Basin (South Africa). The main aim of the study is to improve the quality of the final seismic images through careful reprocessing of the data for further understanding of the complex geometry of the gold-bearing quartz pebble conglomerate (locally termed Kimberley Reef) near Burnstone mine, as well as providing more details of complex structures and their relationship with the orebody. To the author's knowledge, there are no publications regarding the 1993 legacy 2D seismic profile near Burnstone mine. The mine is still in the developmental stages, and our new reprocessing results could contribute to the development of the mine and the evaluation of its resources.

Velocity information obtained from the latest 3D seismic surveys in the basin and geological information obtained from the drilling and geological mapping can help to produce synthetic models that can be used to constrain our seismic processing and interpretation. Several authors (e.g., Malehmir *et al.* 2019; Manzi *et al.* 2019; Westgate *et al.* 2020) have demonstrated through various case studies from hard rock environments how legacy reflection seismic data can be revisited and reprocessed to improve the quality of the data and delineate the complex geological structures that host mineral deposits.

Herein, we show the improvements of the seismic images through reprocessing of the 1993 data by applying up-to-date seismic processing approaches. We also propose some geological interpretations using the new results. We first review the legacy seismic data and identify poor quality areas. Then, we discuss the new processing and imaging results by comparing them with the 1993 legacy seismic data. We also tested and compared pre-stack time migration and pre-stack depth migration approaches, and the results were compared against the post-stack time migration results achieved in 1993. Finally, we discuss the improvement of structural imaging using updated velocity information.

BURNSTONE MINE AND SOUTH RAND GOLDFIELD

General information

The Burnstone mine is a relatively new gold mine in the South Rand goldfield, the north-eastern edge of the Mesoarchaean Witwatersrand Basin in the Kaapvaal Craton. Figure 1 shows a simplified geological map of the Witwatersrand Basin (Figure 1a) as well as the location of the Burnstone mine and surrounding areas in the South Rand goldfield (Figure 1b). The mine commenced exploration under Great Basin Gold (GBG) in 2011 until placed under care about a year later, and in 2014 it was bought by Sibanye Stillwater. Pretorius (1964) outlined a detailed history of mining operations in the South Rand goldfield. In summary, exploration in the South Rand goldfield commenced in 1886 yielding 4.8 grams of gold per ton, a minimum amount of gold in comparison with the other goldfields (Pretorius 1964; Spencer 1992). Small scale mines were being explored in the area for ~70 years until they came to a holt in 1962. Amongst these mines, the old Roodepoort-Kildare mine (Figure 1b) was one of the largest producers of gold in the area. Burnstone mine is currently the only mine being explored for gold in the South Rand goldfield, yielding approximately 6 – 23 grams of gold per ton (Frimmel and Nwaila 2020). Sibanye Stillwater is assessing the feasibility of deepening the Burnstone mine to access gold reserves up to a depth of 1.3 km below surface. The new project, covering Burnstone mine and surrounding areas, aims to access the Kimberley reefs (known as UK9A) located approximately 200 m below the basaltic rocks of the Ventersdorp Supergroup and approximately 100 m above the Chloritoid Shale Marker (MK1) of the Kimberley Formation (Figures 2 and 3). Sibanye Stillwater is concerned about structural complexity of the lease area around the mine. Therefore, we envision

that the reprocessing of the legacy seismic data could provide improved structural information and minimize geological risks during drilling.

Geological and structural setting

There is a vast amount of literature on the geology and stratigraphy of the Witwatersrand goldfields, including Dankert and Hein (2010), Tucker *et al.* (2016), and Manzi *et al.* (2013). However, due to the thinness of the basin edge, the South Rand goldfield has not attracted a lot of studies as it is believed to comprise only one economically viable gold-bearing horizon (UK9A) (Spencer, 1992; Van der Heever, 2009; Frimmel, 2019). The simplified stratigraphy of the South Rand goldfield is presented in Figure 2. In summary, the Witwatersrand Supergroup is subdivided into the West Rand Group (lower) and Central Rand Group (upper) (Dankert and Hein 2010). The West Rand Group comprises the lower Hospital Hill Subgroup, middle Government Subgroup, and upper Jeppestown Subgroup. The Central Rand Group, hosting 93% of the gold deposits being currently mined in the Witwatersrand Basin, is divided into the lower Johannesburg Subgroup and upper Turffontein Subgroup. The upper Central Rand Group is overlain by the basaltic lavas (Klipriviersberg Group) of the Ventersdorp Supergroup (Tucker *et al.* 2016).

The target orebody (UK9A) is a narrow gold-bearing conglomerate band (up to 2-m thick) and hosted within the quartzites and conglomerates of the Kimberley Formation of the Turffontein Subgroup. It is the only economically viable orebody in the South Rand goldfield; it is considered a composite reef and it is part of a group of multi-conglomerate bands that were previously regarded as secondary reefs due to their low grade (Tucker *et al.* 2016; Frimmel and Nwaila 2020). The Kimberley Formation unconformably overlies the Booysens shales and is overlain by the Elsburg Formation, which is in turn overlain by the Mondeor Formation in the upper portion of the Turffontein Subgroup (Tucker *et al.* 2016). The economic horizon of the Kimberley Formation is divided into four members, the basal MK3, overlain by the padding stone (MK2), which is in turn overlain by the Chloritoid Shale Marker (MK1) (Spencer 1992).

Structurally, the South Rand goldfield is characterized by major east-west trending fault systems that bound the area of interest in the north and south. The most dominant structures include: Sugarbush, Meyerskop, Balfour, and Bergsig faults, as well as their associated drag folds (e.g., Greylingstad monocline and Rietbult-Rustfontein antiform), which are attributed to extensional tectonics (Frimmel and Nwaila 2020) (Fig. 1b). The Sugarbush fault is downthrown to the south

by a maximum displacement of up to 3 km and is the reason for the preservation of the South Rand goldfield (Pretorius 1964; Spencer 1992; Van der Heever 2009). The regional faults and folds in the area deform the Witwatersrand Supergroup and the overlying Ventersdorp Supergroup (Pretorius 1964; Spencer 1992; Van der Heever 2009). The east-west trending Bergsig Fault (Fig. 1b) is particularly interesting since is crosscut by the 1993 seismic profile. The delineation of this structure through reprocessing of the legacy seismic is important for future mine planning and safety in this region.

LEGACY 2D SEISMIC DATA AND 2D SEISMIC MODELLING

Seismic data acquisition

We received the 18 km long legacy 2D seismic profile as raw shot gathers, stacked and post-stack migrated data with the acquisition parameters in the observer's report as a hard copy. The raw shot gathers were in SEG-Y format with the geometry information saved in the header files. The profile is located within the vicinity of the Burnstone project area, approximately 20 km south of the Burnstone mine (see Fig. 1). Table 1 provides the summary of the acquisition parameters of the profile.

In summary, the 2D seismic legacy profile was acquired in 1993 using a vibroseis truck as the energy source. The survey was designed with a sweep length of 16 s and a linear sweep frequency of 10 – 61 Hz, sampling at a rate of 2 ms to obtain high-resolution data. The receiver traces for each shot record were cross-correlated with the sweep signal during the acquisition process. The data were initially stored in SEGD format and later converted to the SEG-Y format. The line has an orientation that exhibits a NE-SW trend over the Klipriviersberg basalt outcrop. It runs from the centre of the goldfields near the old Roodepoort-Kildare mine to the southern edge of the South Rand goldfield near the old Hexrivier mine (see Fig. 1b). The profile was collected along the dirt road using a crooked seismic line geometry due to the variation of the terrain along the length of the line (Fig. 1b).

The seismic line has a total of 358 shots spaced at 50 m, using a fixed receiver geometry with 120 receivers active for each shot bringing the nominal fold to 56. The survey geometry was a split spread with 60 receivers on either side of the shot spaced at 50 m. The data were recorded using the recorder SN368, correlator-stacker CS 2502 and the vibrator controller P II equipment. The

equipment allowed for the seismic data quality control to be conducted in the field during acquisition.

2D seismic modelling and source of seismic reflectivity

Pretorius (1964), Antrobus (1986) and Spencer (1992) provided a detailed geological model of the South Rand goldfield. The seismic data cover the area south of the town of Greylingstad parallel to the geological model created by Antrobus (1986) from exploration drilling results. Fig. 3a shows the geological model along the 1993 2D legacy seismic profile. To investigate the potential source of reflectivity in our legacy seismic data, 2D acoustic finite-difference modelling was performed using the geological information from Pretorius (1964) and Antrobus (1986) and physical properties (density and seismic velocities) obtained from Manzi *et al.* (2013) (Fig. 3b). There is a wide range of successful applications of this approach in hard rock environment (e.g., Ahmadi *et al.*, 2016 and references therein).

The method was only used to model the reflections that span the economic orebody (UK9A). Therefore, the model comprises the first major lithological boundaries and major faults in the area. It has a length of 24 km and a maximum depth of 2,500 km (Fig. 3b). To generate the synthetic shot gathers, a Ricker wavelet with a dominant frequency of 60 Hz was used. A seismic velocity of 3100 m/s was assigned to the thin Karoo cover, 6300 m/s assigned to the Klipriviersberg metabasalt, 5400 m/s assigned to Central Rand Group quartzites, and 6200 m/s assigned to the Kimberley shales. The Karoo cover, basaltic lavas, quartzites, and shales were also assigned densities of 2400 kg/m^3, 2900 kg/m^3, 2670 kg/m^3, and 2700 kg/m^3, respectively. The acquisition geometry for the synthetic data were set to be similar to that of the legacy seismic data for better comparisons. Fig. 4a shows the generated synthetic shot gather vs real shot gathers (Fig. 4b, c). The synthetic and real shot gathers show strong seismic reflections that originate from major lithological contacts (R1-R3), with a shift of approximately 200 ms due to non-collocation nature of real and synthetic data.

2D seismic processing

The processing workflow of the 2D seismic profile is outlined in Fig. 5. The raw data had an outdated and incompatible format with the processing software which necessitated several pre-processing steps. Firstly, some header names were stored in nonconventional byte locations and

were subsequently extracted to their correct locations. Secondly, the geometry stored in the headers was edited since the shot and receiver elevations were offset. As per the Shuttle Radar Topography Mission (SRTM) data, the source elevation honoured the true topography of the line, therefore the receiver elevation was interpolated from the shot elevation. To finalise the geometry, the traces were stored in common midpoint (CMP) bins spaced 25 m apart using a spline curve fitting with a bin size of 50 m along the line and 1375.2 m perpendicular to the line.

Pre-stack, the raw shot gathers were contaminated by a 50 Hz spiking noise most likely to be from the AC power lines in the area, which was cut-off by a notch filter. The raw short gathers had clear first breaks as shown in Fig. 4b. The attenuated amplitudes in the data were recovered using an automatic gain control (AGC) window of 250 ms. The target strata were mostly dominated by the surface waves (shaded with the blue colure) because of their shallow location in the shot gathers (Fig. 4b). The surface waves were attenuated using an f-k filter designed to mute lineaments with an S-wave velocity of 3200 m/s or less and a bandpass filter of [0-10 60-70] Hz. Fig. 4c raw shot shows the successfully attenuated surface waves. The final step in the pre-stack processing steps was deconvolution using the spiking deconvolution to broaden the spectrum. Following deconvolution, a constant velocity stack was used to create the velocity model during velocity analysis.

The aim of reappraising the legacy seismic data were to illuminate the reflective strata that span the UK9A reef between 200 ms and 1000 ms two-way time (TWT). The pre-stack processing steps show improvement of the raw shot gathers as illustrated in Fig. 4c. For example, the ground roll noise (shaded blue on the raw shot in Fig. 4b) was successfully eliminated while preserving the target reflections (indicated by the white arrows on the processed shot in Fig. 4c). The first break muting improved the AGC amplitude recovery and illuminated the target shallow reflections on the reprocessed shot gather. Before stacking the refraction top mute was removed to preserve the very near surface reflections. Appropriate statics were calculated and applied to the data by firstly, manual picking a total of 32846 P-wave first breaks and calculating the floating datum using the maximum elevation of 1700 m as the fixed datum with the replacement velocity of 6000 m/s (Fig. 6). The statics was calculated using least-squares inversion for first arrivals with the RMS error less than 6.5 ms. The weathered layer and the bedrock were modelled with velocities of 3000 m/s

and above 5500 m/s (± 50 m/s), respectively. Refraction tomography was calculated to constrain the interpretation of the line at a maximum depth of 1300 m (Fig. 6).

A significant amount of effort was invested in creating a velocity model that honours the complex geology of the area. In addition to this, a series of passes of residual statics were conducted to improve the coherency of reflections. A series of interactive velocity analysis were conducted for pre-stack migration computation. Both Kirchoff pre-stack time migration (PreSTM) and pre-stack depth migration (PreSDM) were applied on the data. A series of passes of the velocity analysis were done on the PreSTM and PreSDM outputs to improve the quality of the stacked data. The Residual Moveout (RMO) analysis was applied following the Kirchhoff migrations. The data were then stacked and processed (post-stack) to suppress the surface waves and enhance the continuity of the reflections. Finally, the PreSTM data were converted to depth using the stacking velocities.

Generally, the 2021 PreSTM and 2021 PreSDM data provide much better imaging of the structures when compared to the 1993 legacy PostSTM data (Figs 7 and 8). Furthermore, the PreSDM data exhibit high signal-to-noise ratio (SNR) than PreSTM (Fig. 7). For example, the results from the PreSTM missed the very near surface reflection (U1) as shown in Fig. 8a, which is well defined by PreSDM (Fig. 8b). The PreSDM was applied with velocity ranges of 4000 - 6900 m/s choosing the velocity model with the most coherent reflections. The velocities used were derived from the physical properties studies conducted in the Witwatersrand Basin (Manzi *et al.* 2015). The effectiveness of PreSDM in complex hard rock environment is well documented by various authors (e.g., Bradford *et al.* 2006; Buske *et al.* 2009; Hu *et al.* 2009; Manzi *et al.* 2012b; Storch *et al.* 2021).

RESULTS AND INTERPRETATION

According to the surface geological map (Fig. 1) the 1993 2D seismic profile was collected over an outcrop of the Klipriviersberg metabasalt. The low fold CDPs (edges of the profile) were sitting on the thin Karoo cover, with the Karoo dolerite intrusion covering the south-western edge and the Ecca group sediments covering the north-eastern edge. The strata dipping to the north is supported by the presence of the overlying Karoo (Ecca group sediments) on the northern edge of the 1993 2D seismic profile. This supports the documented dip direction of the strata on the 1986 geological model (see Fig. 3).

Analysis and comparison between the synthetic shot gather from 2D acoustic finite-difference modelling and the reprocessed 1993 2D seismic profile sample shot gather is shown in Fig. 4. The main lithological contacts are mapped as strong reflections due to a significant acoustic impedance contrast between the overlying and underlying rocks (Figs 7-8): Karoo sediments-Ventersdorp metabasalt (U1), dolerite sill (U2), Ventersdorp basaltic lavas-Central Rand Group quartzites (R1), and Central Rand Group quartzites-top of MK1 (R2). These results concur with the synthetic modelling results, with a shift of approximately 200 ms due to non-collocation nature of the synthetic model and real data (see Fig. 4a).

Fig. 7 shows the comparison between the 1993 legacy Post-stack time migrated (PostSTM) section and the 2021 reprocessed PreSTM up to 2 s TWT, with the outcrop data along the profile. The U1, U2 and R1 reflections are clearly defined by both 2021 PreSTM (Fig. 7b) and PreSDM (Fig. 8b) reprocessing results when compared to 1993 legacy data (Fig. 7a). In fact, these reflections are completely missed by the 1993 legacy data. The final interpreted PreSDM seismic section is shown in Fig. 9b with the velocity model overlain (Fig. 9a).

DISCUSSION

The two unconformities (U1 and R1) are clearly mapped due to the high acoustic impedance contrast between the overlying Karoo strata with low velocities (~ 4000 m/s) and densities (~ 2.10 g/cm^3) and the underlying Ventersdorp basaltic lavas with high velocities (~ 6400 m/s) and densities (~ 2.90 g/cm^3) (Westgate *et al.* 2020). The contact between the Ventersdorp basaltic lavas and the underlying Central Rand Group quartzite with relatively lower velocities (~ 5400 m/s) and densities (~ 2.67 g/cm^3) also exhibit a significant acoustic impedance contrast (Manzi *et al.* 2015). MK1 (R2 reflector) is imaged as a strong reflector due to its relatively high densities (~ 3.01 g/cm^3) and velocities (~ 5800 m/s) as compared to quartzites (Manzi *et al.* 2015). The thin gold orebody (UK9A) overlying the MK1 is seismically transparent because it is embedded between quartzite and conglomerates with similar physical properties. However, for mining purposes, its orebody model can be derived from its closest overlying R1 and underlying R2 reflections.

Previous publications and recorded exploration drilled cores show the thickness of the Witwatersrand Supergroup to be approximately 5 km (Manzi *et al.* 2015). The thickness of the layers associated with the Witwatersrand Supergroup package on the reprocessed 2021 PreSDM data has a thickness of ~ 4.5 km, which corresponds to the expected thickness of the Supergroup.

The borehole (SD1) information published by Antrobus (1986) intersected the reflector R1 at a depth of 1042 m, which corresponds to the observed position of the reflection on the PSDM data. Reflector R2 is associated with the shales underlying the gold-bearing orebody (UK9A) intersected by a borehole (SD1) approximately 750 m below R1. The underlying reflections are interpreted to be associated with the West Rand Group strata. The Westrand Group strata are not interpreted in detail as there is no published borehole information from this area.

The faulting (see Fig. 9b) in the area clearly displaces the Turffontein Subgroup strata as observed by the displacement on reflection R2. The publications from Pretorius (1964), Antrobus (1986), and Spencer (1992) on the structural geology of the study area had no conclusive results on the geometry of the faults in the study area. Fault F1 is interpreted in this study as a normal fault downthrown to the south, displacing reflection packages associated with shales with a near-vertical dip. Fault F3 (corresponding to Bergsig Fault in Fig. 1b) is interpreted as a reverse fault downthrown to the north and is moderately dipping to the south. F3 displaces the reflection package associated with R2 and the overlying reflections R1 and U1. Fault F4 is a reverse fault downthrown to the north and is dipping to the south. It displaces the strata associated with the R2 reflections and the overlying R1 reflections. Minor faulting (F2, F5, and F6) in the section is not conclusively interpreted as the reflections do not have clear vertical displacements.

The geological model documented by Antrobus (1986) (Fig. 3a) does not correspond to the interpretation model from the reprocessed 2021 PreSDM data (Fig. 9), with an exception of the southern edge of the data which resemble the same dipping nature as the 1986 model. The thin Karoo cover is observed to be continuous towards the south of the profile as shown by the well-defined unconformity (U1) (Fig. 9b). The reflectors R1 and R2 are seen to be near horizontal with a minor dip to the north. The major faulting documented in the 1986 geological model, Bergsig and Rooiwal faults (Fig. 3a), correspond to the imaged faults (F3 and F4) on the 2021 PreSDM section (Fig. 9b).

CONCLUSIONS

We significantly improved the quality of the 1993 legacy seismic data through reprocessing using up-to-date processing algorithms and updated velocity models. The 2021 reprocessed high-quality data highlight many new geological features that may have a direct impact on future mining in the Burnstone mine in the South Rand goldfield. These are:

1. Unconformity (U1) at the base of the Karoo sediments, which is completely missed by the 1993 legacy seismic data.
2. Dolerite sill above the orebody (UK9A). The sill is mapped as a strong reflection, and its close proximity to the orebody could have a direct impact on mining in the region.
3. MK1 (R2) reflection, located a few hundred metres below the orebody (UK9A). The imaging of this shale unit is important because it can be used as a proxy to map the seismically transparent orebody, its dip variations, and geological structures crosscutting it.
4. Unconformity (R1) at the base of the Ventersdorp Supergroup, located hundreds of meters above the orebody, could assist in depth positioning the orebody. Similar to R2, this R1 could be used to derive the structural model of the orebody.
5. Geological structures (mainly faults) beneath the Karoo sediments that crosscut and displace orebody. The delineation of these faults is important for both mine safety and planning. These faults can be associated with a series of smaller faults that are likely to cause poor ground conditions during mining. These faults (in the case of normal faulting) can also bring the orebody to mineable depths, thus enhancing the resource evaluation.

ACKNOWLEDGEMENTS

We are thankful for the financial support from DST-NRF CIMERA and the MATLAB licensing from the University of the Witwatersrand Seismic Research Centre. We appreciate the sponsorship of Globe Clarita seismic processing licenses from HiSeis Pty Ltd. and Tesseral Technologies for sponsoring the licenses for Tesseral seismic modelling software. We gratefully acknowledge Sibanye Stillwater for the donation of the legacy 2D seismic data.

LIST OF FIGURES

Figure 1. Simplified geological map of the Witwatersrand Basin (a) as well as the location map of the Burnstone mine (red star) and the surrounding areas in the South Rand goldfield (b). The geological structures are overlain on the geological map of the South Rand goldfield (b) (modified from Dankert and Hein 2010).

Figure 2. The simplified stratigraphy of the South Rand goldfields (modified from Van der Heever et al. 2009).

Figure 3. The geological model along the 2D legacy seismic profile as presented by Antrobus (1986) (a), and the model used for 2D acoustic finite-difference calculation (b).

Figure 4. Comparison between synthetic shot gather (a), raw shot gather (b), and reprocessed shot gather (c) with the corresponding amplitude spectrum graphs. The shaded area demonstrates the attenuated surface waves, and the arrows show preserved and amplified reflections. R1 highlights the reflections from the contact between the Klipriviersberg metabasalt and the Central Rand Quartzites. R2 highlights the Reflections from the contact between Booysens shales and the overlying Central Rand Quartzites. R3 highlights the deeper West Rand group reflections.

Figure 5. The processing workflow of the 2D seismic profile.

Figure 6. Refraction Tomography of the 2D legacy seismic profile. The top rectangles show the geological outcrop along the profile as seen on the geological map.

Figure 7. Comparison between PreSTM (a) and PreSDM (b), with the main lithological contacts: Karoo sediments-Ventersdorp basaltic lavas (U1), dolerite sill (U2), Ventersdorp basaltic lavas-Central Rand Group quartzites (R1), and Central Rand Group quartzites-top of MK1 (R2), and the geological outcrop along the profile.

Figure 8. Comparison between 1993 legacy PostSTM data (a) and the 2021 reprocessed PreSTM data (b), with the main lithological contacts: Karoo sediments-Ventersdorp basaltic lavas (U1), dolerite sill (U2), Ventersdorp basaltic lavas-Central Rand Group quartzites (R1), and Central Rand Group quartzites-top of MK1 (R2), and the geological outcrop along the profile.

Figure 9. The reprocessed PreSDM section with the velocity model overlain (a) and the final interpreted section (b).

REFERENCES

Ahmadi, O., Koyi, H., Juhlin, C. and Gessner, K. (2016) Seismic signatures of complex geological structures in the Cue-Weld Range area, Murchison domain, Yilgarn Craton, Western Australia. *Tectonophysics,* 689, 56–66. https://doi.org/10.1016/j.tecto.2016.02.020

Antrobus, E.S.A. (1986) The South Rand goldfield. In: Anhaeusser, C.R., Maske, S. (Eds.).

Mineral Deposits of Southern Africa, *vol. 1. Geological Society of South Africa, Johannesburg*, 689–703.

Buske, S., Gutjahr, S. and Sick, C. (2009) Fresnel volume migration of single-component seismic data. *Geophysics*, 74, (6), WC47-WC55. https://doi.org/10.1190/1.3223187

Bradford, J. H., Liberty, L. M., Lyle, M. W., Clement, W. P. and Hess, S. (2009) Imaging complex structure in shallow seismic-reflection data using prestack depth migration. *Geophysics*, 71, (6), B175-B181. https://doi.org/10.1190/1.2335659

Coward, M. P., Spencer, R. M. and Spencer, C. E. (1995) Development of the Witwatersrand Basin, South Africa. *Geological Society, London, Special Publications*, 95, (1), 243–269. https://doi.org/10.1144/GSL.SP.1995.095.01.15

Dankert, B. T. and Hein, K. A. A. (2010) Evaluating the structural character and tectonic history of the Witwatersrand Basin. *Precambrian Research*, 177, (1-2), 1–22. https://doi.org/10.1016/j.precamres.2009.10.007

Durrheim, R. J. (1986) Recent reflection seismic developments in the Witwatersrand Basin, In: M. Barazangi and L. Brown, (eds.). Geodynamics Series, *Vol. 13. American Geophysical Union*, 77–83. https://doi.org/10.1029/GD013p0077

Frimmel, H.E. (2019) The Witwatersrand Basin and Its Gold Deposits. In: Kroner, A., and A. Hofmann, (eds.). The Archean Geology of the Kaapvaal Craton, South Africa. DOI: 10.1007/978-3-319-78652-0_10

Frimmel, H. E. and Nwaila, G. T. (2020) Chapter 31 Geologic Evidence of Syngenetic Gold in the Witwatersrand Goldfields, South Africa. In: Sillitoe, R. H., R. J. Goldfarb, F. Robert, and S. F. Simmons, (eds.). Geology of the World's Major Gold Deposits and Provinces, *vol 23, Society of Economic Geologist.* https://doi.org/10.5382/SP.23.31

Hu, C. and Stoffa, P. L. (2009) Slowness-driven gaussian-beam prestack depth migration for low-fold seismic data. *Geophysics*, 74, (6), WCA35 - WCA45. https://doi.org/10.1190/1.3250268

Malehmir, A., Donoso, G., Markovic, M., Maries, G., Dynesius, L., Brodic, B., Pecheco, N., Marsden, P., Bäckström, E., Penney, M. and Araujo, V. (2019) Smart Exploration: from legacy data to state-of-the-art data acquisition and imaging. *First Break*, 37, (8), 71–74. https://doi.org/10.3997/1365-2397.n0049

Manzi, M. S.D., Malehmir, A. and Durrheim, R. J. (2018) 3D Reflection Seismics for Deep

Platinum Exploration in the Bushveld Complex, South Africa. *2nd Conference on Geophysics for Mineral Exploration and Mining, 1–5*. https://doi.org/10.3997/2214-4609.201802751

Manzi, M. S. D., Malehmir, A. and Durrheim, R. J. (2019) Giving the legacy seismic data the attention they deserve. *First Break*, 37, (8), 89–96. https://doi.org/10.3997/1365-2397.n0050

Manzi, M. S. D., Cooper, G. R. J., Malehmir, A., Durrheim, R. J. and Nkosi, Z. (2015) Integrated interpretation of 3D seismic data to enhance the detection of the gold-bearing reef: Mponeng Gold mine, Witwatersrand Basin (South Africa). *Geophysical Prospecting*, 63, (4), 881–902. https://doi.org/10.1111/1365-2478.12273

Manzi, M. S. D., Gibson, M. A. S., Hein, K. A. A., King, N. and Durrheim, R. J. (2012a) Application of 3D seismic techniques to evaluate ore resources in the West Wits Line goldfield and portions of the West Rand goldfield, South Africa. *GEOPHYSICS*, 77, (5), WC163–WC171. https://doi.org/10.1190/geo2012-0133.1

Manzi, M. S. D., Durrheim, R. J., Hein, K. A. A. and King, N. (2012b) 3D edge detection seismic attributes used to map potential conduits for water and methane in deep gold mines in the Witwatersrand basin, South Africa. *GEOPHYSICS*, 77, WC133–WC147. https://doi.org/10.1190/geo2012-0135.1

Manzi, M. S. D., Hein, K. A. A., King, N. and Durrheim, R. J. (2013) Neoarchaean tectonic history of the Witwatersrand Basin and Ventersdorp Supergroup: New constraints from high-resolution 3D seismic reflection data. *Tectonophysics*, 590, 94–105. https://doi.org/10.1016/j.tecto.2013.01.014

Pretorius C.C., Muller M.R., Larroque M. and Wilkins C. (2003). A review of 16 years of hardrock seismics on the Kaapvaal Craton, Hardrock Seismic Exploration. In: Developments in Geophysics Series. (ed. Eaton, D., Salisbury, M. and Milkereit, B.) SEG, Houston. 2003, 247–268. https://doi.org/10.1190/1.9781560802396.ch16

Pretorius, D.A. (1964b) The geology of the South Rand Goldfield. In: Haughton, S.H. (Ed.). The Geology of Some Ore Deposits in Southern Africa. Geological Society of South Africa, Johannesburg, 219–282.

Spencer, R.M. (1992) Late Archaean Tectonics and Sedimentation of the South Rand Area, Witwatersrand Basin. PhD Thesis, University of the Witwatersrand, Johannesburg.

Storch, I., Buske, S. Victor, P. and Oncken, O. (2021) Seismic images of the Northern Chilean subduction zone at 19^{0}45'S, prior to the 2014 Iquique earthquake. *Geophysical Journal International,* 225, (2), 1048 - 1061. https://doi.org/10.1093/gji/ggab035

Tucker, R. F., Viljoen, R. P. and Viljoen, M. J. (2016) A Review of the Witwatersrand Basin - The World's Greatest Goldfield. *Episodes,* 39, 104–133. DOI: 10.18814/epiiugs/2016/v39i2/95771

Van der Heever, D., Oelofse, J. and Bentle, P. (2009) Revised Technical Report Update of the June 21, 2007, Technical Report (Optimized Feasibility Study), Inclusive of Updated. Mineral Resource and Reserve Estimates for the Burnstone Gold Project. Unpublished Company Report to Great Basin Gold Limited.

Westgate, M., Manzi, M. S. D., James, I. and Harrison, W. (2020) New insights from legacy seismic data: reprocessing of legacy 2D seismic data for imaging of iron-oxide mineralization near Sishen Mine, South Africa. *Geophysical Prospecting,* 68, (7), 2119–2140. https://doi.org/10.1111/1365-2478.12996

FIGURES

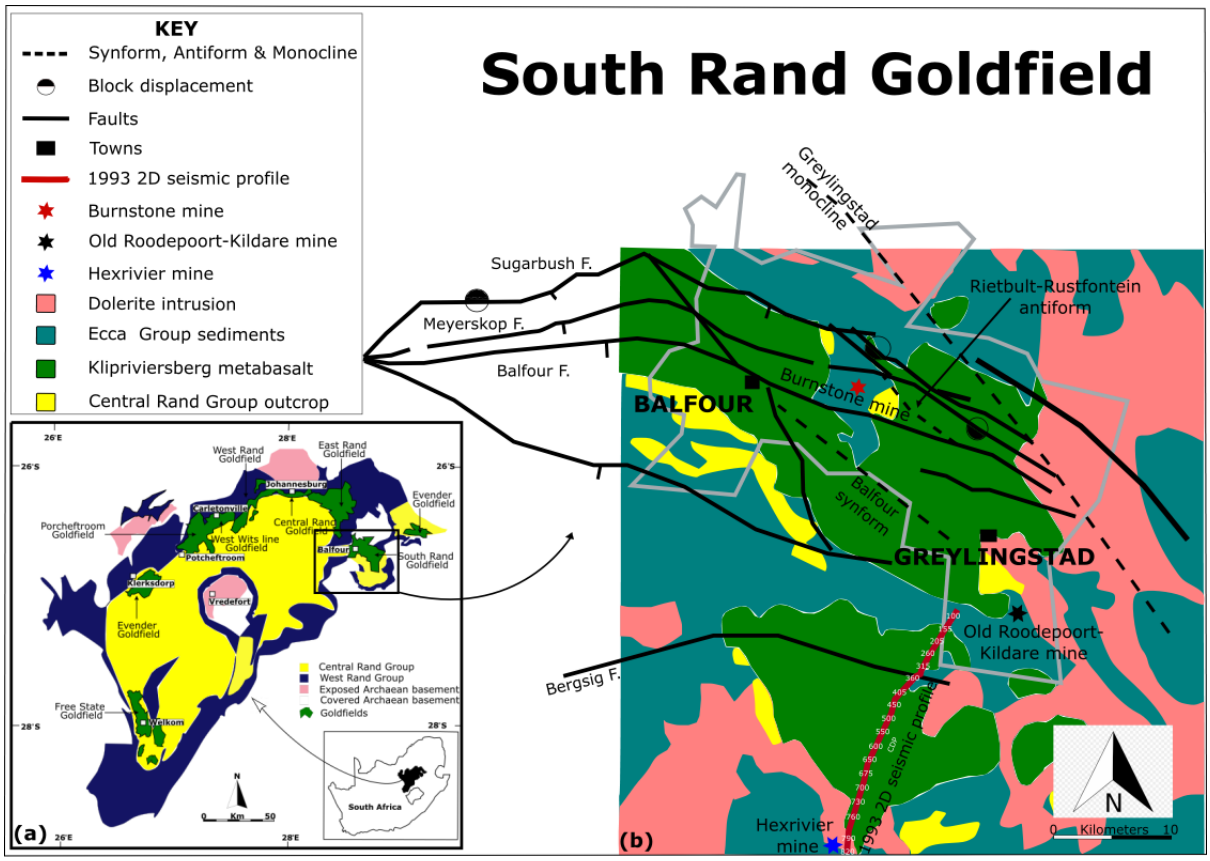


Figure 1. Simplified geological map of the Witwatersrand Basin (a) as well as the location map of the Burnstone mine (red star) and the surrounding areas in the South Rand goldfield (b). The geological structures are overlain on the geological map of the South Rand goldfield (b) (modified from Dankert and Hein 2010).

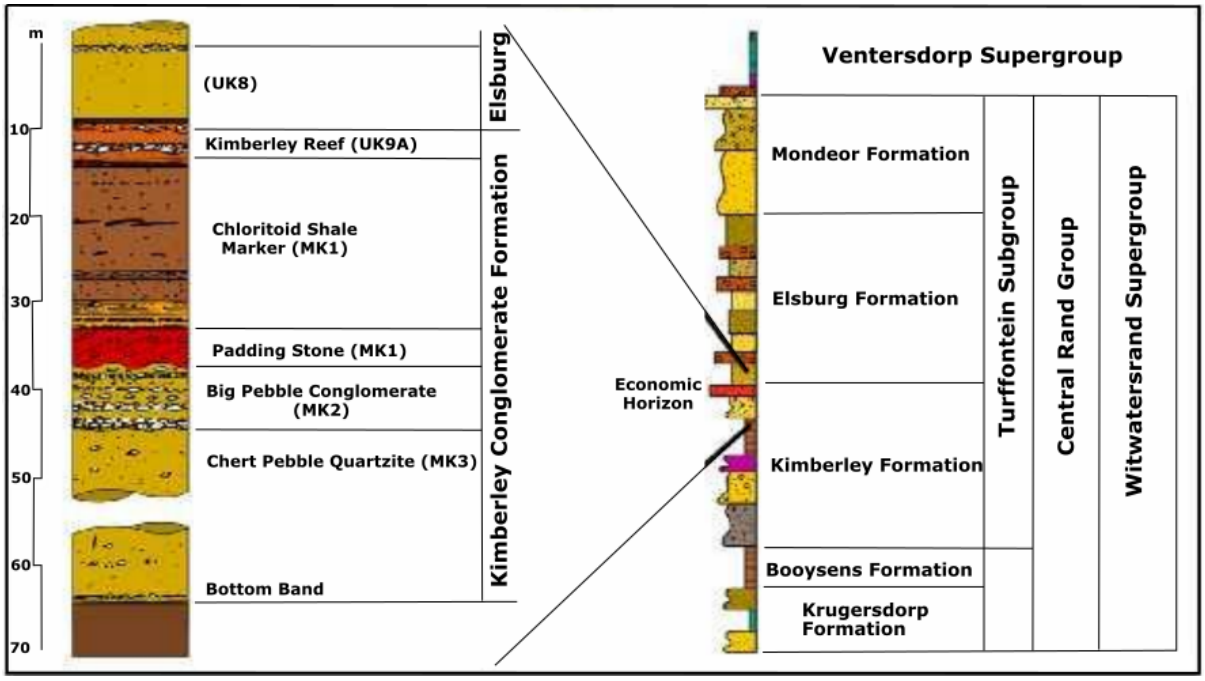


Figure 2. The simplified stratigraphy of the South Rand goldfields (modified from Van der Heever et al. 2009).

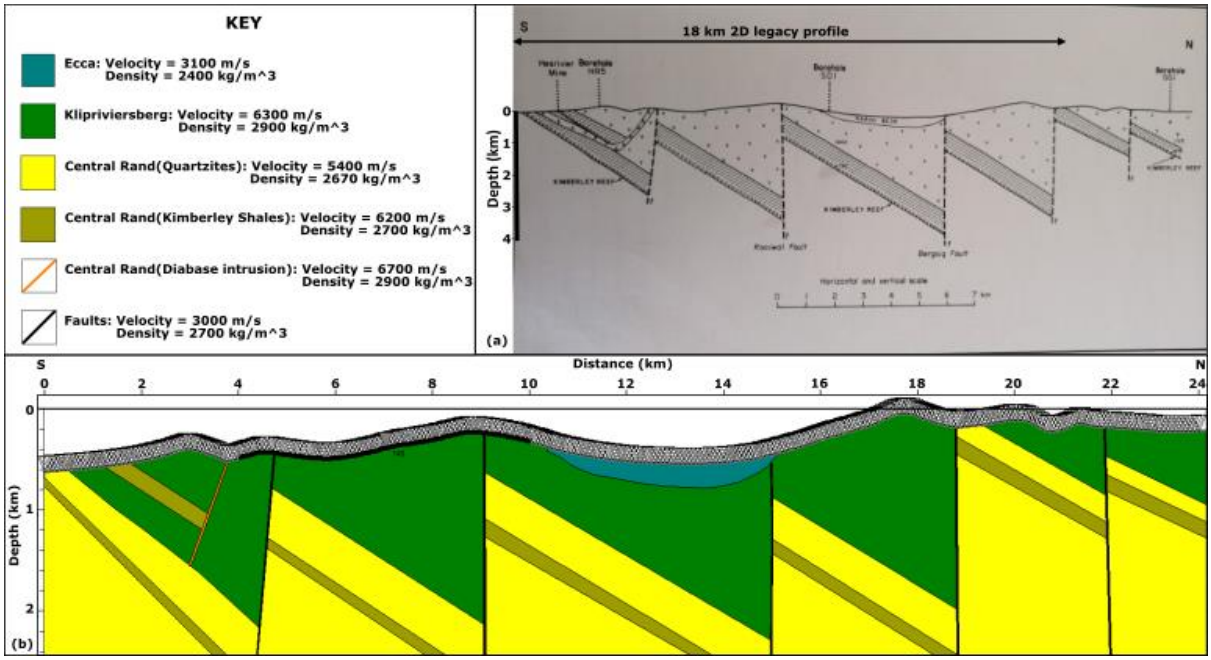


Figure 3. The geological model along the 2D legacy seismic profile as presented by Antrobus (1986) (a), and the model used for 2D acoustic finite-difference calculation (b).

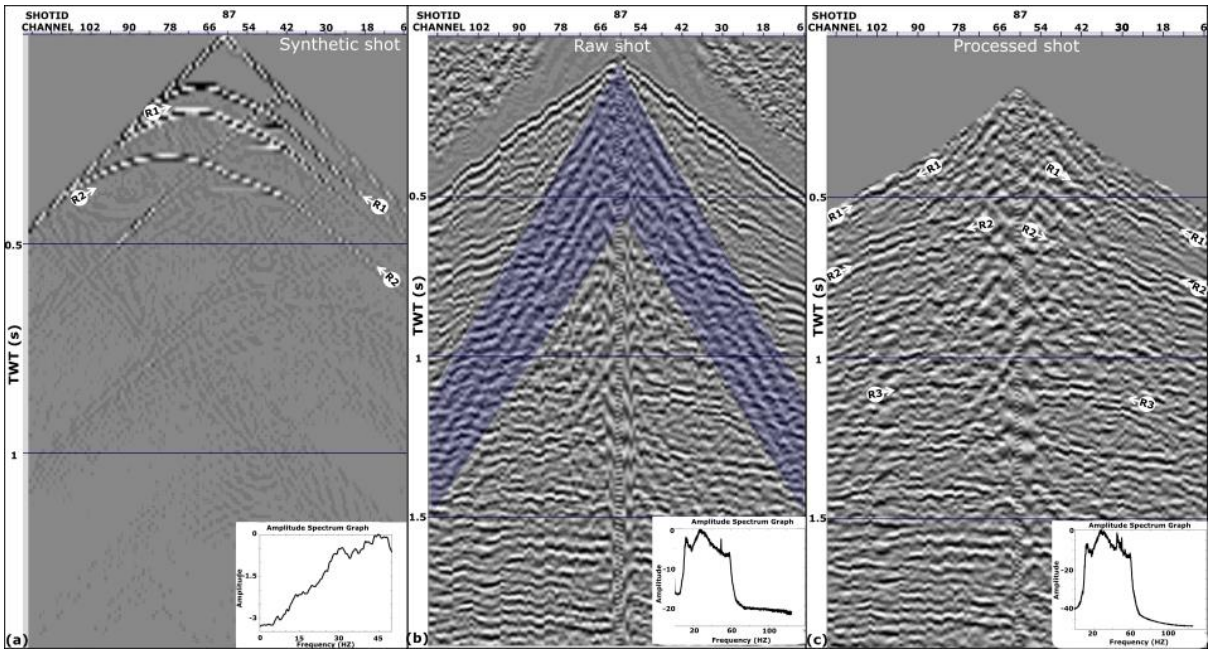


Figure 4. Comparison between synthetic shot gather (a), raw shot gather (b), and reprocessed shot gather (c) with the corresponding amplitude spectrum graphs. The shaded area demonstrates the attenuated surface waves, and the arrows show preserved and amplified reflections. R1 highlights the reflections from the contact between the Klipriviersberg metabasalt and the Central Rand Quartzites. R2 highlights the Reflections from the contact between Booysens shales and the overlying Central Rand Quartzites. R3 highlights the deeper West Rand group reflections.

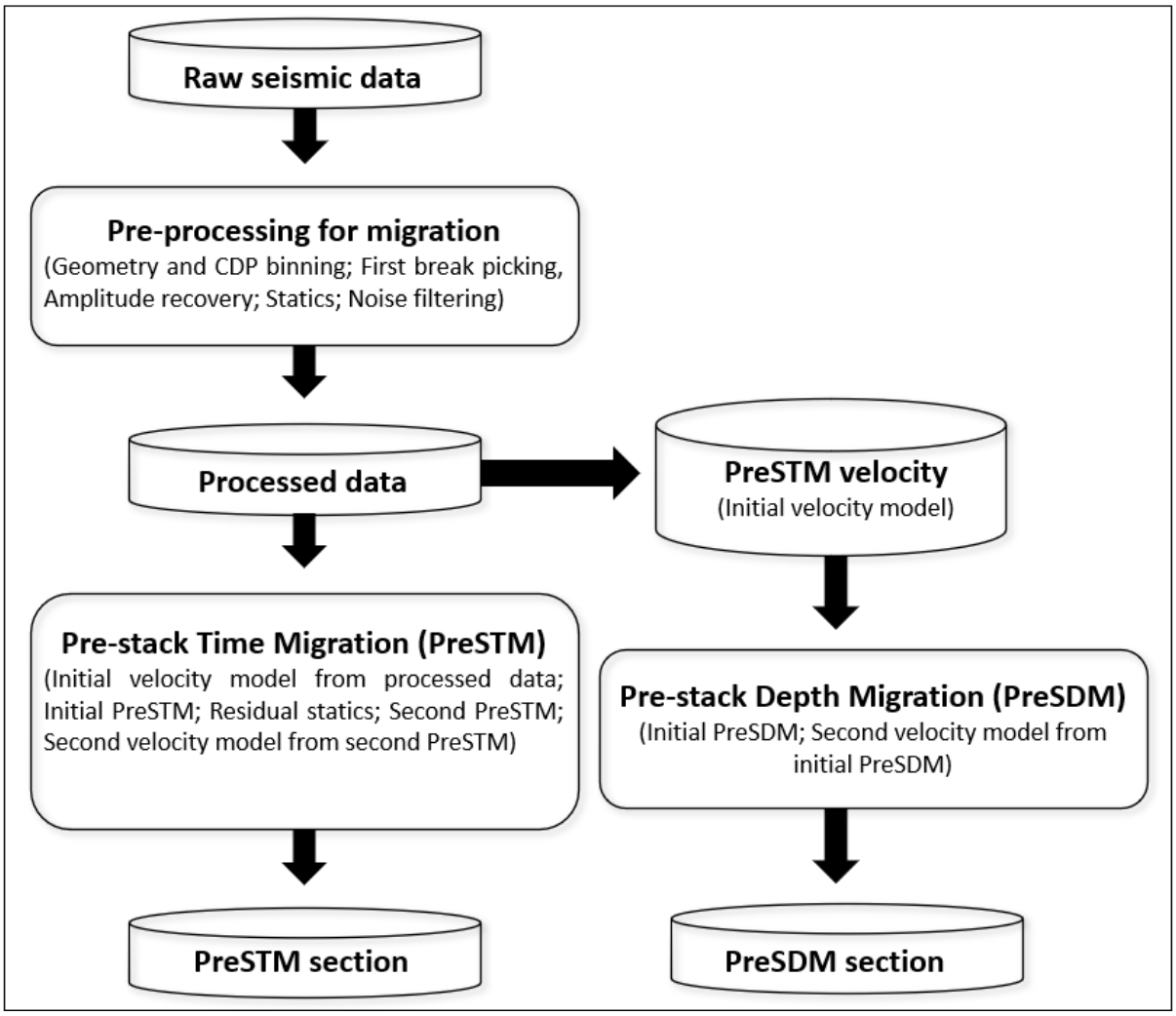


Figure 5. The processing workflow of the 2D seismic profile.

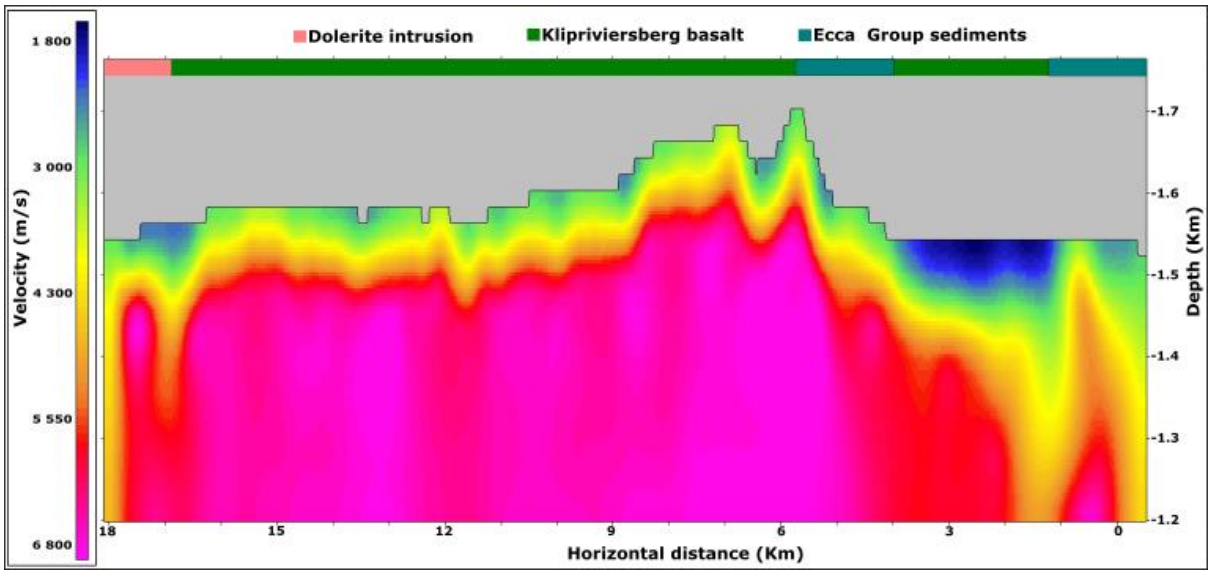
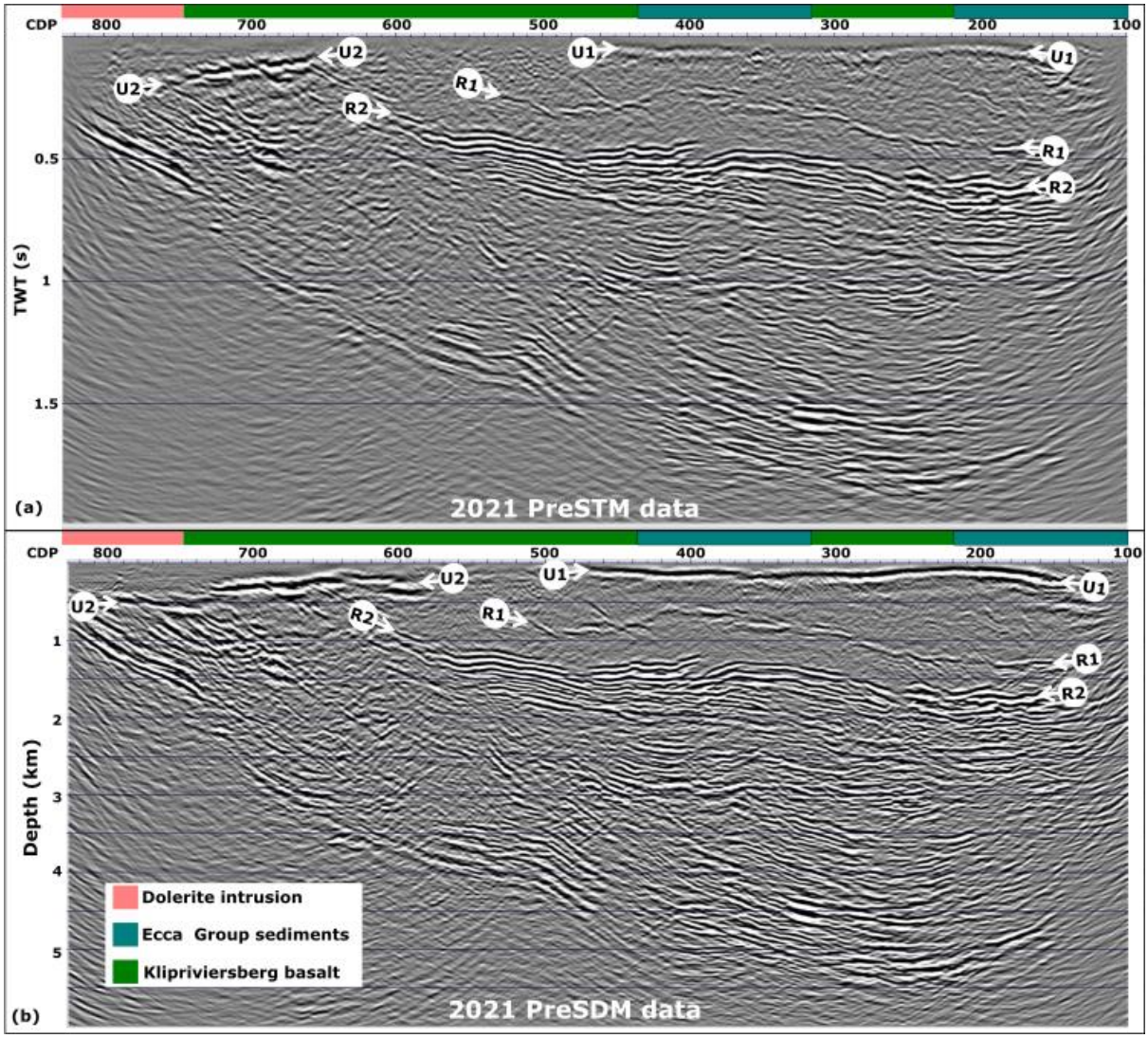


Figure 6. Refraction Tomography of the 2D legacy seismic profile. The top rectangles show the geological outcrop along the profile as seen on the geological map.



1797

1798 **Figure 7.** Comparison between PreSTM (a) and PreSDM (b), with the main lithological contacts:
1799 Karoo sediments-Ventersdorp basaltic lavas (U1), dolerite sill (U2), Ventersdorp basaltic lavas-
1800 Central Rand Group quartzites (R1), and Central Rand Group quartzites-top of MK1 (R2), and the
1801 geological outcrop along the profile.

1802

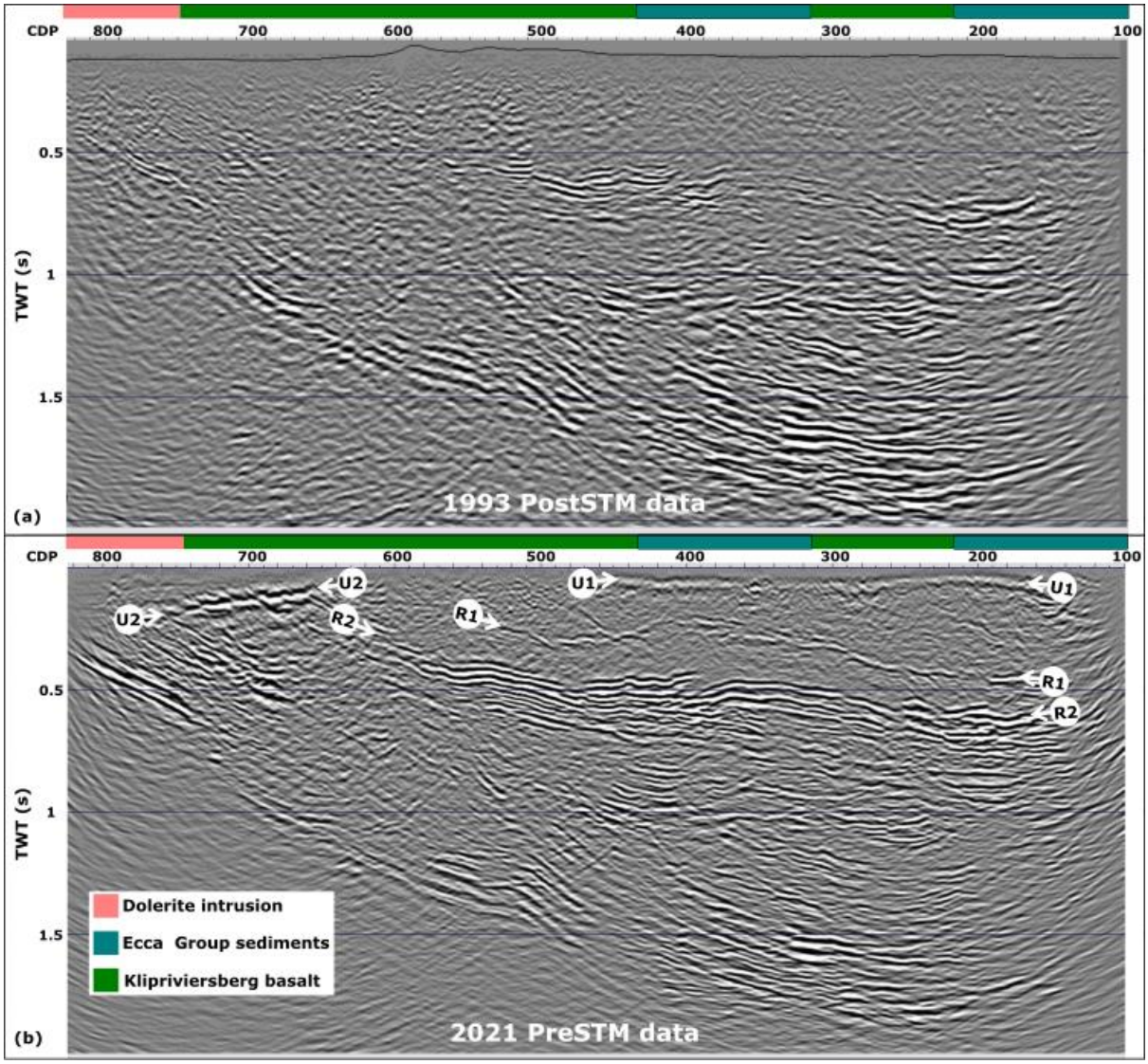


Figure 8. Comparison between 1993 legacy PostSTM data (a) and the 2021 reprocessed PreSTM data (b), with the main lithological contacts: Karoo sediments-Ventersdorp basaltic lavas (U1), dolerite sill (U2), Ventersdorp basaltic lavas-Central Rand Group quartzites (R1), and Central Rand Group quartzites-top of MK1 (R2), and the geological outcrop along the profile.

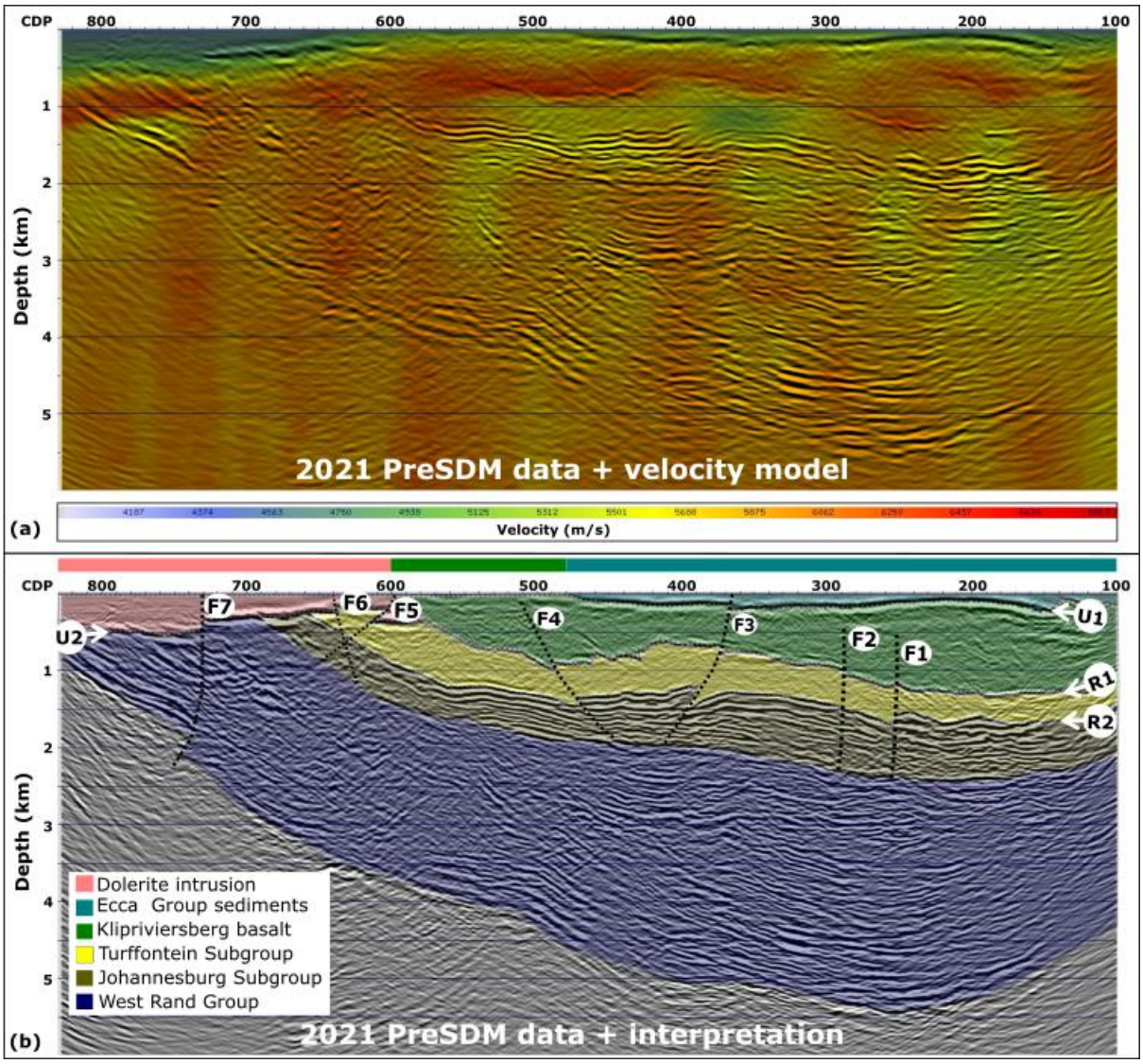


Figure 9. The reprocessed PreSDM section with the velocity model overlain (a) and the final interpreted section (b).

Tables

Table 1: Line RS507 acquisition parameters.

Survey Parameters	
Survey type	2D crooked line
Year	1993
Length	18 km
Direction	NE-SW
Spread	2975-25-X-25-2975
Nominal Fold	56
Recording System	
Recording Device	Sercel SN368
Stacking Device	CS2502
Sample Rate	2 ms
Recording Length	6 s
Sweep Length	16 s
Sweep Frequency range	10 – 61 Hz
Source Information	
Source Device	Vibroseis
Vibrator Controller	P II
Source Spacing	50 m
Receiver Information	
Receiver Spacing	50 m
Geophone Type	SM4U

6 **Paper II:** Seismic imaging of the complex geological structures in the southwestern edge of the Western Limb, Bushveld Complex through focusing prestack depth migration of legacy 2D seismic data

6.1 Paper Summary

The 50 km long 2D reflection seismic profile presented in this paper was collected in the Western Limb of the Bushveld complex in 1986 by the Geophysical Survey of South Africa (now Council for Geosciences). The profile traverses the southwestern edge of the Western Limb from north Pretoria towards the centre of the centre of the complex. The detailed acquisition parameters of the profile are outlined in chapter 7 acquisition table. The profile was collected over the Transvaal Supergroup rocks outcrop in the southern edge. The central part traverses over the Bushveld complex rocks outcrop, from the basal Rustenburg Layered Suite (RLS) mafic cumulates to the overlying Lebowa Granite suite (LGS) and Rashoop Granophyre Suite (RGS) felsic cumulates. The northern edge is over younger Karoo sediments near the centre of the complex.

The unmigrated stack of the data were initially interpreted in the 1980s followed by detailed processing and interpretation of the post-stack time migrated section in the 1990s. The Southern half of the profile has gently dipping continuous reflections with analogous interpretation from legacy processing and reprocessing from this study. The basal high amplitude high frequency reflections are interpreted as the Transvaal Supergroup, overlain by low amplitude low frequency reflections interpreted as the RLS mafic cumulate. The overlying seismically transparent part of the section is interpreted as the LGS and RGS felsic cumulate rocks of the Bushveld Complex. These reflections are mapped by both the 2023 coherency migrated section and the 1993 post-stack time migrated stack.

The northern half of the profile is characterized by a low signal-to-noise ratio (SNR) which was interpreted with contrasting conclusions in the 1980s and 90s. Initial interpretation of the unmigrated section in 1986 concluded that there are no RLS mafic cumulate rocks present in the northern half of the profile, they terminate against the Mabopane fault. The interpretation of the post-stack time migrated section in 1993 concluded that the RLS mafic cumulate rocks are present in the northern half of the profile highly faulted. The low SNR in the northern half of the profile

was attributed to the poor source and receiver ground coupling, dispersion of the wavefield and presence of out-of-plane reflection energy with no conclusive results.

In this study to better image the northern half of the profile pre-stack depth migration through coherency migration (CM) was applied to the data, and aeromagnetic data were used to constrain the interpretation. Chaneng structure present in the northern half of the profile was clearly delineated by the aeromagnetic data and the extent of the magnetic rocks of RLS was constrained using aeromagnetic data. These rocks are not present in the northern section of the profile, and the Chaneng structure was not clearly delineated by the seismic data because it is a near-vertical dyke associated with a fault. CM provided better imaging of the northern section of the profile compared to the legacy post-stack time migrated section and conventional Kirchoff pre-stack depth migrated section. The 2D crooked profile was 3D migrated to access cross-profile information and 3D volume showed the presence of out-of-plane reflection energy with ambiguous source position. The lack of sources or receivers in the cross-profile direction to constrain the source of reflectivity implies that the out-of-plane energy could have been reflected anywhere in the cylindrical position around the profile. The presence of an anticlinal structure in the northern half of the profile was concluded to be part of the Crocodile River dome, which is a Transvaal inlier outcropping northwest of the profile. The tectonic evolution of Bushveld complex rocks is outlined in this study along the profile.

6.2 Manuscript

Seismic imaging of the complex geological structures in the southwestern edge of the Western Limb, Bushveld Complex through focusing prestack depth migration of legacy 2D seismic data

Mpofana Sihoyiya[1], Felix Hloušek[2], Musa S. D. Manzi[1*], Moyagabo K. Rapetsoa[1], Stefan Buske[2], David Khoza[3]

[1]University of the Witwatersrand, Johannesburg, South Africa

[2]TU Bergakademie Freiberg, Freiberg, Germany

[3]Council for Geoscience, Pretoria, South Africa

*Email: musa.manzi@wits.ac.za

ABSTRACT

We reprocessed a 50 km long legacy 2D reflection seismic profile acquired in 1986 by the Geological Survey of South Africa (now known as the Council for Geosciences) to improve the delineation of complex geological structures that host the platinum-bearing horizons (known as the UG2 reef; a chromitite horizon) on the south-eastern edge of the Western limb of the Bushveld Complex and to investigate the continuity of the reef below the thick cover. The pre-stack seismic data quality was improved through careful processing, including modifying the predictive deconvolution algorithm to simulate spiking deconvolution. We applied standard Kirchhoff pre-stack depth migration (KPreSDM) as well as advanced coherency migration (CM) techniques. Both imaging techniques yielded good structural images of the platinum deposits, their hanging wall and footwall rocks. In particular, the CM technique has provided significantly better images in complex faulted regions, yielding a better understanding of the interrelationship between fault activity and platinum deposit distribution, and the relative chronology of tectonic events. Moreover, the regional geological structures (Crocodile River fault and Chaneng structure) that crosscut the profile are clearly defined.

Keywords: Seismics, processing, exploration, imaging

INTRODUCTION

The Paleoproterozoic age (2.06 Ga) Bushveld Complex (Figure 1a) is the world's largest igneous intrusion (~ 64 000 km^2), which is associated with the platinum-group element (PGE) deposits of South Africa (Manzi *et al.*, 2019a). The Bushveld Complex PGEs occur within the mafic stratiform horizons locally known as reefs (Basson, 2019; Sehoole *et al.*, 2020). These deposits are mined from the outcrop on the complex margin to depths over a kilometre concealed beneath cover rocks. Between the 1970s and 1980s greenfield traditional approaches of mineral exploration (mainly geological mapping, exploration drilling, and potential field methods) were successfully employed to map the extent of the Bushveld Complex. To date, mature brownfield mineral exploration

requires innovative and novel geological and geophysical techniques to improve the delineation of deeply buried platinum-bearing horizons (Donoso *et al.*, 2020; Manzi *et al.*, 2019a). However, these methods are not widely used because they are deemed to be expensive, and cost beyond the exploration budget of some mining companies. Therefore, these companies do not have the financial ability required to sufficiently employ these techniques and improve the imaging of lithological and structural contacts at depth. Consequently, companies that revise and improve their existing data stand to benefit (Manzi *et al.*, 2019b; Malehmir *et al.*, 2019).

Revision and re-processing of legacy reflection seismic data have been utilized successfully by several authors (e.g., Malehmir and Bellefleur, 2010; Manzi *et al.*, 2019a, b; Donoso *et al.*, 2020; Westgate *et al.*, 2020; Sihoyiya *et al.*, 2022, and references therein) for hard rock mineral exploration. Challenges presented by these datasets are related to bad storage and documentation, such as outdated tapes and hard copies, respectively. Several pre-processing steps are needed to correct inaccurate coordinates and set up new geometry. Despite these challenges, these data are still valuable, cost-effective, and have the potential to be revised and reworked (Malehmir *et al.*, 2019). Particularly in the Bushveld Complex where the PGE mineral endowment started in 1924 with the discovery of the first economically viable PGE deposit (Cawthorn, 1999; Manzi *et al.*, 2019a). In the 1980s, the reflection seismic method was introduced in the Bushveld Complex, and since then a seismic database with tens of 2D and 3D seismic surveys has been acquired across the Complex to delineate the platinum-bearing horizons and geological structures under thick cover rocks (Pretorius *et al.*, 2000, 2003; Manzi *et al.*, 2019b).

In this study, we reprocessed a 50 km long, 16 s two-way traveltime (TWT) legacy 2D reflection seismic profile acquired by the Geological Survey of South Africa in 1986 near Eland mine on the southeastern edge of the Western limb of the Bushveld Complex. The complex is subdivided into four different lobes namely the Northern, Eastern, Southern, and Western limbs. Most PGE deposits in the Western limb are associated with the Critical Zone (Figures 1a and b) of the Rustenburg Layered Suite (RLS) on the complex. The Critical Zone diminishes in thickness from west to east (Rustenburg to Pretoria), and this diminution has resulted in a lack of interest in mineral exploration in the southeastern edge of the Western limb, near Pretoria (Cawthorn and Webb, 2001; Scheiber-Enslin and Manzi, 2018; Sehoole *et al.*, 2020). The main aim of the study is to apply careful reprocessing workflows (mainly pre-stack depth-imaging) on the 1986 legacy

seismic profile to produce improved seismic images for a better understanding of the continuity of the platinum-bearing horizons on the southeastern edge of the Western limb, as well as the tectonic evolution of the geological structures in general. The legacy seismic line was collected from south to north (Figure 1c), traversing towards the centre of the complex, and the results from the study could provide insight regarding the discussion around the connectivity between the Western and Eastern limbs of the Bushveld Complex at depth (Cawthorn and Webb, 2001; Shithigona *et al.*, 2018).

In addition to the 2D legacy seismic profile, we integrate the magnetic data to gain an understanding of the geological structures and their relationship with the platinum-bearing horizon. Owing to the fact that some geological structures have thicknesses and dips that make them difficult to image using seismic methods, the regional high-resolution aeromagnetic data (Figure 1d) are used to provide constraints on the geometry of the faults and magnetic dykes that crosscut the legacy seismic line (Scheiber-Enslin and Manzi, 2018). Herein, we demonstrate a suitable depth imaging workflow through reprocessing of the 1986 data with a special focus on pre-stack depth migration (PSDM). We compare the results from two PSDM methods: conventional Kirchhoff pre-stack depth migration (KPreSDM) and a focusing pre-stack depth migration technique namely coherency migration (CM).

ELAND MINE AND WESTERN LIMB OF THE BUSHVELD COMPLEX

Background information

The Eland mine (triangle in Figure 1a) is a relatively new platinum mine on the southeastern edge of the Western limb of the Bushveld Complex. The mine started with opencast mining operations in 2007, and underground production commenced in 2010 until placed under care approximately five years later. Potgieter and Malan (2010) detailed the mining method at the Eland platinum mine and one of the complicating factors is the dip of the ore body at ~18° to the North. After a feasibility study in 2015, Northam platinum mine bought Eland mine operations from Glencore in 2017. Northam Platinum is assessing the feasibility of extending the Eland mine infrastructure to access reserves down dip and along the strike of the platinum-bearing horizons, with a hybrid mining method (a semi-mechanized development as well as traditional stoping). Eland mine is currently mining the Merensky reef (MR) and the UG2, and the Merensky is not well developed on the eastern edge of the mining rights area. The underdevelopment of the Merensky reef is due to the

thinning of the Critical Zone from west to east in the Western limb. Consequently, on the eastern edge, Eland mine conducted a feasibility study to employ an open-pit mining operation. Therefore, we envision that the results from this legacy seismic profile could provide insight into understanding the thinning of the Critical Zone further east (~ 10 km east of the Eland mine).

Geological background

The Western limb of the Bushveld Complex has been studied by several authors, including Cawthorn and Webb (2001), Scheiber-Enslin and Manzi (2018), Manzi *et al.* (2019b), and Sehoole *et al.* (2020). However, the southeastern edge of the Western limb has not been studied in detail due to thinning of the mineralized Critical Zone (Cawthorn and Webb, 2001). Figure 1b shows a simplified stratigraphic column of the Western limb of the Bushveld Complex. Summarily, the mafic cumulate rocks of the Bushveld Complex are called the Rustenburg Layered Suite (RLS) and are divided into five zones, namely the Marginal, Lower, Critical, Main, and Upper zone. The RLS overlies the Transvaal Supergroup sediments and is in turn overlain by the felsic cumulate rocks of the Bushveld Complex called the Rashoop Granophyre Suite and Lebowa Granite Suite (Scheiber-Enslin and Manzi, 2018). The Critical Zone of the RLS, reaching a maximum thickness of ~ 1.5 km, is divided into Lower and Upper Critical Zone according to the plagioclase crystal's appearance (Sehoole *et al.*, 2020). The two economically viable PGE deposits in the study area, Merensky reef and UG2 occur near the top of the Upper Critical Zone. Merensky reef is hosted within the Merensky pyroxenite between 15 and 400 m above the UG2 chromitite and has a thickness range of 0.5 m to 2 m (Manzi *et al.*, 2019b; Rapetsoa *et al.*, 2022).

Structurally, the southeastern edge of the Western limb is characterized by a major right-lateral Crocodile River fault trending NNW. This fault is accompanied by NNE trending mafic dykes with low magnetic signature and minor NE trending left-lateral scissor faults such as Lindiwe and Schietfontein faults (Figure 1c) (Dube, 2010, unpublished data). Dube (2010) and Basson (2019) interpreted these fault structures to postdate the Bushveld Complex mineralized mafic units, as well as being hinged by the Crocodile River fault on the northeastern edge and exhibit maximum displacement of approximately 150 m on the southwestern edge. The Crocodile River fault is particularly interesting since it crosscuts the 1986 legacy seismic profile in the south (Figure 1c). Another large-scale EW trending geological lineament of interest is the strongly magnetized Chaneng structure (Figures 1c and d) that crosscuts the legacy profile in the north. The Chaneng

structure is a normal fault with a magnetic signature that is associated with a dyke (Scheiber-Enslin and Manzi, 2018; Basson, 2019). The imaging of these structures through reprocessing of the legacy seismic data are significant for future mine planning and characterization of their geometry in the region.

Transvaal Supergroup inliers

The Bushveld Complex mafic and granitic rocks intruded the Transvaal Supergroup, and several inliers of highly deformed Transvaal rocks occur in the Bushveld Complex (Figure 1a). The Crocodile River dome and the Rooiberg fragment in the western limb and Dennilton-Marble Hall dome, and Stavoren fragment in the eastern limb are the most prominent Transvaal Supergroup inliers (Hartzer, 1995). Understanding the geology and tectonic evolution of these inliers provides insight into the distribution and geometry of the target mineralized RLS and regional tectonics of the Bushveld Complex. The Crocodile River dome lithostratigraphy and tectonic relationship with the Bushveld Complex is of interest in this study because it forms the northern half of the reprocessed legacy profile. Several authors (e.g., Humphrey, 1906, 1909; Fockema, 1947, unpublished data; Groeneveld, 948, unpublished data; Hartzer, 1989, 1995, and references therein) provide a detailed geological description of the dome, which is over 1 560 m thick (Hartzer, 1995).

LEGACY 2D SEISMIC DATA

Seismic data acquisition

We received the 50 km long 2D legacy reflection seismic profile as raw shot gathers and a cropped post-stack migrated image with acquisition information in hardcopy observer's reports. The raw shot gathers were in SEG-Y format without geometry information in the header files, which required manual digitizing from the observer's reports. The profile was collected on the southeastern edge of the Western limb of the Bushveld Complex, approximately 10 km east of the Eland mine. Table 1 outlines the summary of the acquisition parameters of the profile. The 2D legacy reflection seismic profile was acquired in 1986 using a vibroseis truck as an energy source. We recovered a total of 998 correlated shot records with 96 channels per shot, 50 m shot spacing and 25 m receiver spacing. The survey was designed with a 16 s sweep length, 20-90 Hz linear sweep frequency band and a sampling interval of 2 ms. The profile was acquired with a split spread geometry with a maximum offset of 1200 m and 24-fold coverage.

Seismic data reprocessing

The seismic profile was initially processed through a conventional post-stack time migration workflow (Odgers *et al.*, 1993). In this study, we applied a pre-stack depth imaging workflow (Figure 2). Moreover, the focus of the workflow is the application of an advanced focusing pre-stack depth-migration approach (coherency migration) as well as the usage of a reliable migration velocity model in depth. The velocity analysis is carried out conventionally by picking semblance peaks from a velocity spectrum to determine the moveout velocity assuming a horizontally layered medium. However, semblance velocity analysis cannot be easily adapted to hardrock environments that have strong lateral velocity variations and steeply dipping reflectors. The results from using the wrong velocity model for the normal moveout correction strongly affect the quality of the stacked section. In this study, the velocity model used for pre-stack depth migration is a smoothed interval velocity model derived directly from the depth domain.

A summary of the processing workflow applied to the data set is shown in Figure 2. The legacy data were recovered and resorted through various pre-processing steps to revamp it to contemporary standards compatible with modern seismic processing software. The header information was digitized from handwritten observer's reports to set up a new geometry with traces stored in common midpoint (CMP) bins spaced 12.5 m apart using a spline curve. A 50 Hz notch filter was applied to the data already during acquisition to remove the spiking noise resulting from the AC power lines in the study area.

Figure 3 shows an example of the raw and reprocessed shot gathers. The data generally have good quality with most shot gathers showing clear first breaks (indicated by the FB arrow in Figure 3a). Following the geometry setup of the data, a total of 89882 first arrivals were manually picked for the application of appropriate statics. The floating datum was calculated using a maximum elevation of 1368 m as a fixed datum with a replacement velocity of 6000 m/s. The statics were calculated with the RMS error of less than 7 ms using the least-squares inversion method (Woodward, 1991). The attenuated amplitudes were recovered using an automatic gain control (AGC) with a window length of 1000 ms.

Additionally, we applied f-k filtering, spiking deconvolution, and frequency filtering. The direct surface wave arrivals have an average velocity of 3200 m/s, therefore an f-k filter was applied to mute any linear signal velocity less than 3300 m/s. We broadened the spectrum using predictive

deconvolution with a 4 ms gap length and 180 ms filter length to simulate spiking deconvolution. A frequency bandpass filter was applied to remove frequencies outside the frequency band [5-20-100-110 Hz]. Finally, a refraction top mute was applied to the data. As indicated by reflections A, D, and E in Figure 3b, reflection continuity and resolution of the processed shot gathers have improved.

Analysis and comparison between the raw and reprocessed 1986 2D seismic profile sample shot gathers is shown in Figure 3. The strong reflections observed on the exemplary reprocessed shot gather are the main lithological contacts with significant acoustic impedance contrast between the overlying and underlying rocks (Figure 3b): Rashoop Granophyre-Upper Zone ferrogabbros (A), Transvaal Supergroup-Rustenburg Layered Suit norites (D), and an intrusive Diabase sill (E).

Refraction tomography velocity model

Interactive interval velocity analysis was performed for the construction of a migration velocity model in the depth domain. The migration velocity model needs to incorporate realistic information about the near surface as well as deep-seated geology. The near surface velocity information used in this study is derived directly from refraction tomographic velocity analysis. A conventional velocity analysis was conducted with interval velocities derived from the previous studies conducted in the Bushveld Complex (Odgers *et al.*, 1993; Rapetsoa *et al.*, 2022).

After manually picking a total of 89882 P-wave first breaks, a three-layered initial model was defined by fitting the gradients in the first break picks for the first arrival traveltime inversion. Using the geometry of the data, the synthetic traveltimes were calculated for the initial model using the ray tracing method. The tomographic approach that was applied to the data set to calculate synthetic traveltimes is a nonlinear refraction traveltime tomography method developed by Zhang and Toksöz (1998).

A first break travel time tomography to a depth of 600 m, which accounted for elevation variation to a datum of 1398 m, was computed across the profile with a maximum shot gather offset of ~ 1 200 m and padding airwave velocity of 340 m/s. The ray paths and velocity model are displayed in Figures 4a and b, respectively, with vertical exaggeration. The velocity model shows low-resolution velocity boundaries between strata with velocities ranging between 2000 m/s and 6800 m/s. The uppermost layer of the initial model is relatively thin, only occurring on the southern and

northern edges of the profile and possibly represents Karoo cover sediments with velocities ranging from 2500 m/s to 3500 m/s. The second layer has a strong velocity gradient from 3500 m/s to 5500 m/s. The observed strong velocity gradient in the upper few hundred meters is possibly the weathered layer. The host rocks have an average velocity of 6500 m/s with low-resolution lateral velocity variation characteristic of weak zones which are interpreted as faults (Figure 4b).

Depth imaging

Seismic imaging in hardrock environments is more challenging in comparison with softrock settings because of the complex geology, disrupted reflectors, and scattered seismic energy. Prestack depth migration especially in a Kirchhoff type implementation has proven its success in such complex crystalline hardrock environments since at least two decades (Buske, 1999). Further developments towards incorporating a focusing migration operator resulted in advanced prestack depth migration techniques, e.g. Fresnel Volume Migration (Lüth *et al.*, 2005; Buske *et al*., 2009), coherency migration and coherency-based Fresnel Volume Migration (Hloušek *et al.*, 2015a). Successful applications of these focusing PSDM methods range from imaging crustal fault systems (Hloušek and Buske, 2016) over the characterization of geothermal reservoirs (Hloušek *et al.*, 2015b; Schreiter *et al.*, 2015; Riedel *et al.*, 2015; Jusri *et al.*, 2018) to the high-resolution imaging of mineral deposits (Heinonen *et al.*, 2019; Singh *et al.*, 2019; Bräunig *et al.*, 2019; Hloušek *et al.*, 2022; Cheraghi *et al.*, 2022).

Therefore, the application of these newly developed seismic imaging tools for hardrock environment is worthwhile. Here, we demonstrate again the effectiveness of these approaches by applying the coherency migration (CM) technique to the 2D legacy seismic profile from the Bushveld Complex known for its hardrock PGE exploration.

CM is one of the possible implementations of focusing prestack depth migration approaches. It is based on Kirchhoff pre-stack depth migration (KPreSDM), which is an integral solution for the wave equation in the form of a diffraction integral (Schneider, 1978). Therefore, the resultant image value for a random point in the subsurface is described by the weighted summation over the corresponding diffraction surface for the given point. The weighting function along the diffraction curve accounts for the directivity-based energy losses and spherical divergence. The image for a single surface shot wavefield which is scattered by a single diffraction point in a homogeneous medium and recorded by a single receiver on surface is constructed by smearing the amplitudes

along their corresponding TWT isochrones. This concept can be extended for multiple shots and receivers on surface by treating every single point along the reflector as a point diffractor and a migrated image of the reflector can be constructed by constructive interference of all TWT isochrones along the reflector.

Focusing migration approaches limit the migration operator to the physically relevant part along the TWT isochrone. This is achieved by adding an additional weighting factor to the Kirchhoff integral solution dependent on the image point, which ensures that the amplitudes are smeared in the physically pertinent region along the traveltime isochrone.

CM uses a weighting factor obtained directly from the input data (Hloušek *et al.*, 2015b). This weighting factor is computed by evaluating the semblance coefficients (Neidell and Taner, 1971) of the recorded wavefield along the theoretical diffraction curves, defined by the individual two-way traveltime for the same image point at different neighboring receivers. The semblance coefficient is one when the image point is equal to the true diffraction point and zero when no coherent signal is present. The computed value can directly be used to weight the amplitudes during migration (Hloušek *et al.*, 2015b).

RESULTS AND INTERPRETATION

According to the surface geological map (Figure 1c) the 1986 2D seismic profile was collected over an outcrop of the Transvaal Supergroup in the southern portion, Bushveld Complex in the middle portion, and Karoo Sequence in the north portion. The strata are documented to be dipping to the north in the southern section at approximately 20°. This is supported by the presence of Karoo sediments on the northern edge of the data and the outcrop of the Transvaal and Bushveld strata on the southern edge (Odgers *et al.*, 1993).

Comparison between legacy data and reprocessed data

The new imaging results (Figures 5b and 6) of the southern section of the legacy profile are in general analogous to the results presented by Du Plessis and Levitt (1987) of an unmigrated stacked section of the profile. Odgers *et al.* (1993), aiming to collapse diffractions, migrate dipping reflections to their true subsurface position, and suppress multiple reverberations reprocessed the profile and presented a detailed interpretation of the post-stack time migrated section (Figure 5a). The results correspond to the interpretation of the southern section of the CM result (Figure 5b).

The high amplitude reflections marked D, E, F, and G (Figures 5a and b) correspond to the Transvaal Supergroup, with reflection D marking the contact between the overlying RLS norites and the Transvaal sequence. Reflection E is the 85 m thick diabase sill, with its continuity clearly mapped by the CM at depth. Reflections F and G mark the base of Timeball Hill Formation and Chuniespoort Group or Black reef, respectively, and their continuity is better imaged by the CM. The contact between the low amplitude reflections of high frequency from the RLS norites and the overlying low amplitude reflections of low frequency from the RLS gabbros is marked C in Figures 5a and b. Makers A and B represent the RLS gabbros-RLS ferrogabbros contact and the RLS ferrogabbros-Rashoop Granophyre Suit contact, respectively (Odgers *et al.,* 1993).

The northern section of the profile (Figure 6, highlighted by rectangles in Figure 5) was interpreted with contrasting results by Du Plessis and Levitt (1987), and Odgers *et al.* (1993). Du Plessis and Levitt (1987) concluded that the RLS rocks terminate against a major fault called Mabopane fault and the geology is analogous to the neighbouring Crocodile River dome. Odgers *et al.,* (1993) interpreted the low signal-to-noise ratio (SNR) character of the northern section of the legacy time migrated profile to be due to out-of-plane reflection energy, poor source-to-ground coupling, or energy scattering and interference. Therefore, concluding that the RLS rocks occur as a highly faulted anticlinal structure which formed during the intrusion of the complex rocks (Odgers *et al.,* 1993). The CM result (Figure 6b) resolved the anticlinal structure better than the legacy post-stack time migrated section (Figure 6a). This region exhibits high amplitude discontinuous reflections overlain by low amplitude discontinuous reflections. The distinction between these reflections is not clear in the legacy stack, and it allows for the delineation of major geological structures like the Chaneng structure and the Mabopane fault (Figure 6b). The high amplitude reflections are interpreted to correspond to highly faulted Transvaal Supergroup rocks, and the overlying low amplitude reflections correspond to the RLS norite-gabbros.

Figures 7a and b show the comparison between the conventional KPreSDM section and the CM section down to a depth of 16 km, with the outcrop data along the profile overlain. The A, B, C, D, E, F, and G reflections are clearly defined in the CM section (Figure 7b) compared to the KPreSDM section (Figure 7a).

Aeromagnetic data

The regional aeromagnetic data acquired at a terrain clearance of 100 – 150 m lines with flight lines spaced at 1 km imaging the Upper Zone sequence outcrop mapped in the four lobes, due to the strong positive magnetic signature of the ferrogabbro and magnetite horizons is shown in Figure 1d (Campbell, 2011). Figure 8a shows the magnetic profile along the seismic section in Figure 8b, with the geological structures mapped by magnetic data overlain on the seismic section. This data adequately map the regional faults and dykes that crosscut the seismic profile (e.g., the Chaneng structure and the Crocodile River fault). The low magnetic signature observed in the northern section of the profile is interpreted to result from the absence of the Upper Zone positively magnetized rocks (RLS Magnetic-Gabbro).

Out-of-plane reflectivity

A 2D reflection seismic line collected with a high-fold crooked line geometry is a limited swath 3D survey of the subsurface reflectivity near the line (Nedimovic and West, 2003). Therefore, reflection energy from out-of-plane structures can migrate to the profile imaging plane at later, equal, or earlier TWT compared to energy reflected within plane depending on their geometry. The reflections from out-of-plane energy can interfere (constructively or destructively) with reflections within plane leading to distorted amplitudes and low SNR. Here, 2D seismic data are pseudo-3D migrated producing a 3D volume (Figure 9) to access cross-profile information about the subsurface reflectivity. The green arrows show constructive interference out-of-plane with ambiguous possible source of reflectivity. The reflectivity could be from anywhere in the cylindrical curve around the surface. However, this shows that there is a presence of out-of-plane reflectivity in the northern half of the profile contributing to the low SNR.

Figure 9 is a 3D view of the crooked line CM section with the surface geological map (Figure 1c) overlain, and the regional geological structures (e.g., Crocodile River fault and Chaneng structure marked) together with the target PGE reefs (MR and UG2). The migration velocity model (Figure 10a) and the final interpreted section of the 2D legacy reflection seismic profile (Figure 10b) are shown in Figure 10. The proposed tectonic evolution along the profile is outlined in Figure 11.

DISCUSSION

The previous interpretation of the profile carried out by Du Plessis and Levitt (1987) and Odgers *et al.* (1993) was focused primarily on reflection contacts associated with the geological sequences

on the post-stack time migrated section correlated to the mapped surface geological outcrop. The dominant reflections Marked A, B, C, D, E, F, and G outlined on the reprocessed data correspond with the results from the previous interpretation. The geological models were supported by regional gravity data along the profile (Odgers, 1992, unpublished data). However, the previous interpretation did not outline detailed tectonic information along the profile and recommended the application of prestack depth imaging techniques (Odgers, 1992, unpublished data).

The RLS sequence of the Bushveld Complex is of particular interest in this study as it hosts PGE deposits in the complex. Our interpretation is constrained by the limitations of 2D seismic data imaging. True dips and thicknesses cannot be determined from 2D data due to signal from out-of-plane reflections that can be misinterpreted as in-plane features. This is exaggerated in hardrock rock environment with layered igneous rocks of the RLS that might course seismic energy scatters resulting in low amplitude and coherency in the reflections. The interpretation presented in this study is based on constraining datasets (e.g., post-stack time migrated data, regional aeromagnetic data, and surface geological mapping) from previous studies. Moreover, the presence of the Karoo sediments on the northern half of the profile leads to high seismic signal energy attenuation. The Karoo Supergroup is laden with dolerite intrusions and has unconsolidated younger sediments which lead to seismic energy scattering and poor source-to-ground coupling, respectively. Therefore, the interpretation of the data in the northern half is of rather low-confidence compared to the southern half.

The presence of the anticlinal structure on the seismic section is associated with the Chaneng structure (Figure 10b) in the northern half of the profile. This corresponds to the interpretation of the Chaneng structure by Scheiber-Enslin and Manzi (2018) on the western edge of the Western limb (near Rustenburg). This structure is interpreted to cause shallowing of the PGE mineralization near the intrusive Pilanesberg complex, and it is linked with the upwelling of basement rocks during the intrusion of the complex (Scheiber-Enslin and Manzi, 2018). Campbell (2011) interpreted the northern sector of a seismic profile (traversing 50 km NNE from Rustenburg) as a complex pseudo graben structure where it is crosscut by the Chaneng structure. In this study, the anticlinal structure is interpreted to be a southern extension of the Crocodile River dome covered by younger Karoo sediments.

Tectonic model

Our reprocessing results, integrated with existing geological information, are also being used to constrain the strato-structural model of the region. Transvaal Supergroup sedimentation started approximately 2642 Ma (Walraven and Martini, 1995) with the deposition of Wachteenbeetje Formation along a series of east-northeasterly trending depressions. After thin fluvial sheet sandstones of the Black reef Formation, a series of regressions and transgressions triggered the development of shallow shelf carbonate-banded iron formation platform succession of the Chuniespoort Group (~ 2557 ± 49 – 2430 Ma) (Nelson *et al.*, 1999; Eriksson *et el.*, 2002). Following a period of erosion and marine transgression, Pretoria Group siliciclastic sedimentary rocks were deposited approximately 2224 ± 21 Ma (Hartzer, 1989; Walraven and Martini, 1995; Eriksson *et al.*, 2002)

Pre-Bushveld Complex deformation following the Transvaal Supergroup deposition includes, firstly, updoming of the sediments which resulted in the deposition of thinner Pretoria Group sediments in the Crocodile River dome area. Secondly, the development of northwest striking folds followed by east-northeast striking folds from compressional forces. Finally, possible faulting along weak zones is shown by the south-north tectonic model along the legacy profile (Figure 11a) (Hartzer, 1989).

Bushveld Complex intrusion into the upper Pretoria Group rocks approximately 2055 Ma terminated the sedimentation of the Transvaal Supergroup. The location of the feeders and the exact composition of the parental magmas are still subject to debate. The coarse-grained Bushveld igneous rocks with composition ranging from ultramafic to felsic were emplaced from different feeder channels and their rate and effective mixing are yet to be resolved. The updoming of the Transvaal rocks advanced to a stage where the domes acted as barriers controlling the magma to either spread out against them or extend across as shown in Figure 11b. The intrusion reactivated pre-existing deformation structures and caused low-medium grade metamorphism in the Transvaal sediments (Hartzer, 1989).

Post-Bushveld Complex deformation reactivated the northwest and east-northeast striking seismically defined fault zones like the Crocodile River fault and Chaneng structure, respectively. Isostatic readjustment due to the intrusion probably exerted further compressional forces on the folds leading to a relative upward movement of the Transvaal inlier (Crocodile River dome) and subsequent erosion (Figure 11c) (Hartzer, 1989).

CONCLUSION

Reprocessing of the 2D legacy seismic profile using coherency migration (CM) has yielded an improved depth image of the southeastern edge of the Western limb of the Bushveld Complex. Despite the challenges associated with seismic energy attenuation, the platinum group element (PGE) bearing horizons of the Rustenburg Layered Suite (RLS) have been imaged with considerable confidence. Moreover, the information from the previous seismic, magnetic and geological studies in the Bushveld complex has contributed with the imaging of the complex geological structures. The low signal-to-noise ratio in the northern half of the profile is attributed to the presence of out-of-plane reflectivity. Despite the presence of out-of-plane reflectivity, the signal-to-noise ratio of the northern half of the profile has been improved.

The northern half of the profile interpretation provides evidence for the presence of the geological structures interpreted in the previous studies, namely Mabopane fault and Chaneng structure. The anticlinal structure present in the northern half of the profile was successfully imaged by the CM technique. The upwelling and erosion of the RLS lithologies provides possible evidence of depletion of PGE mineralisation in this region. The tectonic evolution outlined along the profile provides insight into the possible depletion of the PGE mineralisation in the northern edge of the profile. A 3D reflection seismic acquisition method is recommended to improve the signal-to-noise ratio of the northern edge of the profile to account for out-of-plane reflectivity.

ACKNOWLEDGEMENTS

We are grateful for the financial support from DST-NRF CIMERA and Wits Seismic Research Centre. The coordinates were sorted on MATLAB and prestack time domain seismic data reprocessing was done on the Globe Claritas; we appreciate the sponsorship of the software licences by Globe Claritas to the University of the Witwatersrand, Johannesburg. We acknowledge the Council of Geoscience for providing access to the raw seismic data for the study.

DATA AVAILABILITY STATEMENT

The data are available on request from the corresponding author, subject to approval by the Council of Geoscience.

CONFLICT OF INTEREST

The authors declare no conflict of interest.

REFERENCES

Basson, I. J., (2019) Cumulative deformation and original geometry of the Bushveld Complex. *Tectonophysics* 750, 177-202. https://doi.org/10.1016/j.tecto.2018.11.004

Buske, S., (1999) Three-dimensional pre-stack Kirchhoff migration of deep seismic reflection data. *Geophysics*. J. Intern., 137:243-260. https://doi.org/10.1046/j.1365-246x.1999.00789.x

Buske, S., Gutjahr, S. and Sick, C., (2009) Fresnel volume migration of single-component seismic data. *Geophysics* 74(6), WCA47-WCA55. https://doi.org/10.1190/1.3223187

Bräunig, L., Buske, S., Malehmir, A., Bäckström, E., Schön, M. and Marsden, P., (2019) Seismic depth imaging of iron-oxide deposits and their host rocks in the Ludvika mining area of central Sweden. *Geophysical Prospecting* 68(1), 24-43. https://doi.org/10.1111/1365-2478.12836

Campbell, G., (2011) Exploration geophysics of the Bushveld Complex in South Africa. *The Leading Edge* 30(6), 622-638. https://doi.org/10.1190/1.3599148

Cawthorn, R. G. and Webb, S. J., (2001) Connectivity between the western and eastern limbs of the Bushveld Complex. *Tectonophysics* 330(3-4), 195-209. https://doi.org/10.1016/S0040-1951(00)00227-4

Cawthorn, R. G., (1999) The discovery of the platiniferous Merensky Reef in 1924. *South African Journal of Geology* 102(3), 178-183. https://hdl.handle.net/10520/EJC-112518d32d

Cheraghi, S., Hloušek, F., Buske, S., Malehmir, A., Adetunji, A., Haugaard, R., Snyder, D. and Vayavur, R., (2022) Reflection seismic imaging across a greenstone belt, Abitibi (Ontario)-Canada. *Geophysical Prospecting*. https://doi.org/10.1111/1365-2478.13284

Donoso, G. A., Malehmir, A., Pecheco, N., Araujo, V., Penney, M., Carvalho, J., Spicer, B. and

Beach, S., (2020) Potential of legacy 2D seismic data for deep targeting and structural; imaging at the Neves-Corvo massive sulphide-bearing deposit, Portugal. *Geophysical Prospecting* 68, 44-61. https://doi.org/10.1111/1365-2478.12861

Du Plessis, A. and Le, Levitt J. G., (1987) On the structure of the Rustenburg Layered Suite – insight from seismic reflection data. Presented at the Indaba on the tectonic setting of layered intrusives. *Geol. Soc. S. Afr.* University of Pretoria, Inst. Geol. Res. Bushveld Complex.

Eriksson, P. G., Condie, K. C., van der Westhuizen, W., van der Merwe, R., de Bruiyn, H., Nelson, D. R., Altermann, W., Cetuneanu, O., Bumby, A. J., Lindsay, J. and Cunningham, M. J., (2002) Late Archaean superplume events: a Kaapvaal-Pilbara perspective. *Journal of Geodynamics* 34, 207-247. https://doi.org/10.1016/S0264-3707(02)00022-4

Hartzer, F. J., (1995) Transvaal Supergroup inliers: geology, tectonic development and relationship With the Bushveld complex, South Africa. *Journal of African Earth Sciences* 21(4), 521-547. https://doi.org/10.1016/0899-5362(95)00108-5

Hartzer, F. J., (1989) Stratigraphy, structure and tectonic evolution of the Crocodile River Fragment. *S. Afr. J. Geol.* 92, 110-124.

Heinonen, S., Malinowski, M., Hloušek, F., Gislason, G., Buske, S., Koivisto, E. and Wojdyla, M., (2019) Cost-effective seismic exploration: 2D reflection imaging at the Kylylahti massive sulfide deposit, Finland. *Minerals* 9(5), 263. https://doi.org/10.3390/min9050263

Hloušek, F., Malinowski, M., Bräunig, L., Buske, S., Malehmir, A., Markovic, M., Sito L., Marsden, P. and Bäckström, E., (2022) Three-dimensional reflection seismic imaging of the iron oxide deposits in the Ludvika mining area, Sweden, using Fresnel volume migration. *Journal of Geophysical Research: Solid Earth* 13(5), 917-934. https://doi.org/10.5194/se-13-917-2022

Hloušek, F., Hellwig, O. and Buske, S., (2015a) Improved structural characterization of the Earth's

crust at the German Continental Deep Drilling Site using advanced seismic imaging techniques. *Journal of Geophysical Research: Solid Earth* 120(10), 6943-6959. https://doi.org/10.1002/2015JB012330

Hloušek, F., Hellwig, O. and Buske, S., (2015b) Three-dimensional focused seismic imaging for geothermal exploration in crystalline rock (Schneeberg, Germany). *Geophysical Prospecting* 63(4), 999-1014. https://doi.org/10.1111/1365-2478.12239

Humphrey, W. A., (1906) On a portion of the Bushveld lying south of the Rooiberg and east of the Crocodile river. Geological Survey Transvaal, Pretoria, South Africa. *Annual Report* 1906, 109-115.

Humphrey, W. A., (1909) On a portion of the Bushveld bordering the Crocodile River and including the Rooiberg Tin-Field. Geological Survey Transvaal, Pretoria, South Africa. *Report* 1908, 103-112.

Jusri, T., Bertani, R. and Buske, S., (2018) Advanced three-dimensional seismic imaging of deep supercritical geothermal rocks in Southern Tuscany. *Geophysical Prospecting* 67(2), 298-316. https://doi.org/10.1111/1365-2478.12723

Lüth, S., Buske, S., Giese, R. and Goertz, A., (2005) Fresnel volume migration of multicomponent data. *Geophysics* 70(6), S121-S129. https://doi.org/10.1190/1.2127114

Malehmir, A., Donoso, G., Markovic, M., Maries, G., Dynesius, L., Brodic, B., Pecheco, N., Marsden, P., Backstrom, E., Penney, M. and Araujo, V., (2019) Smart Exploration: from legacy data to state-of-the-art data acquisition and imaging. *First Break* 37(8), 71-74. https://doi.org/10.3997/1365-2397.n0049

Malehmir, A. and Bellefleur, G., (2010) Reflection seismic imaging and physical properties of base-metal and associated iron deposits in the Bathurst Mining Camp, New Brunswick, Canada. *Ore Geology Reviews* 38(4), 319-333. https://doi.org/10.1016/j.oregeorev.2010.08.002

Manzi, M. S. D., Cooper, G. R. J., Malehmir, A. and Durrheim, R. J., (2019) Improved structural interpretation of legacy 3D seismic data from Karee platinum mine (South Africa) through the application of novel seismic attributes. *Geophysical Prospecting* 68(1), 145-163. https://doi.org/10.1111/1365-2478.12900

Manzi, M. S. D., Malehmir, A. and Durrheim, R. J., (2019b) Giving the seismic data the attention they deserve. *First Break* 37(8), 89-96. https://doi.org/10.3997/1365-2397.n0050

Nedimović, M. R. and West, G. F., (2003) Crooked-line 2D seismic reflection imaging in crystalline terrains: Part 2, migration. *Geophysics* 68(1), 286-296. https://doi.org/10.1190/1.1543214

Neidell, N. S. and Taner, M. T., (1971) Semblance and other coherency measured for multichannel data. *Geophysics* 36(3), 482-497. https://doi.org/10.1190/1.1440186

Nelson, D. R., Trendall, A. F. and Altermann, W., (1999) Chronological correlations between the Pilbara and Kaapvaal cratons. Precambrian Research 97, 165-189. https://doi.org/10.1016/S0301-9268(99)00031-5

Odgers, A. T. R., Hinds, R. C. and Von Gruenewaldt, G., (1993) Interpretation of a seismic reflection survey across the southern Bushveld Complex. *South African Journal of Geology* 96, 205-212.

Podvin, P. and Lecomte, I., (1991) Finite difference computation of traveltimes in very contrasted velocity models: a massively parallel approach and its associated tools. *Geophysical Journal International* 105(1), 271–284. https://doi.org/10.1111/j.1365-246X.1991.tb03461.x

Potgieter, G. S. and Malan, D. F., (2010) Preliminary evaluation of the proposed mining method at Eland Platinum Mine. *The 4th International Platinum Conference, Platinum in transition 'Boom or Bust'.*

Pretorius, C. C., Muller, M. R., Larroque M. and Wilkins, C., (2003) A review of 16 years of

hardrock seismic of the Kaapvaal Craton, in: D.W. Eaton, B. Milkereit, and M. H. Salisbury, eds., Hardrock Seismic Exploration, Geophysical Developments. *Society of Exploration Geophysicists* 10, 247-268. https://doi.org/10.1190/1.9781560802396.ch16

Pretorius, C. C., Trewick, W. F. and Irons, C., (2000) Application of 3D-seismics to mine planning at the Vaal Reefs gold mine, number 10 shaft, republic of South Africa. *Geophysics* 65, 1862-1870. https://doi.org/10.1190/1.1444870

Rapetsoa, M. K., Manzi, M. S. D., Westgate, M., Sihoyiya, M., James, I., Onyebueke, E., Kubeka, P., Durrheim, R. J. and Kgarume, T., (2022) Cost-effective in-mine seismic experiments to image platinum deposits and associated geological structures at Maseve platinum mine, South Africa. *Near Surface Geophysics* 70(6). https://doi.org/10.1002/nsg.12216

Riedel, M., Dutsch, C., Alexandrakis, C., Dini, I., Ciuffi, S. and Buske, S., (2015) Seismic depth imaging of a geothermal system in southern Tuscany. *Geophysical Prospecting* 63(4), 957-974. https://doi.org/10.1111/1365-2478.12254

Scheiber-Enslin, S. E. and Manzi, M. S. D., (2018) Integration of 3D reflection seismics and magnetic data for deep platinum mine planning and risk mitigation: a case study from Bushveld Complex, South Africa. *Exploration Geophysics* 49(6), 928-939. https://doi.org/10.1111/1365-2478.12254

Schreiter, L., Hlousek, F., Hellwig, O. and Buske, S., (2015) Characterization of seismic reflections from faults in a crystalline environment, Schneeberg, Germany. *Geophysical Prospecting* 63(4), 1015-1032. https://doi.org/10.1111/1365-2478.12255

Schneider, W. A., (1978) Integral formulation for migration in two and three dimensions. *Geophysics* 43, 49-76. https://doi.org/10.1190/1.1440828

Sehoole, L., Manzi, M. S. D., Zhang, S. E. and Bourdeau, J. E., (2020) An innovative seismic and statistical approach to understand 3D magmatic structures and ore deposits in the western Bushveld Complex, South Africa. *Ore Geology Reviews* 126, 103784. https://doi.org/10.1016/j.oregeorev.2020.103784

Shithigona, O., Manzi, M. S. D., Ashwal, L. D., Bybee, G. M. and Webb, S. J., (2018) Experimental studies of elastic wave velocities and densities in rocks from the Bushveld Complex, South Africa: implications for deep reflection seismic surveys. *South African Journal of Geology* 121(3), 311-326. https://doi.org/10.25131/sajg.121.0029

Sihoyiya, M., Manzi, M. S. D., James, I., Rapetsoa, M. K., Westgate, M., Nwaila, G., Linzer, L., Durrheim, R. J. and Staley, P., (2022) Seismic delineation of the gold-bearing structures in the South Rand Goldfield (South Africa) – comparison of pre-stack time and depth migration approaches on legacy seismic data. *Near Surface Geophysics* 70(6). https://doi.org/10.1002/nsg.12209

Singh, B., Malinowski, M., Hloušek, F., Koivisto, E., Heinonen, S., Hellwig, O., Buske S., Chamarczuk, M. and Juurela, S., (2019) Sparse 3D seismic imaging in the Kylylahti mine area, Eastern Finland: comparison of time versus depth approach. Minerals, 9(5). https://doi.org/10.3390/min9050305

Walraven, F. and Martini, J., (1995) Zircon Pb-evaporation age determinations of the Oak Tree Formation, Chuniespoort Group, Transvaal Sequence: Implications for Transvaal-Griqualand West basin correlations. *South African Journal of Geology* 96, 58-67. https://hdl.handle.net/10520/EJC-929187cc0

Westgate, M., Manzi, M. S. D., James, I. and Harrison, W., (2020) New insight from legacy seismic data: reprocessing of legacy 2D seismic data for imaging of iron-Oxide mineralization near Sishen Mine, South Africa. *Geophysical Prospecting* 68(7), 2119-2140. https://doi.org/10.1111/1365-2478.12996

Woodward D. J. 1991. Inversion of seismic refraction data. *Geophysics Division Technical Report No. 114.*

Zhang J. and Toksöz M. N. 1998. Nonlinear refraction traveltime tomography. *Geophysics* **63**(5), 1726-1737. https://doi.org/10.1190/1.1444468

LIST OF FIGURES

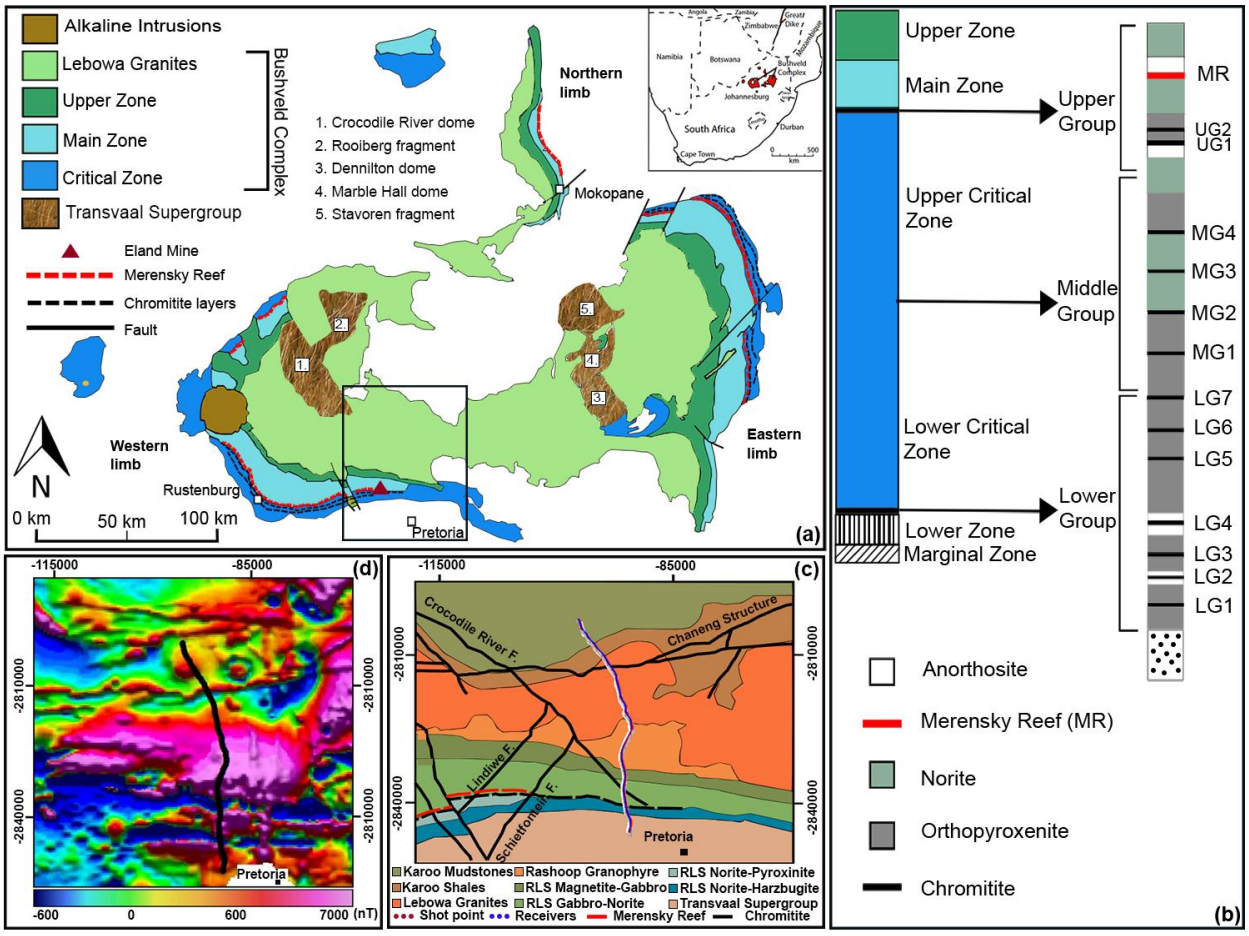


Figure 1: (a) Simplified geological map of the Bushveld Complex showing the study area, (b) simplified stratigraphy of the Bushveld Complex, (c) geological map covered by the seismic line and (d) aeromagnetic map covered by the line.

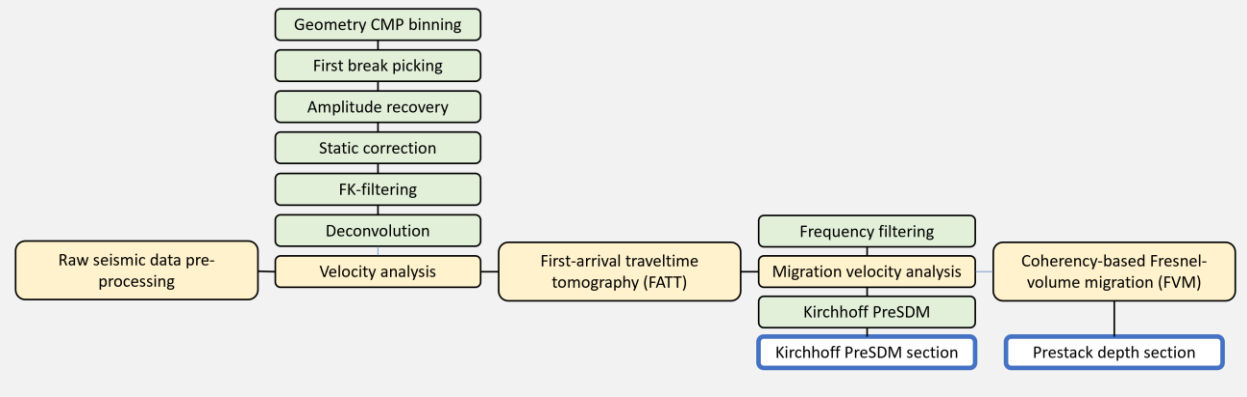


Figure 2: Summary of the depth imaging workflow.

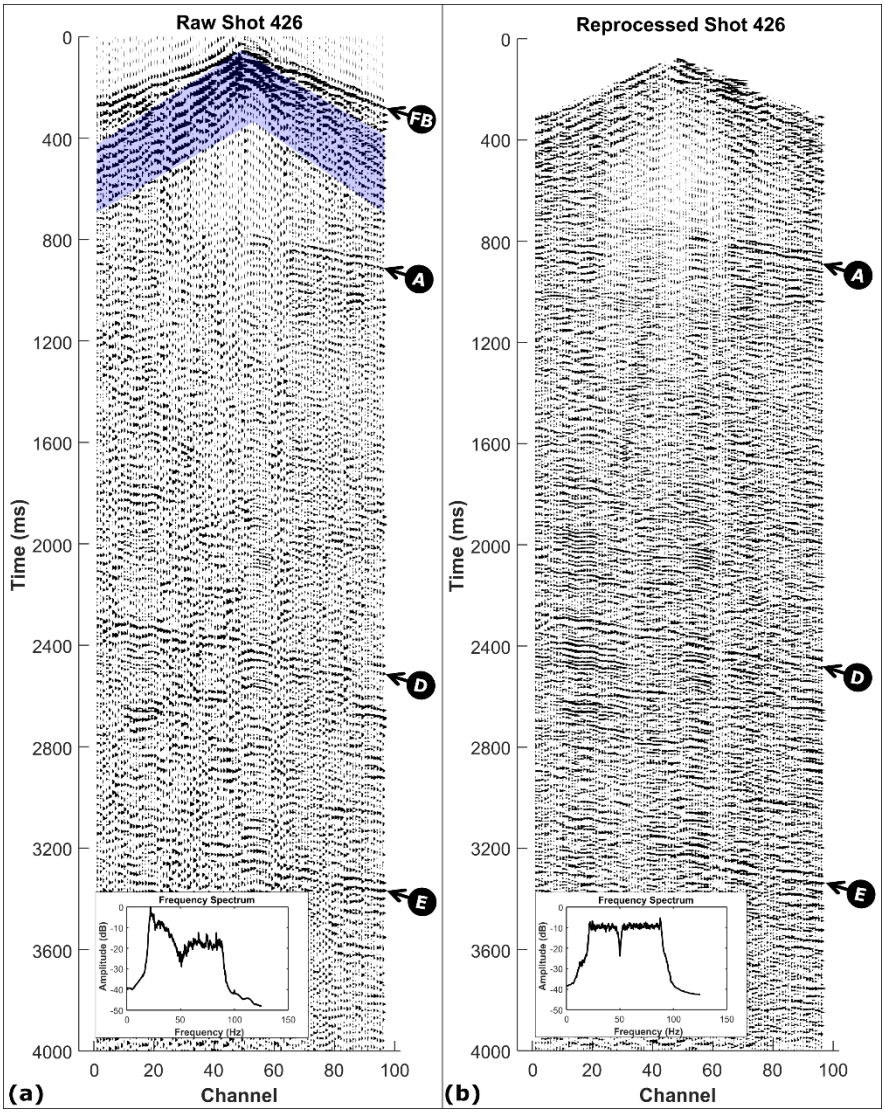
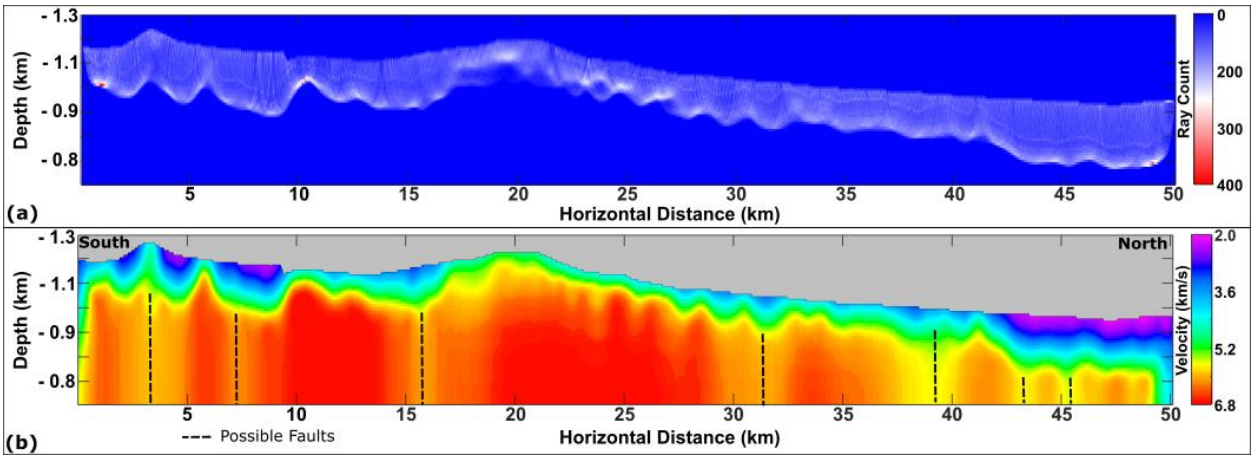


Figure 3: Raw (a) vs reprocessed (b) sample shot gathers of the seismic legacy profile, with the raw data shot gather showing clear first breaks (FB). The reprocessed shot gather shows continuous and preserved reflection contacts: Rashoop Granophyre-Upper Zone ferrogabbros (A), Transvaal Supergroup-Rustenburg Layered Suit norites (D), and a Diabase sill (E), as well as attenuated surface waves, shaded blue on the raw shot gather.



2451

2452 **Figure 4:** Refraction ray path (a) and velocity model (b) of the profile.

2453

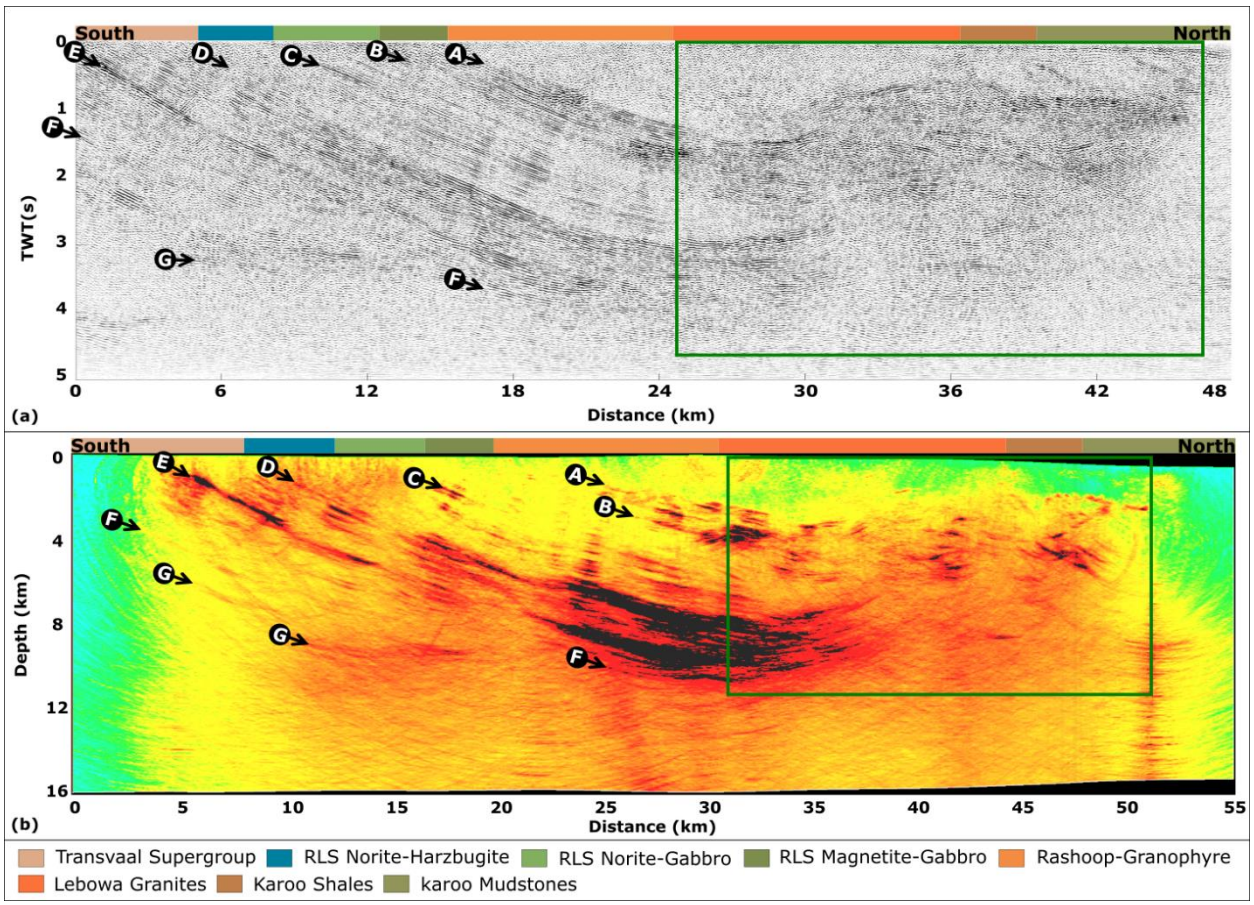


Figure 5: Comparison of the post-stack time migrated section (a) (Odgers *et al.* 1993) and reprocessed CM depth section (b). The region of notable improvement in the data are outlined by rectangles (see figure 7 for closeup). The main lithological contacts: Rashoop Granophyre-RLS ferrogabbros (A), RLS ferrogabbros-RLS gabbros (B), RLS gabbros-RLS norites (C), Transvaal Supergroup-RLS norites (D), a Diabase sill (E), base of Timeball Hill Formation (F), base of Chuniespoort group (G) as well as the geological outcrop along the profile are shown.

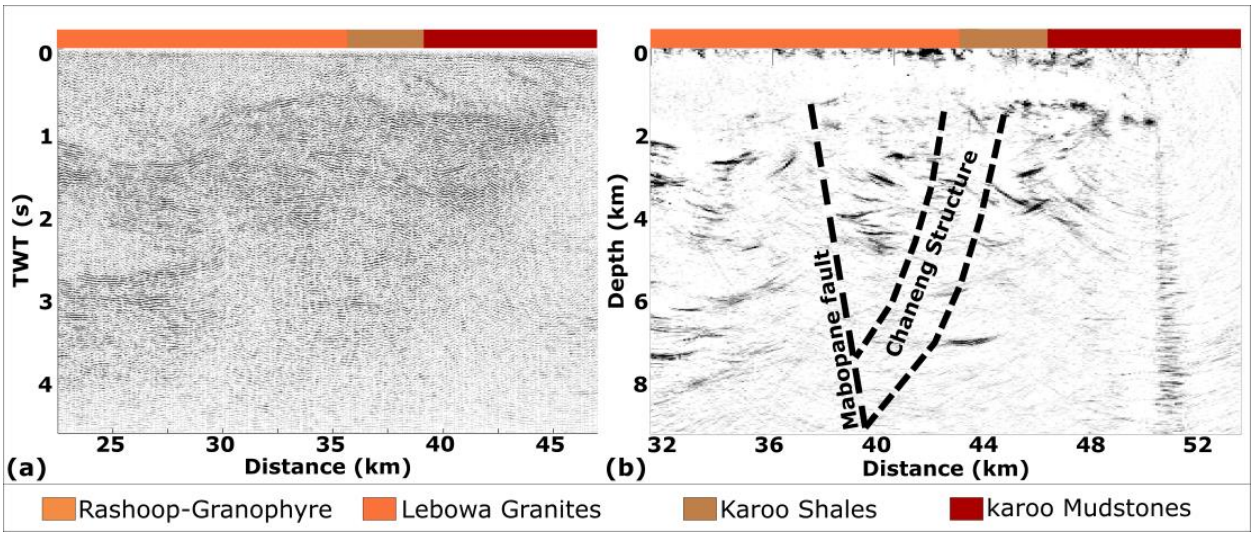


Figure 6: Zoomed region of the legacy stack (a) and reprocessed stack (b) as indicated by green triangles in figure 5.

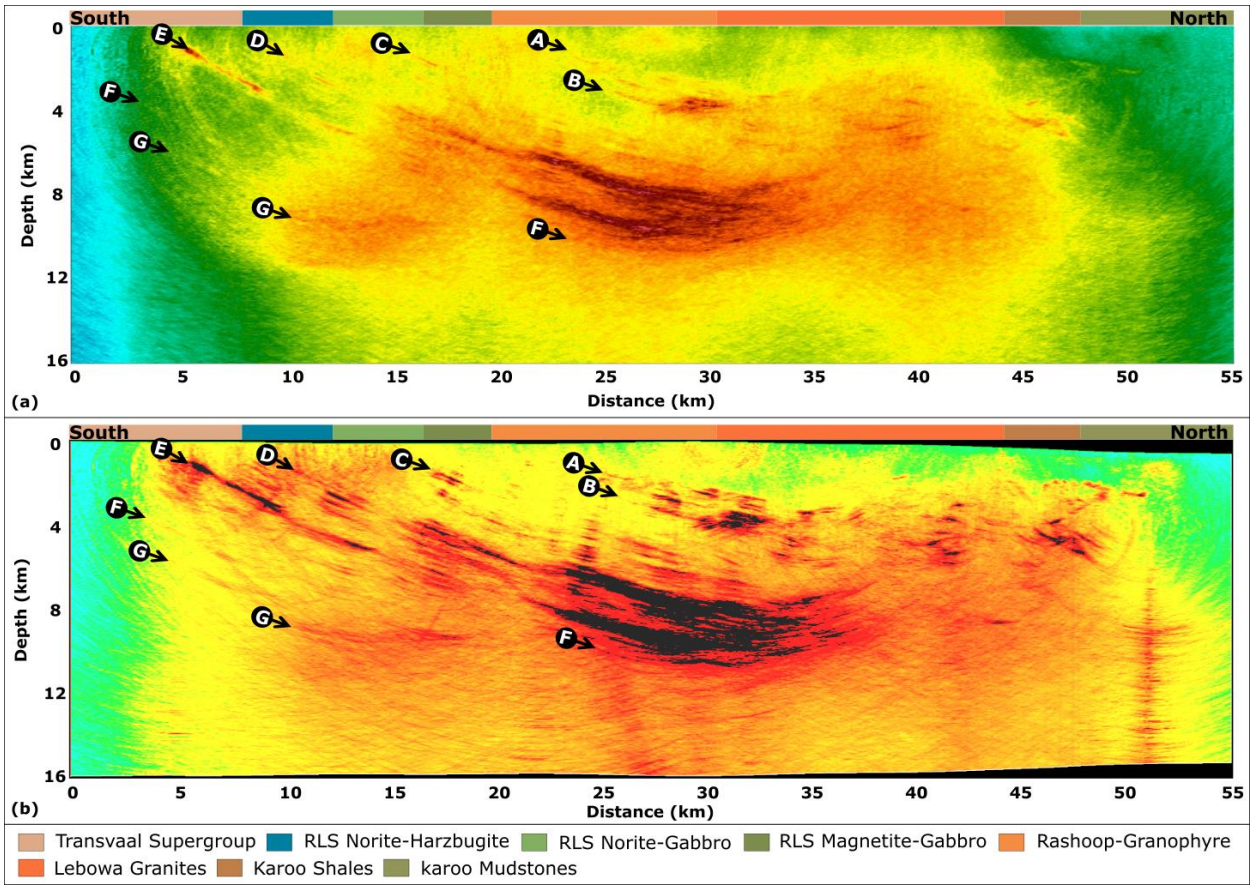
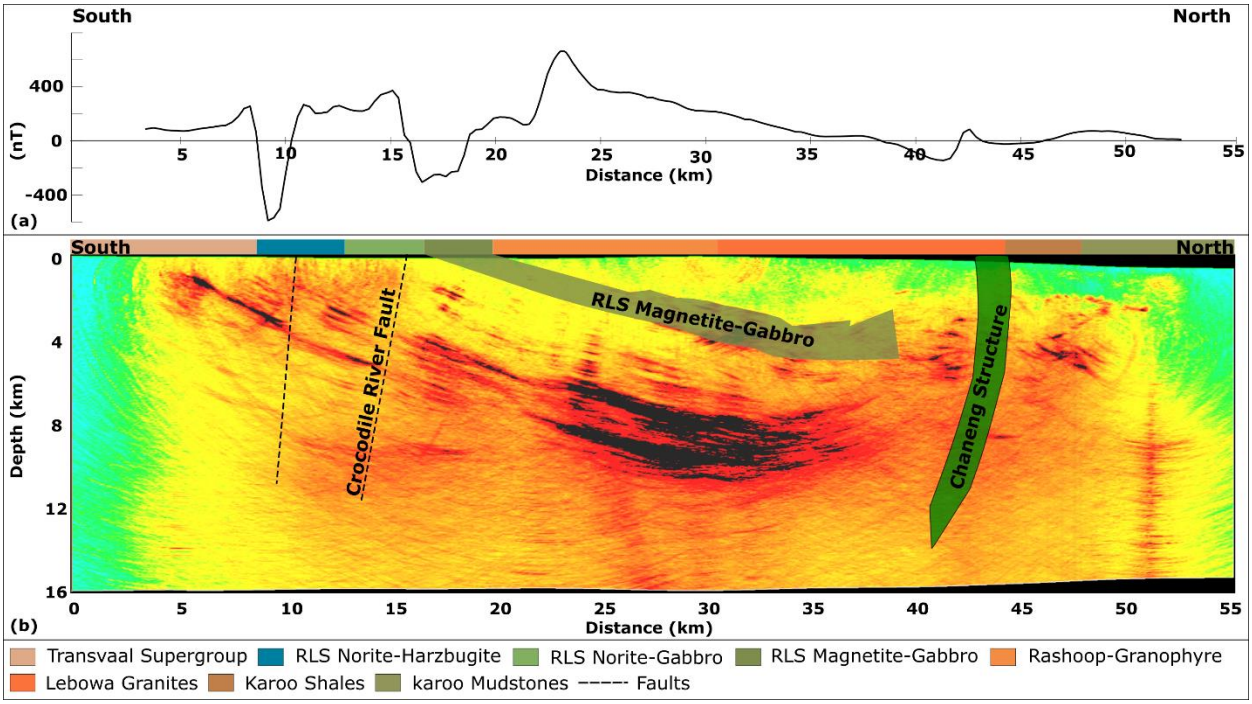


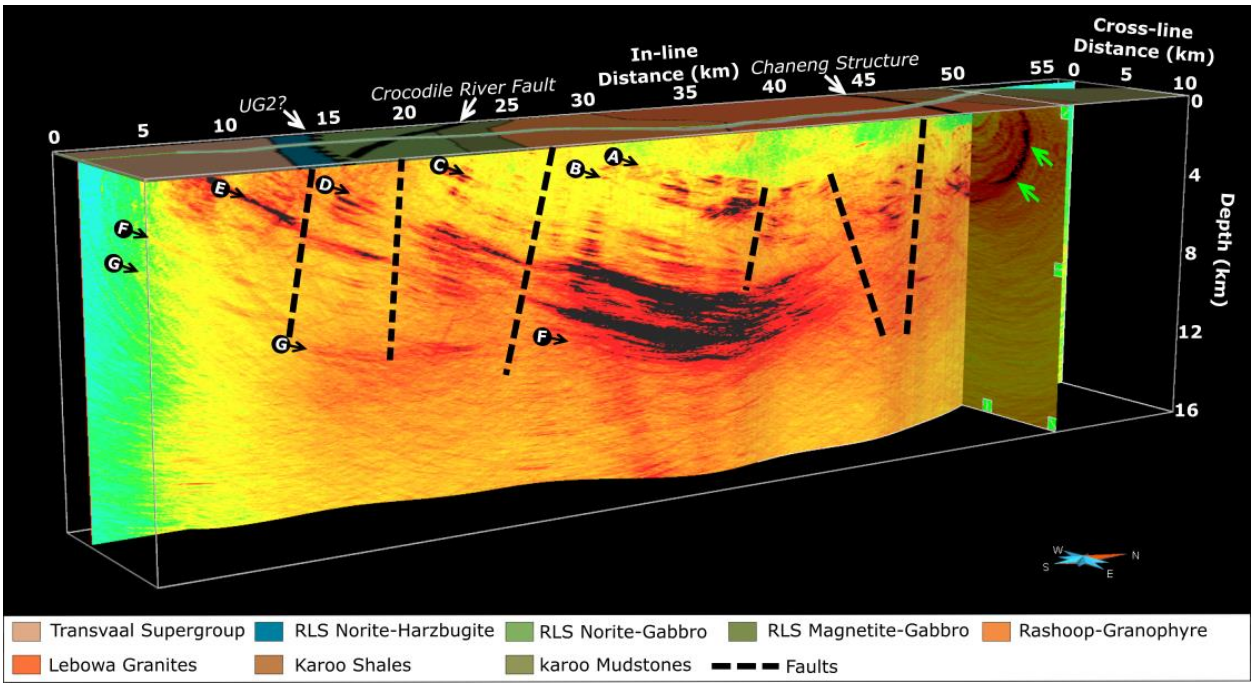
Figure 7: (a) KPreSDM section and (b) CM section, with the main lithological contacts: Rashoop Granophyre-RLS ferrogabbros (A), RLS ferrogabbros-RLS gabbros (B), RLS gabbros-RLS norites (C), Transvaal Supergroup-RLS norites (D), a Diabase sill (E), base of Timeball Hill Formation (F), base of Chuniespoort group (G) as well as the geological outcrop along the profile.



2472

2473 **Figure 8:** (a) Aeromagnetic profile along the (b) CM section, with the geological features mapped
2474 by magnetic data overlain.

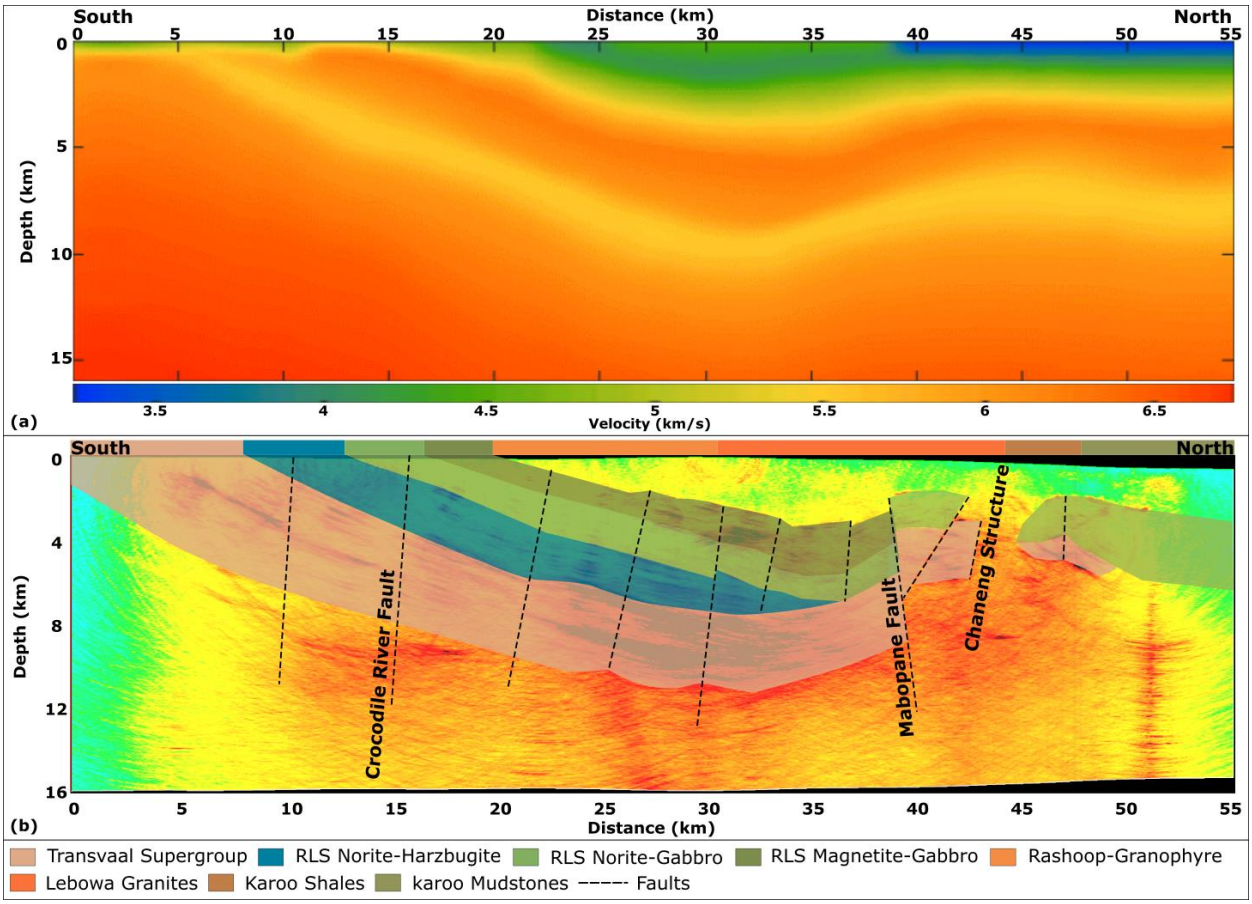
2475



2476

2477 **Figure 9:** 3D view of the CM section with the overlying surface geology showing the regional
2478 structures (Chaneng Structure and Crocodile River Fault), and the Merensky reef (MR) and UG2
2479 possible outcrop. The main lithological contacts: Rashoop Granophyre-RLS ferrogabbros (A),
2480 RLS ferrogabbros-RLS gabbros (B), RLS gabbros-RLS norites (C), Transvaal Supergroup-RLS
2481 norites (D), a Diabase sill (E), base of Timeball Hill Formation (F), base of Chuniespoort group
2482 (G) as well as the geological outcrop along the profile are shown. The green arrows show
2483 constructive interference out-of-plain.

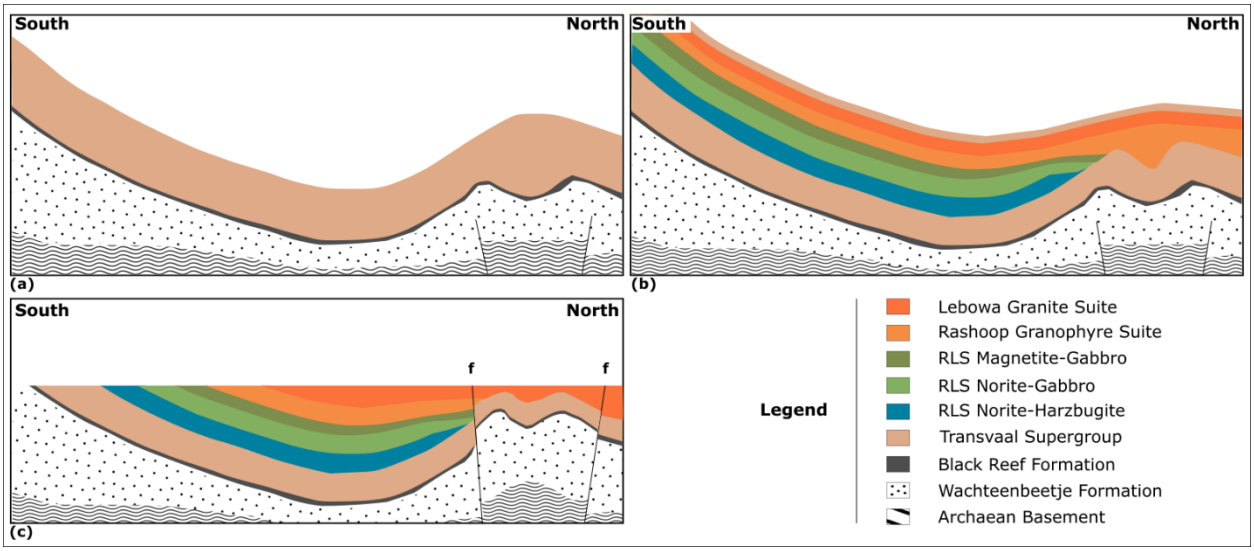
2484



2485

2486 **Figure 10:** The migration velocity model (a) and the final interpreted section (b).

2487



2488

2489 **Figure 11:** Schematic proposed tectonic model along the 2D legacy reflection seismic profile.

2490

Table 1: Legacy profile acquisition parameters.

Survey Parameters	
Survey type	2D crooked line
Year	1986
Length	50 km
Direction	S-N
Spread	1200-112.5-X-112.5-1200
Nominal Fold	24
Recording System	
Recording Device	MDS-10, 96 channel
Sample Rate	2 ms
Recording Length	21 s
Sweep Length	16 s
Sweep Frequency range	20 – 90 Hz
Source Information	
Source Device	3 Vibroseis
Vibrator Controller	P II
Source Spacing	50 m
Receiver Information	
Receiver Spacing	25 m
Geophone Type	10 Hz (SM4U)

7 **Paper III:** Legacy seismic data processing for mineral and coal exploration in the Evander Basin

7.1 Paper Summary

To image the subsurface geology and the complex geological structures of the Evander Basin in South Africa, we processed six legacy reflection seismic profiles acquired in the Evander Basin in 1986. The data were received as raw shot gathers with paper documentations. To the authors' knowledge, these profiles have not been published and there is no record in any documents as to whether they were initially processed or not. Therefore, the purpose of this study is to recover and process the data to image and delineate structures that host gold- and coal-bearing rocks in the Evander Basin. The secondary aim of processing the data is to image and define the Southern Limb strata of the Bushveld Complex in the region, which is critical for future mineral exploration in the region.

This manuscript presents the work in progress, which will further be improved through advanced analysis of the data including pre- and post-stack processing, numerical simulations, seismic interpretation and structural modelling. As it stands, the work demonstrates the effectiveness of the Kirchhoff-based pre-stack depth migration techniques in hardrock environment for mineral and coal exploration. We applied minimal processing such as FK and bandpass frequency filtering on the shot gathers before migration. We then compared the results from the conventional Kirchhoff pre-stack depth migration, Fresnel-volume migration and coherency migration. The comparison was done only on two profiles out of the six, with profile 1 results comparing the Kirchhoff pre-stack depth migration and the coherency migration. Profile 2 results show a comparison between Kirchhoff pre-stack depth migration, Fresnel-volume migration and coherency migration. Fresnel-volume and coherency migration approaches demonstrate superior performance over the conventional Kirchhoff pre-stack depth migration. For example, these algorithms show a degree of horizon continuity and faulting that is not seen in the Kirchhoff pre-stack depth migrated section.

In general, the final seismic sections exhibit strong reflections from the main lithological contacts across the study area. The reflections are from the contacts between the Transvaal Supergroup and the underlying Ventersdorp lavas, the Ventersdorp lavas and the underlying Witwatersrand

Supergroup, and the Witwatersrand Supergroup and the underlying Archaean Basement rocks. Possible faulting and folding of the strata are also observed in the data and are interpreted to be related to the Platberg extension and Ventersdorp volcanics.

7.2 Manuscript

Legacy seismic data processing for mineral and coal exploration in the Evander Basin

ABSTRACT

The Evander Basin stratigraphy has been a target for deep (> 500 m depth) mineral and shallow (< 500 m depth) coal exploration for decades through exploration drilling. In this study, to delineate the subsurface geology and geological structures in the Evander Basin, we have recovered and processed six legacy 2D reflection seismic profiles acquired in 1986 for mineral and coal exploration. We propose contemporary reflection seismic processing workflows that employ new algorithms to provide an improved subsurface image of the structurally complex goldfield. We tested the Kirchhoff pre-stack depth migration algorithm and newly developed Kirchhoff-based depth migration techniques called Fresnel volume migration (FVM) and coherency migration (CM). The preliminary results from the pre-stack processing of the shot gathers show successful attenuation of noise through f-k and bandpass frequency filtering. The processed shot gathers show improved and restored reflections on the data. The legacy seismic lines were collected perpendicular to each other, allowing for pseudo-3D imaging. Further processing improvements on the legacy seismic profile include accurate imaging of the seismic reflective interfaces that can be used as proxies to delineate the mineral and coal deposits and constrain the geometry of the geological structures in the study area.

INTRODUCTION

The Evander Basin (Figure 1) is a subsidiary basin located ~ 120 km east-south-east of Johannesburg, South Africa which hosts the target Evander goldfield rocks of the Mesoarchean Witwatersrand Basin and the Southern Limb rocks of the Paleoproterozoic age Bushveld Complex for mineral exploration, as well as the Highveld and Witbank coalfields (Witthuser et al., 2015; Pretorius et al., 2003; Buchanan, 1975). The Evander goldfield mining operations started in the 1950s exploiting the gold-bearing Central Rand Group of the Witwatersrand Supergroup at depths ranges of 0.4 to 2 km below the surface. The main economic gold-bearing horizon (locally termed

reef) on the Evander goldfield is the Kimberley Reef, which was emplaced during the early deposition stages of the Turffontein subgroup on the upper Central Rand Group. The Winkelhaak, Bracken, Leslie, and Kinross mines were the first gold production mines in the Evander goldfield, and now form part of Evander Gold Holdings with only Kinross shaft 8 still active (Witthuser et al., 2015).

The Southern Lobe of the Bushveld Complex mafic succession is characterized by the Upper Zone which is known not to host the Platinum Group Element (PGE) mineral deposits. The absence of the Main Zone and the mineralized Critical Zone in the Evander Basin is attributed to the possible migration of fractionated magma from the main chamber or the presence of a separate injection centre (Buchanan, 1975). Several mining projects were conducted on the Bushveld Complex rocks in this region for mineral exploration through extensive exploration drilling. Numerous boreholes were drilled to determine the economic value of the Bushveld Complex rocks underneath the Karoo sediments, and these intersected the diorite, gabbro, anorthosite, mineralized mafic pegmatoids, peridotite, diabase and metamorphosed sediments. The mineralized mafic pegmatoids contain traces of copper and nickel in this region (Buchanan, 1975).

The overlying shallow coal mining in the Evander Basin forms part of the Highveld and Witbank coalfields which account for approximately 66% of the remaining coal reserves in South Africa (Bergh, 2011). All South African coalfields form part of the Main Karoo Basin (MKB) and the associated sub-basins, with the Highveld and Witbank coalfields being the most well-documented (Hancox et al., 2014). Witbank coalfield is located in the northern part of the MKB, east of Johannesburg, with a total area greater than 5 680 km^2. The Brugspruit, Steenkoolspruit, Maggies mines and the Douglas Colliery are the first small collieries known for exploiting the Witbank coalfield as early as 1889 (Smith and Whittaker, 1986a, b; Falconer, 1990; Hancox et al., 2014). The coalfield is home to major coal power stations (e.g., Kendal, Duvha, Komati and Arnot power stations) in South Africa and produces about 50% of South Africa's saleable coal. It supplies both the local and international markets with metallurgical and thermal coal (Hancox et al., 2014). The Highveld coalfield is located south of the Witbank coalfield, whilst similar to the Witbank coalfield, they are separated by the Smithfield Ridge and considered separate entities. It covers an area of approximately 7 000 km^2 and holds a sustainable economic value (50 million tonnes a year)

for Sasol's Synthetic Fuels and the Sasol Chemical Industries. It hosts numerous Eskom power stations called Kriel, Matla, and Tutuka power stations (Hancox et al., 2014).

The Evander Basin is completely covered by the younger Karoo sediments, with the outcrops limited to the Karoo dolerite intrusions. The covered Bushveld, Transvaal, Ventersdorp, Witwatersrand, and Archaean basement stratigraphic units were uncovered by several exploration boreholes that were drilled in the 1900s (Jansen et al., 1972; Witthuser et al., 2015). Exploration drilling as well as underground geological mapping played a major role in the study of the Evander Basin stratigraphy. However, in this study, we use the reflection seismic method to better image the subsurface geology and complex geological structures of the Evander Basin. Processing of six perpendicular legacy seismic profiles acquired in the Evander Basin in 1986 is carried out using novel reflection seismic processing workflows.

GEOLOGICAL BACKGROUND

The Evander Basin hosts some of the most famous rocks in South Africa, with the Witwatersrand Supergroup known for gold-bearing quartz pebble conglomerates, the Bushveld Complex known for PGE-bearing horizons, and the Karoo Supergroup famous for the coalfields. As a result, it has been subject to numerous diverse studies (e.g., Buchanan, 1975; Tweedy, 1986; Pinetown et al., 2007; Bergh et al., 2011; Hancox et al., 2014, Witthuser et al., 2015) providing a detailed stratigraphy (Table 1). In summary, the Witwatersrand Basin was deposited on the central Kaapvaal Craton (ca. 3.6 – 3.2 Ga, Manzi et al., 2013) between ca. 2.985 and 2.849 Ga (Kositcin and Krapez, 2004). The supergroup overlies the coarse clastic and bimodal volcanic rocks of the Dominion Group (ca. 3.074 ± 6 Ga, Myers et al., 1989). The Witwatersrand Supergroup comprises the lower West Rand Group and the Upper Central Rand Group (Manzi et al., 2013).

The Dominion Group is unconformably overlain by the clastic and largely marine sedimentary rocks of the West Rand Group (ca. 2.985 – 2.902 Ga, Kositcin and Krapez, 2004). The volcano-sedimentary units of the Dominion Group were tectonically stable during the deposition of The West Rand Group (Frimmel and Minter, 2002; Beach and Smith, 2007; Manzi et al., 2013). The West Rand Group is subdivided into three subgroups, from bottom to top namely, Hospital Hill, Government and Jeppestown Subgroup (Dankert and Hein, 2010). The West Rand Group is unconformably overlain by the sandstone, conglomerate, and shale units of the Central Rand Group (ca. 2.902 – 2.849 Ga, Kositcin and Krapez, 2004) deposited in a shallow marine delta by

a braided system of rivers. The group hosts 93% of the gold deposits currently being mined in the basin, including the Bird, Carbon Leader, North Leader, and Middelvlei reefs hosted by the basal Johannesburg Subgroup. The upper Turffontein Subgroup hosts the Elsberg, Kloof, Libanon, and Kimberley reefs (De Kock, 1964). The Kimberley reef is the only economically viable gold-bearing conglomerate band in the Evander Basin and is hosted within the quartzites and conglomerates (Tucker et al., 2016). It is considered a composite reef and it is part of a group of multi-conglomerate bands that were previously regarded as secondary reefs due to their low grade (Tucker et al., 2016; Frimmel and Nwaila, 2020).

The Central Rand Group is unconformably overlain by the Ventersdorp Contact Reef (VCR) of the Venterspost Formation with a maximum age of ca. 2.729 Ga (Kositcin and Krapez, 2004). The gold-bearing conglomerates of the VCR are in turn unconformably overlain by the Ventersdorp Supergroup (ca. 2.72 – 2.63 Ga), which comprises the ultramafic and mafic metavolcanic rocks of the Klipriviersberg Group, and metasedimentary and bimodal metavolcanic rocks of Platberg Group (Crow and Condie, 1988; Van der Westhuizen et al., 1991). The Klipriviersberg Group comprises 5 formations, i.e., the Westonaria, Alberton, Orkney, Jeannette, and Edenville Formations. The Ventersdorp Supergroup is unconformably overlain by the Transvaal Supergroup (ca. 2.588 Ga, Jolley et al., 2004; Krapez, 1985; Vos, 1975; Manzi et al., 2013), which comprises the Black Reef Formation (BLF), Chuniespoort Group and Pretoria Group. The BLF consists of quartzites with poorly developed basal conglomerates. The Chuniespoort Group consists of carbonate (dolomite), banded iron formation and lacustrine deposits (Eriksson et al., 1995; Frimmel, 2005). The intercalated mudstone - sandstone, andesite, and subordinate conglomerates of the Pretoria Group non-conformably overlie the Chuniespoort Group (Eriksson et al., 2007; Manzi et al., 2013).

The Bushveld Complex mafic cumulate rocks called the Rustenburg Layered Suite (RLS) overlay the Transvaal Supergroup and are in turn overlain by the felsic cumulate rocks called the Rashoop Granophyre Suite (RGS) and Lebowa Granite Suite (LGS) (Eales and Cawthorn, 1996). The RLS is divided into five zones, namely from bottom to top, Marginal, Lower, mineralized Critical, Main and Upper Zones (Cawthorn and Webb, 2001). The Evander Basin comprises only the Upper Zone rocks, which consist of ferrogabbros (Buchanan, 1975). The youngest rocks on the Evander Basin are the Karoo sediments covering the pre-Karoo strata, which comprises the Dwyka, Ecca,

Beaufort and Drakensberg Groups, as well as the Molteno and Elliot Formations (Pinetown et al., 2007). The Witbank and Highveld coalfields comprise several post-Karoo age dolerite sills and dykes, as well as the Ecca Group and Vryheid Formation rocks. The coalfields are characterized by five bituminous coal seams interbedded within the sandstones, carbonaceous shales, siltstones and minor conglomerates of the Vryheid and Dwyka Group stratigraphy (Cairncross, 2001; Pinetown et al., 2007). The coal-bearing sediments were deposited on an undulating floor which impacted the sedimentary succession distribution and quality of the coal seams (Smith and Whittaker, 1986b; Pinetown et al., 2007).

Tweedie (1986) noted three different ages of intrusion in the Evander Bain, namely:

- The Karoo-age intrusives characterized by two phases of Karoo dolerites, the older and younger generation as described by Witthuser (2015). These intrusives are responsible for the devolatilization and rendering the coal seams inapt in this region (Smith and Whittaker, 1986b; Pinetown et al., 2007).
- Ventersdorp-age intrusives characterized by near-vertical and north-south striking dykes, which dominate the Evander goldfield (Witthuser et al., 2015).
- Bushveld-age intrusives characterized by the highly altered medium- to fine -grained ophitic diabase dykes and sills (Witthuser et al., 2015).

Figure 2 shows boreholes drilled near the profile in the survey area (Figure 1b shows locations), with Figure 2a showing the (W - E) cross-section A-to-B along boreholes EVGP 4, EVGP 3, EVGP 2, and 1785. Figure 2b shows the (N - S) cross-section C-to-D along boreholes EVGP 3, EVGP 1, 2188, and 2068.

LEGACY 2D SEISMIC DATA

Seismic data acquisition

The acquisition parameters of the seismic profiles are summarized in Table 2. All the seismic data were collected in 1993 using four vibroseis trucks at 50 m source and receiver spacing following a crooked line geometry due to uneven surface conditions and terrain as shown in Figure 1b. Profiles 2 to 6 surveys were acquired with a sweep length of 18 s and a recording length of 24 s sampled at 4 ms over a sweep frequency of 10 – 68 Hz. Profile 1 survey was slightly different with 16 s recording length and 10 s sweep length of the same sweep frequency. The data were recovered

as correlated shot gathers with the acquisition stored on handwritten observer's logs. The seismic profiles had 96 channels per shot set up as 4 strings of 6 geophones in a linear array. The receivers had a natural frequency of 10 Hz (vertical single component), and the data were recorded with a low-cut filter of 8 Hz.

Seismic data processing

The profiles were acquired with the same acquisition parameters; therefore, a standard processing workflow was applied to all the profiles. Several pre-processing steps were applied to the data as it was stored in an outdated format not compatible with modern processing software. Firstly, we corrected the byte location of the header names that were stored in the wrong byte numbers. Secondly, we interpolated the receiver elevation from the shot elevation, as they were offset in the header information. To finalise the geometry, we sorted the traces in common midpoint (CMP) bins with a spacing of 25 m using a spline curve fitting following a wiggly line geometry. A 50 Hz notch filter was applied to the data during acquisition to attenuate the spiking noise from the AC power lines in the study area. A summary of the processing workflow is shown in Figure 3.

Figure 4 shows an example of the raw and processed shot gathers from legacy profiles 1 and 2. The other profiles are not shown as they were processed using the same parameters and show similar improvements. We recovered the attenuated amplitudes using an automatic gain control (AGC) window of 1000 ms. We applied an f-k filter to mute the surface waves (purple arrows in Figures 4a and c) with an S-wave velocity of less than 3 200 m/s, and also applied a bandpass filter of [0-10 70-80] Hz. We also broadened the spectrum using predictive deconvolution with a 16 ms gap length and 180 ms filter length to simulate spiking deconvolution. We also applied top mute to remove the first breaks (green arrows in Figures 4a and c).

Depth imaging

Due to complex geology, disrupted reflectors, and scattered seismic energy the process of seismic imaging in hardrock environments is much more difficult in comparison to softrock settings. During at least the last two decades pre-stack depth migration, especially in a Kirchhoff-type implementation, has proven its superiority in such complex crystalline hardrock environments (Buske, 1999). Advanced pre-stack depth migration techniques, e.g., Fresnel volume migration (Lüth et al., 2005; Buske et al., 2009), coherency migration and coherency-based Fresnel volume

migration (Hloušek et al., 2015a) are new successful developments of focused volume migration methods. Successful applications of these focusing pr-stack depth migration methods range from imaging crustal fault systems (Hloušek and Buske, 2016) to the high-resolution imaging of mineral deposits (Heinonen et al., 2019; Singh et al., 2019; Bräunig et al., 2019; Hloušek et al., 2022; Cheraghi et al., 2022). and the characterization of geothermal reservoirs (Hloušek et al., 2015b; Schreiter et al., 2015; Riedel et al., 2015; Jusri et al., 2018).

It is, therefore, worthwhile to apply these newly developed seismic imaging tools in hardrock environments. In this study, we demonstrate the effectiveness of these methods by applying the Fresnel volume migration and coherency migration (CM) technique to six 2D legacy seismic profiles from the Evander Basin.

CM is one of the potential implementations of focusing pre-stack depth migration methods. It is based on Kirchhoff pre-stack depth migration (KPreSDM), a diffraction integral solution to the wave equation (Schneider, 1978). Therefore, the resultant image value for a random point in the subsurface is described by the weighted summation over the corresponding diffraction surface for the given point. The directivity-based energy losses and spherical divergence are accounted for by the weighting function along the diffraction curve. The image for a single surface shot wavefield which is scattered by a single diffraction point in a homogeneous medium and recorded by a single receiver on the surface is constructed by smearing the amplitudes along their corresponding two-way-traveltime (TWT) isochrones. This concept can be extended for multiple shots and receivers on the surface by treating every single point along the reflector as a point diffractor and a migrated image of the reflector can be constructed by constructive interference of all TWT isochrones along the reflector.

Focused migration strategies confine the migration operator to the TWT isochrone's physically relevant region. This is accomplished by adding weighting factor to the Kirchhoff integral solution based on the image point, which ensures that the amplitudes are smeared in the physically pertinent region along the traveltime isochrone (the Fresnel zone).

CM employs a weighting factor derived from the input data (Hloušek et al., 2015b). This weighting factor is calculated by evaluating the semblance coefficients of the recorded wavefield along the theoretical diffraction curves, which are specified by the individual two-way traveltime for the same image point at different surrounding receivers (Neidell and Taner, 1971). When the image

point is equal to the actual diffraction point, the semblance coefficient is one; otherwise, it is zero. The calculated value can be utilized directly to weight the amplitudes during migration (Hloušek et al., 2015b).

PRELIMINARY RESULTS AND DISCUSSION

The profiles were acquired over Karoo Supergroup rocks, with the covered pre-Karoo strata dipping to the north. Figure 4 shows the comparison between the raw and processed shot gathers, an example from profiles 1 and 2. The quality of the data is good as demonstrated by the shot gathers with clear first breaks (green arrows in Figure 4a and c). Figures 4b and d show the processed shot gathers with the preserved and enhanced reflections shown (red arrows on Figures 4b and d). The main lithological contacts mapped as clear reflections due to a significant impedance contrast between underlying and overlying strata (Figures 5 - 7) are Transvaal Supergroup – Ventersdorp lavas (A), Ventersdorp lavas – Witwatersrand Supergroup (B), and the base of the Witwatersrand Supergroup (C).

Figure 5 shows the comparison between the Kirchhoff pre-stack depth migrated section (Figure 5a) and the coherency migrated section (Figure 5b) from legacy profile 1. The coherency migrated section has a higher signal-to-noise ratio compared to the Kirchhoff pre-stack depth migrated section. Figure 6 shows the comparison between the Kirchhoff pre-stack depth migrated section (Figure 6a), the Fresnel volume migrated section (Figure 6b) and the coherency migrated section (Figure 6b), an example from legacy profile 2. The Fresnel volume migrated and coherency migrated sections have a higher signal-to-noise ratio compared to the Kirchhoff pre-stack depth migrated section and possible faults are outlined by the dotted lines. Figure 7 shows the Kirchhoff pre-stack depth migrated sections (a - d) from profiles 3 – 6, respectively. Figure 8 shows a 3D perspective view of the data outlining the correlation and continuity of reflections among the profiles.

Imaging of the Ventersdorp lavas-Witwatersrand Supergroup contact by seismics is particularly important because this horizon unconformably overlies the gold-bearing Central Rand Group conglomerates, and thus can be used as a proxy to derive the gold orebody model for future exploration. Furthermore, the interface is dissected by faults (e.g., Figures 6 and 7) that could have a major impact on mine planning and development. The stratigraphy above and below the B interface is also affected by a syncline-like structure, implying that the gold deposits are deeper at

the apex of the syncline and shallowest at the edges of the syncline (see Figure 7). This implies that the lower portion of the syncline might have preserved the deposits from erosion and the upper portion could have brought the deposits closer to the surface for easy access for exploration and mine development. It is worth noting that the base of the Karoo Supergroup and the overlying strata hosting the coal seams are not imaged by seismics. This is surprising as the base of the Karoo is expected to produce a strong seismic reflection due to a significant acoustic impedance contrast between the overlying sandstones and shales and underlying dolomitic rocks of the Transvaal Supergroup (Manzi et al., 2013). However, the imaging of these units could be improved by further processing of the data, particularly focusing on statics corrections. Although the Karoo sediments are not visible in the migrated sections, it is safe to assume that the faults that crosscut the Ventersdorp and Transvaal supergroups also affect the coal seams within the Karoo Supergroup. Alternatively, the base of the Transvaal Supergroup (A) could be used as a proxy to constrain the geometry of the coal seams located 500 m above this interface. This has implications for future coal exploration in the region, implying that the structures that crosscut A will need to be incorporated in the coal mine planning for coal resource evaluation (see Figures 5-7).

CONCLUSION

Even though minimal preprocessing was applied to the data before migration using a constant velocity model, the results successfully imaged the main lithological contacts in the Evander Basin. The reflections from the gold-bearing Witwatersrand Supergroup are clearly mapped and the possible crosscutting geological structures are delineated. An improved migration velocity model will play a major role in improving the imaging of the reflections. Furthermore, iterative static corrections will improve the continuity of the reflections. To better image the near surface reflections associated with the coal seams, the first break mute on the processing workflow will need to be removed, since near surface reflections are very close to the first breaks. Unfortunately, we do not have access to the legacy stacked and migrated sections from the initial processing applied to the data (if any processing was conducted). This would afford us an opportunity to compare both results to better judge the effectiveness of our novel processing workflows.

ACKNOWLEDGEMENTS

We are grateful for the financial support from DST-NRF CIMERA and Wits Seismic Research Centre. The coordinates were sorted on MATLAB and pre-stack time domain seismic data

reprocessing was done on Globe Claritas; we appreciate the sponsorship of the software licences by Globe Claritas to the University of the Witwatersrand, Johannesburg.

DATA AVAILABILITY STATEMENT

The data are available on request from the corresponding author.

CONFLICT OF INTEREST

The authors declare no conflict of interest.

REFERENCES

Beach, A. and Smith, R., (2007) Structural geometry and development of the Witwatersrand Basin, South Africa. In: Ries, A. C., Butler, R. W. H., Graham, R. H. (Eds.), Deformation of the Continental Crust: The Legacy of Mike Coward: Geological Society, London, Special Publications, 272, pp. 533–542.

Bergh, J. P., Falcon, R. M. S. and Falcon, L. M., (2011) Trace element concentration reduction by beneficiation of Witbank Coalfield no. 4 Seam. *Fuel Processing Technology*, 92(4), pp.812-816. https://doi.org/10.1016/j.fuproc.2010.09.035

Buchanan, D. L., (1975) The petrography of the Bushveld Complex intersected by boreholes in the Bethal area. *South African Journal of Geology*, 78(3), pp.335-348. https://hdl.handle.net/10520/EJC-1ac8c348be

Buske, S., (1999) Three-dimensional pre-stack Kirchhoff migration of deep seismic reflection data. *Geophysics Journal International* 137, 243-260. https://doi.org/10.1046/j.1365-246x.1999.00789.x

Buske, S., Gutjahr, S. and Sick, C., (2009) Fresnel volume migration of single-component seismic data. *Geophysics* 74(6), WCA47-WCA55. https://doi.org/10.1190/1.3223187

Bräunig, L., Buske, S., Malehmir, A., Bäckström, E., Schön, M. and Marsden, P., (2019) Seismic depth imaging of iron-oxide deposits and their host rocks in the Ludvika mining area of central Sweden. *Geophysical Prospecting* 68(1), 24-43. https://doi.org/10.1111/1365-2478.12836

Cairncross, B., (2001) An overview of the Permian (Karoo) coal deposits of southern Africa. *Journal of African Earth Sciences* 33, 529–562.

Cawthorn, R. G. and Webb, S. J., (2001) Connectivity between the western and eastern limbs of the Bushveld Complex. *Tectonophysics* 330(3-4), 195-209. https://doi.org/10.1016/S0040-1951(00)00227-4

Cheraghi, S., Hloušek, F., Buske, S., Malehmir, A., Adetunji, A., Haugaard, R., Snyder, D. and Vayavur, R., (2022) Reflection seismic imaging across a greenstone belt, Abitibi (Ontario)-Canada. *Geophysical Prospecting*. https://doi.org/10.1111/1365-2478.13284

Crow, C. and Condie, K. C., (1988) Geochemistry and origin of Late Archaean volcanics from the Ventersdorp Supergroup, South Africa. *Precambrian Research* 42, 19–37

Dankert, B. T. and Hein, K. A. A., (2010) Evaluating the structural character and tectonic history of the Witwatersrand Basin. *Precambrian Research* 177, (1-2), 1–22. https://doi.org/10.1016/j.precamres.2009.10.007

De Kock, W. P., (1964) The geology and economic significance of the West Wits Line. In: Haughton, S.H. (Ed.), The Geology of Some Ore Deposits of Southern Africa, 1. Geological Society of South Africa, Johannesburg, pp. 323

Cawthorn, R. G. and Webb, S. J., (2001) Connectivity between the western and eastern limbs of the Bushveld Complex. *Tectonophysics* 330(3-4), 195-209. https://doi.org/10.1016/S0040-1951(00)00227-4

Eales, H. V. and Cawthorn, R. G., (1996) The Bushveld Complex. In: Cawthorn, R. G. (Ed.), Layered Intrusions. Elsevier, Amsterdam, pp. 181–230.

Eriksson, P. G., Hattingh, P. J. and Altermann, W., (1995) An overview of the geology of the Transvaal Sequence and Bushveld Complex, South Africa. *Mineralium Deposita* 30, 98–111.

Eriksson, P. G., Altermann, W. and Hartzer, F. J., (2007) The Transvaal Supergroup and its precursors. In: Johnson, M. R., Anhaeusser, C. R., Thomas, R. J. (Eds.), The Geology of South Africa. Geological Society of South Africa, Johannesburg/Council for Geoscience, Pretoria, pp. 237–260.

Falconer, K. W., (1990) Spotlight on 100 years of coal mining in Witbank. *Journal of the South African Institute of mining and Metallurgy* 90(4), pp. 78.

Frimmel, H. E. and Minter, W. E. L., (2002) Recent developments concerning the geological history of the Witwatersrand gold deposits, South Africa. In: Goldfarb, R., Nielsen, R. L. (Eds.), Global Exploration 2002 — Integrated Methods for Discovery: Special Publication, 9. Society of Economic Geologists, Littleton, pp. 17–45.

Frimmel, H. E. and Nwaila, G. T., (2020) Chapter 31 Geologic Evidence of Syngenetic Gold

in the Witwatersrand Goldfields, South Africa. In: Sillitoe, R. H., R. J. Goldfarb, F. Robert, and S. F. Simmons, (eds.). Geology of the World's Major Gold Deposits and Provinces, *vol 23, Society of Economic Geologist.* https://doi.org/10.5382/SP.23.31

Frimmel, H. E., (2005) Archaean atmospheric evolution evidence from the Witwatersrand gold fields, South Africa. *Earth-Science Reviews* 70, 1–46.

Hancox, P. J. and Götz, A. E., (2014) South Africa's coalfields—A 2014 perspective. *International Journal of Coal Geology* 132, pp.170-254. https://doi.org/10.1016/j.coal.2014.06.019

Heinonen, S., Malinowski, M., Hloušek, F., Gislason, G., Buske, S., Koivisto, E. and Wojdyla, M., (2019) Cost-effective seismic exploration: 2D reflection imaging at the Kylylahti massive sulfide deposit, Finland. *Minerals* 9(5), 263. https://doi.org/10.3390/min9050263

Hloušek, F., Malinowski, M., Bräunig, L., Buske, S., Malehmir, A., Markovic, M., Sito L., Marsden, P. and Bäckström, E., (2022) Three-dimensional reflection seismic imaging of the iron oxide deposits in the Ludvika mining area, Sweden, using Fresnel volume migration. *Journal of Geophysical Research: Solid Earth* 13(5), 917-934. https://doi.org/10.5194/se-13-917-2022

Hloušek, F., Hellwig, O. and Buske, S., (2015a) Improved structural characterization of the Earth's crust at the German Continental Deep Drilling Site using advanced seismic imaging techniques. *Journal of Geophysical Research: Solid Earth* 120(10), 6943-6959. https://doi.org/10.1002/2015JB012330

Hloušek, F., Hellwig, O. and Buske, S., (2015b) Three-dimensional focused seismic imaging for geothermal exploration in crystalline rock (Schneeberg, Germany). *Geophysical Prospecting* 63(4), 999-1014. https://doi.org/10.1111/1365-2478.12239

Jansen, H., Schalk, F.S., Leube, A., Snyman, A. A., Steyn, A. P. A., De Jager, F. S. J. and Beer, H. M., (1972) The geology of the country around Standerton, with a contribution on the Evander Goldfield by the Mines Geological Department, Evander (Union Corporation Ltd). Department of Mines, Geological Survey. Government Printer, Pretoria, South Africa, 99p.

Jolley, S. J., Freeman, S. R., Barnicoat, A. C., Phillips, G. M., Knipe, R. J., Pather, A., Fox, N. P.

C., Strydom, D., Birch, M. T. G., Henderson, I. H. C. and Rowland, T. W., (2004) Structural controls on Witwatersrand gold mineralisation. *Journal of Structural Geology* 26, 1026–1086.

Jusri, T., Bertani, R. and Buske, S., (2018) Advanced three-dimensional seismic imaging of deep supercritical geothermal rocks in Southern Tuscany. *Geophysical Prospecting* 67(2), 298-316. https://doi.org/10.1111/1365-2478.12723

Kositcin, N., Krapež, B., (2004) Relationship between detrital zircon age-spectra and the tectonic evolution of the Late Archaean Witwatersrand Basin, South Africa. *Precambrian Research* 129, 141–16

Krapež, B., (1985) The Ventersdorp Contact placer: a gold–pyrite placer of stream and debris-flow origins from the Archaean Witwatersrand Basin of South Africa. *Sedimentology* 32, 2.

Lüth, S., Buske, S., Giese, R. and Goertz, A., (2005) Fresnel volume migration of multicomponent data. *Geophysics* 70(6), S121-S129. https://doi.org/10.1190/1.2127114

Manzi, M. S. D., Hein, K. A. A., King, N. and Durrheim, R. J., (2013) Neoarchaean tectonic history of the Witwatersrand Basin and Ventersdorp Supergroup: New constraints from high-resolution 3D seismic reflection data. *Tectonophysics* 590, 94–105. https://doi.org/10.1016/j.tecto.2013.01.014

Myers, R. E., McCarthy, T. S. and Stanistreet, I.G., (1989) A tectono-sedimentary reconstruction of the development of the Witwatersrand Basin, with particular emphasis on the Central Rand Group. *Economic Geology Research Unit Information Circular* 216, pp. 497–540.

Neidell, N. S. and Taner, M. T., (1971) Semblance and other coherency measured for multichannel data. *Geophysics* 36(3), 482-497. https://doi.org/10.1190/1.1440186

Pinetown, K. L., Ward, C. R. and van der Westhuizen, W. A., (2007) Quantitative evaluation of minerals in coal deposits in the Witbank and Highveld coalfields, and the potential impact on acid mine drainage. *International Journal of Coal Geology* 70, pp. 166 – 183.

Pretorius, C. C., Muller, M. R., Larroque, M. and Wilkins, C., (2003) A review of 16 years of

hardrock seismics on the Kaapvaal Craton, Hardrock Seismic Exploration. In: Developments in Geophysics Series. (ed. Eaton, D., Salisbury, M. and Milkereit, B.) SEG, Houston. 2003, 247–268. https://doi.org/10.1190/1.9781560802396.ch16

Riedel, M., Dutsch, C., Alexandrakis, C., Dini, I., Ciuffi, S. and Buske, S., (2015) Seismic depth imaging of a geothermal system in southern Tuscany. *Geophysical Prospecting* 63(4), 957-974. https://doi.org/10.1111/1365-2478.12254

Schreiter, L., Hlousek, F., Hellwig, O. and Buske, S., (2015) Characterization of seismic reflections from faults in a crystalline environment, Schneeberg, Germany. *Geophysical Prospecting* 63(4), 1015-1032. https://doi.org/10.1111/1365-2478.12255

Schneider, W. A., (1978) Integral formulation for migration in two and three dimensions. *Geophysics* 43, 49-76. https://doi.org/10.1190/1.1440828

Singh, B., Malinowski, M., Hloušek, F., Koivisto, E., Heinonen, S., Hellwig, O., Buske S., Chamarczuk, M. and Juurela, S., (2019) Sparse 3D seismic imaging in the Kylylahti mine area, Eastern Finland: comparison of time versus depth approach. *Minerals* 9(5). https://doi.org/10.3390/min9050305

Smith, D. A. M. and Whittaker, R. R. L. G., (1986a) The coalfields of Southern Africa: and introduction, in: Anhausser, C. R. and Maske, S., (Eds) Mineral Deposits of Southern Africa-Volume II, The Geological Society of South Africa, 1875 – 1878.

Smith, D. A. M. and Whittaker, R. R. L. G., (1986b) The Springs-Witbank coalfields 1969-1994: an introduction, in: Anhausser, C. R. and Maske, S., (Eds) Mineral Deposits of Southern Africa-Volume II, The Geological Society of South Africa, 1875 – 1878.

Tucker, R. F., Viljoen, R. P. and Viljoen, M. J., (2016) A Review of the Witwatersrand Basin - The World's Greatest Goldfield. *Episodes* 39, 104–133. DOI: 10.18814/epiiugs/2016/v39i2/95771

Tweedie, E. B., (1986) The Evander Goldfield. In: Anhaeusser, C. R. and Maske, S., (Eds), Mineral Deposits of Southern Africa Vol. 1. Geological Society of South Africa, Johannesburg, South Africa, 705-730

Van der Westhuizen, W.A., De Bruiyn, H. and Meintjes, P.G., (1991) The Ventersdorp

Supergroup: an overview. *Journal of African Earth Sciences* 13, 83–105

Vos, R. G., (1975) An alluvial plain and lacustrine model for the Precambrian Witwatersrand deposits of South Africa. *Journal of Sedimentary Petrology* 45, 480–493.

Witthüser, K. T., Holland, M., Seidel, T. and König, C. M., (2015) Numerical modelling of mine dewatering and flooding in the Evander gold basin, South Africa. *South African Journal of Geology* 118(1), pp.71-82. https://doi.org/10.2113/gssajg.118.1.71

LIST OF FIGURES

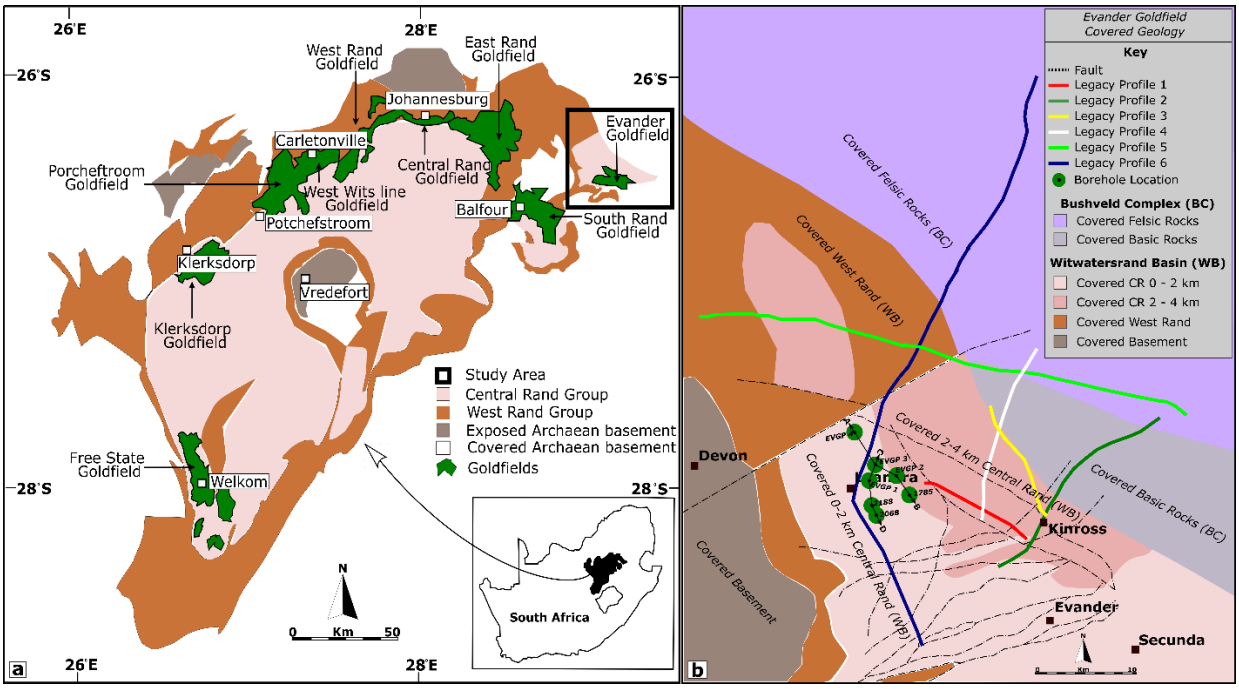
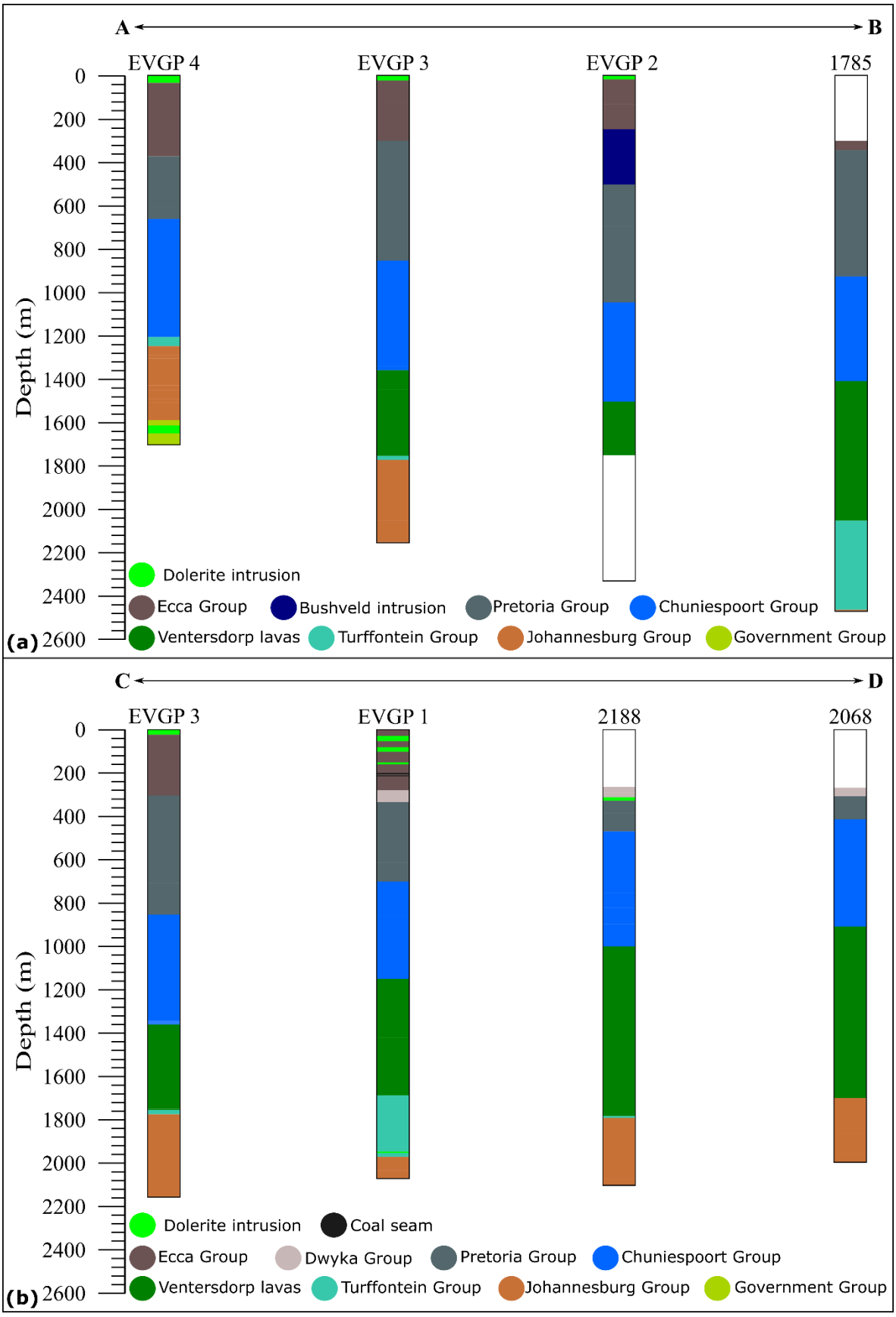


Figure 1: (a) The geological map of the Witwatersrand Supergroup showing the location map of the study area (black box) (modified from Dankert and Hein 2022). (b) The geological map of the covered Evander goldfield rocks showing the location of the legacy seismic profiles and the borehole location.


A
B
EVGP 4
EVGP 3
EVGP 2
1785
Depth (m)
0
200
400
600
800
1000
1200
1400
1600
1800
2000
2200
2400
2600
Dolerite intrusion
Ecca Group
Bushveld intrusion
Pretoria Group
Chuniespoort Group
Ventersdorp lavas
Turffontein Group
Johannesburg Group
Government Group
(a)
C
D
EVGP 3
EVGP 1
2188
2068
Depth (m)
Dolerite intrusion
Coal seam
Ecca Group
Dwyka Group
Pretoria Group
Chuniespoort Group
Ventersdorp lavas
Turffontein Group
Johannesburg Group
Government Group
(b)

2945

Figure 2: Boreholes drilled near the profile in the survey area (Figure 1b shows locations), with Figure 3a showing the (W - E) cross-section A-to-B along boreholes EVGP 4, EVGP 3, EVGP 2, and 1785. Figure 3b showing the (N - S) cross-section C-to-D along boreholes EVGP 3, EVGP 1, 2188, and 2068.

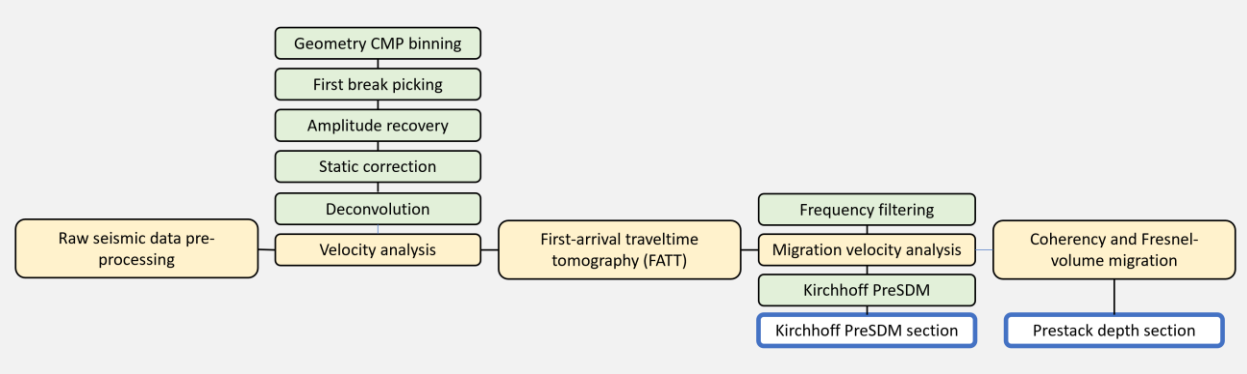


Figure 3: Summary of the depth imaging workflow.

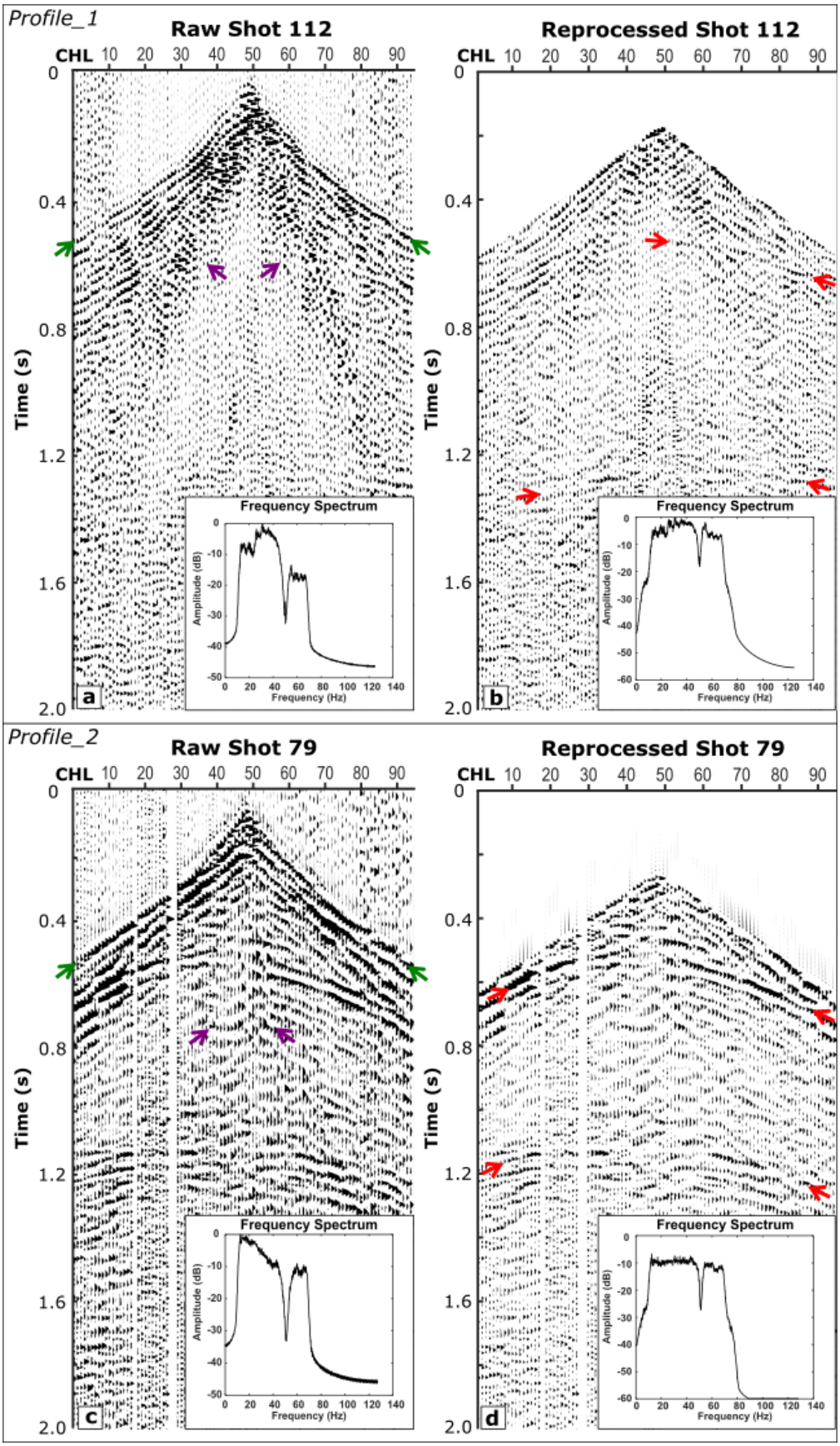
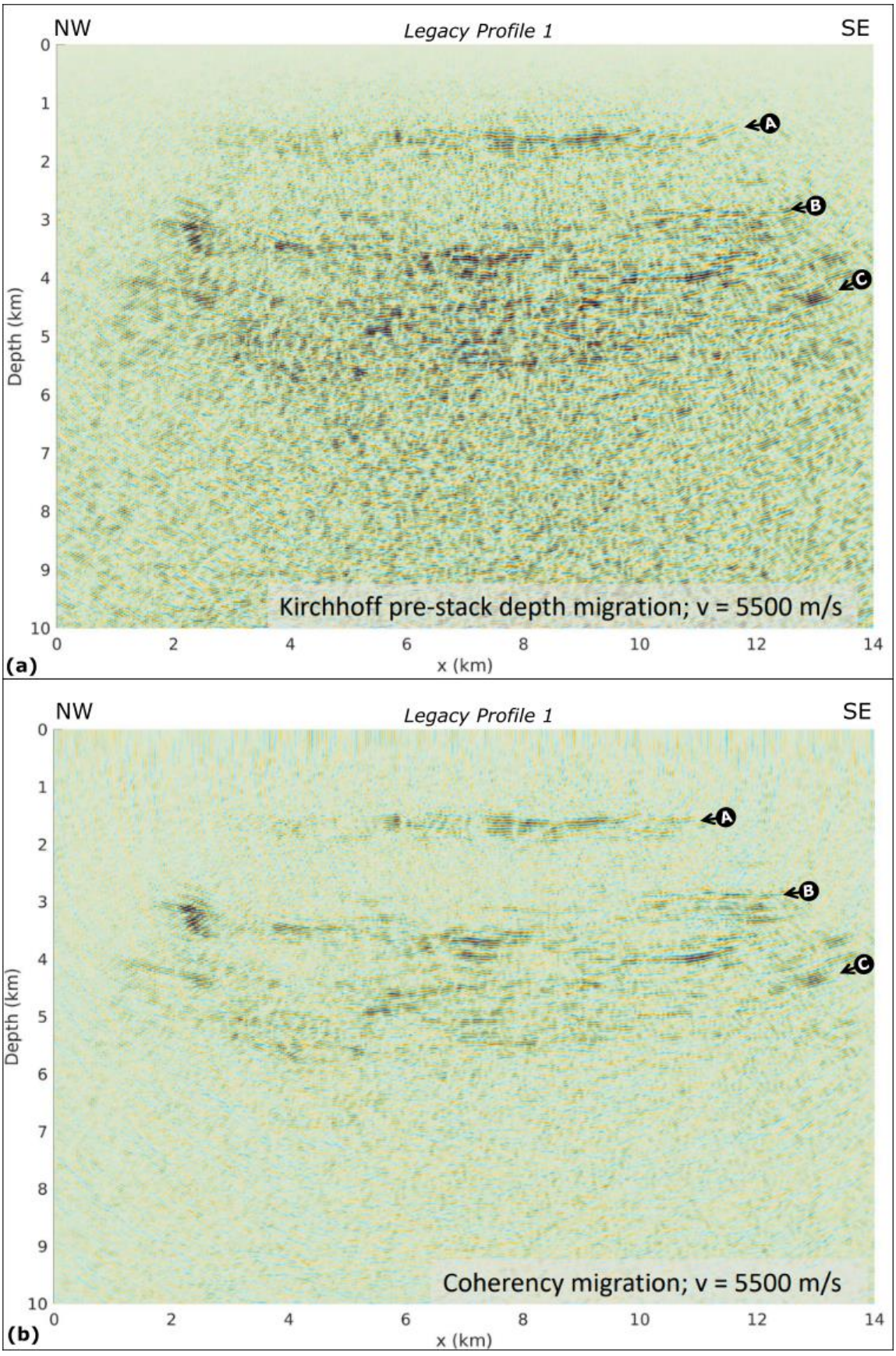
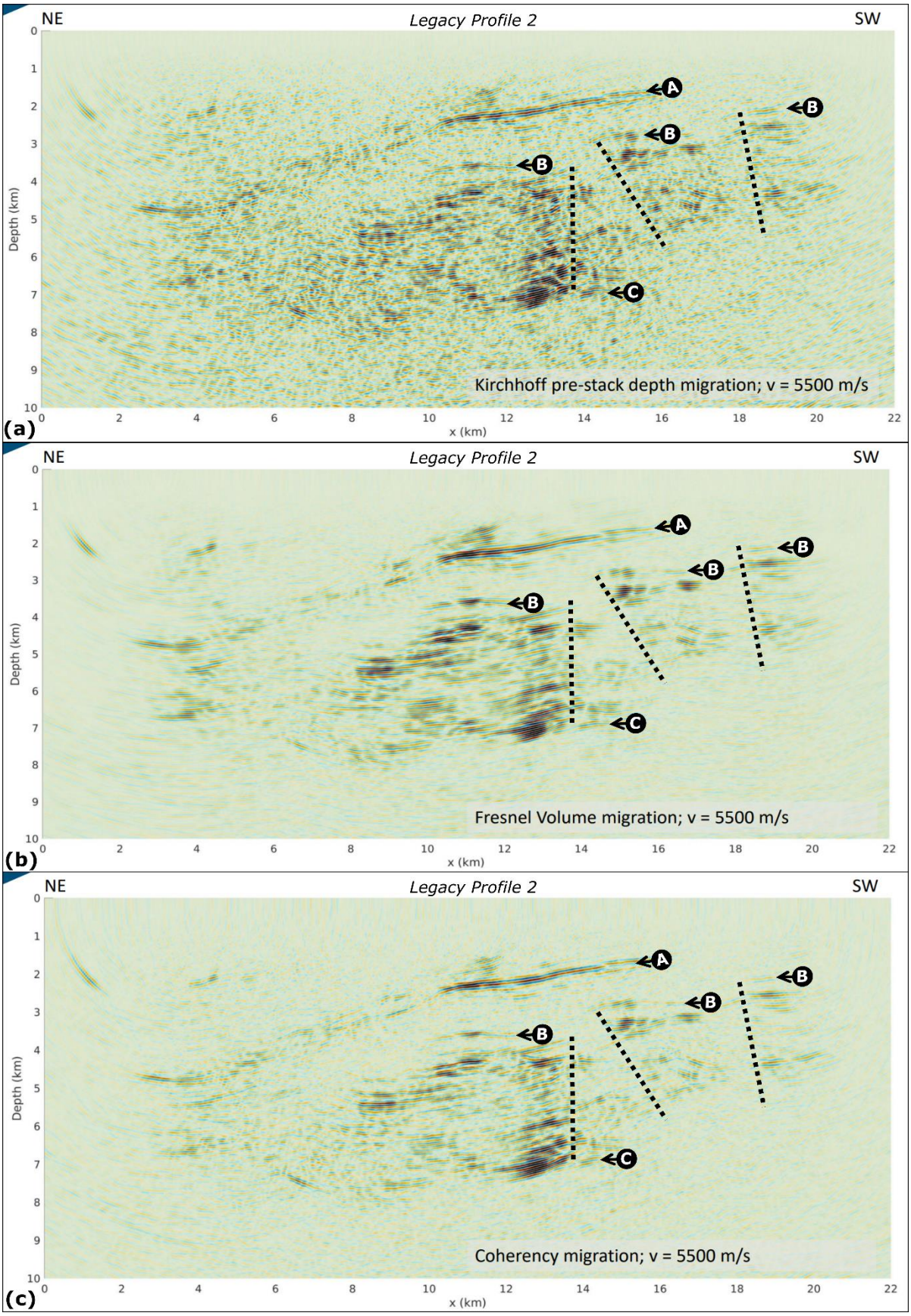

Profile_1
Raw Shot 112
Reprocessed Shot 112
CHL 10 20 30 40 50 60 70 80 90
Time (s)
0 0.4 0.8 1.2 1.6 2.0
Frequency Spectrum
Amplitude (dB)
Frequency (Hz)
a
b
Profile_2
Raw Shot 79
Reprocessed Shot 79
c
d

Figure 4: The raw (a) and (c) and processed (c) and (d) shot gathers. The preserved reflection after processing are shown by the red arrows, the attenuated surface waves outlined by the purple arrows, and the muted first breaks are shown by the green arrows**.**


NW
Legacy Profile 1
SE
Depth (km)
x (km)
A
B
C
Kirchhoff pre-stack depth migration; v = 5500 m/s
(a)
NW
Legacy Profile 1
SE
Depth (km)
x (km)
A
B
C
Coherency migration; v = 5500 m/s
(b)

2959

Figure 5: Comparison between the Kirchhoff pre-stack depth migration (a) and coherency migration (CM) (b), examples from profile 1. The main reflective contacts: Transvaal Supergroup – Ventersdorp lavas (A), Ventersdorp lavas – Witwatersrand Supergroup (B), and the base of the Witwatersrand Supergroup (C) are shown.


NE
Legacy Profile 2
SW
Depth (km)
x (km)
A
B
C
Kirchhoff pre-stack depth migration; v = 5500 m/s
(a)
Fresnel Volume migration; v = 5500 m/s
(b)
Coherency migration; v = 5500 m/s
(c)

2965

Figure 6: Comparison between the Kirchhoff pre-stack depth migration (a), Fresnel volume migration (b) and coherency migration (CM) (c), example from profile 2. The main reflective contacts: Transvaal Supergroup – Ventersdorp lavas (A), Ventersdorp lavas – Witwatersrand Supergroup (B), and the base of the Witwatersrand Supergroup (C) and possible faulting (doted lines) are shown.

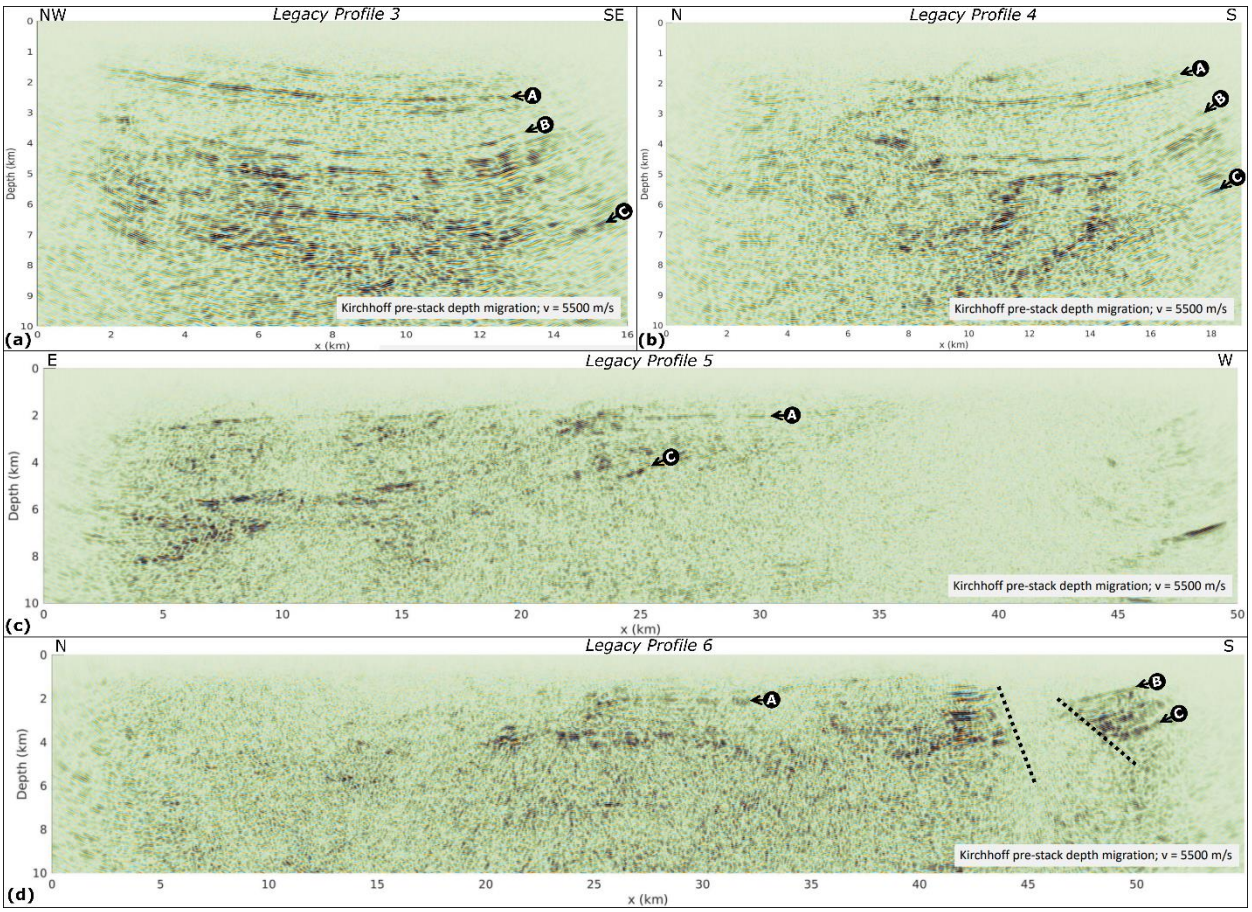


Figure 7: Kirchhoff pre-stack depth migrated sections (a - d) from profiles 3 - 6. The main reflective contacts: Transvaal Supergroup – Ventersdorp lavas (A), Ventersdorp lavas – Witwatersrand Supergroup (B), and the base of the Witwatersrand Supergroup (C) and possible faulting (doted lines) are shown.

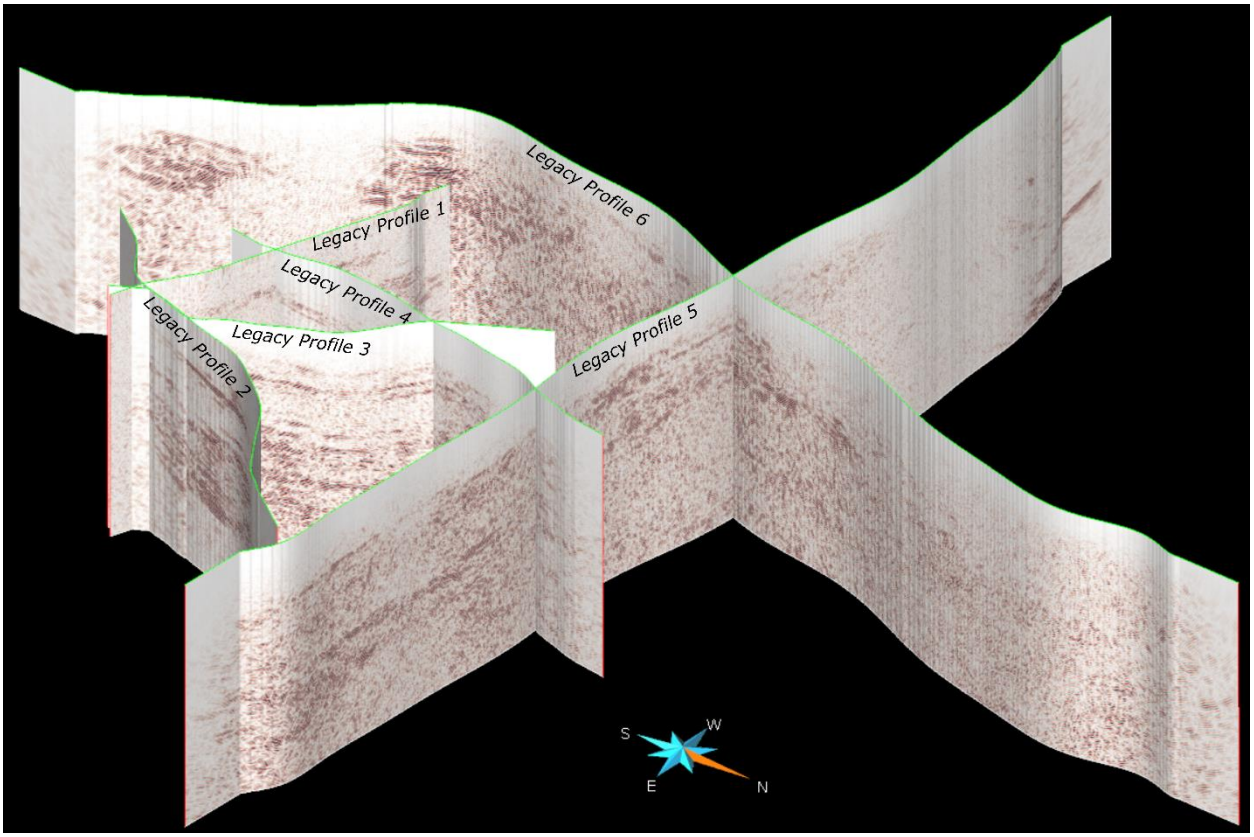


Figure 8: 3D view of the Kirchhoff pre-stack depth migrated sections from profiles 1 – 6, showing correlation and continuity of reflections.

Supergroup	Group or series	Max. thickness (m)	Description
Karoo	Ecca Dwyka	50 to 300	Sandstones, shales, and coal Conglomeratic sandstones and tillites
Unconformity			
Bushveld Complex	Felsic Mafic		Granite and Granophyre Highly differentiated Upper Zone ferro gabbronorite with Ti-V-magnetitite layers
Unconformity			
Transvaal	Pretoria Chuniespoort Black Reef	+ 275 427 5	Black shales with intercalated lavas Dolomites and cherts Quartzites with poorly developed basal conglomerate
Unconformity			
Ventersdorp	Klipriviersberg	1 220	Amygdaloidal, non-amygdaloidal and porphyritic andesitic lavas
Ventersdorp Contact Reef			
Witwatersrand	Central Rand West Rand	327 +430	Quartzites, shales, conglomerates, and lavas (Including the Kimberley reef) Greywackes, quartzites, poorly developed conglomerates, tillites, and magnetic shales.
Unconformity			
Archaean Complex			Schists, gneisses, granites, phyllites, and shales

Table 1: Generalised stratigraphy of the Evander Basin (modified from Witthuser *et al.*, 2015).

Parameters	Profile 1	Profile 2	Profile 3	Profile 4	Profile 5	Profile 6
Survey type	2D crooked	2D crooked	2D crooked	2D crooked	2D crooked	2D crooked
Year	1986	1986	1986	1986	1986	1986
Length	12 km	18 km	12 km	16 km	45 km	50 km
Direction	E-W	SW-NE	SE-NW	S-N	E-W	S-N
Recording System						
Recording Device	SN338 HR/ ADDIT III/ CMA I	SN338 HR/ ADDIT III/ CMA I	SN338 HR/ ADDIT III/ CMA I	SN338 HR/ ADDIT III/ CMA I	SN338 HR/ ADDIT III/ CMA I	SN338 HR/ ADDIT III/ CMA I
Sample Rate	4 ms	4 ms	4 ms	4 ms	4 ms	4 ms
Recording Length	16 s	24 s	24 s	24 s	24 s	24 s
Sweep Length	10 s	18 s	18 s	18 s	18 s	18 s
Sweep Frequency range	10 – 68.5 Hz	10 – 68.5 Hz	10 – 68.5 Hz	10 – 68.5 Hz	10 – 68.5 Hz	10 – 68.5 Hz
Source Information						
Source Device	4 Vibroseis	4 Vibroseis	4 Vibroseis	4 Vibroseis	4 Vibroseis	4 Vibroseis
Controller	P II	P II	P II	P II	P II	P II
Source Spacing	50 m	50 m	50 m	50 m	50 m	50 m
Receiver Information						
Receiver Spacing	50 m	50 m	50 m	50 m	50 m	50 m
Geophone Type	SM4U 10 Hz	SM4U 10 Hz	SM4U 10 Hz	SM4U 10 Hz	SM4U 10 Hz	SM4U 10 Hz

Table 2: A summary of acquisition parameters for the legacy profiles.

8 **Paper IV:** Cost-effective in-mine seismic experiments to image platinum deposits and associated geological structures at Maseve platinum mine, South Africa

8.1 Paper Summary

Cost-effective in-mine seismic experiments were conducted at Maseve mine in the Western Limb of the Bushveld Complex for the delineation of Platinum Group Element (PGE) horizons (known as reefs) and associated geological structures. These structures can affect mine safety and efficiency if they are not known ahead of time. Both the active and the passive seismic experiments were conducted, with passive experiments conducted on the surface using single vertical component 5 Hz wireless nodes. The active experiments were conducted on the developmental tunnel at a depth of ~ 550 m using a 5 kg sledgehammer as the seismic source and a land streamer with 4.5 Hz single vertical component geophones.

A total of seven in-mine 2D reflection seismic profiles were acquired covering a total length of 600 m. These profiles were acquired over known orebodies for improved delineation of the orebodies and cross-cutting geological structures. Three profiles out of the seven were merged and processed covering a total length of 300 m. Processing of the merged profiles was challenging because they were acquired in a structurally complex hardrock environment inside underground mine tunnels. The data were contaminated by noise arising from tunnel conditions, e.g., poor ground coupling of the land streamer, flooding inside the tunnel, and wave field scattering from the tunnel infrastructure. Despite the challenges, the data were encouraging, and they were processed using novel seismic processing techniques. This paper focuses on imaging the economic PGE-bearing Merensky and Upper Group 2 (UG2) layers and their associate geological structures using only active datasets. Improved imaging was achieved through iterative denoising techniques (e.g., frequency filtering) and post-stack time Kirchhoff migration. The Merensky reef and UG2 were successfully delineated approximately 55 m and 124 m below the tunnel floor, respectively. Furthermore, the faults and dykes cross-cutting the economic horizons were successfully delineated and relatively strong and highly faulted reflections below the UG2 horizon were observed suggesting the presence of other chromitite-enriched horizons. However, these orebodies can only be confirmed by further experiments or exploration drilling.

8.2 Manuscript

Cost-effective in-mine seismic experiments to image platinum deposits and associated geological structures at Maseve platinum mine, South Africa

Moyagabo K. Rapetsoa[1*], Musa S.D. Manzi[1], Michael Westgate[1], Mpofana Sihoyiya[1], Ian James[2], Emmanuel Onyebueke[1], Phumlani Kubeka[3], Raymond J. Durrheim[1], Thabang Kgarume[4]

[1] School of Geosciences, University of the Witwatersrand, Johannesburg, Private Bag 3, Wits, 2050, [2]Terraspect Geophysics, Perth, Australia, [3]Royal Bafokeng Platinum, The Pivot, No 1 Monte Casino Boulevard, Block C, 4th floor, Fourways, 2055, [4]Council for Scientific and Industrial Research, Pretoria, South Africa.

ABSTRACT

The detection of mineral deposits and their related geological structures is of great importance to the mining industry as structures (such as dykes and faults) can affect the safety, cost, and efficiency of mining. With the goal of testing cost-effective seismic methods for mineral exploration and mining, active and passive seismic experiments were conducted at Maseve platinum mine in the Bushveld Complex (South Africa) in 2020. The experiments involved surface-passive (using 5 Hz wireless nodes; single vertical component) and in-mine active reflection seismic surveys (using 4.5 Hz land streamer and 5 kg sledgehammer) to image geological structures and delineate economic platinum-group elements (PGEs) bearing Merensky and Upper Group-2 (UG2) chromitite layers (known as reefs). This paper presents only the results from the in-mine active seismic experiments. The in-mine seismic surveys consisted of seven 2D reflection seismic profiles in the development tunnels, which were located ~550 m below ground surface and a few tens of meters above known mineralizations; the UG2 and Merensky Reef (MR). The data were carefully processed to enhance the reflections and suppress noise generated by mine infrastructure (e.g., equipment and ventilation). We successfully imaged the MR and UG2 orebodies ca 55 m and 124 m below the tunnel floor, respectively, and delineated faults and dykes that crosscut them. Furthermore, the seismic data reveal relatively strong amplitude and faulted reflections below the UG2 that may represent deeper chromitite-enriched orebodies. However, the economic value of these horizons can only be confirmed through drilling. The processed seismic data were combined with borehole data, synthetic modelling, and geological models to constrain

the interpretation. This study encourages the use of in-mine seismics for future mineral exploration, mine development and planning.

Keywords: Mining, minerals, exploration, seismic imaging, tunnel.

INTRODUCTION

The Bushveld Complex (BC), located in the northern parts of South Africa, is the world's largest layered igneous intrusion with an estimated area of 64,000 km^2. It hosts the world's largest reserves of platinum-group elements (PGEs), and accounts for almost 80% of all platinum that is mined worldwide (Chistyakova *et al.* 2019).

The PGE deposits occur at various locations around the perimeter of the Bushveld Complex. The Maseve mine is located ~ 38 km NW of Rustenburg and ~ 10 km south of the Pilanesberg Alkaline Intrusive Complex in the North West Province, South Africa. The mine is situated on the western limb of the Bushveld Complex, next to the Styldrift and Wesizwe mines (Figs. 1 and 2). The mine was placed under care and maintenance in 2017 due to economic reasons and is currently used to test new mining technologies, making it an ideal site for field research.

Underground mining operations in the Bushveld Complex occur between 0.5 and 2.0 km below surface. Geological structures (e.g., faults, dykes, potholes, and Iron Rich Ultramafic Pegmatites (IRUPs)) are encountered more frequently as mining depth increases (Eales and Cawthorn 1996; Sehoole *et al.* 2020). These geological structures delay development and production, but also threaten the safety of mineworkers by increasing the risk of fall of ground that can result in injuries and fatalities (Guo and Luo 2014). Furthermore, faults and dykes may act as conduits for flammable gases and groundwater to the mining levels which may lead to several disasters in the mines. These structures can also be re-activated during mining activities and cause rock bursts. The heightened risks compromise the fundamental principles governing South African mining, i.e., safety and optimized ore extraction. These problems highlight the growing need for these geological structures to be identified ahead of mining.

The reflection seismic method is one of the most important geophysical methods because of its ability to detect both large and small-scale subsurface features (Malehmir *et al.* 2012). In South Africa, the reflection seismic method is mainly used for exploration, mine design and planning

due to its ability to delineate complex geological features (Stevenson and Durrheim 1997; Manzi *et al*. 2012; Manzi *et al*. 2019).

Active surface reflection seismic surveys have been conducted since the 1980s in South Africa to address challenges related to deep and near-surface mineral exploration, with the goal of reducing drilling and exploration costs, maximizing mine safety, increasing the possibility of finding new prospects, and the life of mine. In the 1990s, exploration and mining companies started conducting high-resolution surface 2D and 3D reflection seismic surveys in the Bushveld Complex to map economic platinum-bearing horizons (known as reefs) and other subsurface features (faults, dykes, folds, and potholes). The 3D reflection seismic surveys were particularly designed to map major faults, dykes, potholes (slump structures), and IRUPs. However, the surface seismic surveys were unable to accurately map and provide the geometry of smaller geological structures ahead of mining tunnels (Trickett *et al*. 2004). In the early 2000s, trials were conducted to investigate technologies that can delineate subtle structures with a throw of ~ 2 m (Stevenson e*t al*., 2003). The trials mainly involved borehole seismic techniques (e.g., cross-well reflection seismics, seismic tomography and vertical seismic profiling), which produced resolutions of 1 to 3 m; however these techniques exhibited low resolutions in noisy mining environments (Stevenson *et al*., 2003; Manzi *et al*. 2012).

As an alternative solution, and despite suffering from noise produced by mine operations such as blasting, ventilation, and drilling, in-mine seismics has proven useful in improving the imaging resolution of the mineral deposits and geological structures (Brodic *et al*. 2017; Brodic *et al*. 2021; Donoso *et al*. 2021). The application of in-mine seismic techniques has grown worldwide; however, the techniques are not yet well established in deep South African mines.

In this study, we conducted 2D in-mine seismic surveys at Maseve platinum mine in the Bushveld Complex (South Africa) to characterize geological structures using different seismic data acquisition techniques. The seismic experiments were conducted in an area covered by Ground Penetrating Radar (GPR) and Electrical Resistivity Tomography (ERT) surveys for integrated interpretation purposes. Integration of geophysical and geological data has played a key role in mapping the deep seismic reflectors and obtaining information on/ahead of the tunnel face. GPR and ERT are commonly used to mapping tunnel roofs and sidewalls, the information of which is

in turn utilized to assess and mitigate fall of grounds due to unstable hanging walls (Kgarume et al. 2019). However, in this paper we present only the results from the in-mine seismic trials.

The extent to which in-mine seismic techniques can image structures depends on multiple factors: acoustic impedance contrast, the geometry and structural characteristics of the target, host rock properties, survey design (receiver and source position), and the mine noise level along the tunnel. To better design in-mine seismic surveys and conduct high-resolution seismic surveys, noise levels need to be assessed and appropriate sources and receivers need to be used. Furthermore, accurate velocity models for the rock mass around the tunnel need to be determined for numerical modelling, seismic processing, interpretation and time-to-depth conversion (Malehmir *et al*. 2013; Manzi *et al*. 2017).

STUDY AREA AND GEOLOGICAL BACKGROUND

The emplacement of the Bushveld Complex (BC) has been the subject of academic debate and its geology has been documented by several authors (Eales and Cawthorn 1996; Buchanan and Reimold 1998; Kinnaird 2005; Hunt *et al*. 2018). The intrusive rocks of the Bushveld Complex were emplaced at ~2.06 Ga into the intra-cratonic sedimentary sequence of the Transvaal Supergroup (Cawthorn and Webb 2001). The Bushveld Complex is known for its remarkable size, covering an area of about 64 000 km^2. The complex (Fig. 1) is composed of four major limbs, with only the eastern, western, and northern limbs outcropping. The southern limb is visible only from gravity data and has been confirmed by drilling. Over the years, several authors have debated about the limbs being connected (Webb *et al*. 2004; Kinnaird 2005). The successive injections of magma resulted in the geology of the area being divided into three plutonic suites: Rashoop Granophyre Suite (RGS), mafic to ultramafic Rustenburg Layered Suite (RLS), and the Lebowa Granite Suite (LGS) (Eales and Cawthorn 1996; Hunt *et al*. 2018). Based on mineralogical variation the RLS is further divided into the (from bottom to top): Marginal, Lower, Critical, Main, and Upper Zone (Kinnaird 2005).

The Critical Zone is about 900 – 1500 m thick and has been divided into the Lower Critical Zone (LCZ) and the Upper Critical Zone (UCZ) based on the appearance of cumulus plagioclase. The LCZ is characterized by pyroxenites, Lower Group chromitite layers (LG); and Middle Group chromitite layers (MG1 and MG2), whereas the UCZ is characterized by the Merensky Reef (MR; a package of platinum-bearing chromitite-feldspathic orthopyroxenite), Upper Group chromitites

(UG1 and UG2), Middle Group chromitites (MG3 and MG4), pyroxenites, norites, and anorthosites (Kinnaird, 2005; Seabrook, 2005). The upper limit of the UCZ is marked by the Bastard reef (referred as cyclic/rhythmic unit) (Cawthorn 2015). The MR and the UG2 chromitite are the two major economic horizons for PGE deposits. The thickness of the MR ranges from 0.5 m to 2 m, with an average thickness of 1 m. The UG2 chromitite layer contains the largest PGE resources on earth, with a thickness ranging between 0.5 and 1 m. The Middle Group (MG) is made up of four major and minor chromitite layers with a thickness of 1-5 cm; whereas, the Lower Group (LG) consists of seven chromitite layers, with the thickest being 0.8 – 1.2 m (Lee 1996; Nex *et al*. 1998; Kinnaird 2005). The MR and the UG2 are mined at depths greater than 500 m below surface at Maseve mine, with the UG2 occurring between 15 m and 400 m below the MR in the Bushveld complex (Manzi *et al*. 2020; Sehoole *et al*. 2020).

The Bushveld Complex is crosscut by multiple dykes of different ages and compositions, with diabase and dolerite dykes being dominant in the area. A few dykes at Maseve mine have been confirmed through drilling and underground mapping. Knowledge of the dykes is important as they reduce the ore reserve and may present mining difficulties. The dykes in the BC are often associated with fault zones (Ledwaba 2012; Scheiber-Enslin and Manzi 2018). Furthermore, the Bushveld Complex is affected by slump structures (locally known as 'potholes') and IRUPs that result in challenges to mining operations. BC is generally faulted, and the regional structural interpretation suggests that the ENE-WSW trending Chaneng Fault Zone (Fig. 1b) is the most dominant structure in the Maseve area (Basson 2019). To the south of the Pilanesburg complex, a dense conjugate network of faults and fractures trending NE and NW is displayed on the high-resolution aeromagnetic images (Scheiber-Enslin and Manzi 2018; Basson 2019). These faults (e.g., RFZ Fig. 1b) and fractures have been confirmed through drilling at Maseve mine and incorporated in the geological model (Fig. 2). Most of the faults strike north to northwest and dip at an average of about 70^0 to 80^0 (Scheiber-Enslin and Manzi 2018).

PHYSICAL PROPERTY MEASUREMENTS

Physical property measurements were collected following the procedure described by Nkosi *et al.* (2017). The main objective was to investigate the potential source of seismic reflectivity of the mineralization (MR and UG2) with respect to their host rocks. The ultrasonic velocity (P-wave) measurements were conducted using a UK1401 SURFER ultrasonic tester, operating at

frequencies of 50 kHz. Throughout the seismic P-wave velocity measurements the repetition frequency of the instrument was kept constant between 2 and 4 Hz, depending on the size of the sample. Five P-wave velocity measurements were taken on each sample and an average was taken as the final velocity value (Table 1). Although the ideal conditions for measuring these samples are at elevated pressures (~ 20-60 MPa) to mimic the in-situ environment, our measurements were conducted at atmospheric temperature and pressure. The bulk density measurements were conducted using water immersion method (based on Archimedes' principle) (Nkosi *et al.*, 2017). Another factor that affects acoustic impedance is porosity, however in this study we did not conduct porosity measurements as the rock samples are from a crystalline environment and have comparable porosity (Malehmir *et al.* 2013; Nkosi *et al*. 2017).

Synthetic seismogram

This section presents results of the physical properties measurements (bulk density and seismic velocities) of rocks in the Bushveld Complex that make up the hangingwall and footwall of the MR and UG2. Previous studies have reported seismic velocities and densities of rocks in the Bushveld Complex (Campbell 2011; Manzi *et al*. 2017), therefore this study reports in detail the individual density and velocity measurements of the hangingwall and footwall in the study area. We used the information to design the seismic experiments to investigate "near surface" geological structures, i.e. within 150 m of the mine tunnel in which the survey was conducted. Table 1 summarizes the ultrasonic velocities and density measurements of the MR, MR hanging wall, MR footwall, and UG2. Whilst the velocity and density of feldspathic and pegmatoidal pyroxenite are from Manzi et al. 2019. The densities and velocities of the rocks are within a narrow range, except for the chromitite sample that is much denser than the host rocks and the water-saturated top layer of norite that has a lower velocity. The average P-wave velocity measurements of the core samples range from 5088 m/s to 6118 m/s and the average density measurements range from 2744 kg/m^3 to 4392 kg/m^3. To compute the synthetic seismograms we used the measured densities, velocities and depths from borehole 1 (BH1; see Figs. 2 and 3). The borehole has a total depth of 577.5 m from the Earth's surface and intersected the MR and UG2 at 515.14 m and 570.94 m, respectively. We used a Ricker wavelet with a dominant frequency of 130 Hz and a sampling rate of 0.25 ms to compute the seismograms for the lower 75 m of the borehole, which covered the ore zones beneath the tunnel (Fig. 3). The acoustic impedance contrast between the hangingwall and footwall of the MR suggests that the interface is associated with a strong reflection, which can be used as a proxy

for MR mineralization. The UG2 has a higher acoustic impedance contrast with the host rocks, hence a noticeable reflection at the interface (Fig. 3), which is in agreement with studies conducted by Scheiber-Enslin and Manzi (2018) and Manzi *et al.* (2020).

2D acoustic modelling and seismic reflectivity

The geology of the Maseve platinum mine is detailed in the mine's resource estimation report (Muller and Visser, 2010). The Bushveld Complex has been well studied (Nex *et al.* 1998; Webb *et al.* 2004; Kinnaird 2005; Cawthorn 2015) and the geological structures in certain areas makes it an ideal place to conduct numerical modelling to investigate the seismic response of mineralizations and other geological structures. However, the Bushveld Complex rocks (anorthosite, norite, and pyroxenite) have similar physical properties (mainly seismic velocities). Acoustic impedance contrast in the Bushveld Complex is mainly controlled by noticeable differences in densities of the rocks, which in turn provides a strong reflective interface between the mineralization and the host rocks. The MR has a slightly higher seismic velocity than the host rock, whilst the UG2 has higher density compared to the host rocks (Table 1). The focus of the study is to image the near-tunnel-floor mineralization and geological structures, therefore, the complex geology of the area is not presented in detail. The thickness and depth of the targeted mineralizations were obtained from the available surface boreholes in the study area (Figs. 2 and 3). The MR (~ 1- 2 m thick) and UG2 (~ 1-2 m thick) were intersected by surface borehole (BH1) at depths of 515 m and 571 m, respectively. These horizons are faulted and folded (asymmetrical synclinal fold with a NW - SE trending fold plane), resulting in the MR and the UG2 outcropping on the west-south-west (WSW) side of the seismic line (Fig. 2b). The acquired seismic profiles (mainly P5 and P6) transverse a major dolerite dyke and Rapetsoa Fault Zone (RFZ) that crosscut the MR and UG2 (Fig. 2). Seismic modelling only considers the rock beneath the tunnel. The rock between the tunnel and the Earth's surface is considered to be free space. The elevation of the inclined tunnel is used as the datum for reflection seismic processing. Therefore, the complex characteristics of the full 3D wave field are not analysed in this paper.

The modelling was conducted using Tesseral Pro^{TM} software. Fig. 4 shows the geological model built (Ahmadi *et al.* 2016; Singh *et al.* 2020) from borehole data and mine information (Fig. 2). The 2D acoustic finite difference modelling was conducted to assist with the planning of the in-mine seismic surveys, investigate the source of seismic reflectivity in the data, and constrain seismic interpretation. The structures identified from the mine plan (Fig. 2b) were used to build a

geological model (Fig. 4) of the rock mass beneath the incline tunnel. The Finite Difference model was 360 m (horizontal extent) x 140 m (depth), with a grid cell of 1 m in both vertical and horizontal directions. A synthetic 2D seismic survey was designed to generate 2D synthetic shot gathers using acoustic modeling (Fig. 5a) of the first few hundreds of meters for two shot examples (Figs. 5a, d: first and center shot). The main objective of numerical modeling was to simulate the seismic response of the targets (MR and UG2) and geological structures (faults and dykes). The synthetic data were generated using the acquisition parameters very close to the ones used for real seismic surveys, except that the model used a single profile (360 m long) while the real survey data had three merged profiles (115 m long). The synthetic seismic modelling had a maximum two way travel time (TWT) of 500 ms. A Ricker wavelet of 130 Hz was used for modeling, with a sampling rate of 0.25 ms. The measured average velocities and densities in Table 1 were used in the model. The shot gathers of the synthetic data (Fig. 5a, d) were then compared with those of the acquired data (Figs. 5b, e). The comparison between the synthetic and real data are discussed later.

SEISMIC DATA ACQUISITION

Prior to the seismic surveys, a preparatory mine site visit was made for few days to check the tunnel conditions and decide on the location of shots and receivers. Information from the GPR and ERT surveys conducted in the tunnel a few weeks prior assisted in designing our surveys to better delineate the targets (depth and lateral extent of the deposits, as well geological structures).

In November 2020 seven 2D in-mine seismic profiles were acquired with a total length of about 0.6 km over known orebodies (Figs. 2a, b). Our final set-up included: one profile in the development tunnel (P1), two around Michelle's pillar (P2 and P4), and one profile in a crosscut (P3), and three profiles (P5, P6 and P7) in the incline tunnel (IT) (Fig. 2b). The three IT profiles, namely P5 (115 m long), P6 (115 m long) and P7 (115 m long), were collected in segments that are collinear to each other, orientated in an east-north-east (ENE) to west-south-west (WSW) direction (Figs. 2b). P5, P6 and P7 profiles are the focus of this paper and were designed to cover the area along the incline tunnel. P1 was collected perpendicular to P5 - P7, with the goal of imaging the folded MR and UG2 located at about 20-70 m depths below the incline tunnel (Fig. 2b). P2 and P4 were experimental lines collected around the pillar of interest. The idea was to test the response of the 4.5 Hz geophone (1C) attached to the land streamer along the pillar; the shots were generated horizontally along the pillar using a 5 kg sledgehammer. P2 was conducted at the base of the pillar, whereas P4 had receivers supported on the sidewall. P3 was collected with

planted cabled sensors (1C; 4.5 Hz and 14 Hz), while the other 5 segments were collected using a 4.5 Hz seismic land streamer. The profiles collected with the land streamer had a receiver spacing of 5 m, providing a total spread of 115 m.

A day was spent testing different sources (24 kg accelerated weight drop (AWD) and a 5 kg sledgehammer), and one-component sensors (cabled 100 Hz horizontal, 14 Hz vertical, and 4.5 Hz land streamer). We also drilled holes along the tunnel floor to plant the cabled geophones and increase the coupling, however this process proved time consuming as it took us about half a day to plant geophones along one profile. This encouraged us to use the land streamer as receivers in all our seismic profiles because it was quick and provided better coupling with the tunnel surface. Shots were generated with both sources to check the S/N of the data and decide on the most suitable seismic source for the surveys. Although the 24 kg AWD provided a better signal, it was not safe to use due to the conditions of the tunnel sidewall and hangingwall (e.g., loose fragments of the hanging wall). A 5 kg sledgehammer was used as a seismic source instead, with a shot spacing of 5 m. The sledgehammer was chosen over the 24 kg accelerated weight drop due to the conditions of the tunnels (e.g., loose fragments of the hanging wall). To improve signal-to-noise ratio (S/N), four shot records were vertically stacked at every shot position. A range of sampling rate parameters were also tested to ensure that guided waves and other mine-related noise, for example, were not contaminating the records. Following the analysis of the shot gathers at various sampling rates, a sampling rate of 0.25 ms was chosen as it provided better results with respect to the limitations of the resonant and spurious frequencies of sensors used in the survey. The survey parameters are detailed in Table 2. One of the advantages of the sledgehammer is its light weight and low cost when compared to other seismic sources. The mine is also prone to flammable gases (e.g., methane) so we carefully ensured that the hammer's impact on a base plate did not generate any sparks that could lead to explosions inside the tunnel.

In addition to the seismic surveys conducted along mine tunnels, five active seismic profiles were collected on the surface, simultaneously with passive seismic surveys using three broadband seismometers and remote acquisition units (RAUs). The surface experiments were an attempt to test the feasibility of conducting tunnel-surface experiments. In this paper, only the results obtained from active in-mine seismic profiles (P5 – P7) are presented.

SEISMIC DATA PROCESSING

Fig. 5 shows the comparisons between the synthetic (Fig. 5a, d), raw (Fig.5b, e), and processed (Fig. 5c, f) shot records. The raw seismic data exhibit high S/N (Fig. 5b). However, few traces exhibit some noise due to air waves (Fig. 5b, e: black arrows) or poor coupling of geophones on the muddy areas along the tunnel. Table 3 provides the workflow followed in the processing of the data, subdivided into pre-conditioning and processing steps. The main aim of the processing workflow was to preserve primary reflections and remove source-generated and ambient noise (e.g., water pipes, moving vehicles, and blasting from neighboring mines) to improve data quality.

The first step was to fix the coordinates and merge the seismic profiles (P5-P7) before processing because the headers had receiver and shot positions as coordinates. Coordinates from the mine pegs were used to determine the shot and receiver locations, using linear and spline interpolation functions. The second step was to fix the geometry. From the coordinates created, a Shell-Processing-Support (SPS) file was set up for the geometry. The geometry was then merged with the seismic data. For the seismic profile, we assigned Common-Depth-Points (CDPs) with a spacing of 2.5 m, followed by removing noisy traces, mainly caused by poor ground coupling.

The data are of fair quality with clear P-wave first breaks in the raw shot gathers (indicated by blue arrows in Figs. 5b, e). Some reflections (R1 and R2) observed in the raw shot gathers (red arrows in Fig. 5b, e) matched reflections in the synthetic shot gathers (Figs. 5a, d). R1 is interpreted to originate from MR and is not clearly defined in the first shot synthetic gather (Fig. 5a); it is masked by first breaks as the reflecting MR is close to tunnel floor on the east of the model (Fig. 4). R2, on the other hand, is well defined at 25 ms with a weak reflection compared to R1. Possible reflected refractions from the fault (RFZ) zone and dyke are also observed in the synthetic data (Figs. 5a, d: green arrows). R1 (30 ms) and R2 (45 ms) are clearly observed on the center synthetic shot gather and the raw shot gather. An additional reflection (R3: 55 ms) is also observed on the raw shot gather.

As one of the most important steps in the pre-stack data processing stage, the P-wave first breaks were picked using an automatic method (envelope threshold) combined with manual picking. The picks were used to compute the refraction statics. A total of 1778 picks were used over 72 receivers and 76 shots across the three profiles. The picks were inverted for the two-layer based refraction model, with four iterations and a RMS error of 1.45 - 2 ms. Fig. 6 shows a refraction tomogram

(Fig. 6a) and ray path model with low ray coverages (white arrows in Fig. 6b). The low ray coverage is as a result of merging the three segments into one profile (Fig. 6b). The refraction tomogram (Fig. 6a) was produced to aid with interpretation of the data for about 20 -50 m depth below the incline tunnel. The maximum elevation along the profile is 602 m (above mean sea level), and was chosen as a matching datum elevation together with a replacement velocity of 4000 m/s for floating datum statics. The next step was to apply refraction, residual (using only short wave-length component), and elevation statics correction to enhance the continuity of the reflections and improve the quality of the final seismic section.

Fig. 5b,c shows the raw shot gathers and a processed shot gather (trace editing, refraction static, bandpass filter, and top mute), respectively. The raw data are contaminated by some noise that could be related to ambient sources (i.e., ventilation and water pumps) (Fig. 5b). The frequency of the acquired data ranges from 50 Hz to 1800 Hz. The higher frequencies (> 250 Hz) are most likely related to spurious frequencies of the 4.5 Hz geophones used. A bandpass filter (50 – 170 Hz) was applied to constrain the data within the source energy frequencies. The amplitudes of the first breaks (Fig. 5b, e) are high, affecting the near-surface reflections. To remedy this, we applied top mutes on the first breaks with care in order to not mute some shallow reflections. The processing steps applied illuminated reflections (R2 and R3) in the shot records (Fig. 5f). Although the above-mentioned processing steps enhanced some of the reflections, some noise (probably related to air waves) were still present in some shot records (Fig. 5b, e: black arrows) and overshadowed the reflections (e.g., R2). To eliminate these an f-k filter was applied to the data. The f-k filter targeted events with velocities below 4100 m/s, in order to enhance the targeted events that have apparent velocities between 5700 to 6400 m/s.

Velocity analysis was conducted using a series of constant velocity stacks generated to select the velocity that shows high coherency of the reflections. Prior to stacking, NMO corrections were applied to account for the hyperbolic curvature of the reflections and stacked using the NMO velocities of ~ 5500 m/s. We calculated and applied residual statics using the updated NMO-corrected gathers, resulting in continuous reflections on the stacked sections. Dip moveout (DMO) was applied to stack the dipping reflections simultaneously. A second bandpass filter (80 – 160 Hz) was applied to remove low-frequencies that were still present in the data. Fig. 7 show the final unmigrated time (Fig.7a) and depth-converted (Fig.7b) stacked sections, respectively. A Kirchhoff migration algorithm was applied using a constant velocity of 5500 m/s, which was decided based

on the P-wave velocity distribution on the data and published velocities (Manzi et al., 2020). Finally, following a series of tests on velocity fields that provided the best migrated sections, 5500 m/s was used for time-to-depth conversion. Together with mine modelled structures and surface boreholes, the final depth-converted seismic section was imported into the 3D visualization software package for final geological interpretation and comparison with other geological datasets.

RESULTS AND INTEPRETATION

Seismic processing and interpretation were mainly constrained to the top 100 ms (approximately 275 m depth below the tunnel floor) because the main targets (MR and UG2) for future mining and exploration at Maseve mine fall within this window (Figs. 5-9). The first step was to make a comparison of the synthetic, raw, and processed shot gathers (Fig. 5). Clear first arrivals (blue arrows) are seen in the 2D acoustic finite-difference modelled shot record, raw short record, and processed shot record (Fig. 5). The air waves (indicated by black arrows) observed in the raw shot gather (Figs. 5b, e) have been attenuated (Figs. 5c, f) by applying filters (mainly f-k) and DMO, resulting in a dataset with an improved S/N. The main reflections observed in the seismic data interpreted to have originated from the mineralizations are: MR (R1) at 20 ms, UG2 (R2) at 45 ms, and a possibly unknown mineralization (R1) at 55 ms (Figs. 5e, f). MR is shallower toward the ENE on the model. Therefore the strong reflection (R1) originates from MR and is coupled with the first breaks, while the feint reflection (R2) originates from the UG2. R3 is not modelled in the synthetic data (Figs. 4, 5a) as it was not known, but is visible in Fig. 5b, e. R3 is interpreted to originate from the UG1, which is a chromitite mineralization that is well known in other mines within the Bushveld Complex. UG1 is, however, not intersected by drilling at Maseve mine as the drilling only targeted MR and UG2 (Fig. 2c). Our interpretation of this seismic reflection (and others observed in the data) is not conclusive as these events could be associated with complicated wave field characteristics caused by side tunnels connected to the main exploration tunnel, fracture systems, the rock mass around the tunnel, and mine infrastructure (or developments). In addition, there is no borehole information to further constrain our seismic interpretation below the UG2 horizon.

P-wave velocities obtained from the first break tomograms show a good definition of two zones in our area: fractured top layer (~ 10 m thick) exhibiting velocities between 1000 m/s and 4000 m/s and the hard rock exhibiting variable thicknesses (10-40 m) with velocities between 4000 m/s and 6500 m/s. These velocities show a good match with the known velocities from (norite and

pyroxenite; Manzi *et al.*, 2020) and borehole stratigraphy, and complement P-wave reflectivity observed on the final stacked sections (Figs.7 and 8). Based on the refraction tomograms, existing borehole, geological models (Fig. 2), tunnel observations (i.e., outcropping MR and UG2 ~ 110 m and ~180 m WSW of the centre of the merged profile, respectively), the stratigraphy generally dips at ~ 10^0 towards WSW and dips 60^0 ENE due to folding and faulting (Fig.4).

The unmigrated time (Fig. 7a) and depth-converted (Fig. 7b) stacked seismic sections suggest that the reflections are well delineated in our study. The strong reflectivity observed at 20 ms (black arrows) on the time stack section corresponds to 55 m depth on the depth stack section. The reflections (Figs. 7a, b: marked with arrows) are more prominent at the center of the seismic section. The shallow reflection occurring at about 55 m is attributed to be the MR as discussed previously. The far ends of each seismic profile (P5 - P7) (Fig. 8a) show weak reflections whose coherency increases towards the middle section (CDP 160-180 and 200 – 230); due to low fold-of-coverage at the edges of the profiles. Overlying the borehole log and 1D synthetic data onto the depth-converted migrated section (Fig. 8b) confirms that the strong reflections (R1) at about 55 m depth can be attributed to the MR, whilst the reflection at ~ 124 m (R2) is associated with the UG2. The reflector (R2) dips towards west-south-west and loses coherency at CDP 130. The area is structurally complex as interpreted in Fig. 9. MR and UG2 are affected by folding (e.g., a synclinal structure is observed between CDP 160 and 200) and crosscut by dykes (dotted green and red lines) and faults (indicated by pink lines) different orientation (Fig. 9). In addition to faults and dykes, the seismic section exhibits a vertical low-seismic amplitude and chaotic feature along the MR and UG2 horizons, which is interpreted to be associated with the IRUP (Fig. 9; IRUP: dotted brown). Similar to faults and dykes, this feature appears to disrupt both the MR and UG2 (Figs. 8 and 9), and it occurs in the vicinity of the fault zone. In particular, the seismic sections show the delineation of F4 that coincides with the RFZ interpreted in the mine geological model and described by several authors. Identification of these structures by the seismic data are important as this information can be used to enhance the existing geological model.

DISCUSSION

To better understand the quality of the data and interpret geological structures, it is important to first address the seismic resolution limit of the data. The quality of the acquired data are dependent on many factors such as: the impedance contrast between the target and the host rock, the geometry (e.g., shape) and thickness of the target, survey design, instruments used, tunnel conditions, and

noise level. The seismic resolution limit is controlled by the dominant wavelength (λ) in the data, seismic velocity of the targets, and the dominant frequency of the data. Theoretically, the top and bottom of geological features cannot be resolved if its thickness is less than a quarter of the dominant seismic wavelength (i.e., Rayleigh criteria of the vertical resolution limit). However, smaller features down to λ/32 can still be detected, although the detection will depend on the diffractions, not solely on the seismic amplitude (Manzi *et al*. 2014; Malehmir *et al*. 2018).

The dominant seismic frequency of the reflected signal at the MR, for example, is ~ 130 Hz. By taking into account the stacking velocity (~ 5500 m/s) used in our processing workflow, the dominant seismic wavelength (λ) is ~ 42 m. This gives us the vertical resolution limit of ~ 10.5 m, which is the minimum thickness needed to resolve the top and bottom of a layer. However, the MR (~1 - 2 m thick) and UG2 (1 – 2 m) are too thin to be resolved. However, the structure of such thin mineralized reefs can be mapped indirectly using the seismic reflective interfaces between hangingwall and footwall rocks as proxies (Manzi *et al*., 2020). For example, the MR is associated with the reflections arising from the contact between pegmatoidal anorthosite hanging wall and norite footwall. This implies that the MR is not imaged directly because of the low acoustic impedance contrast between the reef (ρ = 2744 kg/m^3; v= 5950 m/s) and the surrounding rocks (norite: ρ = 2951 kg/m^3; v = 5667 m/s; anorthosite: ρ = 2947 kg/m^3; v = 5530 m/s). Due to weathering of the hangingwall, the MR is imaged indirectly due to the high acoustic impedance between the hanging wall (weathered anorthosite: ρ = 2851 kg/m^3; v = 3088 m/s) and the footwall (norite: ρ = 2951 kg/m^3; v = 5667 m/s). The UG2, on the other hand, is directly imaged because of the significant acoustic impedance contrast (mainly controlled by a high density associated with chromitite) between the UG2 (ρ = 4392 kg/m^3; v = 6118 m/s and the footwall (ρ = 2700 kg/m^3; v = 5900 m/s) (R2 in Fig. 9).

The lateral extent of the geological feature cannot be discerned if it is narrower than the diameter of the first Fresnel zone (i.e., horizontal resolution limit) (Yilmaz et al., 2001), which governs the horizontal positional accuracy of structural information that can be obtained from seismic data. It is worth noting that this horizontal resolution limit assumes that the seismic data are un-migrated. After migration, as is the case with our seismic data, this limit can be enhanced to approximately half-the dominant wavelength, i.e., 21 m. Theoretically, this implies that that two or more geological features within 21 m of each other will not be resolved as separate features. However,

smaller features could still be detected, but this will depend on S/N of the data, the velocity field and migration algorithm used for migration (Manzi *et al.*, 2014; Westgate *et al.*, 2020).

A general assessment of the in-mine seismic results reveals that the data, although acquired in noisy mine environment, are of high quality from which structural interpretation can be drawn. The strong, seismic reflections associated with the MR (~ 20-25 ms in Fig. 7a) and UG2 (~ 45-70 ms in Fig. 7a), although disrupted by faults and folds, are prominent and reliable indicators of mineralizations throughout the seismic profile (see Figs. 7, 8 and 9). The depth position, shape and dips of the interpreted MR and UG2 have been constrained with the geological information. Fig. 10a-d shows the 3D visualisation of the integrated borehole data, seismic data, mine modelled structures (MR, UG2, fault and dyke), seismically defined structures (faults and dykes). Generally, seismics has a good tie (within 3 m discrepancy) with the borehole information (Fig. 10a). For example, BH1 intersected the MR and UG2 at a depth of 68 m and 120 m below the tunnel respectively, which correspond to the depth position of reflections R1 and R2 on the migrated section (Fig. 10a). The seismic reflections R1 and R2 show a good correlation with the mine MR and UG2 orebodies, respectively (Fig.10b). Surface boreholes (e.g., BH2) on the western side of the seismic line (Fig 2b) intersected the MR at an average depth of 510 m and UG2 at an average depth of 555 m below surface, while the boreholes on the eastern side of the seismic profile intersected the MR and UG2 at 515 m and 570 m respectively, indicating that these two target mineralizations are closer to each other on the western side (Fig. 10b). The boreholes were targeting the MR and UG2, thus did not extend to depths below UG2. Therefore, these boreholes were not used to constrain the source of R3 reflectivity in the seismic data. The minor discrepancies (0-3 m) in depth positions between seismics, orebodies, and borehole data might be due to three reasons: (1) the boreholes were projected onto the seismic profile as they were not drilled directly along the seismic line, resulting in the interpreted reflection on the seismic profile having an apparent dip compared to the borehole data, therefore we expect a mismatch of the on a seismic line and the geological model (Fig. 4), and (2) the velocity model used to depth convert the seismic sections may be in error, and (3) the mine orebody models are poorly constrained in areas that are not covered by the borehole information (western portion of the study area).

In terms of structural interpretation, our results confirm the existence of previously known faults and dykes (e.g., RFZ and dyke 2 in Figs. 4 and 10c) and further constrain their interpretation. F4 corresponds to the Rapetsoa Fault Zone (RFZ) that has been studied in detail by several authors

(e.g., Scheiber-Enslin and Manzi 2018; Basson 2019) and confirmed through underground and surface mapping and drilling. Along the fault zone, we have also interpreted a dyke (D2) that corresponds to the one found in the mine model (Fig. 4). Therefore, our results suggest that the RFZ was active (or reactivated) and provided planes of weakness along which dyke 2 intruded. Furthermore, this work has identified more faults (e.g., f1 – f7 in Figs. 9, 10c, d) and dykes (dyke 1 and dyke 2 in Fig 10c, d) that were not incorporated in the existing mine geological model. The majority of the faults in the area are dipping at 60-90^{o} WSW. The faults (Fig. 9; f1, f4, f5 and f7) are mainly reverse faults with a WSW upthrow, displacing the MR and UG2 horizons. F2 and f3 are normal faults dipping WSW, while f6 dips ENE (Fig. 10c)

In general, the geometry of R1 and R2 correspond with the geometry of the mine MR and UG2 orebodies. Good correlation between seismics and mine orebodies is mainly observed from the centre (CDP no. 160) to the eastern end (CDP no. 100) of the profile (Fig. 10b, d). However, the seismic data suggest that these two horizons (R1 and R2) are faulted towards the far western end of the profile (CDP no. 160-240) with the down throw in the west. This suggests that MR and UG2 are continuous on the western side of the outcrop position, which contradicts the geometry shown in the mine orebodies (Figs. 2c, 10b). If our interpretation is correct, the continuity of these horizons beyond the outcrop position will need to be incorporated in the current mine model to enhance the resource evaluation. The seismic results suggest that faults and dykes crosscut and displace (in the case of faults) the MR, UG2 and R3 horizons, which constrains their timing of activity (i.e., they were active after the reefs depositions). The delineation of these structures is important for future mine planning at Maseve mine as these indicate areas that may not be mineable because of the loss of ground. Although these faults are detected on the seismic section, their throws cannot be determined with confidence as their displacements (throws) are below the seismic resolution limit of the data. In addition to this, the seismic data provide information on a potential chromitite-rich horizon (reflection R3 in Fig. 9) 10s of meters in the footwall of the UG2 horizon, which is interpreted as the UG1.

In future we plan to overlap (at least by 50% of each profile length) the profiles to avoid obtaining low folds at the end of each profile. In the new data, other processing approaches (such as pre-stack depth and diffraction imaging) will be tested to further improve the imaging of the structures in this area and further investigate the sources of other reflections (including R3). While a longer single profile would have provided better results and allowed deeper imaging, the study was

constrained by the available recording system we have (48 channel recording system) and the limited budget to hire a suitable seismic system. In addition to this study, other seismic profiles are being processed and the results will be integrated with the GPR data collected along the same profiles to constrain the geological interpretation.

Given the cost-effective nature of the instruments used and the limitation posed by mine infrastructure to properly design in-mine seismic surveys, the results demonstrate that in-mine seismic surveys can be an asset for mineral exploration and mining. Furthermore, these experimental surveys are considered to be cost-effective as the approach was approximately > 60% cheaper than if the survey was acquired by commercial contractors on surface (assuming that there would be no infrastructure limitations, environmental and permitting issues) using more expensive and heavier geophysical equipment (such as vibroseis trucks and 100s of receives on surface).

CONCLUSIONS

In-mine seismic experiments were conducted at Maseve underground mine to image the host rocks, geological structures and the platinum deposits. The surveys involved careful planning through mine visits and using mine geological models and borehole data. This project is a joint effort between South African academic, research, government, and mining industry institutions. While the results of the experiments are encouraging considering they were conducted inside underground mine tunnels in structurally complex hard rock mining environment, the survey designs and processing of the data were challenging due to: flooded mining tunnels causing issues with land streamer sensor-ground coupling; the hard rock environment making it difficult to plant geophones (cabled); loose tunnel hangingwall limiting the use of a heavier energy sources; and fractured tunnel walls and mine infrastructure producing complicated wave field characteristics (e.g., tunnel guided waves) that are difficult to handle in a 2D scenario.

We demonstrate that the seismic method can be used inside mine tunnels to delineate geological features associated with mineral deposits and improve mining. The processing of the in-mine seismic data provided insight on the location of the MR and UG2 below the mine tunnel, and an additional potential resource below UG2. Despite the challenges faced in the design and processing of the data, the target MR and UG2 orebodies have been imaged with confidence, supported by the geological model. Synthetic data constrained our seismic interpretations, although the model can be improved with more borehole data to constrain the targeted mineralizations. The reported data are only a portion of the full dataset, not including seismic and GPR profiles that are nearly

perpendicular to the reported merged profiles. Exploitation of the full dataset will enable characterization of both the MR and the UG2 in detail. The study forms a pilot concept for the mining industry to utilize in-mine seismics development and mine planning. This survey set-up is cost-effective because it uses an affordable energy source and land streamer, which do not require extensive planning and mobilization.

Acknowledgements

This study was sponsored by the Mandela Mining Precinct. Mandela Mining Precinct has received funding from the Department of Science and Innovation (DSI) together with Minerals Council of South Africa. We thank the staff of Maseve platinum mine, especially Sipho Sithole, for the help during mine visit and data acquisition. Michelle Pienaar for the coordination and management of the project. PhD and Masters students from the University of the Witwatersrand are thanked for their help during data acquisition. HiSeis Pty Ltd. and Petrosys are highly appreciated for sponsoring the licences for Globe Claritas™ processing software. We also thank Tesseral™ Technologies Inc. for supporting us with Tesseral software licences. Finally, we would like to thank the Associate Editor and two anonymous reviewers for providing constructive criticism in their reviews, which improved the quality of this manuscript.

List of Figures

Figure 1: *(a) Geological map of the Bushveld Complex (modified from Cawthorn, 2015) showing the location of the Maseve mine site. (b) Map of the Maseve mine showing the location of the study area at the North Shaft and the Surrounding mines that are used for seismic surveys. (c) Stratigraphic column of the Critical zone showing the chromitite layers and Merensky Reef (MR). RBPM: Royal Bafokeng Platinum Mine; UG: Upper Group; MG: Middle Group; LG: Lower Group.*

Figure 2*: (a) Map view of the Maseve mine surface workings and underground working indicating the seismic profile (black) collected. (b) Underground mine plans, showing the location of the seismic profiles (red) and geological structures such as fault (blue) and dolerite dyke (green) for in-mine seismic experiments. (c) A schematic 3D geological model of the study area, showing the Merensky Reef (MR), Upper Group 2 reef (UG2) and the incline tunnel (red) (the green arrow is pointing to the south). The position of the seismic line is indicated along the incline tunnel. BH1:*

Borehole 1; BH2: Borehole 2; P1: Profile 1, P2 – P 4: Profile 2 to profile 4; P5: Profile 5; P6: Profile 6; P7: Profile 7.

***Figure 3**: Stratigraphic column derived from borehole 1 (BH1) of Maseve mine. Reflection coefficients were derived from the acoustic impedance, and synthetic seismograms were generated using the reflection coefficient and a Ricker wavelet (130 Hz). Generated reflections are associated with the two major reefs (Merensky Reef and UG2). The impedance contrast of the Merensky Reef and the top layer is high, due to the water saturated top layer that results in relatively low velocities in norite rocks. The acoustic impedance of the UG2 and the surrounding rock is typically high compared to that of the Merensky Reef (MR) (see Manzi et al., 2018). UG2: Upper Group 2.*

***Figure 4:** Geological/finite difference model at the Maseve mine. The model shows the two-target mineralizations (MR and UG2) and geological structures (fault and dyke). The velocity and density of the rocks are noted. The receiver (brown) and shot (red) positions are shown, together with the acquisition direction (ENE-WSW) over an incline. The boreholes used for the model as shown (purple) MRHW: Merensky Reef hangingwall (Weathered Anorthosite; MR: Merensky Reef (orthopyroxenite); MRFW: Merensky footwall (norite); UG2HW: Upper Group 2 hangingwall (feldspathic-pyroxenite); UG2: Upper Group 2 (chromitite); UG2FW: Upper Group 2 footwall (pegmatoidal-pyroxenite); msl: mean sea level; BH: Borehole.*

***Figure 5**: Shot gathers examples from P5 (see Fig. 2b) first shot and middle shot, with their frequency spectra Shot gathers highlight clear reflections marked by red arrows. (a and d) Show synthetic shot gathers modelled from the geological model, (b and d) show raw shot gathers, while (c and d) show processed shot gathers. (a) Clear reflection (R1: 10ms, R2: 27 ms) from the UG2 and diffractions (green) due to the dyke and fault zone. (b) Raw shot gathers with reflections overshadowed by high frequencies (black circle), air waves are indicated by black arrows and first breaks are indicated by blue arrows. The frequency spectrum has frequency ranges of 0 - 1800 Hz as a result of the sampling rate of 0.25 ms. (c) The processed shot gathers, showing clear reflections, with one of the reflections not easily identified on the synthetic gather and the raw shot gather. (d) R1 (29 ms) originates from the Merensky Reef and R2 (45 ms) originates from the UG2. The modelled dyke and fault zone disturb R2 (red circle). (e) R1 at 20 ms, R2 at 45 ms and R3 at 55 m are observed on the raw shot gather. (f) The three reflection observed (R1, R2 and R3) are enhanced after prestack filtering.*

***Figure 6**: (a) Near surface P-wave velocity model showing the upper 70 m of the incline tunnel. Black arrows indicated lower velocity zones, which are associated with geological structures intercepted alone the line. (b) Ray path model showing ray coverage of the velocity model. The white arrows indicate an area of low fold and where the three segments where merged. msl: mean sea level.*

***Figure 7**: Comparison of unmigrated (time) stack (a) and depth stack (b) sections. Clear reflections (shown with black arrows) are more prominent at the center of the sections. Time stack section shows strong reflections at 20 ms (black), which correspond to 55 m depth in (b), whilst the dipping reflections (green arrows) at about 45 ms correspond to 124 m on the depth section. Third reflection (red arrows) is shown at 55 ms and is expected at depth 151 m.*

***Figure 8:** Depth-converted migrated seismic section; red outline shows the focus area where borehole 1 and 2 are overlaid. (a) Migrated stack section of P5 - P7 with (b) borehole 1 and synthetic seismogram overlaid (BH1; see Fig. 2). Reflection R1 correlates with the Merensky Reef (MR) and reflection R2 correlates with UG2. The arrows mark the identified reflector detailed in the text. (c) Borehole 2 correlated with the migrated section.*

***Figure 9:** Interpreted migrated section (in depth). The Merensky Reef (MR) reflector marked with dotted lines (R1), UG2 is marked with dashed line (R2). Third reflection marked with a solid line is linked with the UG1. The reflections are not continuous at areas of low fold. The reflector is displaced by a combination of normal and reverse faults (purple solid lines). Dashed lines (green) are the interpreted dykes, whilst the red dashed line is the position of the dyke and fault zone (see Fig. 4). R1 is bent (grey dashed line) between CDP 160 to 190, which is interpreted as a fold, while the brown dotted lines represent an interpreted Iron Rich Ultramafic Pegmatite (IRUP).*

***Figure 10:** Depth-converted migrated seismic section plotted in 3D view together with the mine tunnel around 550 m below Earth's surface. (a) Correlation between the seismic section and borehole intersections of the MR (red) and UG2 (blue). (b) Correlation between the seismic reflections (R1 and R2) with MR (grey, red, and blue surface) and UG2 (green contoured surface) mine orebodies. (c) Seismic section together with interpreted and mine modelled faults and dykes overlaid. The Rapetsoa Fault Zone (RFZ) is shown in blue, crosscutting the mineralizations (MR, UG2 and R3). (d) Seismic section with boreholes, Merensky Reef (MR) and UG2 mine orebodies, structural interpretations (faults and dykes). The green arrow is pointing to the south.*

3620

REFERENCES

Ahmadi, O., Koyi, H., Juhlin, C., & Gessner, K. 2016. Seismic signatures of complex geological structures in the Cue-Weld Range area, Murchison domain, Yilgarn Craton, Western Australia. *Tectonophysics*, *689*, 56–66. https://doi.org/10.1016/j.tecto.2016.02.020

Basson, I. J. 2019. Cumulative deformation and original geometry of the Bushveld Complex. *Tectonophysics*, *750*, 177–202. https://doi.org/10.1016/j.tecto.2018.11.004

Brodic, B., Malehmir, A., & Juhlin, C. 2017. Delineating fracture zones using surface-tunnel-surface seismic data, P-S, and S-P mode conversions. *Journal of Geophysical Research: Solid Earth*, *122*(7), 5493–5516. https://doi.org/10.1002/2017JB014304

Brodic, B., Malehmir, A., Pacheco, N. B. M., Juhlin, C., Carvalho, J., Dynesius, L., et al. 2021. Innovative seismic imaging of VMS deposits, Neves-Corvo, Portugal: Part I - In-mine array. *Geophysics*, 1–76. https://doi.org/10.1190/geo2020-0565.1

Buchanan, P. C., & Reimold, W. U. 1998. Studies of the Rooiberg Group, Bushveld Complex, South Africa: No evidence for an impact origin. *Earth and Planetary Science Letters*, *155*(3–4), 149–165. https://doi.org/10.1016/S0012-821X(97)00216-1

Campbell, G. 2011. Exploration geophysics of the Bushveld Complex in South Africa. *The Leading Edge*, *30*(6), 622–638. https://doi.org/10.1190/1.3599148

Cawthorn, R. G. 2015. The Bushveld Complex, South Africa. In B. Charlier, O. Namur, R. Latypov, & C. Tegner (Eds.), *Layered Intrusions* (pp. 517–587). Dordrecht: Springer Netherlands. https://doi.org/10.1007/978-94-017-9652-1_12

Cawthorn, R.G., & Webb, S. J. 2001. Connectivity between the western and eastern limbs of the Bushveld Complex. *Tectonophysics*, *330*(3–4), 195–209. https://doi.org/10.1016/S0040-1951(00)00227-4

Chistyakova, S., Latypov, R., & Youlton, K. 2019. Multiple Merensky Reef of the Bushveld Complex, South Africa. *Contributions to Mineralogy and Petrology*, *174*(3), 26. https://doi.org/10.1007/s00410-019-1562-x

Donoso, G. A., Malehmir, A., Brodic, B., Pacheco, N., Carvalho, J., & Araujo, V. 2021. Innovative seismic imaging of VMS deposits, Neves-Corvo, Portugal: Part II - Surface Array. *Geophysics*, 1–39. https://doi.org/10.1190/geo2020-0336.1

Eales, H. V., & Cawthorn, R. G. 1996. The Bushveld Complex. In *Developments in Petrology* (Vol. 15, pp. 181–229). *Elsevier*. https://doi.org/10.1016/S0167-2894(96)80008-X

Guo, J., & Luo, C. 2014. Application of tunnel seismic image approach to the advanced geological prediction for tunnel. *Journal of Multimedia*, *9*(7), 879–886. https://doi.org/10.4304/jmm.9.7.879-886

Hunt, E., Latypov, R., & Horváth, P. 2018. The Merensky Cyclic Unit, Bushveld Complex, South Africa: Reality or Myth? *Minerals*, *8*(4), 144. https://doi.org/10.3390/min8040144

Kinnaird, J. A. 2005. The Bushveld Large Igneous Province, Review Paper. *University of the Witwatersrand, Johannesburg*, 39 pp. Retrieved 11 November, 2021 from http://www.largeigneousprovinces.org/sites/default/files/BushveldLIP.pdf

Ledwaba, L. S. 2012, February 15. Seismic damage mechanism at impala platinum mine (Msc). *University of the Witwatersrand, Johannesburg.*

Lee, C. A. 1996. A Review of Mineralization in the Bushveld Complex and some other Layered Intrusions. In *Developments in Petrology* (Vol. 15, pp. 103–145). Elsevier. https://doi.org/10.1016/S0167-2894(96)80006-6

Malehmir, A., Durrheim, R., Bellefleur, G., Urosevic, M., Juhlin, C., White, D. J., et al. 2012. Seismic methods in mineral exploration and mine planning: A general overview of past and present case histories and a look into the future. *Geophysics*, *77*(5), WC173–WC190. https://doi.org/10.1190/geo2012-0028.1

Malehmir, A., Andersson, M., Lebedev, M., Urosevic, M., & Mikhaltsevitch, V. 2013. Experimental estimation of velocities and anisotropy of a series of Swedish crystalline rocks and ores: Velocities and anisotropy of a series of crystalline rocks and ores. *Geophysical Prospecting*, *61*(1), 153–167. https://doi.org/10.1111/j.1365-2478.2012.01063.x

Malehmir, A., B. Bergman, B. Andersson, R. Sturk, and M. Johansson, 2018. Seismic imaging of dyke swarms within the Sorgenfrei–Tornquist Zone (Sweden) and implications for thermal energy storage: Solid Earth, **9**, 1469–1485.

Manzi, M. S. D., K. A. A. Hein, R. J. Durrheim, and N. King, 2014, The Ventersdorp Contact Reef model in the Kloof Gold Mine as derived from 3D seismics, geological mapping and exploration borehole datasets: International Journal of Rock Mechanics and Mining Sciences, **66**, 97–113.

Manzi, M., Durrheim, R., & Webb, S. 2017. 3D seismic attributes for platinum exploration and mine planning in the Bushveld Complex (South Africa). In *International Geophysical*

Conference, Qingdao, China, 17-20 April 2017 (pp. 665–668). Qingdao, China: Society of Exploration Geophysicists and Chinese Petroleum Society. https://doi.org/10.1190/IGC2017-169

Manzi, M., Malehmir, A., & Durrheim, R. 2019. The Value of Seismics in Mineral Exploration and Mine Safety. In *81st EAGE Conference and Exhibition 2019* (pp. 1–5). London, UK,: European Association of Geoscientists & Engineers. https://doi.org/10.3997/2214-4609.201901667

Manzi, M. S. D., Durrheim, R. J., Hein, K. A. A., & King, N. 2012. 3D edge detection seismic attributes used to map potential conduits for water and methane in deep gold mines in the Witwatersrand basin, South Africa. *Geophysics*, *77*(5), WC133–WC147. https://doi.org/10.1190/geo2012-0135.1

Manzi, M. S. D., Cooper, G. R. J., Malehmir, A., & Durrheim, R. J. 2020. Improved structural interpretation of legacy 3D seismic data from Karee platinum mine (South Africa) through the application of novel seismic attributes. *Geophysical Prospecting*, *68*(1), 145–163. https://doi.org/10.1111/1365-2478.12900

Muller, C. J., & Visser. 2010. Resource cut estimation of the western Bushveld joint venture (WBJV) located on the western limb of the Bushveld igneous complex, South Africa (p. 67). *Minxcon*. Retrieved 11 November, 2021 from http://s1.q4cdn.com/169714374/files/doc_downloads/Technical-Report-WBJV-Project-3-10-08-31-filed-10-10-05-Certificate.pdf

Nex, P. A., Ingle, L. J., Kinnaird, J. A., van der Vyver, B. A., & Cawthorn, R. G. 1998. A new stratigraphy for the Main Zone of the Bushveld Complex, in the Rustenburg area. *South African Journal of Geology*, *101*(3), 215–223.

Nkosi, N. Z., Manzi, M. S. D., Drennan, G. R., & Yilmaz, H. 2017. Experimental measurements of seismic velocities on core samples and their dependence on mineralogy and stress; Witwatersrand Basin (South Africa). *Studia Geophysica et Geodaetica*, *61*(1), 115–144. https://doi.org/10.1007/s11200-016-0804-x

Scheiber-Enslin, S. E., & Manzi, M. 2018. Integration of 3D reflection seismics and magnetic data for deep platinum mine planning and risk mitigation: a case study from Bushveld Complex, South Africa. *Exploration Geophysics*, *49*(6), 928–939. https://doi.org/10.1071/EG17083

Seabrook, C. L. 2005. The Upper Critical and Lower Main Zones of the eastern Bushveld Complex, Ph.D. Thesis, *University of the Witwatersrand, Johanesburg,* South Africa. p284.

Sehoole, L., Manzi, M. S. D., Zhang, S. E., & Bourdeau, J. E. 2020. An innovative seismic and statistical approach to understand 3D magmatic structures and ore deposits in the western Bushveld Complex, South Africa. *Ore Geology Reviews*, *126*, 103784. https://doi.org/10.1016/j.oregeorev.2020.103784

Singh, B., Górszczyk, A., Malehmir, A., Hlousek, F., Buske, S., Sito, Ł., & Marsden, P. 2020. 3D Velocity Model Building in Hardrock Environment Using FWI: A Case Study from Blötberget Mine, Sweden. In *NSG2020 3rd Conference on Geophysics for Mineral Exploration and Mining* (pp. 1–5). : European Association of Geoscientists & Engineers. https://doi.org/10.3997/2214-4609.202020122

Stevenson, F., & Durrheim, R. J. 1997. Reflection seismics for gold, platinum and base metal exploration and mining in southern Africa, In *Proceedings of Exploration 97: 4th Decennial International Conference on Mineral Exploration*, G. Gubins (ed.), 391-398.

Stevenson, F., Higgs, R. M. A., & Durrheim, R. J. 2003. Seismic imaging of precious and base metal deposits in southern Africa, Chapter 9: In *Hardrock Seismic Exploration*, D Eaton, M Salisbury and B Milkereit (editors), Developments in Geophysics Series, Society of Exploration Geophysicists, Houston, pp. 141-156.

Kgarume, T.E., Van Schoor, A.M. & Nontso, Z. 2019. The use of 3D ground penetrating radar to mitigate the risk associated with falls of ground in Bushveld Complex platinum mines. The Journal of the Southern African Institute of Mining and Metallurgy, vol. 119, pp. 973-982

Trickett, J. C., Duweke, W. A., & Kock, S. 2004. Three-dimensional reflection seismics: worth its weight in platinum. *Journal of the South African Institute of Mining and Metallurgy*. p105

Webb, S. J., Cawthorn, R. G., Nguuri, T., & James, D. 2004. Gravity modeling of Bushveld Complex connectivity supported by Southern African Seismic Experiment results. *South African Journal of Geology*, *107*(1–2), 207–218. https://doi.org/10.2113/107.1-2.207

Westgate, M., Manzi, M. S. D., James, I., & Harrison, W. 2020. New insights from legacy seismic data: reprocessing of legacy 2D seismic data for imaging of iron-oxide mineralization near Sishen Mine, South Africa. *Geophysical Prospecting*, *68*(7), 2119–2140. https://doi.org/10.1111/1365-2478.12996

Yilmaz, O., Yilmaz, Ö., & Doherty, S. M. 2001. Seismic Data Analysis: Processing, Inversion, and Interpretation of Seismic Data. *Society of Exploration Geophysicists*. Retrieved from https://books.google.co.za/books?id=ceu1x3JqYGUC

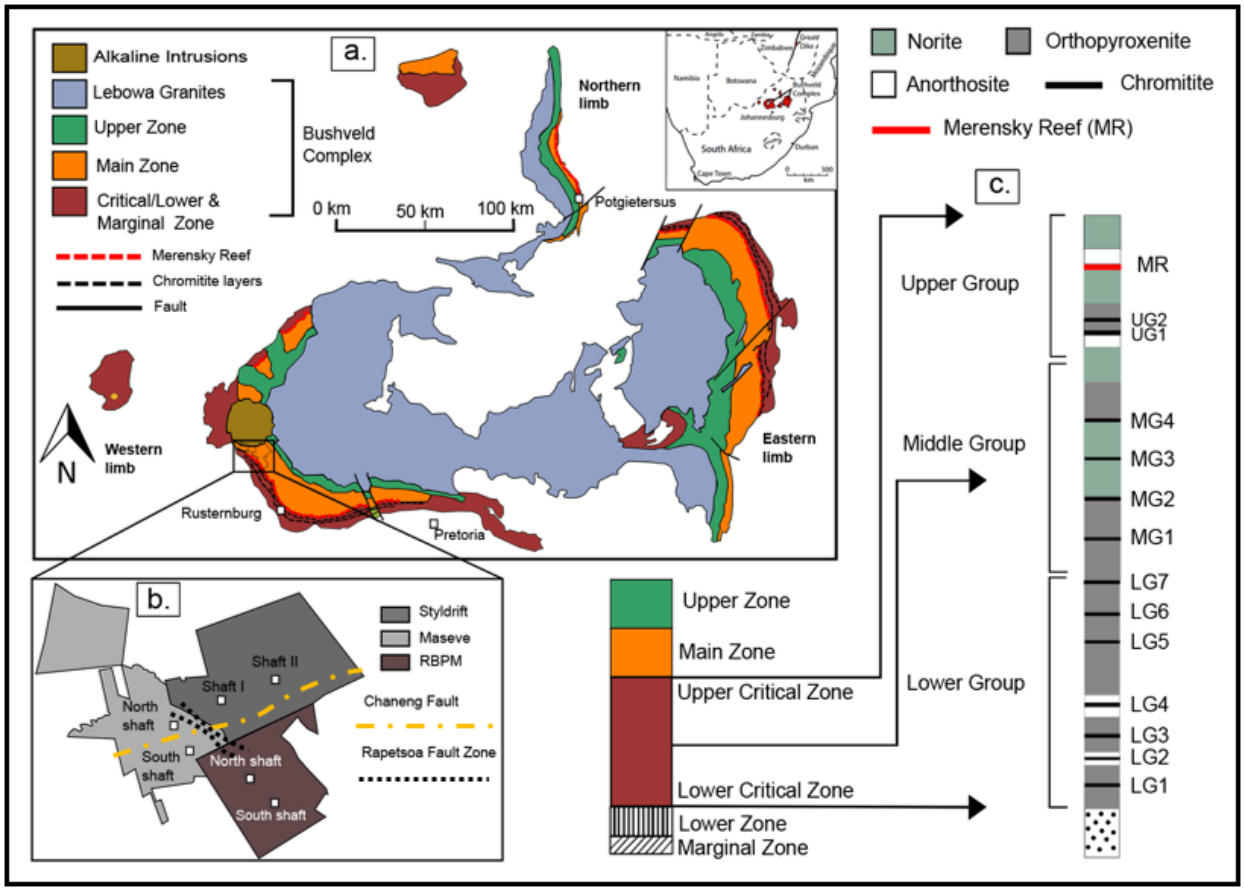
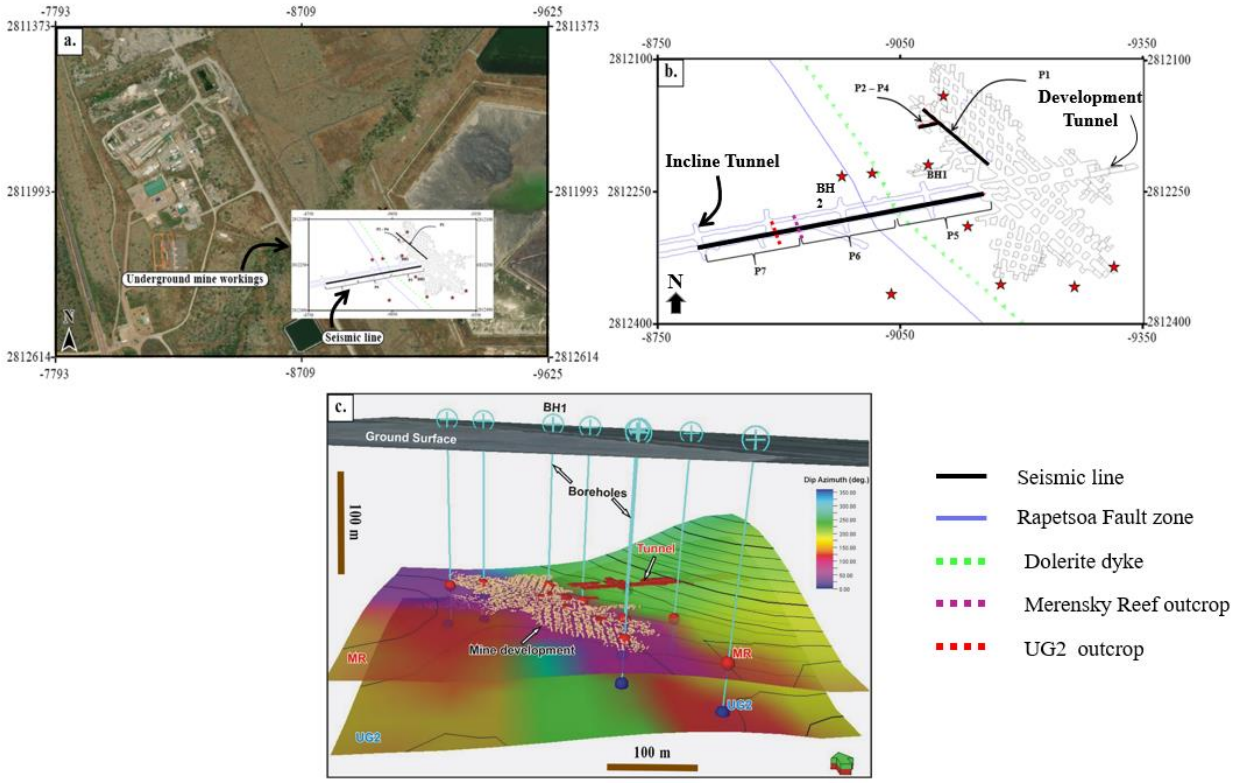


Figure 1: *(a) Geological map of the Bushveld Complex (modified from Cawthorn, 2015) showing the location of the Maseve mine site. (b) Map of the Maseve mine showing the location of the study area at the North Shaft and the Surrounding mines that are used for seismic surveys. The orange dashed lines show the ENE – WSW trending Chaneng fault, while the black dotted lines show the NE-NW trending Rapetsoa Fault Zone (RFZ). (c) Stratigraphic column of the Critical zone showing the chromitite layers and Merensky Reef (MR). RBPM: Royal Bafokeng Platinum Mine; UG: Upper Group; MG: Middle Group; LG: Lower Group.*



3757

3758 ***Figure 2****: (a) Map view of the Maseve mine surface workings and underground working indicating*
3759 *the seismic profile (black) collected. (b) Underground mine plans, showing the location of the*
3760 *seismic profiles (red) and geological structures such as fault (blue) and dolerite dyke (green) for*
3761 *in-mine seismic experiments. (c) A schematic 3D geological model of the study area, showing the*
3762 *Merensky Reef (MR), Upper Group 2 reef (UG2) and the incline tunnel (red) (the green arrow is*
3763 *pointing to the south). The position of the seismic line is indicated along the incline tunnel. BH1:*
3764 *Borehole 1; BH2: Borehole 2; P1: Profile 1, P2 – P 4: Profile 2 to profile 4; P5: Profile 5; P6:*
3765 *Profile 6; P7: Profile 7.*

3766

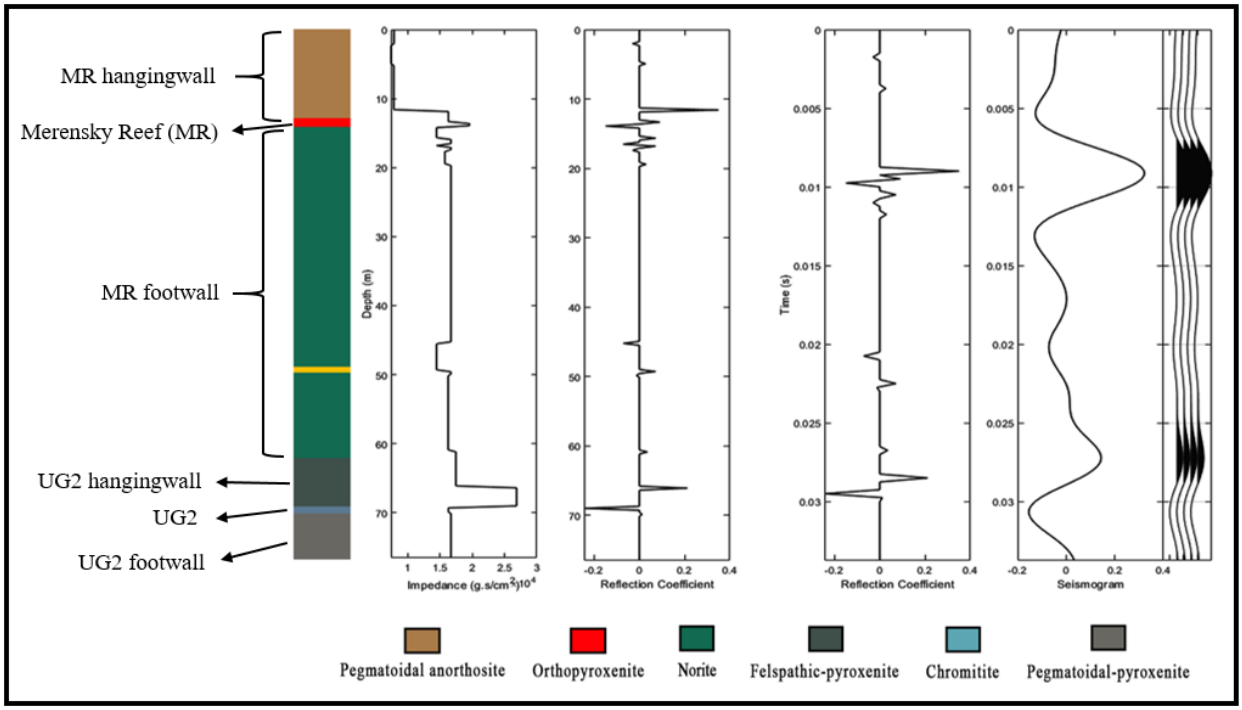


***Figure 3**: Stratigraphic column derived from borehole 1 (BH1) of Maseve mine. Reflection coefficients were derived from the acoustic impedance, and synthetic seismograms were generated using the reflection coefficient and a Ricker wavelet (130 Hz). Generated reflections are associated with the two major reefs (Merensky Reef and UG2). The impedance contrast of the Merensky Reef and the top layer is high, due to the water saturated top layer that results in relatively low velocities in norite rocks. The acoustic impedance of the UG2 and the surrounding rock is typically high compared to that of the Merensky Reef (MR) (see Manzi et al., 2018). UG2: Upper Group 2.*

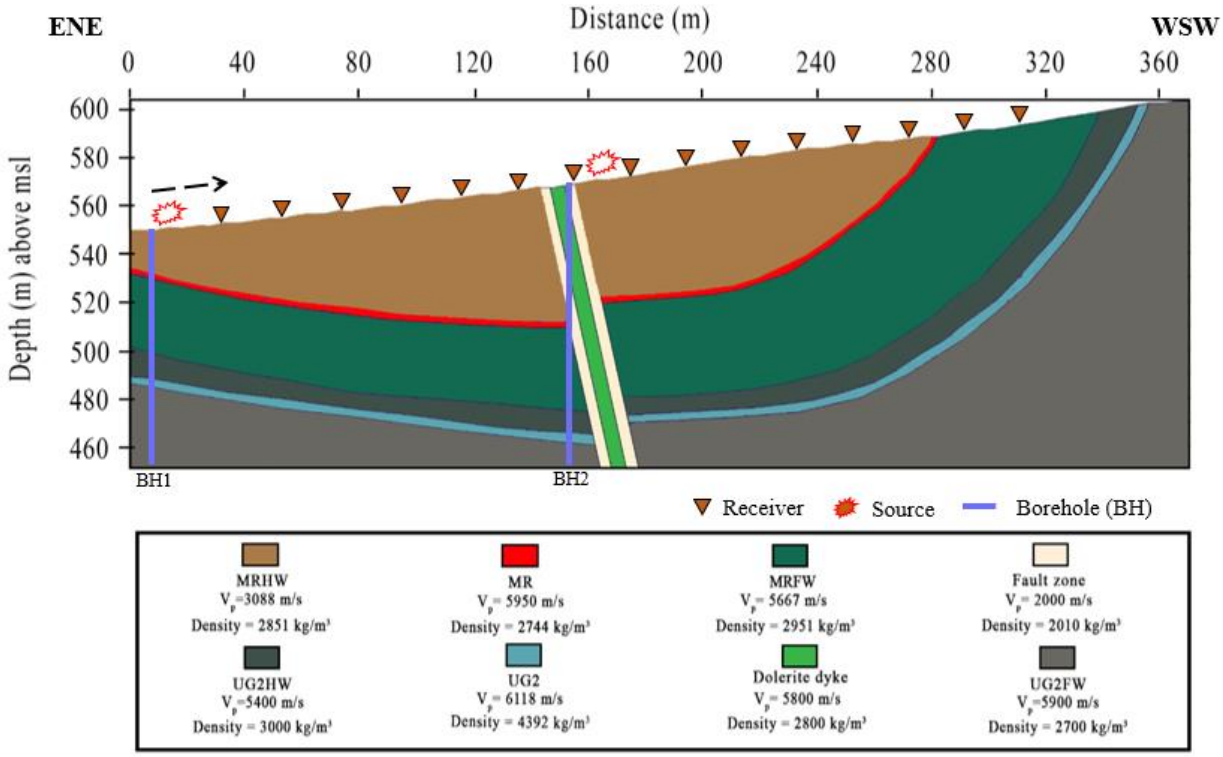


Figure 4: *Geological/finite difference model at the Maseve mine. The model shows the two-target mineralizations (MR and UG2) and geological structures (fault and dyke). The velocity and density of the rocks are noted. The receiver (brown) and shot (red) positions are shown, together with the acquisition direction (ENE-WSW) over an incline. The boreholes used for the model as shown (purple) MRHW: Merensky Reef hangingwall (Weathered Anorthosite; MR: Merensky Reef (orthopyroxenite); MRFW: Merensky footwall (norite); UG2HW: Upper Group 2 hangingwall (feldspathic-pyroxenite); UG2: Upper Group 2 (chromitite); UG2FW: Upper Group 2 footwall (pegmatoidal-pyroxenite); msl: mean sea level; BH: Borehole.*

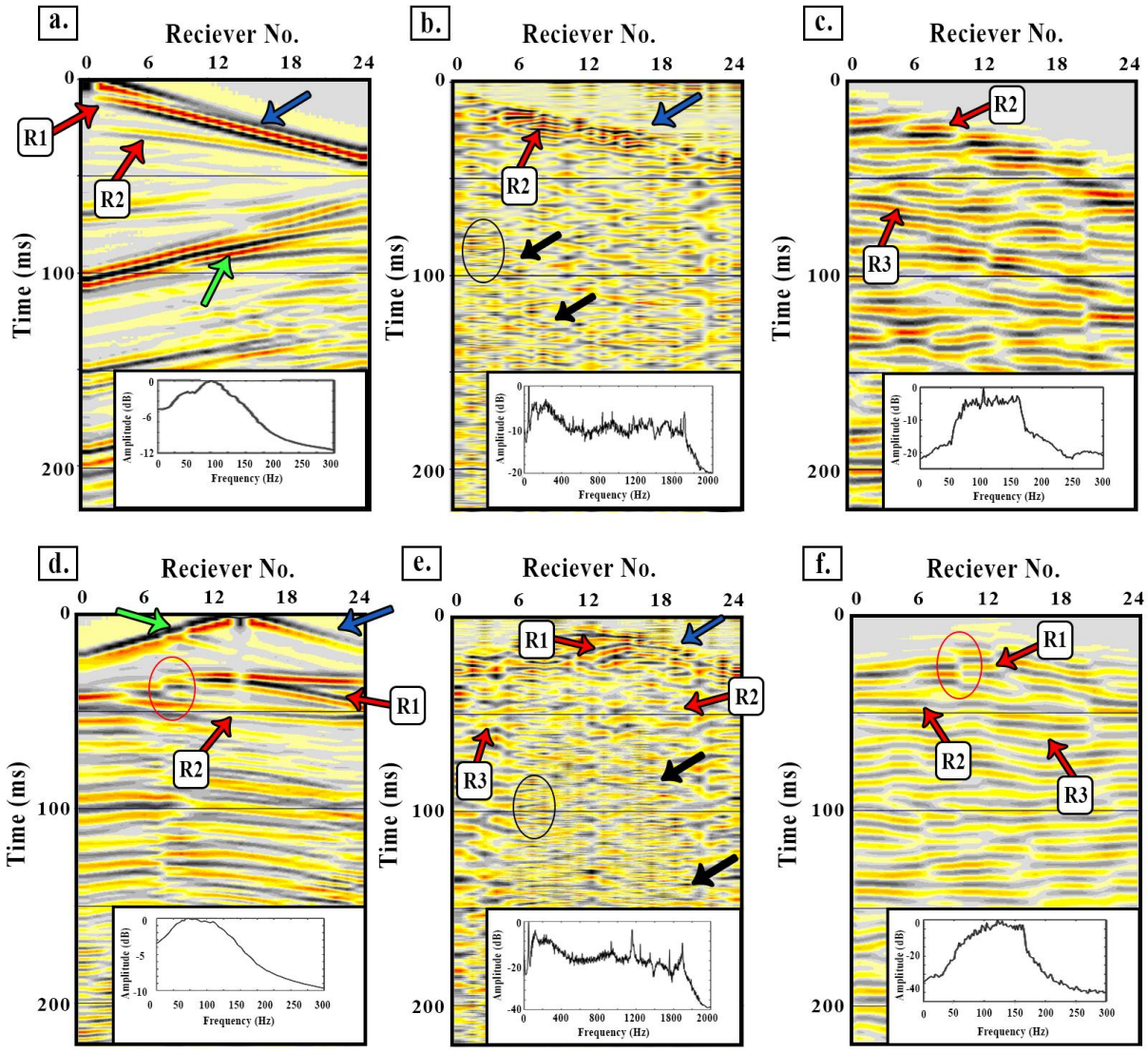


***Figure 5**: Shot gathers examples from P5 (see Fig. 2b) first shot and middle shot, with their frequency spectra Shot gathers highlight clear reflections marked by red arrows. (a and d) Show synthetic shot gathers modelled from the geological model, (b and d) show raw shot gathers, while (c and d) show processed shot gathers. (a) Clear reflection (R1: 10ms, R2: 27 ms) from the UG2 and diffractions (green) due to the dyke and fault zone. (b) Raw shot gathers with reflections overshadowed by high frequencies (black circle), air waves are indicated by black arrows and first breaks are indicated by blue arrows. The frequency spectrum has frequency ranges of 0 - 1800 Hz as a result of the sampling rate of 0.25 ms. (c) The processed shot gathers, showing clear reflections, with one of the reflections not easily identified on the synthetic gather and the raw shot gather. (d) R1 (29 ms) originates from the Merensky Reef and R2 (45 ms) originates from the UG2.*

The modelled dyke and fault zone disturb R2 (red circle). (e) R1 at 20 ms, R2 at 45 ms and R3 at 55 m are observed on the raw shot gather. (f) The three reflection observed (R1, R2 and R3) are enhanced after prestack filtering.

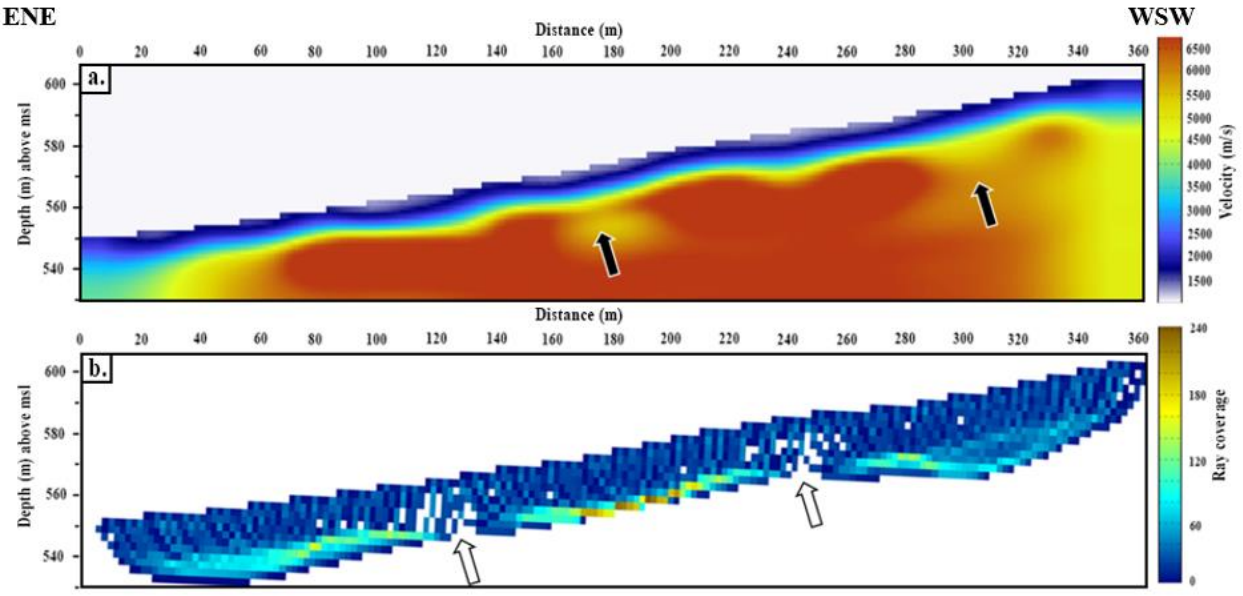


Figure 6*: (a) Near surface P-wave velocity model showing the upper 70 m of the incline tunnel. Black arrows indicated lower velocity zones, which are associated with geological structures intercepted alone the line. (b) Ray path model showing ray coverage of the velocity model. The white arrows indicate an area of low fold and where the three segments where merged. msl: mean sea level.*

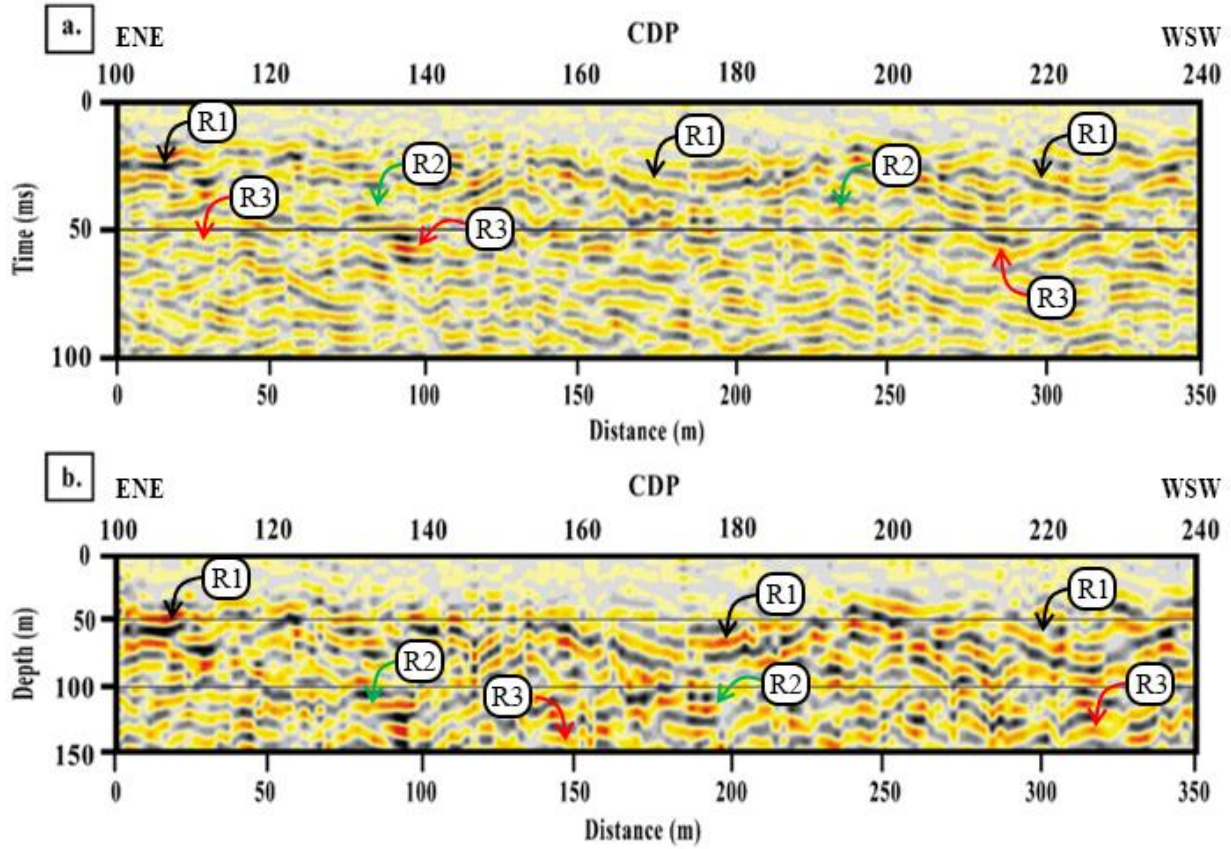


***Figure 7**: Comparison of unmigrated (time) stack (a) and depth stack (b) sections. Clear reflections (shown with black arrows) are more prominent at the center of the sections. Time stack section shows strong reflections at 20 ms (black), which correspond to 55 m depth in (b), whilst the dipping reflections (green arrows) at about 45 ms correspond to 124 m on the depth section. Third reflection (red arrows) is shown at 55 ms and is expected at depth 151 m.*

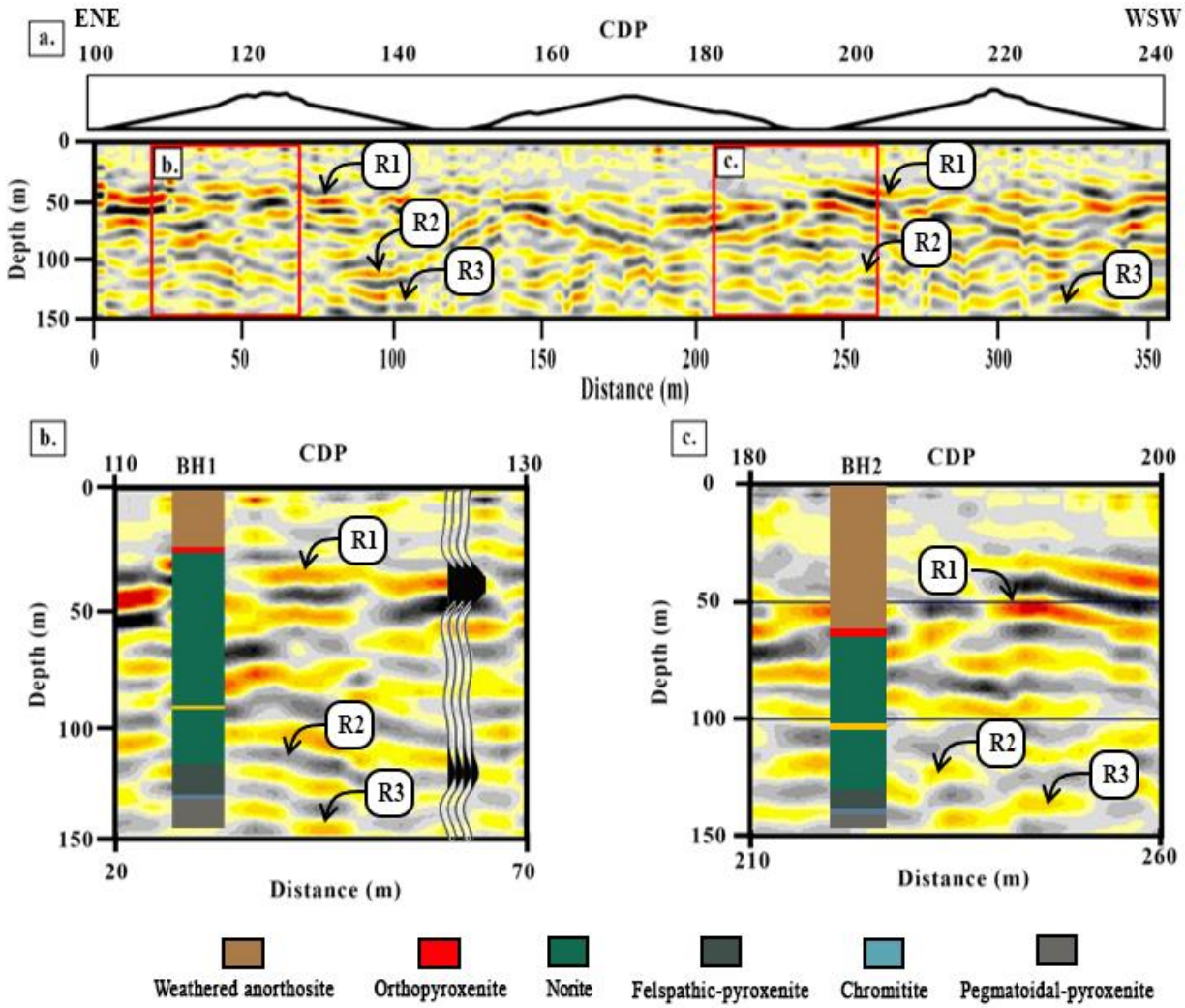
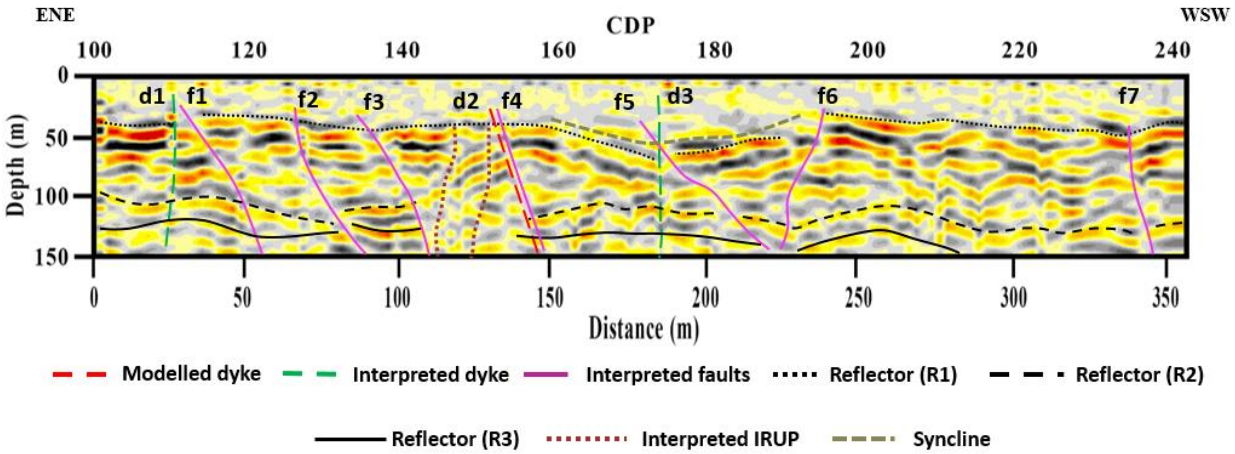


Figure 8: *Depth-converted migrated seismic section; red outline shows the focus area where borehole 1 and 2 are overlaid. (a) Migrated stack section of P5 - P7 with (b) borehole 1 and synthetic seismogram overlaid (BH1; see Fig. 2). Reflection R1 correlates with the Merensky Reef (MR) and reflection R2 correlates with UG2. The arrows mark the identified reflector detailed in the text. (c) Borehole 2 correlated with the migrated section.*



3822

3823 ***Figure 9:*** *Interpreted migrated section (in depth). The Merensky Reef (MR) reflector marked with*
3824 *dotted lines (R1), UG2 is marked with dashed line (R2). Third reflection marked with a solid line*
3825 *is linked with the UG1. The reflections are not continuous at areas of low fold. The reflector is*
3826 *displaced by a combination of normal and reverse faults (purple solid lines). Dashed lines (green)*
3827 *are the interpreted dykes, whilst the red dashed line is the position of the dyke and fault zone (see*
3828 *Fig. 4). R1 is bent (grey dashed line) between CDP 160 to 190, which is interpreted as a fold, while*
3829 *the brown dotted lines represent an interpreted Iron Rich Ultramafic Pegmatite (IRUP).*

3830

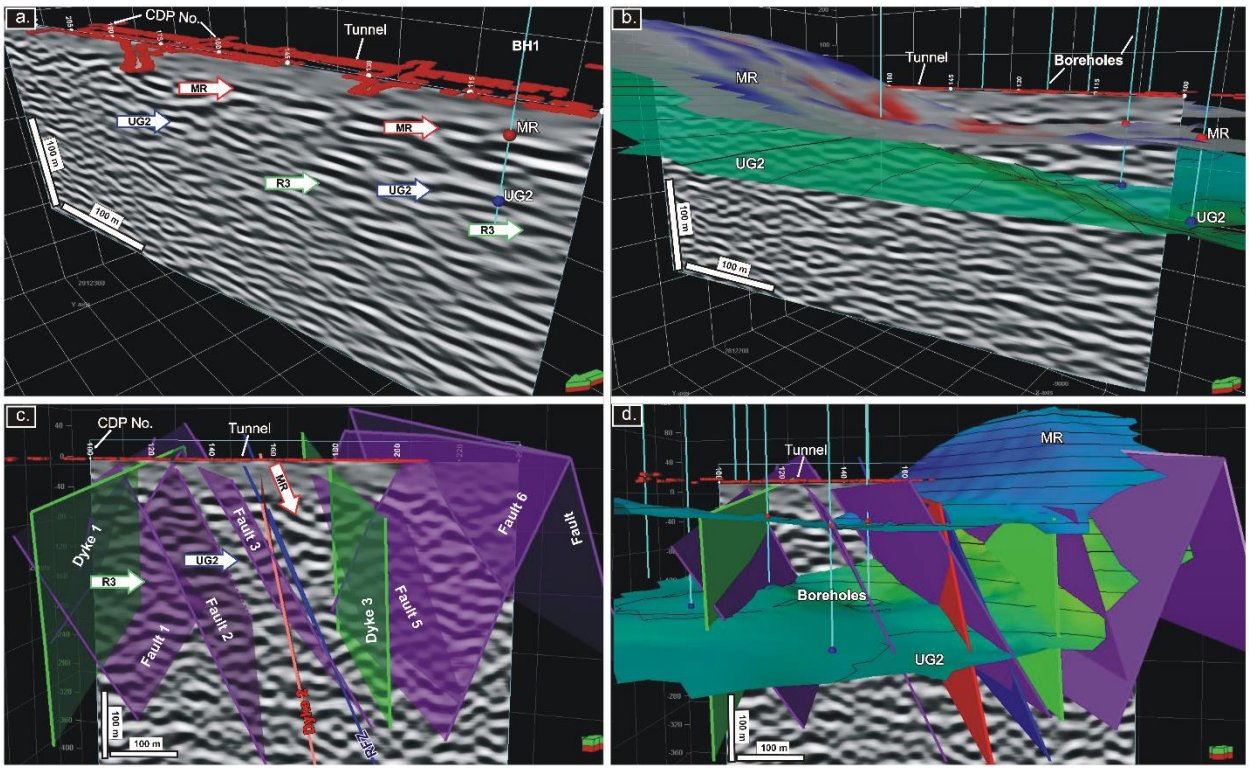


Figure 10: *Depth-converted migrated seismic section plotted in 3D view together with the mine tunnel around 550 m below Earth's surface. (a) Correlation between the seismic section and borehole intersections of the MR (red) and UG2 (blue). (b) Correlation between the seismic reflections (R1 and R2) with MR (grey, red, and blue surface) and UG2 (green contoured surface) mine orebodies. (c) Seismic section together with interpreted and mine modelled faults and dykes overlaid. The Rapetsoa Fault Zone (RFZ) is shown in blue, crosscutting the mineralizations (MR, UG2 and R3). (d) Seismic section with boreholes, Merensky Reef (MR) and UG2 mine orebodies, structural interpretations (faults and dykes). The green arrow is pointing to the south.*

List of tables

Table 1: *Physical property measurements of Bushveld Complex rocks. Velocity and density of feldspathic and pegmatoidal pyroxenite are adapted from Manzi et al. 2020.*

Rock type	v (m/s)	ρ (kg/m^3)
Merensky Reef (orthopyroxenite)	5950	2744
UG2 (chromitite)	6118	4392
Anorthosite (pegmatoidal)	5530	2947
Anorthosite (weathered)	3088	2851
Norite	5667	2951
Feldspathic-pyroxenite	5400	3000
Pegmatoidal pyroxenite	5900	2700

v = P-wave velocity ρ = density

***Table 2**: In mine seismic acquisition parameters at Maseve mine.*

Line	P1	P2	P3	P4	P5	P6	P7
Number of receivers	24	24	24	15	24	24	24
Profile length	115	26	26	28 m	115 m	115 m	115 m
Direction	SW-NE	On Pillar	SE-NW	On Pillar	SE-NW		
Recording length	500 ms	300 ms	150 ms	150 ms	500 ms		
Sample interval	0.25 ms						
Vertical stacks	4						
Source spacing	5 m	2 m			5 m		
Source type	5 kg Sledgehammer						
Receiver spacing	5 m	2 m	1 m	2 m	5 m		
Geophone frequency	4.5 Hz	4.5 Hz	4.5 Hz 14 Hz	4.5 Hz	4.5 Hz		

Table 3: Processing steps applied to Maseve mine, South Africa in-mine seismic dataset

Pre-conditioning		**Parameters**
Create coordinates	✓	Linear and spline interpolation
Create SPS files	✓	Merge the coordinates of P5 – P7.
Processing		**PARAMETERS**
Data input + reformat	✓	From SEGD to SEGY
Geometry assignment + CDP bin	✓	Sources and receivers assigned to each trace + CDP size 2.5 m
Trace editing	✓	Kill noisy traces
First break picking	✓	Automatic, manual picking
Floating datum statics correction	✓	Fixed datum elevation: 602 m (below surface) Replacement velocity: 4000 m/s
Refraction static correction	✓	Two layers model based on the first break picking. Root-mean square error 1.45- 2 ms
Trace muting	✓	Top mute using first breaks
Band pass filtering	✓	50-60-160-170 Hz
Automatic gain control	✓	Window: 50 ms
Balance	✓	500 ms
F-k filtering	✓	Surgical muting, dip = 1.2 m/s per trace
Velocity analysis	✓	Constant velocity stack
NMO corrections	✓	5500 - 6500 m/s, stretch mute: 70%
Residual statics	✓	Repeat NMO corrections twice
DMO	✓	Kirchhoff common-offset
Stack	✓	Normal
Band pass filtering	✓	80-90-150-160 Hz
Post-stack time migration	✓	2D Kirchhoff
Time to depth conversion	✓	Constant velocity: 5500 m/s

9 DISCUSSION

Most of the gold-bearing and Platinum Group Element deposits on the Kaapvaal Craton have been discovered and mined for more than a century. Exploration studies on the craton mainly focus on mapping and imaging the deep-seated mineralisation and geological structures cross-cutting them. Therefore, new techniques for imaging deep-seated mineralisation and complex geological structures are required for future mineral exploration. This dissertation focuses on high-resolution imaging of both shallow and deep-seated mineral deposits and complex geological structures while testing the applicability of newly developed reflection seismic processing workflows on legacy data collected before their inception. Furthermore, cost-effective in-mine seismic experiments were performed at Maseve mine to image the orebody and address the limitations of reflection seismic data acquired on the surface.

Paper I presents the reprocessing results of the legacy profile acquired close to the Burnstone mine for gold-bearing horizon (UK9A) delineation. The target UK9A reef is seismically transparent because it does not have notable acoustic impedance contrast with the host rocks and it is a thin conglomerate strip with thicknesses up to 2 m. The geometry of the orebody is constrained using the hanging wall and foot wall rocks that have notable acoustic impedance contrast with the host rocks resulting in prominent reflections on the reprocessed section. The key reflections come from the near surface unconformities between the overlying low-velocity and density rocks of the Karoo sediments and the underlying high-velocity and density strata of the Ventersdorp basaltic lavas (Manzi et al., 2013; Manzi et al., 2015). These reflections are missed by the legacy migrated profile, possibly because they were not the target reflections for gold exploration as they do not host gold mineralisation. However, imaging the near surface geology is important in a hardrock environment as it hosts complex geological structures (such as dykes and sills) which can complicate mining and introduces static shifts on the reflection seismic data. The Burnstone mine was placed under care in 2012 because they encountered more than expected geological structures. Moreover, as shown by the legacy data presented in **Paper III**, the near surface Karoo Supergroup strata are associated with shallow coal mining in the eastern Witwatersrand Basin. These unconformities are clearly mapped by the Kirchhoff pre-stack depth migration compared to the Kirchhoff pre-stack time migration, demonstrating its superiority in hardrock environment. This is due to the fact that depth migration honors the lateral velocity

variation present in the hardrock environment due to the intrusion of volcanic rocks into horizontally stratified sedimentary rocks and complex tectonics (Etgen and Kumar, 2012; Manzi et al., 2012b).

The hanging wall strata of the Central Rand Group quartzites which have relatively lower densities and velocities exhibit a notable acoustic impedance contrast with the overlying Ventersdorp basaltic lavas with relatively higher densities and velocities. The resultant reflection is used as the upper limit proxy reflection for constraining the geometry of the target UK9A reef. The chloritoid shale marker is clearly mapped due to its higher density and velocity compared to the overlying foot wall Central Rand quartzites (Manzi et al., 2015). The borehole information published along the profile shows that the upper limit proxy reflection associated with the hanging wall is ~ 1 km below the surface and the lower limit proxy reflection associated with the foot wall is ~ 1.7 km below the surface. Therefore, these reflections were used to constrain the gold-bearing conglomerates of the UK9A reef between these depths.

The geological structures cross-cutting the target orebody are mapped as discontinuities on the proxy reflections associated with the hanging wall and the foot wall rocks. The dolerite sill intrusion on the Karoo sediments is clearly mapped and corresponds to the documented dimensions on previous geological studies (Pretorius, 1964; Antrobus, 1986; and Spencer, 1992) in the study area. The interpreted faults along the profile had no conclusive results from previous studies and are interpreted as moderately dipping normal and reverse faults, which are downthrown to the north and some of them are downthrown to the south. The geological model from this study corresponds to previous studies with the exception of the northern half of the profile where the strata were previously thought to be dipping, but this study shows that they are near horizontal. Major faults already documented in the literature were mapped by this study.

Paper II presents results from a reprocessed 50 km long legacy seismic profile from the western Bushveld complex. The profile is of significance because it is one of a few reflection seismic profiles traversing towards the southern edge of the centre of the Bushveld Complex. The unmigrated section of the profile was published in the late 1980s and a reprocessed post-stack time migrated section was published in the early 1990s (Du Plessis and Levitt, 1987; Odgers et al., 1993). The two publications had conflicting conclusions regarding the northern half of the profile towards the centre of the complex, with the former suggesting that the mineralized Rustenburg

Layered Suite (RLS) rocks are not present in this section and the latter suggesting they are. The presence of the platinum group element (PGE) bearing horizons of the RLS in the center of the Bushveld Complex has implications for mining in this region and connectivity between the Eastern Limb and Western Limb of the Bushveld Complex (Cawthorn and Webb, 2001).

The northern section of the profile is characterized by a low signal-to-noise ratio (SNR) which the previous studies concluded is due to the presence of out-of-plane reflections and poor source-ground coupling resulting from younger Karoo cover (Odgers et al., 1993). This thesis leverages the crooked line geometry of the legacy profile and the use of pseudo-3D coherency migration technique to confirm the presence of out-of-plane reflectivity in this region. Several studies use cross-dip correction (Larner et al., 1979) and dip moveout correction (Nedimovic and West, 2003) to reduce the effect of out-of-plane reflections on the SNR (Malehmir et al., 2017). Therefore, the application of these techniques to these legacy data can increase the SNR, and it is something to be tested in future studies.

This study is motivated by the recommendation of previous studies to use depth imaging to try and improve the SNR of the northern section of the profile. Furthermore, the study tested the applicability of the newly developed Kirchhoff-based pre-stack depth migration technique called coherency migration (CM) (Hloušek and Buske, 2016) in hardrock environment. The results from the coherency migrated southern half of the section are analogous to the previous studies (Du Plessis and Levitt, 1987; Odgers et al., 1993) with a minor improvement in the continuity of deeper reflections. In some regions, CM performed poorly compared to the conventional Kirchhoff migration, possibly because it limits the migration operator to the physically pertinent region along the traveltime isochrone. Therefore, constructing the image with constructive interference of the energy from this limited region can reduce the SNR relative to the conventional techniques which smear the energy along the entire travel time isochrone (Hloušek et al., 2015b). The northern half of the section shows improvement in the SNR compared to the previous studies (Du Plessis and Levitt, 1987; Odgers et al., 1993). Using aeromagnetic data, the presence of the magnetic dyke (Chaneng structure) is delineated in the northern half of the profile and the absence of the positive magnetic signature from the magnetite-gabbro rocks of RLS suggests possible tapering of the RLS rocks on the northern section. This tapering does not encourage mining in this region and does not

confirm the interlimb connectivity. Therefore, exploration drilling is advised to confirm these results.

The presence of the anticlinal structure towards the center of the complex is possibly due to the updoming of the basal Transvaal Supergroup rocks in the northern half of the section. This updoming is possibly the continuity of the Transvaal supergroup inlier (Crocodile River dome) beneath the younger Karoo cover suggesting an absence of the RLS rocks in this region. A comprehensive tectonic evolution along the profile is detailed on **Paper II**. To investigate the presence of out-of-plane reflectivity on the northern section of the data, a pseudo-3D migration of the data was performed. The 3D volume shows constructive interference out-of-plane suggesting the presence of out-of-plane reflectivity with no conclusive source due to the ambiguity presented by the 2.5D migration of the data.

Paper IV presents small-scale in-mine seismic experiments conducted at Maseve mine on the developmental tunnel to address the limitations of the reflection seismic data acquired on the surface. The seismic resolution limit of reflection seismic data is related to the dominant wavelength (λ), the velocity, and the dominant frequency of the data. Theoretically, by the Rayleigh criteria of the seismic vertical resolution limit, the top and bottom contact of the geological feature cannot be resolved if it is thinner than a quarter of the dominant wavelength. However, this is the case for the deep target orebodies in the Kaapvaal Craton. As a result, this thesis presents high-quality data and uses proxy reflections to constrain the geometry of the target orebodies because the data acquired from the surface deem them seismically transparent. The in-mine seismic experiments aim to directly image the PGE-bearing Merensky and UG2 horizons by bringing the seismic source and sensors closer to the target horizons (i.e., orebodies are located ~ 100 m below the tunnel floor). This provides constraints on the relative distance between the orebody and the hanging wall and the foot wall proxy reflections delineated on the legacy data.

10 CONCLUSIONS AND OUTLOOK

This thesis demonstrates different techniques to maximize the value and effectiveness of 2D legacy reflection seismic data in hardrock environment for mineral exploration through novel processing workflows. The data acquired in the 1980s covering the central Kaapvaal Craton in the Witwatersrand goldfields and Bushveld Complex have been reprocessed using Kirchhoff-based pre-stack migration workflows. The data have been integrated with conventional techniques, such as iterative static corrections, 2D acoustic finite difference numerical modelling, and aeromagnetic data for efficient delineation of gold-bearing and Platinum Group Element (PGE) deposits and cross-cutting geological structures.

Paper I aimed to delineate the gold-bearing horizons and cross-cutting geological structures in the South Rand goldfield close to the newly developed Burnstone mine through reprocessing of 2D legacy reflection seismic data. Numerical simulations produced synthetic shot gathers used to constrain the source of reflectivity associated with the gold and geological structures. Kirchhoff pre-stack time (KPreST) and depth (KPreSD) migration improved imaging of footwall and hanging wall horizons used to constrain the geometry of the orebody and geological structures missed by the legacy post-stack time migrated section. Particularly, KPreSD migration produced better continuity of reflections in a hardrock environment.

Paper II employed a newly developed focusing depth migration workflow based on the convention Kirchhoff pre-stack depth migration for imaging the PGE deposits in the Western Limb of the Bushveld Complex. The legacy data were collected on the southeastern edge of the Western Limb where the Rustenburg Layered Suite (RLS) mafic cumulate rocks are the thinnest. The profile traverses towards the centre of the complex near the Crocodile River dome, which is a Transvaal inlier, and in the northern region, the profile has an anticlinal structure characterized by a low signal-to-noise ratio (SNR). Coherency migration (CM) of the legacy data provided an improved subsurface, particularly the northern edge of the profile illuminating the anticlinal structure interpreted to be an extension of the Crocodile River dome. 3D migration of the 2D data shows evidence of out-of-plane reflection energy and aeromagnetic data imaged the dyke cross-cutting the profile and constrained the extent of the RLS magnetic rocks to the southern half of the profile.

The potential for the 2D legacy reflection seismic data in the Kaapvaal Craton has endless potential, for example, testing of new reflection seismic processing algorithms and investigating the tectonic evolution of the Kaapvaal Craton. While the ray-based pre-stack depth migration algorithms have significantly improved the resolution of these data, wave equation-based migration techniques have proven their potential in hardrock environment.

11 APPENDICES

Appendix A: Reprocessing Legacy Seismic Data for Imaging PGE Mineralisation: Case Studies from the Bushveld Complex, South Africa

Introduction

Legacy seismic data have proven their significance in mineral exploration and mine planning, and several studies (e.g., Malehmir et al., 2010; Cheraghi et al., 2011; Manzi et al., 2018; Malehmir et al., 2019; Manzi et al., 2019; Westgate et al., 2020) demonstrate their strength. The main advantages of reappraising legacy seismic data in mineral exploration are cost-efficiency, less noise from mining activities and coverage of areas that might not be accessible for acquisition of new data (Malehmir et al., 2019; Manzi et al., 2019). Furthermore, the geological information obtained from these data can be used for future mine planning and constraining acquisition parameters of new seismic surveys especially in the brownfield environment (Manzi et al., 2018; Malehmir et al., 2019).

South Africa has the largest hard rock seismic database in the world covering the Kaapvaal Craton (Manzi et al., 2019; Westgate et al., 2020). In this study, a subset of these legacy seismic data are reprocessed to image the Platinum-bearing horizons in the Bushveld Complex. The complex is the world's largest igneous intrusion (~ 64 000 Km^2) of Paleoproterozoic age (2.06 Ga) emplaced into intra-cratonic sedimentary sequences of the Transvaal Supergroup (2.7 Ga) (Cawthorn and Webb, 2001; Sehoole et al., 2020). It is divided into four lobes: the Northern, Eastern, Southern, and Western limbs (Scheiber-Enslin and Manzi, 2018).

Mineralisation within the Western limb is the target of the 53 km legacy seismic profile and has generally shallow dips (~ 20º) to the north (Fig. 1a). It consists of mafic to ultramafic cumulate rocks termed the Rustenburg Layered Suite (RLS) that have an average thickness of ~ 6 km (Scheiber-Enslin and Manzi, 2018). The RLS is divided into five zones: Marginal, Lower, Critical, Main, and Upper zones. The Marginal zone unconformably overlies the Transvaal Supergroup and is intern overlain by the Lower zone (~ 0.82 km thick). The Critical zone (~ 1.3 km thick) overlies the Lower zone and hosts most of the Platinum-Group Elements (PGEs) on sub-horizontal layers of orthopyroxenite and chromitite (Lower Critical zone), as well as cyclical units of chromitite and pyroxenite, to norite and anorthosite (Upper Critical zone). The major economic PGE-bearing

horizons (Merensky and UG2) are found on the Upper Critical zone which is overlain by the Main Zone (~ 3.1 m thick). The Upper zone (~ 2 km thick) overlying the Main zone unconformably underlies the Lebowa Granite Suite and Roshoop Granophyre Suite (Fig. 1b) (Cawthorn and Webb, 2001; Scheiber-Enslin and Manzi, 2018).

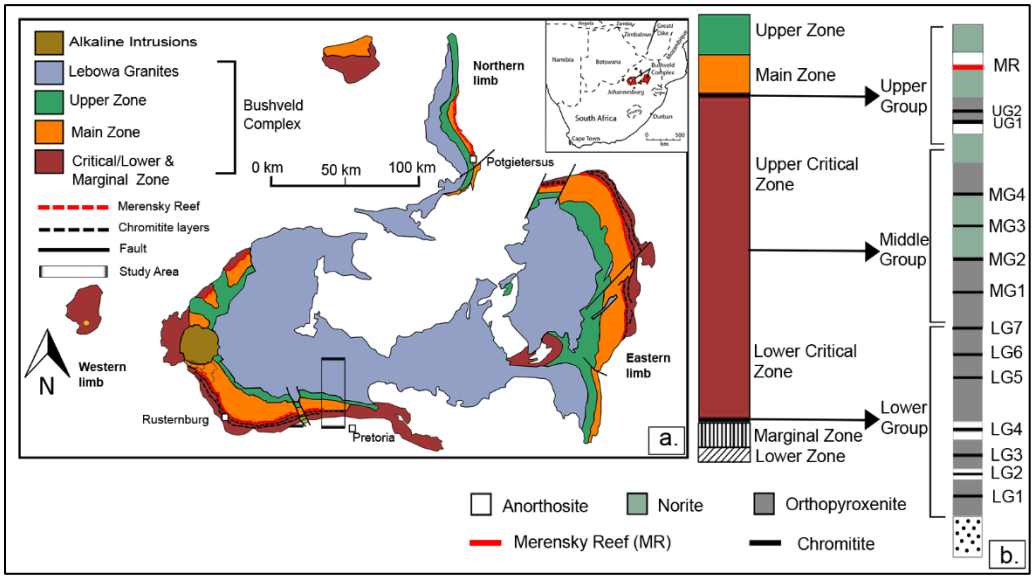


***Figure 1**: The geological map of the Bushveld Complex showing the study area highlighted by a black rectangle (a) (modified from Cawthorn, 2015) and the Stratigraphic column of the Critical zone (b).*

2D legacy seismic data

We recovered and we are reprocessing the 53 km long 2D reflection legacy seismic data from the western limb of the Bushveld Complex for mineral exploration. The seismic data were collected by the Geophysical Survey of South Africa in 1986 using a Vibroseis truck at 50 m source and 25 m receiver spacing. The survey used a sweep length of 16 s, a sweep frequency of 20 – 90 Hz, and a recording length of 16 s sampled at 2 ms. Several pre-processing steps were applied to the data as it was stored in an outdated format that is not compatible with modern processing software. Firstly, we corrected the byte location of the header names that were stored in wrong byte numbers. Secondly, we digitised the geometry information from handwritten observers report as the headers had no information about the geometry of the line and there was no available survey data. To finalise the geometry, we sorted the traces in common midpoint (CMP) bins with a spacing of 12.5 m using a spline curve fitting.

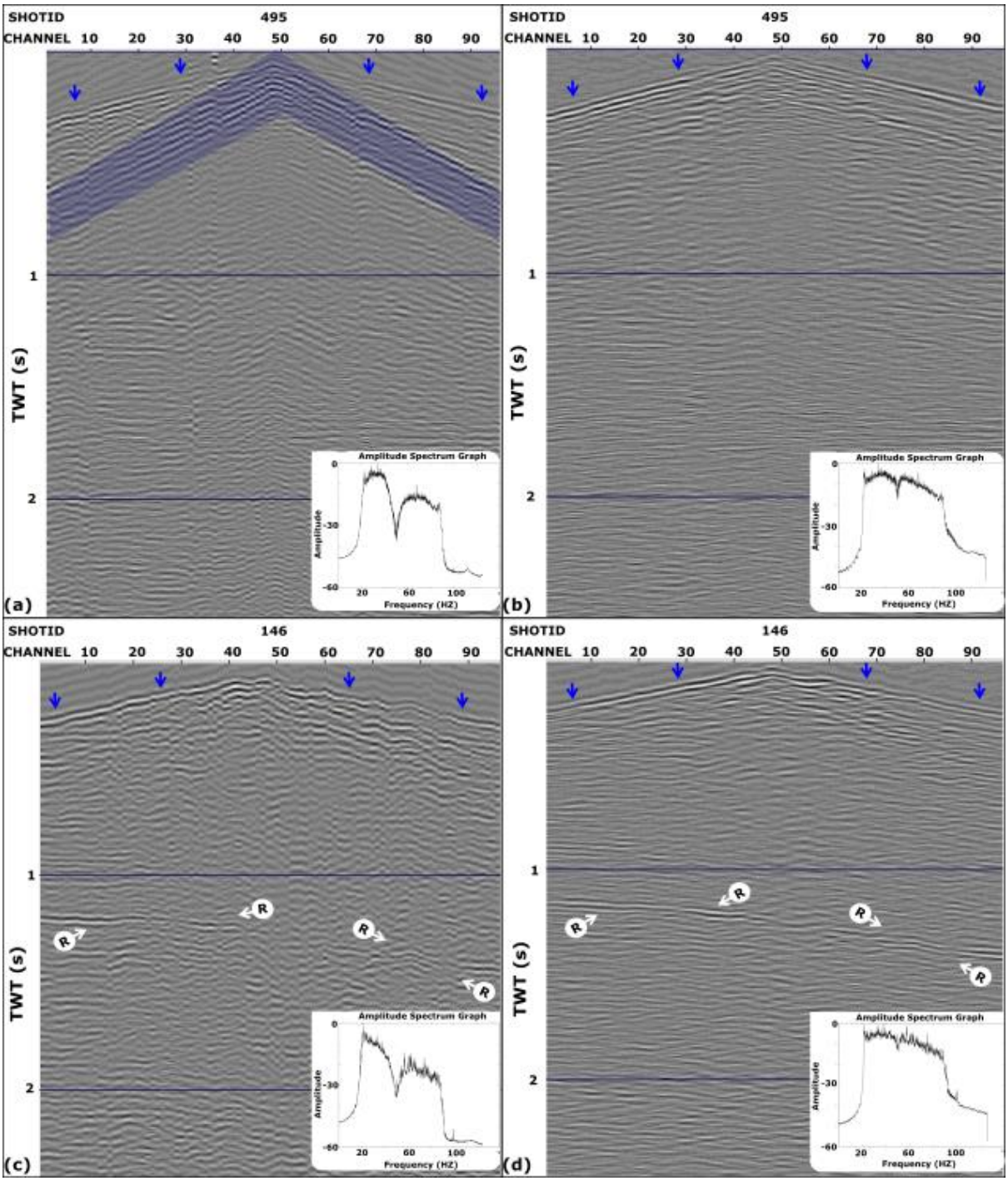


Figure 2*: The raw (a and c) and processed shot gathers (b and d), with a and b showing attenuated surface waves highlighted in blue and c and d showing improved reflection signal R.*

During pre-stack processing, we recovered the attenuated amplitudes using an automatic gain control (AGC) window of 750 ms. We calculated and applied appropriate statics by manually picking a total of 89 882 P-wave first breaks and calculating the floating datum using a reference

datum elevation of 1 368 m with replacement velocity of 6 000 m/s. We broadened the spectrum using Predictive deconvolution with 4 ms gap length and 180 ms filter length to simulate spiking deconvolution. We also applied an f-k filter to mute lineaments with an S-wave velocity less than 3 200 m/s and applied a bandpass filter of [4 22 95 110] Hz.

The raw and processed shot gathers show clear first breaks as indicated by the blue arrows in Fig. 2. Fig. 2a & b represent the raw and processed shot gather indicating the successfully attenuated surface waves which are shaded blue on the raw shot gather. Pre-stack processing clearly improved the shot gathers as shown by the reflection R which is preserved and shows more continuity on the processed shot gather (Fig. 2c & d).

According to literature (Scheiber-Enslin and Manzi, 2018) and surface geological maps the 53 km long legacy seismic profile was collected from south to north over the rim of the western limb of the Bushveld Complex. Fig. 3 shows the brute stack of the legacy seismic profile, with the rectangles on top showing the surface geology as seen on the geological map of the Bushveld Complex. The line was collected over the Transvaal Supergroup on southern edge, and it covers the Bushveld Complex, the Lebowa Granite Suite, and the Karoo Supergroup on the northern edge.

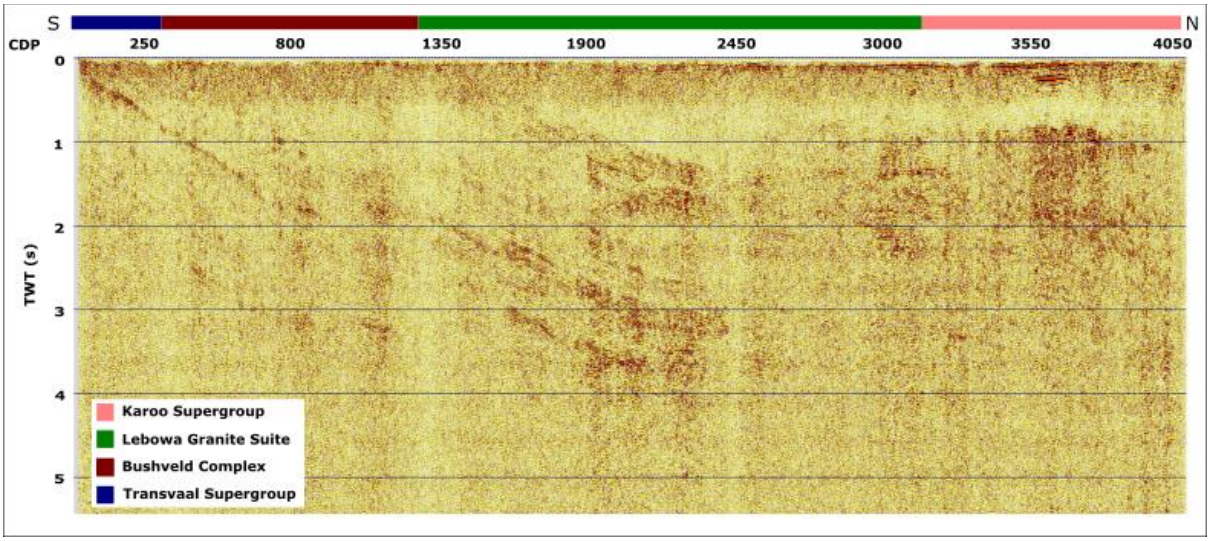


Figure 3: *Brute stack of the legacy seismic profile, with the colours on top showing the surface geology as seen on the geological map of the Bushveld Complex.*

The main lithological contacts expected to show as strong reflections on the seismic profile are: the unconformity between the Transvaal Supergroup and the Bushveld Complex; the unconformity

between the Bushveld Complex; the Lebowa Granite Suite; and the contact between the Lebowa Granite Suite and the Karoo Supergroup. There is no energy below 5 secs, we intend to improve the shallow reflection associated with the mineralisation. The brute stack shows reflections dipping to the north which corresponds to the geology of the Western limb of the Bushveld Complex. The reflections are not continuous which might be due to the existence of first order geological structures that displace these reflections.

Conclusion

The study from the Bushveld Complex demonstrates the insight given by 2D legacy seismic data in imaging the dipping, thin layered PGE deposits. The brute stack shows reflections that can be used as proxies to constrain the delineation of these deposits in the Western Limb of the Bushveld Complex. We envision that the results from this study would aid with the imaging of the PGE's.

Acknowledgements

We are thankful for the financial support from DST-NRF CIMERA, and we appreciate the licenses from Petrosys for Globe Claritas seismic processing software.

References

Cawthorn, R.G., & Webb, S. J. (2001) Connectivity between the western and eastern limbs of the Bushveld Complex. *Tectonophysics*, *330*(3–4), 195–209. https://doi.org/10.1016/S0040-1951(00)00227-4

Cawthorn, R. G. (2015) The Bushveld Complex, South Africa. In B. Charlier, O. Namur, R. Latypov, & C. Tegner (Eds.), *Layered Intrusions* (pp. 517–587) Dordrecht: Springer Netherlands. https://doi.org/10.1007/978-94-017-9652-1_12

Cheraghi, S., Malehmir, A. and Bellefleur, G. (2011) Crustal-scale reflection seismic Investigations in the Bathurst Mining Camp, New Brunswick, Canada. *Tectonophysics, 506, 55-72.* https://doi.org/10.1016/j.tecto.2011.04.011

Malehmir, A. and Bellefleur, G. (2010) Reflection seismic imaging and physical properties of

base-metal and associated iron deposits in the Bathurst Mining Camp, New Brusnwick, Canada. *Ore Geology Reviews 38, 319-333.* https://doi.org/10.1016/j.oregeorev.2010.08.002

Malehmir, A., Donoso, G., Markovic, M., Maries, G., Dynesius, L., Brodic, B., Pecheco, N., Marsden, P., Bäckström, E., Penney, M. and Araujo, V. (2019) Smart Exploration: from legacy data to state-of-the-art data acquisition and imaging. *First Break,* 37, (8), 71–74. https://doi.org/10.3997/1365-2397.n0049

Manzi, M. S.D., Malehmir, A. and Durrheim, R. J. (2018) Improved Subsurface Image through Re-processing of Legacy Seismic Data – A Case Study from a Deep South African Gold. *2nd Conference on Geophysics for Mineral Exploration and Mining, 1–5.* https://doi.org/10.3997/2214-4609.201802705

Manzi, M. S. D., Malehmir, A. and Durrheim, R. J. (2019) Giving the legacy seismic data the attention they deserve. *First Break,* 37, (8), 89–96. https://doi.org/10.3997/1365-2397.n0050

Scheiber-Enslin, S. E., & Manzi, M. (2018) Integration of 3D reflection seismics and magnetic data for deep platinum mine planning and risk mitigation: a case study from Bushveld Complex, South Africa. *Exploration Geophysics*, *49*(6), 928–939. https://doi.org/10.1071/EG17083

Sehoole, L., Manzi, M. S. D., Zhang, S. E., & Bourdeau, J. E. (2020) An innovative seismic and statistical approach to understand 3D magmatic structures and ore deposits in the western Bushveld Complex, South Africa. *Ore Geology Reviews*, *126*, 103784. https://doi.org/10.1016/j.oregeorev.2020.103784

Westgate, M., Manzi, M. S. D., James, I. and Harrison, W. (2020) New insights from legacy seismic data: reprocessing of legacy 2D seismic data for imaging of iron-oxide mineralization near Sishen Mine, South Africa. *Geophysical Prospecting,* 68, (7), 2119–2140. https://doi.org/10.1111/1365-2478.12996

Appendix B: Re-appraising legacy seismic data using modern processing algorithms: case studies from South African Goldfields

Introduction

South Africa hosts several mineral deposits, and the Witwatersrand Basin has contributed more than one-third of the gold produced on the planet. Gold mining in the Witwatersrand basin started in 1886 and has yielded over 52,000 tonnes of gold (Tucker et al., 2016). Our area of interest, the Burnstone mine, is located in the town of Balfour about 75 km southeast of Johannesburg and belongs to the South Rand goldfield (Figure 1) of the Witwatersrand Basin.

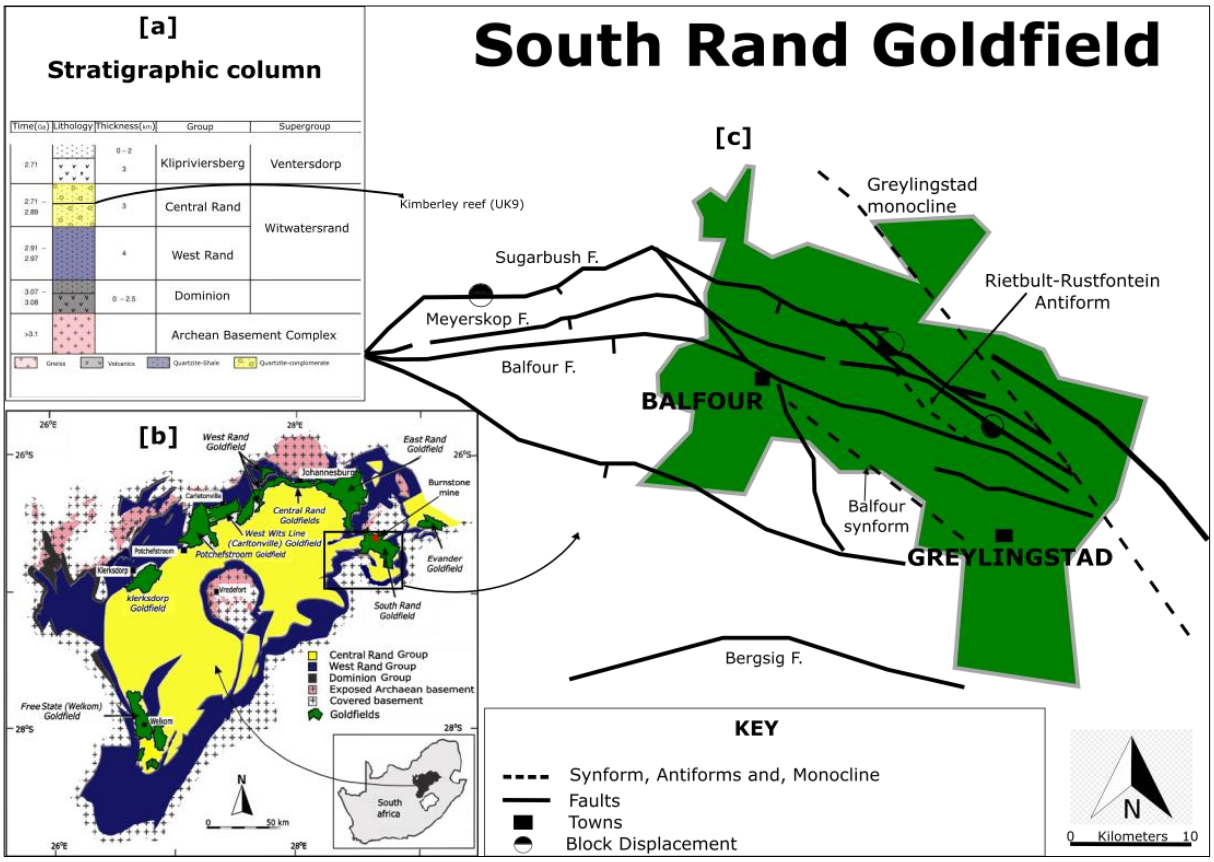


Figure 1 *[a] Simplified stratigraphic column of the Witwatersrand Supergroup modified from (Gibson and Jones, 2002). [b] Map of the Witwatersrand Supergroup without the overlying Supergroups cover. Also showing the location of the goldfields and Burnstone mine (red star) modified from (Dankert and Hein, 2010). Geological map of the South Rand goldfields with first-order structures (faults and folds) modified from (Dankert and Hein, 2010).*

Witwatersrand Basin is a volcano-sedimentary sequence of Mesoarchean age (3.2 – 2.8 Ga) overlying the Kaapvaal Craton (3.6 – 3.2 Ga) (Coward et al., 1995; Manzi et al., 2013). Burnstone mine is exploring the gold-bearing quartz pebble conglomerate known as the Kimberley reef (UK9), which is located few metres below the Ventersdorp Supergroup (Frimmel and Nwaila, 2019).

The intricacy of the first-order geological structures in the area affects the exploitation of these resources (Dankert and Hein, 2010). Thus, additional tools are required to adequately delineate the ore body and aid the mine developments. Manzi et al. (2019, 2020); von Ketelhodt et al. (2019); Westgate et al. (2020a, 2020b) demonstrate the value of re-appraising legacy seismic data for the exploration of natural resources. This study demonstrates the value of re-appraising 2D legacy seismic line near Burnstone mine to delineate the subsurface structures that host gold mineralization. The gold orebody at Burnstone mine cannot be directly imaged using the reflection seismic method because it is interbedded within quartzites and conglomerates with similar densities and seismic velocities. However, this reef could be targeted using seismic methods because it is overlain by basaltic rocks and underlain by shale layer, thus providing a strongly reflective interface that can be used as a proxy to map the reef, its dip variations, and geological structures (faults/dykes) crosscutting it (Figure 1a).

2D legacy seismic data re-appraisal

We received an 18 km 2D reflection seismic line, which is located near Burnstone mine. The seismic data were collected by the Gold Division of Anglo America in 1993 using a Vibroseis truck at 50 m source and receiver spacing. The survey used a sweep length of 16 s, a sweep frequency of 10 – 61 Hz, and a sampling rate of 2 ms. We created a schematic geological model (modified from Antrobus et al., 1986; Figure 2b) of line RS507 (Figure 2a) to calculate the synthetic seismic response of the Booysens Formation shale layer and base of Ventersdorp Supergroup. We ran the 2D acoustic model using a 60 Hz Ricker wavelet applied at 10 ms with acquisition geometry parameters equivalent to those of line RS507.

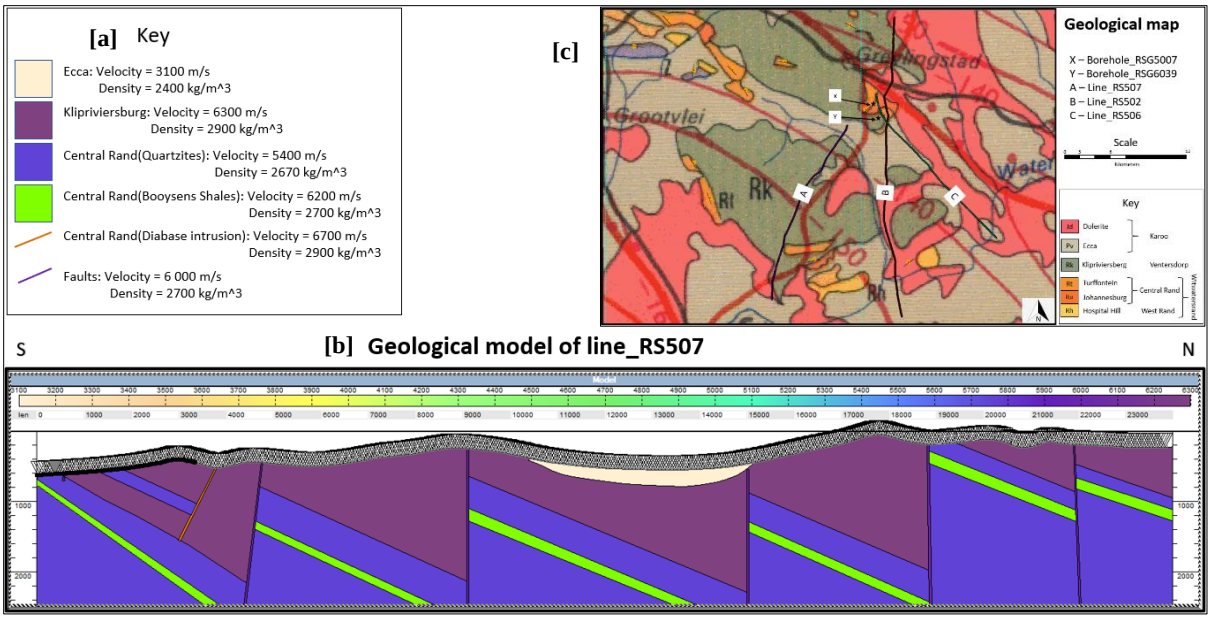


Figure 2 *[a] The key showing physical properties (p-wave velocity and density) of the layers modelled on the schematic geology of line RS507. [b] The schematic geological model of line RS507 showing only the geological layers with significant impendence contrast. [c] 2D legacy seismic lines overlain on the geological map of the study area south of Burnstone mine shaft near Greylingstad.*

Figure 3 shows the raw shot gather from line RS507 versus synthetic shot gather from the schematic geological model of line RS507. Real data and synthetic data show clear first breaks (as indicated by blue arrows Figure 3). The real and synthetic data also show strong corresponding reflections between 500 ms and 1000 ms (as indicated by orange arrows Figure 3). The synthetic data were computed to constrain the processing parameters of the line to illuminate the reflections from Ventersrdorp-Central Rand contact and top of the Booysens Formation.

The 2D legacy seismic lines were prepared for processing. Firstly, trace header editing involved the sorting of the data to be compatible with the processing software Secondly, geometry fixing was done to sort the source and receiver elevations.

Figure 4 shows the 1992 legacy stack (Figure 4a) versus the 2021 re-processed brute stack (Figure 4b). The preliminary re-processed brute stack already exhibits illumination of the target reflectors compared to the legacy stack (indicated by the black arrows in Figure 4). By comparing the schematic geological model and the real stack, the data suggest that the reflections are associated

with the rocks hosting the UK9 reef. This can possibly be caused by the significant acoustic impedance contrast between quartzites and basaltic rocks and between shales and quartzites in the Central Rand Group. Further processing work will be applied to the data to improve the imaging of the subsurface structures.

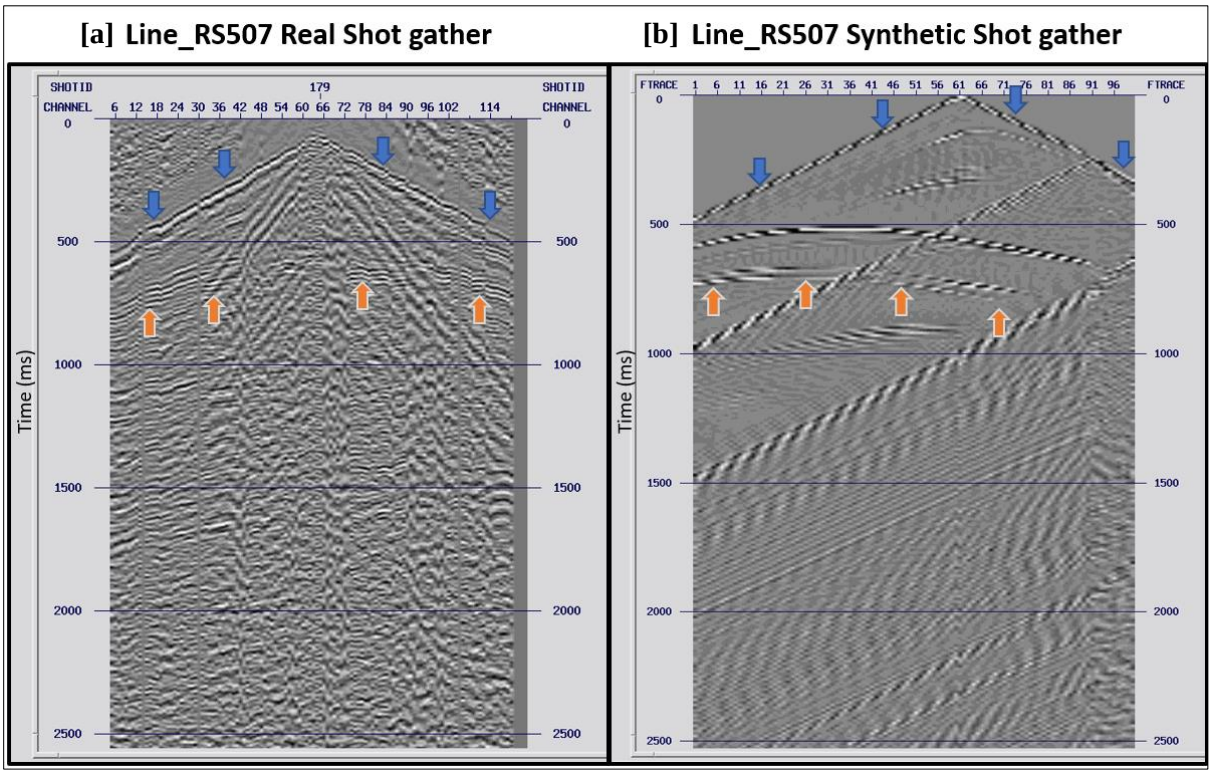


Figure 3 *Shot gathers from real seismic data [a] and synthetic seismic data [b] showing the reflections between 500 ms and 1000 ms as highlighted by the orange arrows. This window correlates to the expected reflections from the Booysens Formation underlying the UK9 reef. The data show clear first breaks highlighted by the blue arrows.*

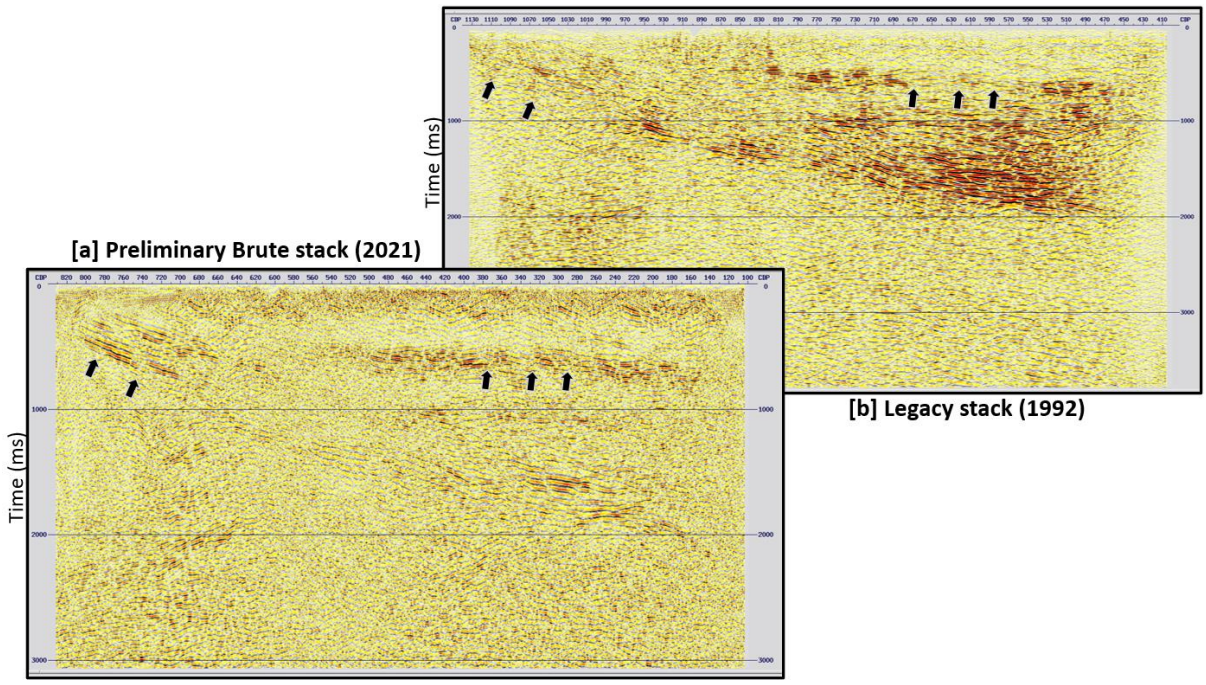


Figure 4 *[a] a preliminary re-processed brute stack of line RS507 and [b] a legacy stack section from 1992 contractor processing archives. The reprocessed stack exhibit improved shallow reflectors (indicated by black arrows).*

Conclusions

The study from the Witwatersrand Basin demonstrates the insight given by 2D legacy seismic data in imaging the thin, layered gold deposit. The results of this study will aid in the development of the Burnstone mine by providing structural information of the orebody.

Acknowledgements

We are thankful for the financial support from DST-NRF CIMERA and the MATLAB licensing from the University of the Witwatersrand Seismic Research Centre. We appreciate the licenses from Petrosys and Tesseral Technologies for Globe Caritas seismic processing software and Tesseral seismic modelling software, respectively. We gratefully acknowledge Sibanye Stillwater for the donation of the legacy 2D seismic data.

References

Antrobus E. S. A., 1986, The South Rand Goldfield. in Mineral Deposits of Southern Africa (Geol. Soc. South Africa), Vol. I, pp. 689–704.

Coward, M. P., R. M. Spencer, and C. E. Spencer, 1995, Development of the Witwatersrand Basin, South Africa: Geological Society, London, Special Publications, **95**, 243–269.

Dankert, B. T., and K. A. A. Hein, 2010, Evaluating the structural character and tectonic history of the Witwatersrand Basin: Precambrian Research, **177**, 1–22.

Frimmel, H. E., and G. T. Nwaila, 2019, Chapter 31 Geologic Evidence of Syngenetic Gold in the Witwatersrand Goldfields, South Africa: SOUTH AFRICA, 24.

Gibson, R. L., and M. Q. W. Jones, 2002, Late Archaean to Palaeoproterozoic geotherms in the Kaapvaal craton, South Africa: constraints on the thermal evolution of the Witwatersrand Basin: Geotherms in the Kaapvaal craton, South Africa: Basin Research, **14**, 169–181.

von Ketelhodt, J. K., M. S. D. Manzi, and R. J. Durrheim, 2019, Post-stack denoising of legacy reflection seismic data: implications for coalbed methane exploration, Kalahari Karoo Basin, Botswana: Exploration Geophysics, **50**, 667–682.

Manzi, M., A. Malehmir, and R. Durrheim, 2019, Giving the legacy seismic data the attention they deserve: First Break, **37**, 89–96.

Manzi, M. S. D., K. A. A. Hein, N. King, and R. J. Durrheim, 2013, Neoarchaean tectonic history of the Witwatersrand Basin and Ventersdorp Supergroup: New constraints from high-resolution 3D seismic reflection data: Tectonophysics, **590**, 94–105.

Manzi, M. S. D., G. R. J. Cooper, A. Malehmir, and R. J. Durrheim, 2020, Improved structural interpretation of legacy 3D seismic data from Karee platinum mine (South Africa) through the application of novel seismic attributes: Geophysical Prospecting, **68**, 145–163.

Tucker, R. F., R. P. Viljoen, and M. J. Viljoen, 2016, A Review of the Witwatersrand Basin - The World's Greatest Goldfield: Episodes, **39**, 104–133.

Westgate, M., M. Manzi, I. James, and W. Harrison, 2020a, Reappraisal of Legacy Reflection Seismic Data for the Prospection of Iron Mineralisation: NSG2020 3rd Conference on Geophysics for Mineral Exploration and Mining, 1–5.

Westgate, M., M. S. D. Manzi, I. James, and W. Harrison, 2020b, New insights from legacy seismic data: reprocessing of legacy 2D seismic data for imaging of iron-oxide mineralization near Sishen Mine, South Africa: Geophysical Prospecting, **68**, 2119–2140.

Appendix C: Seismic solutions utilizing existing in-mine infrastructure for mineral exploration: A case study from Maseve platinum mine, South Africa

Moyagabo K. Rapetsoa[1*], Musa S.D. Manzi[1], Mpofana Sihoyiya[1], Michael Westgate[1], Phumlani Kubeka[2], Emmanuel Onyebueke[1], and Raymond J. Durrheim[1]

[1] School of Geosciences, University of the Witwatersrand, Johannesburg, Private Bag 3, Wits, 2050,[2]Royal Bafokeng Platinum, The Pivot, No 1 Monte Casino Boulevard, Block C, 4th floor, Fourways, 2055.

ABSTRACT

We demonstrate the application of seismic methods using in-mine infrastructures such as exploration tunnels to image platinum deposits and geological structures using different acquisition configurations. In 2020 seismic experiments were conducted underground at the Maseve platinum mine in the Bushveld Complex (South Africa). These seismic experiments were part of the Advanced Orebody Knowledge (AOK) project titled, *"Developing technologies that will be used to obtain information ahead of the mine face".* In these experiments, we recorded active and passive seismic data using surface-nodal arrays and in-mine seismic land streamer. We focus on analyzing only the in-mine active seismic portion of the survey. The tunnel seismic survey consisted of seven 2D profiles in exploration tunnels, located ~550 m below ground surface and a few meters above known platinum deposits. A careful data processing approach was adopted to enhance high-quality reflections and suppress infrastructure-generated noise. Despite challenges presented by tunnel seismics, we successfully imaged the platinum deposits with the aid of borehole data and geological models. The results open opportunities to adapt surface-based geophysical instruments to address the challenging in-mine environments for mineral exploration.

Keywords: Seismic data acquisition, mine tunnel, in-mine seismics, minerals.

INTRODUCTION

The Bushveld Complex of South Africa hosts the richest source of platinum group elements (PGEs) reserves accounting for almost 75% of all globally mined platinum (Scheiber-Enslin and Manzi, 2018). The PGEs are hosted in two major economic horizons (locally termed 'reefs'); the

Merensky reef and Upper Group-2 (UG2) chromitite layers. Starting from surface exploitation in the early 1900s, over the years, mining operations in the Bushveld Complex have increased in depth (between 0.5 and 2 km). The increase in depth is associated with complex geological features such as faults, dykes, potholes, voids, and Iron Rich Ultramafic Pegmatites (IRUPS) intrusions that complicate mining activities (Eales and Cawthorn, 1996; Nkosi et al., 2017; Sehoole, 2020). The complex geological environments cause stoppages to production, mine construction and threaten the safety of mineworkers. With the ideas of better understanding some of these geological structures aiming at improved production and safety, seismic studies were conducted at the Maseve mine, located ~ 38 km NW of Rustenburg and ~ 10 km south of the Pilanesberg Alkaline Intrusive Complex in the Northwest province, South Africa (Figure 1a-c).

In South Africa, the reflection seismic method is mainly used for exploration, mine design and planning due to its ability to resolve complex geological features (Stevenson and Durrheim, 1997; Manzi et al., 2012, 2019). The method has played an important role in imaging the platinum-bearing horizons and geological structures (Manzi et al., 2012, 2019). In the Bushveld Complex, the use of 2D and 3D reflection seismics started in the 1990s to map the platinum bearing horizons and geological features. The 3D reflection seismic surveys were conducted particularly to map major faults, dykes, and IRUPs. However, the surface seismic surveys were unable to resolve geological structures in detail ahead of mining tunnels (Trickett et al., 2004). Borehole seismic techniques (e.g., cross-well reflection seismics, seismic tomography, and vertical seismic profiling) were used to image structures within resolutions of 1 to 3 m. However, these techniques exhibited low resolutions in noisy mine environments (Maccelari et al., 2001; Manzi et al., 2012). In-mine seismics has proven useful in improving the imaging resolution of the mineral deposits (Brodic et al., 2021; Donoso et al., 2021). The progression of in-mine seismic techniques has grown in Europe; however, the techniques are not yet well adopted for deep mineral exploration. The key limitation to in-mine seismics are the high noise levels produced by mine operations such as blasting, cleaning, and drilling, among others. To improve in-mine seismic technique, a better understanding of the acoustic impedance contrast, geometry, and structural characteristics of the target and the host rock is necessary. One of the important aspects is obtaining accurate velocity information that needs to be determined for both numerical simulations and to constrain seismic processing, interpretation, and time-to-depth conversion (Malehmir et al. 2013; Manzi et al., 2017).

The Advanced Orebody Knowledge (AOK) programme was launched aiming at addressing some of the aforementioned issues involving several South African research institutions. The programme involved collection of not only reflection seismic, but multi-geophysical datasets including Ground Penetrating Radar (GPR) and Electrical Resistivity Tomography (ERT) data at the Maseve mine area. Integration of the geophysical and geological data has played a key role in mapping the deep seismic reflectors and obtaining information on/ahead of the tunnel face. The main objective of this study is to characterize geological structures using different seismic data acquisition techniques in deep (> 500 m) platinum mines (Figure 1b).

GEOLOGICAL BACKGROUND

The Bushveld Complex is in the north-western part of South Africa, known for its vast platinum group elements, complex geology and its remarkable size, covering an area of about 64 000 km^2 (Eales and Cawthorn, 1996). The Bushveld Complex has been a subject for abundant research, and it is documented by several authors (Eales and Cawthorn, 1996; Buchanan and Reimold, 1998; Kinnaird, 2005; Hunt, 2006). The complex can be divided into five major limbs: The eastern limb, the western limb, the far western limb, the northern limb, and the southern limb (visible on gravity and magnetic data) (Cawthorn and Webb, 2001; Kinnaird, 2005). The western limb is the focus of our study (Figure 1a). Several mines are currently in operation in the Bushveld Complex, extracting the PGE, chromium, and vanadium deposits. The economic horizons are found in the mafic to ultramafic cumulate rocks of the complex termed the Rustenburg Layered Suite (RLS), with an average thickness of 6 km. The RLS forms part of the successive magma intrusions that intruded the Transvaal Supergroup and the Rooiberg Group volcanics at ~2.06 Ga (Cawthorn and Webb, 2001). The intrusions resulted in the RLS being divided into five mineralogically varying zones (Figure 1c), namely the Marginal zone, Lower, Critical, Main and Upper zone (Eales and Cawthorn, 1996; Kinnaird, 2005; Scheiber-Enslin and Manzi, 2018). The RLS is overlaid by felsic rocks belonging to the Lebowa granite and the Rashoop Granophyre Suite.

The focus is on the critical zone that makes up 15-25% of the RLS in thickness and is subdivided into the Lower Critical Zone (LCZ) and the Upper Critical Zone (UCZ). The zones are characterized by the layering of norites and anorthosites, together with ultramafic layers of pyroxenite and chromitite. The Merensky reef and the UG2 chromitite are the two major economic horizons hosting the PGE deposits (Trickett et al., 2004; Cawthorn, 2015). The thickness of the

Merensky reef ranges from 0.5 m to 2 m and the UG2 forms part of the chromitite layers that are divided into the Upper (UG), Middle (MG), and Lower Group (LG) with a thickness of 0.5-1 m, 1-5 cm, and 0.8-1.2 m, respectively (Lee, 1996; Nex et al., 1998; Kinnaird, 2005). The two major horizons are mined at an average depths of 500 m below the surface, with the UG2 occurring 15 to 400 m below the Merensky reef (Manzi et al., 2020).

The Bushveld Complex is highly faulted, and the regional structural interpretation suggests that rocks may be flat-lying due to the reaction of the NW-SE trending Rustenburg Fault (Campbell, 2011). The majority of faults are striking north to northwest and dipping at an average of about 70^0 to 80^0. Faults separate the rock into upper fault block and lower fault block (hanging wall and footwall, respectively). Existing faults gave way for intrusion of multiple dykes of different ages and composition crosscuting the Bushveld Complex stratigraphy. Diabase and dolerite dykes are the most common in the area. Several dykes in the complex have resulted in the loss of ground of the reef. Furthermore, the Bushveld Complex has slumps structures (e.g., potholes) and IRUPs that result in blockages to mining operations.

SEISMIC MODELING AND DATA ACQUISITION

Evaluation of reflection response at Maseve mine area

To obtain a better understanding of site's reflectivity response, along with subsequent constrain of the origin of reflections in our acquired data, zero-offset synthetic seismograms were calculated (Figure 2) using the borehole (BH1) information provided by the mine. To conduct the synthetic modeling, we firstly needed to collect physical properties measurements (seismic velocity and bulk density) of the data hanging wall and footwall of the rock at Maseve mine. The average velocity measurements of the collected samples range from 5088 m/s to 6118 m/s and the average density ranged from 2744 kg/m^3 to 4392 kg/m^3. The measured velocity and density values are in agreement with previously published values (see Campbell, 2011; Manzi et al., 2017). The borehole BH1 reached depths of 577.5 m and it intersected the Merensky reef and UG2 at 515 m and 571 m, respectively. To compute the seismogram (Figure 2), we used a Ricker wavelet with a dominant frequency of 130 Hz and a sampling rate of 0.25 ms. The Merensky reef and the UG2 are too thin (~ 1 m thick) to be directly resolved, whilethe acoustic impedance contrast (bulk density × seismic velocity) of the hanging wall and the footwall is large enough to provide significant reflection response. The reflections of the UG2 are more prominent as its acoustic

impedance contrast with the host rock is higher (Manzi et al., 2017; Scheiber-Enslin and Manzi, 2018).

2D acoustic modeling as a guide for survey design and final interpretation

Seismic reflections in the study area are guided by the interfaces between the hanging wall and the footwall of the mineralization. The Merensky reef has similar physical properties to the host rock, while the UG2 is much denser compared to the host rock. To build the geological model, we used the information obtained from the borehole (BH1) and geological reports from the mine. The thickness of the Merensky reef in the study area is 0.63 m, whilst that of the UG2 is 0.84 m, with a dip averaging at 7º. The area is prone to faulting and dolerite dykes that crosscut the mineralization, therefore we included the two structures in the model. Modeling in the tunnel is conducted with the assumption that the tunnel floor is the surface.

Figure 3 shows the model built using Tesseral software, with the information obtained from the mine and the borehole. 2D acoustic finite-difference modeling was conducted to investigate the seismic reflectivity of the mineralization and constrain the seismic interpretations. The model had a depth of 140 m and a spread of 360 m, with a grid cell of 1 m in both the vertical and horizontal directions . The target on the model was the first few meters of the lithology, with the target being the Merensky reef and the UG2. The synthetic parameters of the model were kept the same as the acquisition parameters of the collected data, with the maximum two-way travel time of 500 ms, sampling interval of 1 ms, and given that the tunnel seismic surveys in hardrock environemts are rather low attenuative where the surveys conducted with impact seismic sources have demonstrated rather high dominant frequency (e.g., Brodic et al., 2016), a 130 Hz Ricker wavelet was chosen. The measured velocities and densities were used together with the average values from (Manzi et al., 2020).

DATA ACQUISITION

In November 2020, we acquired multiple seismic lines on surface and underground at the Maseve mine. The data acquisition parameters for the tunnel surveys are summarized in Table 1. A dense array of 2D seismic lines was collected on surface using Sercel 1C wireless units, connected to 5 Hz vertical geophones, and a broadband seismometer (Figure 4c, e).This study focuses on a portion of the underground experiments. The in-mine survey consisted of 7 experimental profiles acquired

underground in exploration tunnels, covering about 0.6 km over known platinum deposits and geological structures. This study focuses on the underground experimental profiles. The surface data were acquired using a 48 kg accelerated weight drop (Figure 4a), while a 5 kg sledgehammer (shot spacing of 2 - 5 m) was used as the in-mine seismic source (Figure 4b) due to underground conditions (loose fragments of the hanging wall). Signal penetration was fair for near surface imaging considering the abundance of mining induced noise. To improve the signal-to-noise ratio, four hammer hits were made at every shot location and subsequently vertically stacked. The accurate in-mine coordinates of source and receiver positions were extrapolated using the mine pegs, due to inviability of reliable GPS readings underground. The underground experiments had different objectives, therefore different receiver spacing was used for the profiles (Table 1). Profile P1, P5, P6 and P7 were collected using the 4.5 Hz vertical component geophone-based land streamer with a 5 m receiver spacing to cover a large area and image the subsurface mineralization (Figure 4d). Profiles P2 and P4 were collected around the pillar using 14 Hz vertical geophones with an objective to image the structures around the pillar. Profile P3 had a receiver spacing of 1 m, with a combination of two different types vertical geophones (4.5 Hz and 14 Hz). The 14 Hz geophones were planted in drill holes, while the 4.5 Hz geophones are attached to the land streamer. The objective of P3 was to image structures along the dolerite dyke. During data acquisition, special attention was given to both data quality control and landstreamer deployment to ensure good coupling with the ground. The profiles were designed based on the limited geological information provided before data acquisition, ensuring that the main geological structures are perpendicular to the profiles, such that the target mineralization (Merensky reef and UG2) could be imaged. Although 7 profiles were collected underground, this study focuses on the data obtained from P5, P6 and P7 due to the location and extension, which is essential to image the geological structures and the dipping UG2. P5, P6 and P7 were collected collinear to each other trending NE-SW, covering 350 m. Data were collected at 0.25 ms sampling interval and a recording length of 0.5 s.

DATA PROCESSING

Seismic profiles P5, P6, and P7 covered the bottom part (Block 11) of the incline tunnel at Maseve mine. This is a few meters above the dipping Merensky reef and the UG2. The processing steps are summarized in Table 2. The data were of good quality, with few noisy traces due to low

coupling of the land streamer in the muddy ground of the tunnel. The first breaks were clearly distinguishable along entire profiles lenngths, whilst reflections in some of the shot gathers were masked by the noise. The first step was to add the coordinates to headers as the data were collected without coordinates. The mine pegs did not cover every shot or receiver position, we placed receivers 5 m apart using the land streamer cable between the known points and we interpolated the coordinates using a linear and spline function to get the coordinates of each receiver and shot. The geometry of the shots and receivers including a straight CDP line with bin spacing of 2.5 m was created and added to the seismic profiles. The next step was to edit the bad traces and apply residual, refraction (using only short wave-length component), elevation static corrections. The topography varied over a large distance, and it was corrected using elevation statics. The first breaks were of fair quality, therefore, we combined automatic and manual picking. A total of 1778 picks were used over 72 receivers and 76 shots across the three lines and the picks used for four iterations of layer-based refraction inversion approach with an RMS of 1.45 - 2 ms obtained for final models. The refraction tomograms were produced to aid with the interpretation of the data down to about 30 m depth. A Bandpass filter (50 – 170 Hz) was applied to constrain the data within the source energy frequency and remove significant portion of mine-generated noise. The amplitudes of the first break picks are relatively high, therefore affecting any near surface reflections. A top mute was applied on the first break to ensure that they do not affect the events in the final stack section. Figure 5a, b, c, shows the synthetic shot gather, raw shot gather, and a processed shot gather (trace editing, refraction statics, Bandpass, and top mute), respectively. The ground roll remained dominant in the data, despite the pre-stack processing. To attenuate these, we applied f-k mute to target velocities below 4100 m /s. Velocity analysis was conducted using a series of constant velocity stacks generated to select the velocity field that shows the greatest coherency of reflections. The dipping reflections were stacked coherently with Normal moveout (NMO) velocities of 5500 m/s. The data exhibited steep and gently dipping reflections; therefore, we applied dip moveout (DMO) to stack the reflections simultaneously and enhance any structurally dipping reflections. The consistent low-frequency events were removed by the second pass of frequency filtering (Bandpass: 80 – 160 Hz). Finally, We used a 2D Kirchhoff time migration and applied a depth conversion using a constant velocity of 5500 m /s, which is the average velocity of the rocks in the mine.

RESULTS AND DISCUSSION

The shot gathers (Figure 5) show steeply dipping (R1) and gently dipping reflectors (R2). The two reflections are confidently identified on the processed shot gather (Figure 5c). The synthetic shot gathers (Figure 5a), and raw shot gather (Figure 5b) have high amplitude of the first arrivals, masking near surface reflections. Application of filters, DMO, and first break muting resulted in enhancement of the near surface reflections at about 25 ms. Additional steeply dipping reflections are observed, which are associated with the deep chromitite mineralizations that are not intersected by the boreholes in the study area. The comparison of the shot gathers shows that in-mine seismic studies have potential in imaging the near tunnel geological features, despite noisy mine environments.

The reflections are interpreted based on geological observation and data. The results of the 2D reflection modeling and seismic tomograms (Figure 6) are also used to constrain the interpretation. The seismic tomogram shows the top layer to have velocities ranging between 2300 and 3400 m/s and an average thickness of 3 m. The hard rock is observed at depths of about 10 m, with velocities ranging between 4500 and 6700 m/s. The velocity of the top layer corresponds to the loose rocks and mud regions in the mine, whilst the hard rock velocities match the velocities of the footwall rocks (norites and anorthosites). Merging the three segments has resulted in areas of low ray coverage (see Figure 6).

Figure 7 shows the unmigrated stack section and the processed shot gather section. The reflections appear to be crosscut along the line due to the data being collected as three separate profiles. Therefore, merging them into one profile resulted in a low CDP fold (see Figure 8). Two reflections are identified. R1 is associated with possible deep mineralization (UG1, MGS and LGs) below the UG2, while R2 is associated with the UG2. The reflection (R2) that was hidden by the first arrivals is preserved by stacking, making it more prominent. The steeply dipping reflection (R1) is disturbed by the low fold areas, therefore the continuous reflection observed on the processed shot gather appears to be interrupted.

The depth of the stack section (Figure 8) honours lateral variations of velocity and the reflections are more continuous compared to the stack section in the time domain. Multiple reflections can be observed in Figure 8. The shallow reflection (R2) occurring at about 70 m corresponds to the depth of the UG2 on borehole 1 (Figure 9). The stack sections resolve reflections below 30 m, therefore

the Merensky reef cannot be easily identified as it falls within this region. The first 30 m is resolved by the seismic tomograms, showing high velocity rock starting at depth 6-10 m (see Figure 10).

The seismic data depict clear reflections that can be attributed to the Merensky reef and the UG2. The two reefs are closer at the edges, as the UG2 creates a syncline structure. The two mineralizations cannot be directly resolved as the vertical resolution is limited to an average of 25 m. The delineation of the mineralization depends on the rock packages surrounding it. The reflection (R2) is due to the interbedding of the hanging wall and the footwall. The interbedding is consistent throught out the line. The Merensky reef is associated with reflections that arise from the contact between the Pegmatoidal anorthosites and the norites. Whilst the UG2 is imaged due to the contact between the orthopyroxenite rocks (2700 kg/m^3) and the chromitite (4800 kg/m^3). The UG2 contact has a higher acoustic impedance contrast compared to the Merensky reef (see Figure 2). The Merensky reef package has an average thickness of 7 m, while the UG2 package has an average thickness of 12 m. The migrated section shows that the interbedded reflections of the UG2 have a thickness between 15 and 20 m, which is higher than the thickness intersected by borehole 1. The differences in thickness between the seismic data and the borehole might be due to the borehole not being directly on the seismic line and the low fold areas. However, the borehole intersected the UG2 at a depth of 72 m from the tunnel floors, which corresponds to the depth of the UG2 package (R2). The unmigrated stack section (Figure 7) shows other reflections that can be attributed to possible mineralization packages (UG1, MGS and LGs) below the UG2.

The geological model shows the presence of dykes and faults in the study area. The dyke observed on the geological model is 3 m in thickness, which is below the seismic wavelength (25 m), therefore the dyke will not be resolved. The displacements of the reflections can be linked to the faults. However, the displacement observed on the data are likely to be due to the low fold areas, therefore the interpretation is inconclusive.

CONCLUSION

A total of 12 reflection seismic profiles have been successfully acquired at Maseve mine. Seven profiles were acquired along the mine tunnels to image the host rock, geological structures, and the orebody. Three seismic lines have been successfully processed for the purpose of this study. The profiles show high quality reflections and noisy reflections due to the guided tunnel waves. In this paper, we have focused on introducing in-mine seismic experiments to South African mines.

Careful processing, setup and parameters of the seismic profiles allowed us to observe clear reflections on the dataset. Despite the challenges faced due to spurious frequencies, low fold due to merging the profiles and the interference from mining infrastructures, the combination of 2D modeling, borehole log, and geological information assisted in the interpretation of the seismic data. One reflection is interpreted to originate from the UG2 package (contact between the hanging wall and footwall) where the chromitite layers are hosted. The seismic data clearly depict mineralization and illustrate the potential for in-mine seismics to resolve the targets. The presented data only used a minor part of the full dataset, neglecting surface, passive, and other underground seismic profiles. Exploitation of the dataset and addition of borehole data will enable us to characterize the Merensky reef, UG2 and geological features around the mineralization in detail. This study shows how high resolution in-mine reflection seismic data can be used for development and mine planning. It opens the possibilities of using reflection seismics for exploration in unconventional environments.

DECLARATION OF COMPETING INTEREST

The authors declare that they have no known competing financial interests or personal relationship that could have appeared to influence the work reported in this paper.

ACKNOWLEDGEMENTS

This study was sponsored by the Mandela Mining Precinct. Mandela Mining Precinct has received funding from the Department of Science and Innovation (DSI) together with Minerals Council of South Africa. We thank the staff of Maseve platinum mine, especially Sipho Sithole, for the help during mine visit and data acquisition. Students from Wits University (South Africa) are appreciated for their help with data acquisition. Michelle Pienaar is thanked for the coordination and management of the project. HiSeis Pty Ltd. is highly appreciated for sponsoring the licenses for Globe Claritas processing software. We also thank Tesseral Technologies Inc. for supporting us with Tesseral software.

REFERENCES

Brodic, B., A. Malehmir, N. B. M. Pacheco, C. Juhlin, J. Carvalho, L. Dynesius, jens van den berg, R. de Kunder, G. Donoso, T. Sjölund, and V. Araujo, 2021, Innovative seismic imaging of VMS deposits, Neves-Corvo, Portugal: Part I - In-mine array: GEOPHYSICS, 1–76.

Brom, A., and I. Stan-Kłeczek, 2015, Comparison of seismic sources for shallow seismic: sledgehammer and pyrotechnics: Contemporary Trends in Geoscience, **4**, 39–45.

Buchanan, P. C., and W. U. Reimold, 1998, Studies of the Rooiberg Group, Bushveld Complex, South Africa: No evidence for an impact origin: Earth and Planetary Science Letters, **155**, 149–165.

Campbell, G., 2011, Exploration geophysics of the Bushveld Complex in South Africa: The Leading Edge, **30**, 622–638.

Cawthorn, R. G., 2015, The Bushveld Complex, South Africa, *in* B. Charlier, O. Namur, R. Latypov, and C. Tegner, eds., Layered Intrusions, Springer Netherlands, 517–587.

Cawthorn, R. G., and S. J. Webb, 2001, Connectivity between the western and eastern limbs of the Bushveld Complex: Tectonophysics, **330**, 195–209.

Donoso, G. A., A. Malehmir, B. Brodic, N. Pacheco, J. Carvalho, and V. Araujo, 2021, Innovative seismic imaging of VMS deposits, Neves-Corvo, Portugal: Part II - Surface Array: GEOPHYSICS, 1–39.

Eales, H. V., and R. G. Cawthorn, 1996, The Bushveld Complex, *in* Developments in Petrology, Vol. 15. Elsevier, 181–229.

Hunt, J. P., 2006, Geological Characteristics of Iron Oxide-Copper-Gold (IOCG) Type Mineralisation in the Western Bushveld Complex.Msc, University of the Witwaterrand, 267p.

Kinnaird, J. A., 2005, The Bushveld Large Igneous Province: , 39.

Lee, C. A., 1996, A Review of Mineralization in the Bushveld Complex and some other Layered Intrusions, *in* Developments in Petrology, Vol. 15. Elsevier, 103–145.

Maccelari, M. J., S. Letlotla, and M. Nkwana, 2001, Integration and Optimisation of Seismic Techniques: , 197.

Manzi*, M., R. Durrheim, and S. Webb, 2017, 3D seismic attributes for platinum exploration

and mine planning in the Bushveld Complex (South Africa): International Geophysical Conference, Qingdao, China, 17-20 April 2017, 665–668.

Manzi, M., A. Malehmir, and R. Durrheim, 2019, The Value of Seismics in Mineral Exploration and Mine Safety: 81st EAGE Conference and Exhibition 2019, 1–5.

Manzi, M. S. D., R. J. Durrheim, K. A. A. Hein, and N. King, 2012, 3D edge detection seismic attributes used to map potential conduits for water and methane in deep gold mines in the Witwatersrand basin, South Africa: GEOPHYSICS, **77**, WC133–WC147.

Manzi, M. S. D., G. R. J. Cooper, A. Malehmir, and R. J. Durrheim, 2020, Improved structural interpretation of legacy 3D seismic data from Karee platinum mine (South Africa) through the application of novel seismic attributes: Geophysical Prospecting, **68**, 145–163.

Nex, P. A., L. J. Ingle, J. A. Kinnaird, B. A. van der Vyver, and R. G. Cawthorn, 1998, A new stratigraphy for the Main Zone of the Bushveld Complex, in the Rustenburg area: South African Journal of Geology, **101**, 215–223.

Nkosi, N. Z., M. S. D. Manzi, G. R. Drennan, and H. Yilmaz, 2017, Experimental measurements of seismic velocities on core samples and their dependence on mineralogy and stress; Witwatersrand Basin (South Africa): Studia Geophysica et Geodaetica, **61**, 115–144.

Scheiber-Enslin, S. E., and M. Manzi, 2018, Integration of 3D reflection seismics and magnetic data for deep platinum mine planning and risk mitigation: a case study from Bushveld Complex, South Africa: Exploration Geophysics, **49**, 928–939.

Sehoole, L. T. C., 2020, Application of 3D seismics to enhance mapping of potholes in the western Bushveld Complex, South Africa.167p.

Stevenson, F., and R. J. Durrheim, 1997, Reflection Seismics for Gold, Platinum and Base Metal Exploration and Mining in Southern Africa: Seismic Methods in Mineral Exploration.

Trickett, J. C., W. A. Duweke, and S. Kock, 2004, Three-dimensional reflection seismics: worth its weight in platinum: International Platinum Conference ‘Platinum Adding Value,’ 257–264.

LIST OF FIGURES

Figure 1: (a) Geological map of the Bushveld Complex (modified from Cawthorn, 2015) showing the location of the Maseve mine site. (b) Map of the Maseve mine showing the location of the study area at the North Shaft and the Surrounding mines that are used for passive seismics. (c) Stratigraphic column of the Critical zone showing the chromitite layers and Merensky Reef (MR).

Figure 2: Stratigraphic column derived from borehole 1 of Maseve mine. Reflection coefficients were derived from the acoustic impedance, and synthetic seismograms were generated using the reflection coefficient and a Ricker wavelet (130 Hz). Strong reflections observed are associated with the two major reefs (Merensky Reef and UG2). The acoustic impedance of the UG2 and the surrounding rock is expected to be highest compared to that of the Merensky reef (see Manzi et al., 2018)

Figure 3: Geological/finite difference model at the Maseve mine. The model shows the two-target mineralizations and geological structures. The velocity and density of structures are noted.

Figure 4: Seismic sources and the different receivers that were used during the Maseve mine acquisition (November 2020). (a) Photo of a 48 kg accelerated weight drop mounted on a vehicle along RAU units. (b) Photo of data acquisition in the mine tunnels using a sledgehammer as a source and 4.5 Hz receiver landstreamer. (c) Sercel Unite wireless 1C receivers used for passive seismic studies. (d) Underground mounting of the 4.5 Hz receiver landstreamer on the sidewall supported by roof bolts. (e) Photo of a broadband seismometer buried in the ground to record mine induced events.

Figure 5: Shot gathers examples from P5 shot-5, with their frequency spectrum. Shot gathers highlight clear reflections marked by black arrows. (a) Synthetic shot gather modelled from the geological model, showing one clear reflection (R2) due to the UG2. (b) Raw shot gathers, with reflections overshadowed by high frequencies. The frequency spectrum has frequency ranges of 0 - 1800 Hz as a result of the sampling rate of 0.25 ms. Spurious ringing can be observed on the raw shot gather. (c) The processed shot gathers, showing clear reflections, with one of the reflections not easily identified on the synthetic gather and the raw shot gather.

Figure 6: Near surface tomogram showing the upper 30 m of P5-7. The average top velocities match those of the rock in the area. The tomogram has low confidence at areas were P5, P6 and P7 were merged and edges due to low fold.

Figure 7: (a) Unmigrated time stack section and (b) a processed shot gathers along P5. The reflections identified on the processed shot gather are observed on the unmigrated stack section.

Figure 8: (a) Unmigrated depth stack section of P5-7 showing horizontal to dipping reflectors. Prominent reflections are observed at the edges and the coherency decrease at areas of low fold.

Figure 9: (a) Migrated stack section of P5-7 with borehole 1 (BH1) overlaid (b), showing how reflection R2 correlates with the UG2 package. The arrows mark the identified reflections detailed in the text. Red outline shows the focus area where the seismic tomograms are overlaid.

Figure 10: Seismic sections of P5, P6 and P7 showing a depth of 150 m, overlaid by velocity tomograms to correlate the reflections. The tomograms reach a maximum depth of 30 m, which is above the first prominent reflection (~70 m)

Table 1: Maseve Mine seismic data acquisition parameters of the seven profiles along the incline tunnel.

Table 2: Processing steps applied reflections seismic dataset from Maseve mine.

FIGURES

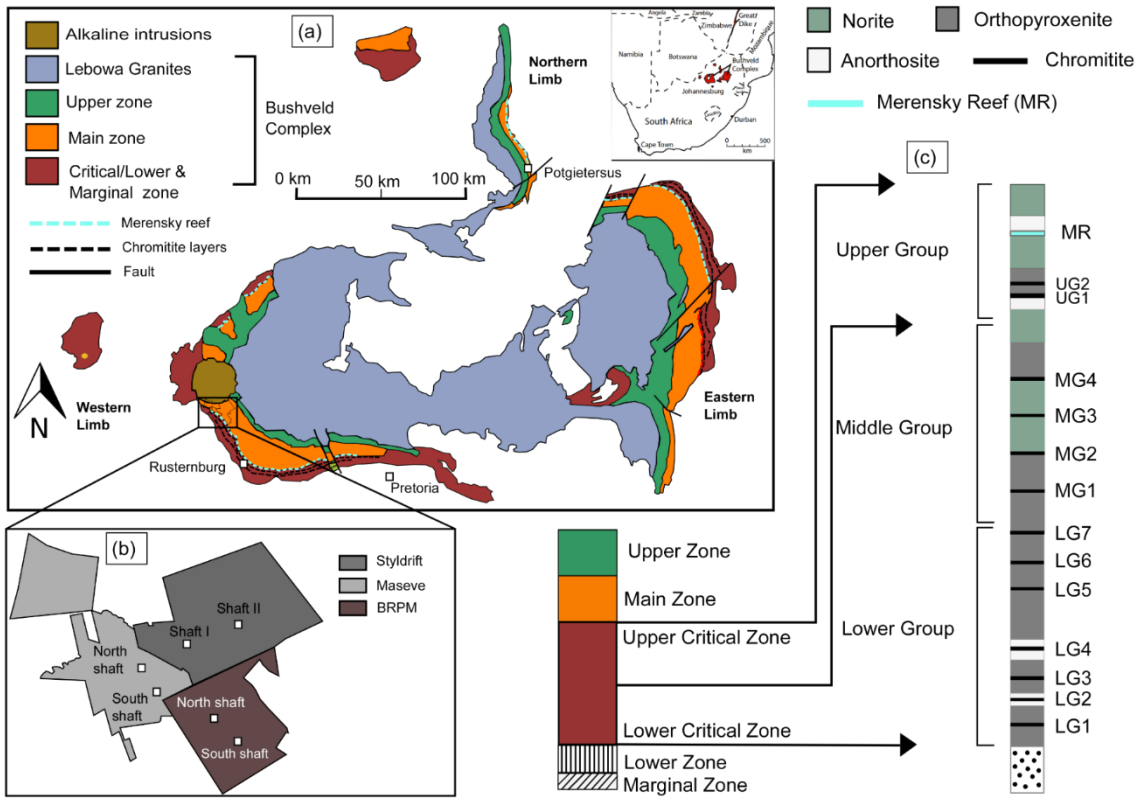


Figure 1: (a) Geological map of the Bushveld Complex (modified from Cawthorn, 2015) showing the location of the Maseve mine site. (b) Map of the Maseve mine showing the location of the study area at the North Shaft and the Surrounding mines that are used for passive seismics. (c) Stratigraphic column of the Critical zone showing the chromitite layers and Merensky Reef (MR).

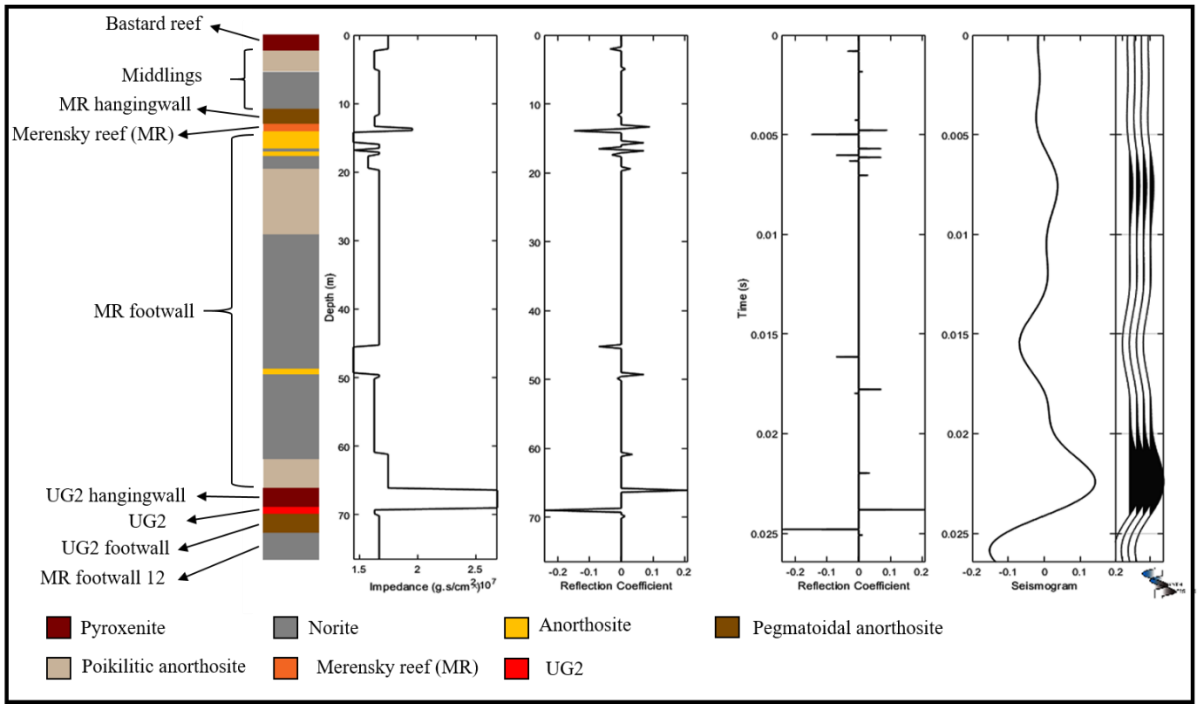


Figure 2: Stratigraphic column derived from borehole 1 of Maseve mine. Reflection coefficients were derived from the acoustic impedance, and synthetic seismograms were generated using the reflection coefficient and a Ricker wavelet (130 Hz). Strong reflections observed are associated with the two major reefs (Merensky Reef and UG2). The acoustic impedance of the UG2 and the surrounding rock is expected to be highest compared to that of the Merensky reef (see Manzi et al., 2018).

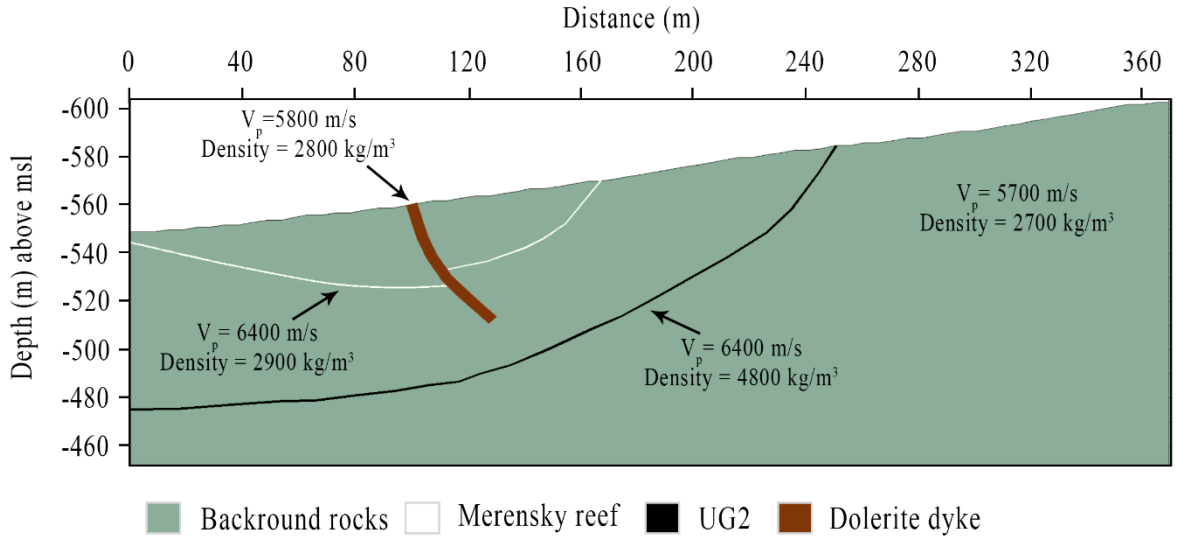


Figure 3: Geological/finite difference model at the Maseve mine. The model shows the two-target mineralizations and geological structures. The velocity and density of structures are noted.



Figure 4: Seismic sources and the different receivers that were used during the Maseve mine acquisition (November 2020). (a) Photo of a 48 kg accelerated weight drop mounted on a vehicle along RAU units. (b) Photo of data acquisition in the mine tunnels using a sledgehammer as a source and 4.5 Hz receiver landstreamer. (c) Sercel Unite wireless 1C receivers used for passive seismic studies. (d) Underground mounting of the 4.5 Hz receiver landstreamer on the sidewall supported by roof bolts. (e) Photo of a broadband seismometer buried in the ground to record mine induced events.

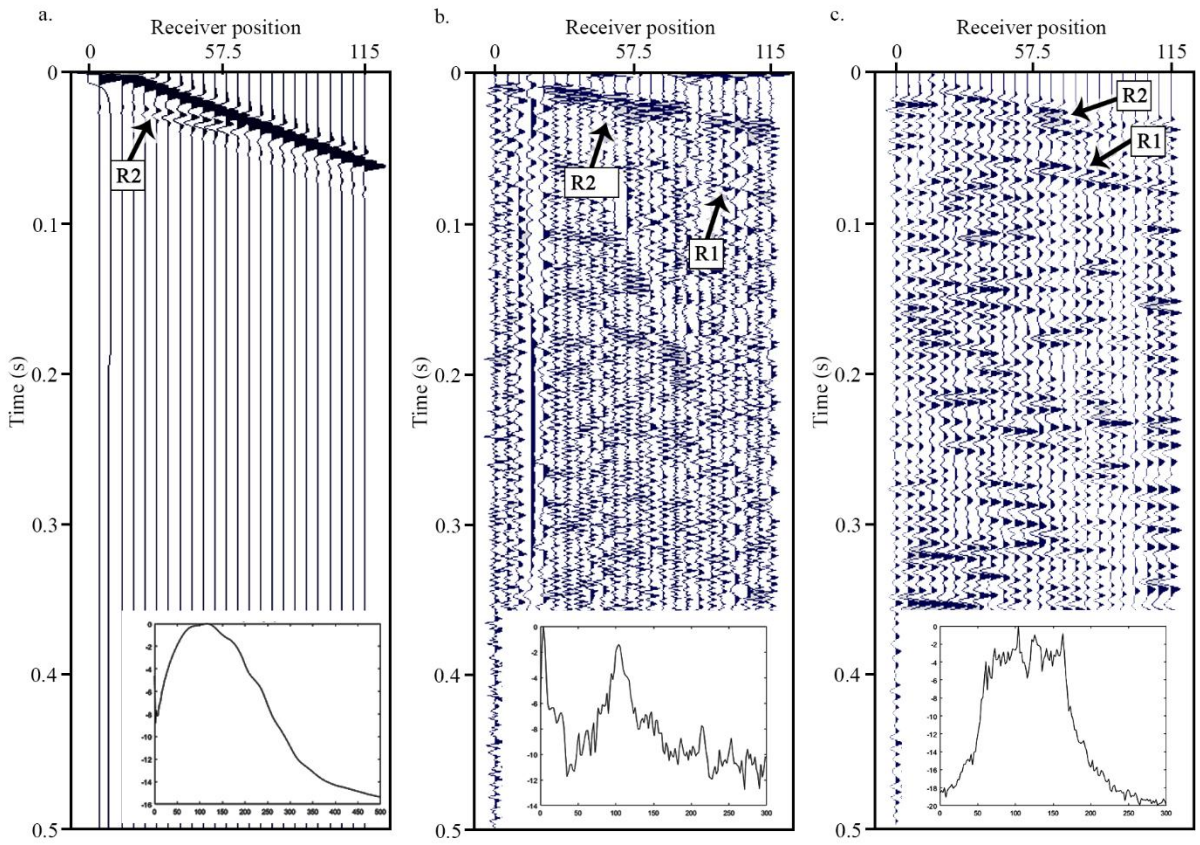
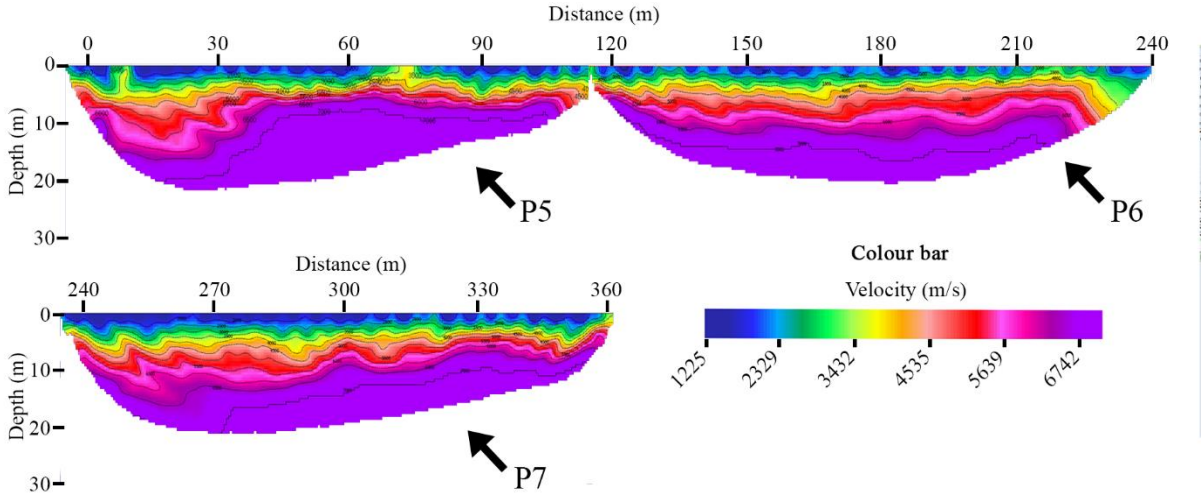
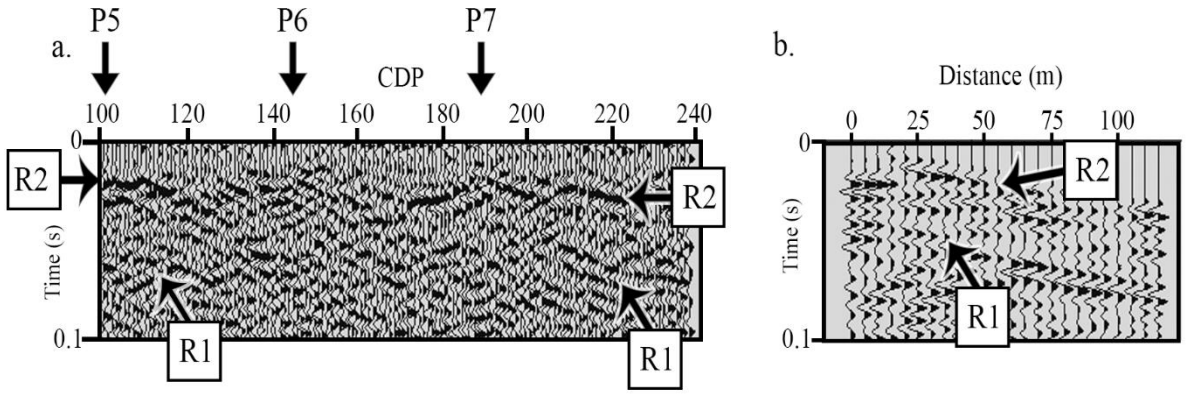


Figure 5: Shot gathers examples from P5 shot-5, with their frequency spectrum. Shot gathers highlight clear reflections marked by black arrows. (a) Synthetic shot gather modelled from the geological model, showing one clear reflection (R2) due to the UG2. (b) Raw shot gathers, with reflections overshadowed by high frequencies. The frequency spectrum has frequency ranges of 0 - 1800 Hz as a result of the sampling rate of 0.25 ms. Spurious ringing can be observed on the raw shot gather. (c) The processed shot gathers, showing clear reflections, with one of the reflections not easily identified on the synthetic gather and the raw shot gather.



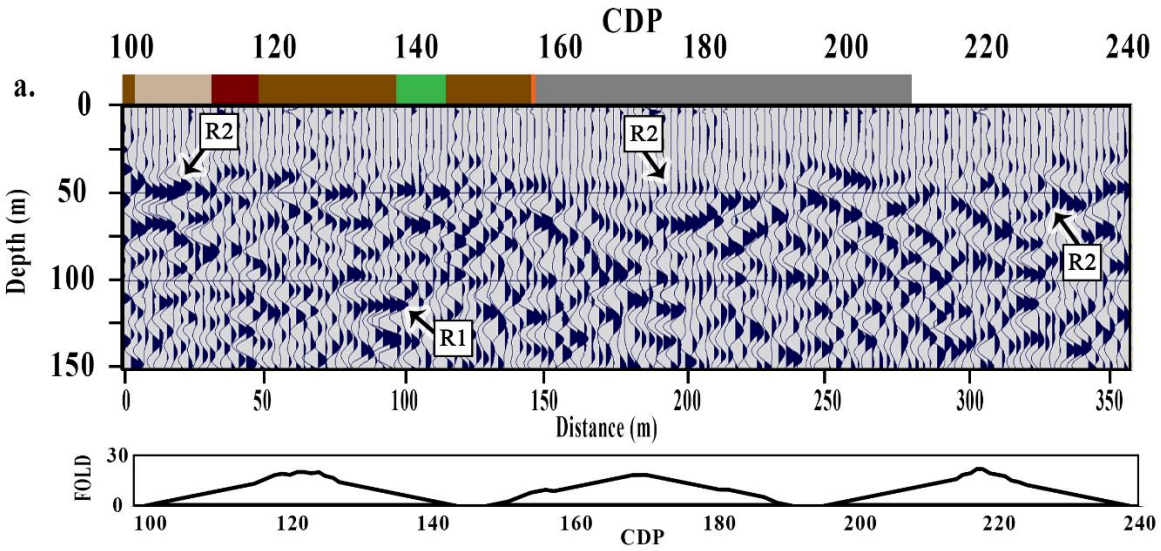
4671

4672 ***Figure 6:*** Near surface tomogram showing the upper 30 m of P5-7. The average top velocities
4673 match those of the rock in the area. The tomogram has low confidence at areas were P5, P6 and
4674 P7 were merged and edges due to low fold.



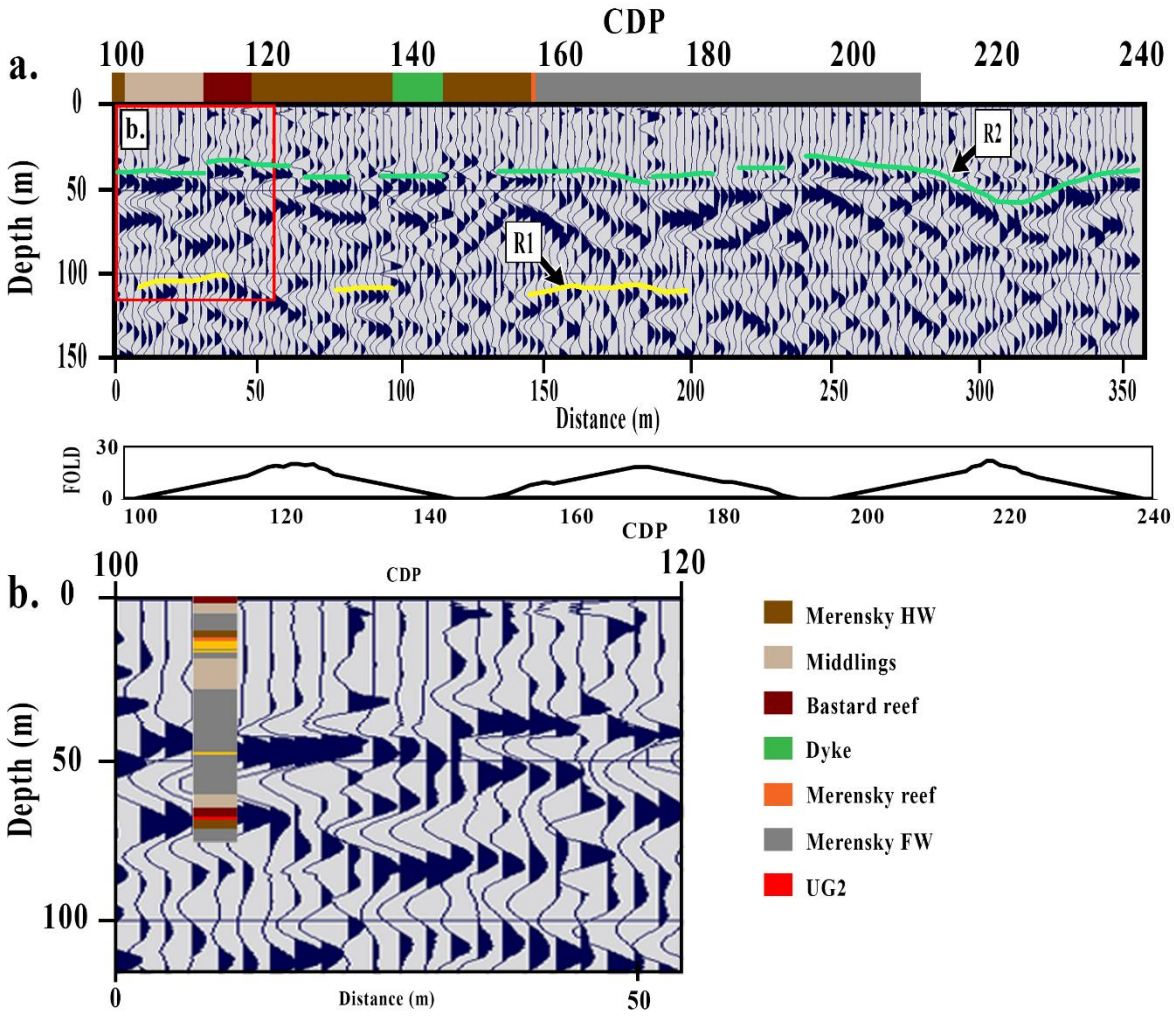
4675

4676 ***Figure 7:*** (a) Unmigrated time stack section and (b) a processed shot gathers along P5. The
4677 reflections identified on the processed shot gather are observed on the unmigrated stack section.



4678

4679 ***Figure 8:*** (a) Unmigrated depth stack section of P5-7 showing horizontal to dipping reflectors.
4680 Prominent reflections are observed at the edges and the coherency decrease at areas of low fold.



4681

4682 ***Figure 9:*** (a) Migrated stack section of P5-7 with borehole 1 (BH1) overlaid (b), showing how
4683 reflection R2 correlates with the UG2 package. The arrows mark the identified reflections detailed
4684 in the text. Red outline shows the focus area where the seismic tomograms are overlaid.

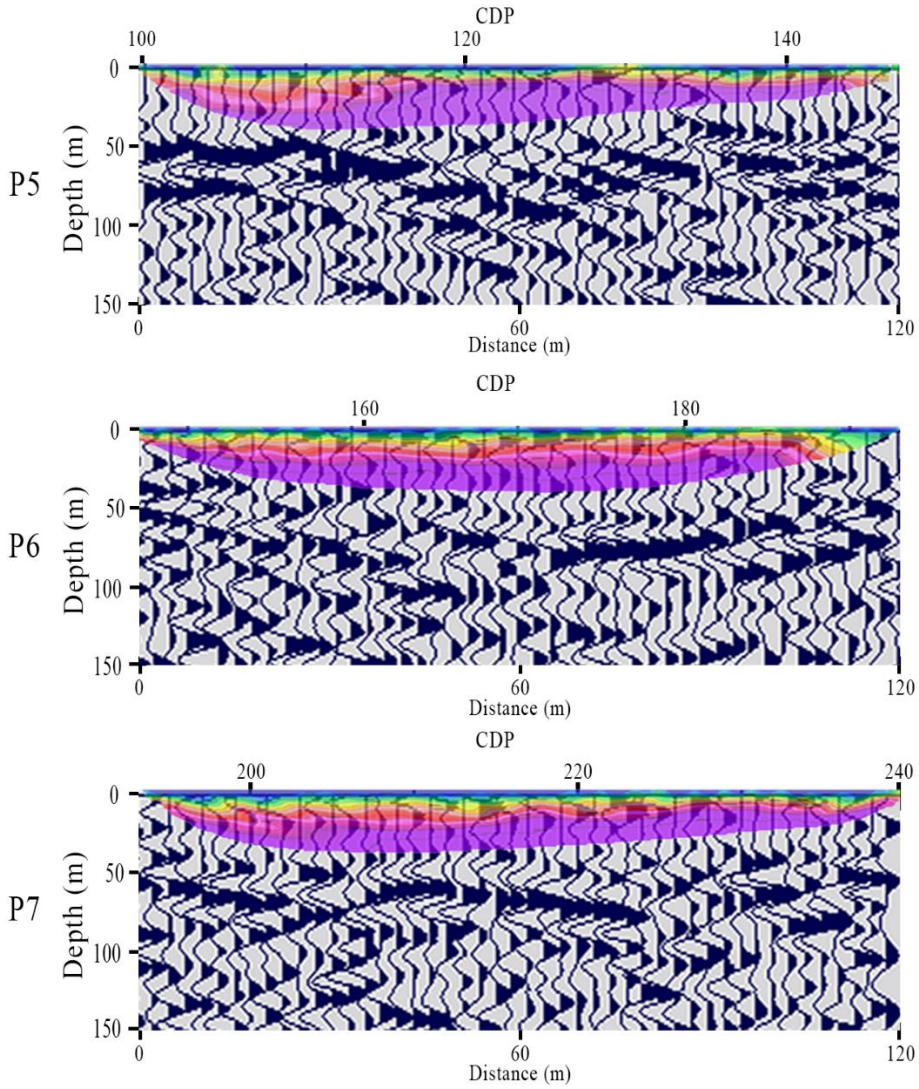


Figure 10: Seismic sections of P5, P6 and P7 showing a depth of 150 m, overlaid by velocity tomograms to correlate the reflections. The tomograms reach a maximum depth of 30 m, which is above the first prominent reflection (~70 m)

LIST OF TABLES

Table 1: Maseve Mine seismic data acquisition parameters of the seven profiles along the incline tunnel.

Line	**P1**	**P2**	**P3**	**P4**	**P5**	**P6**	**P7**
Number of receivers	24	24	24	15	24	24	24
Profile length	115	26	26	28 m	115 m	115 m	115 m
Direction	SW-NE	On Pillar	SE-NW	On Pillar		SE-NW	
Recording length	500 ms	300 ms	150 ms	150 ms		500 ms	
Sample interval	0.25 ms						
Vertical stacks	4						
Source spacing	5 m		2 m			5 m	
Source type	5 Kg Sledgehammer						
Receiver spacing	5 m	2 m	1 m	2 m		5 m	
Geophone frequency	4.5 Hz	4.5 Hz	4.5 Hz 14 Hz	4.5 Hz		4.5 Hz	

Table 2: Processing steps applied reflections seismic dataset from Maseve mine.

	Process	Parameters	
1	Data input + reformat	From SEGD to SEGY	✓
2	Geometry assignment + CDP bin	Sources and receivers assigned to each trace + CDP size 2.5 m	✓
3	Trace editing	Kill noisy traces	✓
4	First break picking	Automatic, manual picking	✓
5	Floating datum statics correction	Fixed datum elevation: -602 m Replacement velocity: 5500 m\s	✓
6	Refraction short wavelength static correction	2 layers model based on the first break picking. RMS error 1.45 - 2 ms	✓
7	Trace muting	Top mute using first breaks	✓
8	Bandpass filtering	50-60-160-170 Hz	✓
9	Automatic gain control	Window: 50 milliseconds	✓
10	Balance	500 milliseconds	✓
11	F-k filtering	Surgical muting, Dip = 1.2m/s per trace	✓
12	Velocity analysis	Constant Velocity Stack	✓
13	NMO corrections	5500 - 6500 m/s, Stretch mute: 70%	✓
14	Residual statics	Repeat NMO corrections twice	✓
15	DMO	Kirchhoff common-offset	✓
16	Stack	Normal	✓
17	Bandpass filtering	80-90-150-160 Hz	✓
18	Post time migration	2D Kirchhoff	
19	Time to depth conversion	1D Constant velocity: 5500 m/s	✓

Appendix D: Integrated geophysical methods for boulder delineation to improve mining.

Sikelela Gomo[1], Moyagabo K. Rapetsoa[1], Musa S. D. Manzi[1]*, Emmanuel Onyebueke[1], Jureya Dildar[1], Mpofana Sihoyiya[1], Ndamulelo Mutshafa[1], Wesley Harrison[3], Julie E. Bourdeau[2], Oleg Brovko[1], Ian James[1] Gordon R. J. Cooper[1], Stephanie Scheiber[1], Raymond J. Durrheim[1]

[1]School of Geosciences, University of the Witwatersrand, Johannesburg, Private Bag, Wits, 2050, Republic of South Africa.

[2]Geological Survey of Canada, 601 Booth Street, Ottawa, Ontario, K1A 0E8, Canada.

[3]SRK Consulting, SRK House, 265 Oxford Rd, Illovo, Johannesburg, 2196, Republic of South Africa.

*Email: musa.manzi@wits.ac.za

Abstract

Near-surface boulders can pose serious challenges to open-cast mining. They often introduce complexities, delays in drilling, blasting and excavation programs, which subsequently decrease mining efficiency, increase mining risks and costs. The location of subsurface boulders and the identification of other geological features that may impact mining activities (e.g., fractures, the presence of iron-rick ultramafic pegmatites, and the variation in weathering across a mining region) is necessary to reduce the challenges posed by these geological features, therefore optimizing mining efficiency. In this study, magnetics, electrical resistivity tomography, seismic refraction tomography, ground penetrating radar, and borehole data are integrated for boulder delineation and mapping of other geological features that may impact mining using an unmined section at Tharisa Mine, Bushveld Complex (South Africa), as a test site. The results obtained from the different geophysical techniques are found to complement each other, and successfully delineate boulders, fractures, iron-rick ultramafic pegmatites and the variation in weathering and layering across the area. The incorporation of geophysical results can thus improve mining efficiency, while reducing mining risks and costs.

KEYWORDSs: Boulders, Magnetics, Resistivity, Seismic refraction, Ground penetrating radar.

INTRODUCTION

The development of mines and the optimum exploitation of mineral resources are paramount factors for the economic, societal and environmental development of countries. The presence of boulders in mining operations is problematic as these represent obstacles that may decrease productivity (e.g., delay blasting, drilling and excavation), as well as increase mining and engineering costs, and risks (Felletti and Beretta, 2009; Dan et al., 2016; Shao et al., 2020). Boulders are defined as rock fragments with a diameter greater than 256 mm, which may occur in different sizes and shapes, and appear as a corestone surrounded by concentric shells and/or embedded in saprolite. They are formed by chemical (spheroidal weathering) and/or mechanical processes (e.g., blasting) (Udden, 1914; Dan et al., 2016; Shao et al., 2020). Boulders formed by chemical processes are referred to as subterranean boulders, while those caused by mechanical processes are referred to as subaerial boulders (Twidale and Romani, 2005).

It is therefore important to locate boulders beforehand to adequately plan, and thus minimise any deleterious effects on mining and engineering operations. Although there is a paucity of integrated geophysics studies to detect and map boulders, Jee and Ha (2007) discuss the viability of using electrical resistivity tomography (ERT), ground penetrating radar (GPR), seismic refraction tomography (SRT) and magnetics to delineate boulders during tunneling. Several other case studies, though not based on boulder delineation, also demonstrate the successful mapping of boulders and boulder zones using various geophysical techniques. For instance, Musil et al. (2002) employed seismic reflection and refraction combined with drilling to map the internal structure, including suspended boulders, of the lower boundary of the Muragl rock glacier (Switzerland). Cardarelli et al. (2010) applied both ERT and SRT to locate cavities in the near subsurface, which, when filled with air, have a response similar to boulders. Ettinger et al. (2014) used GPR to study the internal geometry of a volcaniclastic fan produced by aggradation during a lahar event from the Cotopaxi volcano (Ecuador). Interestingly, GPR results resolved boulders hosted within the volcaniclastic fan. In a similar study, Gomez et al. (2018) utilized GPR, along with other geospatial techniques, to study the spatial distribution of boulder-size clasts at the Semeru volcano (Indonesia), gaining insights on how their distribution relates to valley morphology and the dynamic deposition of lahars.

Subterranean boulders (corestones) in the weathered zone are often by-products of chemical weathering, appearing as more competent and less altered than the host rock (Durgin, 1977; Dan et al., 2016). These boulders are normally separated or compartmentalized by fractures (joints and/or fault zones) and soft cemented materials with lower densities, compaction and competence (Jee and Ha, 2007). A number of such boulders have been observed in the Bushveld Complex of South Africa, where they became exposed by mining operations. The area of interest consists of anorthosite to norite boulders embedded in saprolite clays (weathered rock). The boulders are more competent and have higher magnetic susceptibility compared to the surrounding weathered rocks. As a result, the boulders are more resistive, dense and magnetic as compared to the surrounding weathered rocks.

In this paper, we present the results from integrated geophysical surveys (i.e., magnetics, ERT, SRT and GPR) that were conducted at an unmined section at the Tharisa Mine in the Bushveld Complex. The main aim of the integrated surveys was to delineate and characterise subsurface (or subterranean) boulders in saprolite clays. Generally, boulders measure between one and two meters across, however, in this study we designed our surveys to target boulders larger than four meters since smaller boulders can be easily disposed of by mining operations. A secondary aim was to map geological site features (e.g., lithologies, fractures) that could have a direct impact on mining operations which would ultimately facilitate effective mine planning (Onyebueke et al., 2018). The most significant feature that geophysical methods bring to mineral exploration and mining is the ability to map complex and subsurface geological features at greater resolution than any other geological method (Malehmir et al., 2012).

GEOLOGICAL BACKGROUND

The research was carried out at Tharisa Mine, an opencast Platinum Group Metals (PGMs) and chrome mine, situated in the south-western limb of the Bushveld Complex, which itself is located in the northern portions of the Kaapvaal Craton (Fig. 1a). The Bushveld Complex hosts the largest ultramafic-mafic layered intrusion in the world, with an aerial extent of about 66,000 km^2 and a thickness between 7-9 km (Cawthorn, 2015). The complex formed about 2.05 Ga and hosts stratiform PGM, chromium and vanadium deposits (Scoates et al., 2021). The Bushveld Complex was emplaced through a series of magma injection events, intruding at the unconformity separating the Transvaal Supergroup (Pretoria Group) sedimentary rocks and the Rooiberg Group volcanic

rocks (Kruger, 2005, Perritt and Roberts, 2007; Cawthorn, 2015). The complex is subdivided into three major magmatic units, the: 1) Rustenburg Layered Suite (RLS), 2) Rashoop Granophyre Suite (RGS), and 3) Lebowa Granite Suite (LGS); and is split up into five limbs, i.e., four outcropping limbs (western, far-western, eastern and northern limbs) and one buried limb (south-eastern limb) (Eales and Cawthorn, 1996; Cawthorn and Webb, 2001). The mafic-ultramafic rocks of the RLS host most of the PGM mineralization of the Bushveld Complex.

The RLS is subdivided into five zones known as the (from bottom to top): 1) Marginal (norites), 2) Lower (cyclic pyroxenite-harzburgite-dunite), 3) Critical (cyclic pyroxenite-norite-anorthosite-chromitite), 4) Main (gabbronorites), and 5) Upper zones (ferrogabbro-anorthosite-magnetitite and apatite-bearing diorites) (Fig. 1b; Barnes and Maier, 2002; Cawthorn, 2015). The economically significant PGM deposits are found in the Critical Zone, of which the Merensky Reef (MR) and Upper Group 2 chromitite (UG2) units define two of the world's largest platinum-bearing orebodies (Cawthorn et al., 2005; Fig. 1b). The Critical Zone is further subdivided into the Upper (cyclic orthopyroxenite, norite and anorthosite units) and Lower Critical zones (cyclic chromitite, harzburgite and pyroxenite units) (Fig. 1b; Barnes and Maier, 2002; Hunt et. al., 2018). The transition zone between the Upper and Lower Critical zones occurs where cumulus plagioclase first appears (Eales and Cawthorn, 1996; Barnes and Maier, 2002, Cawthorn, 2015).

Layered rocks of the RLS were subsequently disrupted by the intrusion/infiltration of iron-rich ultramafic pegmatite bodies (IRUPs) which crystallized from iron-rich intercumulus and residual melts (Scoon and Mitchell, 1994; Reid and Basson, 2002). IRUPs are coarse-grained rocks that occur in the form of pipes, veins and occasionally, sub-concordant sheets. Furthermore, IRUPs are normally accompanied by numerous fractures and are predominantly found in the Upper Critical, Main and Upper zones. Tharisa Mine is stratigraphically located in the Critical Zone and is underlain by the Middle Group (MG) chromitite layers (Fig. 1a-b). The MG chromitite layer package is a deposit of five tabular chromitite layers named MG0, MG1, MG2, MG3 and MG4 (Fig. 1b). The main economic horizons of interest at Tharisa Mine are: MG1, MG2, MG3, MG4 and MG4A. In the past, the UG1 was also extracted at the mine, as both the UG2 and UG1 outcrop nearby. The major metal components mined by Tharisa Mine are platinum, followed by palladium and ruthenium.

OCCURANCE AND FORMATION OF BOULDERS

Igneous rocks often contain several fracture types (e.g., net, oblique, vertical and horizontal fractures) of variable origin (e.g., tectonic, thermal, epigenetic, anthropogenetic) (Jinghong et al., 2011; Vitale and Isaia, 2014). Fractures in the Bushveld Complex often consist of planar and non-planar joints, i.e., fractures or cracks with no characteristic shear displacement (Fig. 2a-d). The joins are ubiquitous, often planar in nature and occur in sets with approximately the same orientation. Their intensity varies widely across the complex and are largely attributed to tectonic stress (Wilson et al., 2005; Twidale and Romani, 2005; Roberts and Clark-Mostert, 2010). Some fractures observed in the Bushveld Complex (e.g., the prevalent layer-parallel faults and ramps) are interpreted to have formed due to crustal flexure (folding) caused by the intrusion of high-density mafic-ultramafic rocks (isostatic readjustment) (Eales et al., 1993; Cawthorn and Webb, 2001; Perritt and Roberts, 2007). According to Perritt and Roberts (2007), the Critical Zone commonly displays layered-parallel and ramp faults (duplex, frontal, and lateral ramps) with prominent striations or corrugations, which are subsurface features often exploited by near surface weathering processes to breakdown subsurface rocks.

Joint sets of varying orientation (cross cutting joint sets) often break down large masses of rock into separate fracture-bounded blocks (Fig. 2a). In subsurface environments, spheroidal weathering exploits these fractures (along with other rock features, such as crystal boundaries, cleavages, etc.) to break down the bedrock and initiate the formation of boulders (Fig. 2b-c; Twidale and Romani, 2005; Fletcher et al., 2006). The process is mainly driven by moisture from infiltrating meteoric waters, which contains gases, chemicals and biota, that altogether break down fresh bedrock into regolith (saprolite and boulders; Fig. 2c). The weathering process decays the bedrock starting from the joints and moves inwards into the core of the fracture-bounded blocks, forming boulders (called subterranean boulders) embedded in saprolite. The amount of weathering, and thus the boulder size and shape all depend on prevalent fracture systems, shallow ground water chemistry, duration and intensity of weathering, as well as the rheology of the rock (Twidale and Romani, 2005; Dan et al., 2016). Along with subterranean boulders, subaerial boulders (blasting and excavation-induced boulders) are often present in opencast mining environments, including in the study area (Fig. 2d).

GEOPHYSICAL SURVEYS

Prior to acquiring geophysical data, we collected rock samples and measured their physical properties, such as P-wave seismic velocity and magnetic susceptibility, to examine the feasibility of the study, and investigate if there is any significant physical property contrast between the boulders (fresh anorthosite and norite) and host rocks (weathered anorthosite and norite) (see Table 1). We conducted magnetic, electrical resistivity tomography (ERT), seismic refraction tomography (SRT) and ground penetrating radar (GPR) surveys to map boulders, weathered zones, fresh bedrock zones and other subsurface geological features (i.e., overburden, fractures and IRUPs in the top 10 – 40 m). Figure 3 shows the survey locations of the different geophysical techniques.

Geophysical data acquisition and processing

Magnetic data

The magnetic data were acquired using three portable magnetometers, two G856 proton precession magnetometer and one G895 Cesium vapor magnetometer with an integrated GPS receiver (WGS 84, accuracy of ± 1 m). Both the proton precession magnetometers (G856) were used as base station magnetometers and were placed in separate areas with minimal noise. One of the magnetometers was set to collect data every 15 seconds and the other at every 30 seconds. The magnetometer with the best (least spikes) diurnal curve was used to correct the acquired field data. The Cesium vapor (G859) magnetometer was used as a rover magnetometer. In order to reduce the effect of near-surface magnetic materials and minerals, the proton precision magnetometers were mounted on 2.5 m high vertically positioned, non-magnetic, aluminium poles. The rover magnetometer (G859) was carried on a non-magnetic backpack, with magnetic sensor and GPS receiver antenna heights of approximately 2 - 3 m and 1.7 - 2 m from surface, respectively. To obtain high-resolution data and avoid spatial aliasing, the magnetic data were acquired in a walking mode using a sampling rate of 1 second, line spacing of 2 m, over an area of 150 × 100 m. Seventy-five SSW – NNE, magnetic survey grid lines were collected over the magnetic grid survey area (Fig. 3).

Processing of the magnetic data involved removing diurnal variations, de-spiking and micro-levelling using the Fast Fourier Transform (FFT) frequency domain technique (which involves using the directional cosine filter and Butterworth filters) in order to reduce directional effects and remove long wavelength signals (detrending). Manual deculturing, as to prevent the

removal of important shallow geological signals, of the original total magnetic intensity (TMI) grid and interpolation of the removed data points, using the minimum curvature technique, was subsequently carried out.

Magnetic enhancement techniques were applied to the data so as to correct and enhance specific characteristics of magnetic sources (e.g., magnetisation, position, limits and discontinuities). The reduction to magnetic pole (RTP) technique was applied to correct the position of the magnetic sources and their induced magnetization. The vertical tilt angle filter was applied to sharpen the edges of the magnetic sources (Cooper and Cowan, 2008; Von Dobeneck et al., 2021).

Electrical resistivity tomography data

The resistivity survey consisted of 5 survey lines (RL1 to RL4), with line RL3.1 being a high-resolution resistivity line collected over a smaller section of profile RL3 due to the observation of hard-rock anorthosite to norite boulders at the surface (Fig. 3). Four of the five resistivity lines (RL1, RL2, RL3 and RL3.1, WNW-ESE trending lines) were acquired on a graded sandy road, situated on the original surface of the opencast mine, close to the highwall. The lines were acquired perpendicular to the dip of the Bushveld Complex rocks in the area. Profile RL4, a SSW – NNE trending line, was acquired largely on partly loose sandy sediments, north of the road and parallel to the dip of the rocks in the area (Fig. 3). The data were acquired using an automated ABEM 1200 resistivity system and an electrode spacing of 1 m and 2 m. The profile length of the survey lines (excluding RL3.1) was 160 m, and that of RL3.1 was 80 m. The Dipole-Dipole and Schlumberger methods were used to acquire the data. The area along which profiles RL1, RL2, RL3 and RL3.1 were collected was a flat graded area with negligible topographic variation. Survey RL4 was acquired over an area with slightly more sand cover and topographic variation (~1 m), especially in the northern side of the profile. Due to the effects of metal cased boreholes along profile RL4, the resistivity results of RL4 are not presented in the text.

The collected electrical resistivity tomography (ERT) data were first manually de-spiked and inverted to produce their inverted models. A weighted least-squares objective function coupled with linear filtering was used to carry out the inversion. Furthermore, an unstructured triangular finite element mesh, that allows for complicated model geometry, was used to produce the inverse

models (Binley and Kemna, 2005; Blanchy et al., 2020). All the calculated resistivity inverse models reached the target root square mean error of ~1 in 3 to 4 iterations.

Seismic refraction tomography data

The seismic data, SL1 to SL4, were acquired along the resistivity survey lines for integration purposes (Fig. 3). The data were acquired using 48 (14 Hz) geophones connected to two 24-channel Geometric geode seismographs. To obtain high near-surface resolution, the data were collected using a geophone spacing of 2 m, yielding a common midpoint (CMP) of 1 m. Shots were taken at every receiver. An asymmetric split-spread geometry with fixed receiver location, at a sampling interval of 1 ms and a recording length of 1.5 seconds, were used to acquire the data. The ESS MINI Base System (weight-drop) mounted on a vehicle and/or 5 kg sledgehammer were used as seismic energy sources, and a 20 × 20 × 20 cm^3 aluminium metal base coupling plate was used to improve the source-to-ground coupling. A stack value of four was used to improve the signal-to-noise ratio. A high-cut filter of 250 Hz was used to eliminate the high frequencies that distort the acquired data. During the recording process, the acquired data were carefully monitored to avoid the introduction of noise generated by mining activities (e.g., drilling, blasting, moving vehicles and water pumps).

Figure 4(a-c) shows the comparison of raw seismic shot gathers of survey lines SL1, SL3 and SL4. Marked on the raw shot gathers are refracted (red arrows), possible reflected (blue arrows) that appear to be masked by surface waves, and air waves (blue shaded areas). Across all the gathered seismic data, the P-waves first breaks are present within the first 75 ms. Figure 4(c) (green arrow) shows an example of noise generated by drilling (between receiver 24 and 36) in seismic profile SL4. To construct the 2D P-wave refraction models, we used the 7,200 first arrival picks across profiles SL1, SL2 and SL3. The processing steps are summarized in Table 2. The first break data were picked manually. First break picks and travel-time residuals for the P-wave velocity tomograms are given in Figure 5(a, c, e) and Figure 5(b, d, f) respectively. Both the first break and travel-time residuals are illustrated as a function of offset. After 10 iterations, the final models for SL1, SL2, and SL3 profiles had an rms error of 4.6, 4.7 and 4.9, respectively (Fig. 5 b, d, f). Data acquired along the SL4 survey line are not presented in the text due to poor sensor-ground coupling caused by loose soil dumps along the survey line.

Ground penetrating radar

Table 3 shows the geometry parameters used to acquire ground penetrating radar (GPR) data. The GPR data were acquired using the GSSI – SIR 4000 ground penetrating radar. The acquisition procedures involved moving the GPR cart across the 3D grid (GPR 3D) in zigzag direction and along the 2D lines GL1 and GL3 (Fig. 3). Common-offset reflection survey mode was used for data acquisition with 0.02 m trace spacing, 0.2 ns sampling interval and 120 ns listening time. To improve the signal-to-noise ratio, 10 vertical radargram were stacked at each sampling point.

The processing of the GPR data involved removing the acquisition delay time, applying energy decay gain to correct for the spherical spreading, and intrinsic attenuation of the signal. A bandpass filter (80 – 400 MHz) was used to attenuate unwanted frequency components. The dominant frequency is approximately 300 MHz. Subtract-mean (dewow) and subtracting average/background removal filters were applied to enhance the sub-vertical reflectors as well as suppressing the background noise and the direct arrivals. The synthetic reflection hyperbolas were matched with observed diffraction patterns emanating from underlaying boulders, so that a 2D velocity field can be created. The GPR profiles were migrated and converted to depth with a constant velocity of 0.1/0.2 m/ns.

RESULTS

Magnetics

Figure 6 presents the detailed total magnetic intensity map of the study area, including the results of the magnetic enhancement techniques. Specifically, Figure 6(a-c) presents the total magnetic intensity (TMI), reduced to magnetic pole (RTP) and the vertical tilt angle maps of the study area, respectively. The TMI map, Figure 6(a), shows the variation and distribution of positive and negative magnetic anomalies in the study area. The application of the RTP technique provides the corrected position of the magnetic sources and their induced magnetization (Fig. 6b). From the computation of the RTP conversion, it is observed that a circular feature with remanent magnetisation is present (indicated by a black dotted circle). The vertical tilt angle filter sharpens the variation between the low and high magnetic intensity zones (Fig. 6c). The vertical tilt angle map reveals that, both the high and low magnetic intensity zones are largely interconnected (indicated by arrows in Fig. 6c). The black and white arrows in Figure 6(c) each demonstrate an example of a magnetic low and high zone, respectively. The effects of weathering (gradual variation in magnetic intensity moving from the magnetic low to high regions), the presence of

fractures (zones that separate the red zones, also appearing as blue) and of a feature with remanent magnetisation are well captured in Figure 6(a-c).

Electrical resistivity tomography

The 160 m long survey lines acquired across the study area (Fig. 3) are observed to reach depths between 21 to 30 m, depending on the type of array used. The resistivity tomography results, shown in Figure 7, show a progressive increase of the resistivities of the rocks with depth. The near-surface (top ~6 to 5 m) is demarked by a conductive zone (low resistivity, blue coloured zone) with resistivities of ~3 – 40 ohm.m. The thickness of this low resistivity zone is observed to vary from one resistivity profile to another, but it is between 6 – 7 m (Fig. 7). This top resistivity low zone is underlain by a zone of much higher resistivities (~40 – 3,162 ohm.m), coloured as light green to yellow zone. The contrast observed between these two layers is representative of the sharp contrast observed at the topsoil-fractured bedrock interface, visible on the highwall present a few meters away from the study area (see Fig. 2b). Underlying the green to yellow zone is the light to dark red zone, a zone of much higher resistivity (~3,162 to ~10,000 ohm.m). The variation in the resistivity of these three observed zones is complex, both moving along and across the profiles (Fig. 7). The Schlumberger array is observed to best demonstrate the resistivity variation across depth and the bedrock (high resistivity zones, indicated by white arrows) (Fig. 7a, c, e, g), while the dipole-dipole array (Fig. 7b, d, f, h) best demonstrates potential fractures, highly weathered zones (low resistivity zones separating high resistivity zones, indicated by black arrows) and boulders (semi-circular, high resistivity features in low resistivity zones, indicated by blue arrows).

Seismic refraction tomography

The P-wave refraction tomograms largely demonstrate an increase in P-wave seismic velocities with increasing depth. Figure 8 illustrates the final P-wave refraction models (Fig. 8a, c, e) for profiles SL1, SL2, and SL3, and their ray paths (Fig. 8b, d, f). The tomograms reveal the presence of roughly three P-wave seismic velocity zones (layers) of varying thickness, both along and across the seismic profiles (Fig. 8). The near-subsurface seismic velocity zone, light brown zone (indicated by a white arrow), exhibits the maximum P-wave velocity of ~1,400 m/s. Based on the inversion models, the depth extent of the velocity low zone varies from surface to a maximum depth of about 20 m (Fig. 8). This top light brown layer is underlain by a yellow to green seismic P-wave velocity zone (indicated by a light blue arrow) of relatively higher velocities (~1,400 to

~4,000 m/s). The thickness of this layer varies across the profiles. The layer consists of semi-circles/ellipses of higher velocities embedded within it, which are interpreted as boulders. Underlying this second velocity zone is a light to dark blue seismic velocity zone of higher P-wave velocities (~4,000 to ~6,400 m/s, indicated by a black arrow). This light to dark blue seismic velocity zone exhibits variable depth from the surface. The observed seismic velocity zones consist of zones of disturbed layering, possible fracture (jointing and faulting) and boulder zones (Fig. 8).

Ground penetrating radar

The ground penetrating radar (GPR) sections show radar traces (radargram) plotted against time and distance (Fig. 9). The x-axis represents the distance along the survey line while the y-axis represents the travel-time of the radar pulses. The radargrams show several reflections (dark blue arrows) and diffraction events (light blue arrows), probably emanating from buried boulders and loose soil cover, as well as from the background noise (Fig. 9).

INTERPRETATIONS AND DISCUSSION

Magnetic susceptibility inversion models

Noritic and anorthosite rocks can be magnetic due to the presence of accessory minerals such as magnetite and ilmenite (Dunlop et al., 2010; Soumya et al., 2017). The weathering of such mafic rocks, i.e., norites and anorthosites, results in the formation of soil, with silicate minerals breaking down into clay minerals (conductive minerals), and iron-bearing minerals (e.g., magnetite and ilmenite) breaking down into iron oxides of varying magnetic susceptibility (Lu et al., 2008; von Dobeneck, 2021). The weathering of magnetite initially forms oxidized ferrimagnetic Fe-minerals, such as maghemite, followed by antiferromagnetic minerals such as hematite and goethite, which are far less magnetic (Lu et al., 2008; von Dobeneck, 2021). Both maghemite and hematite are observed at the mine site. In magnetic soils, however, magnetite can be weathered directly to hematite (Santana et al., 2001). Overall, there is a gradual loss of inherited thermoremanent and/or acquired chemical magnetization with progressive weathering, mainly associated with the alteration and the reduction of grain sizes of magnetic minerals in rocks (Lapointe et al., 1986; Harding et al., 1988; von Dobeneck et al., 2021). The reduction in magnetisation with weathering is observed in the magnetic susceptibility measured on hand samples in the laboratory (Table 1). Therefore, magnetic high zones (red- and pink-coloured zones) are interpreted to represent least-

5026 weathered areas, while low magnetic zones are interpreted to represent highly weathered areas
5027 (Figure 6). The high magnetic zones are caused by a shallow, fresher and less fractured bedrock
5028 component, and thus, these zones are likely to form blasting-induced boulders when blasted
5029 inadequately. Surrounding the high magnetic zones are lower magnetic intensity zones (green to
5030 dark blue-coloured zones; Fig. 6). The lower magnetic intensity zones represent highly weathered
5031 and fractured areas. The blue-coloured zones are thought to be the most weathered zones, where
5032 fractures in the rock accelerate chemical weathering processes. Thus, blue-coloured zones are
5033 where fresh rock was broken-down (e.g., formation of hematite and clay minerals) at a faster rate.
5034 The probability of finding isolated subterranean boulders surrounded by regolith should therefore
5035 be higher in such highly weathered zones.

5036 The semi-circular, low magnetic intensity feature at the centre of the magnetic maps (blue-
5037 coloured; Fig. 6) is thought to be a weathered remnant of a magnetised iron-rick ultramafic
5038 pegmatite (IRUP) (Scoon and Mitchell, 1994). IRUPs are typically weakly magnetic bodies (either
5039 positive or reverse magnetisation) that preferentially replace anorthosite-leuconorite lithologies
5040 (Scoon and Mitchell, 1994; Reid and Basson, 2002; Campbell, 2006). Such lithologies are noted
5041 at the Tharisa Mine. Furthermore, the semi-circular shape (when viewed perpendicular to layering)
5042 of the feature is consistent with the pipe-like shape (when viewed parallel to layering) often noted
5043 for IRUP bodies (Scoon and Mitchell, 1994). 3D models of the low magnetic susceptibility feature
5044 are presented in Figure 10(a-d), and confirm that the feature is indeed pipe-shaped. The models
5045 also reveal that the feature is shallow (Fig. 10b), at a depth of about 10 m from surface with a
5046 vertical extent of roughly 6 m (Fig. 10c-d), and has a magnetic susceptibility of 0.0188 SI units.
5047 Given that the feature terminates at depth (Fig. 10b-d) suggests that it is of a replacement nature,
5048 which also corresponds to the hypothesized origin for IRUPs (Scoon and Mitchell, 1994).
5049 However, amplitude inversion models are often biased towards high amplitude anomalies, which
5050 in this case corresponds to the IRUP body. This existing bias results in the attenuation of lower
5051 amplitude features, meaning that they may not be well resolved. Thus, although Figure 10(c)
5052 appears to resolve small-scale semi-spherical features (possible boulders), it is possible that
5053 additional small-scale features are missed because of their lower magnetic susceptibility compared
5054 to the high amplitude IRUP. Considering the high level of weathering encountered in the top
5055 subsurface (10 – 30 m depth), combined with the presence of an IRUP, which is commonly

accompanied by numerous fractures, these are promising factors for the presence of boulders in the area.

Integration of resistivity, seismic, and ground penetrating radar results

The electrical resistivity tomography (ERT), seismic refraction tomography (SRT) and ground penetrating radar (GPR) surveys acquired in this study were collected over an area of varying TMI; thus, over an area of variable weathering and magnetic susceptibility (Fig. 11). Figure 12 compares and correlates the inverted ERT, SRT and GPR sections across survey profile 1 (profile along which SL1, RL1 and GL1 where acquired) along with lithological data from a borehole (BH1) (Figs. 3 and 11). Both the resistivity and seismic inversion results for profile 1 correlate with the borehole BH1 data. At the location of BH1, in both the resistivity and seismic sections, the dark to light blue and light brown zones corresponding to a low resistivity and seismic velocity zone, respectively, represent the top 6 m section (core-loss zone) of BH1 (Fig. 12b, c). The dark to light blue near-surface zone is characterized by resistivities of ≤40 ohm.m and P-wave velocities of ≤1,400 m/s. This zone is interpreted to be the saprolite clay – regolith zone, a zone of high weathering activity. With increasing depth, a large increase in resistivity and P-wave seismic velocity of the subsurface rocks is observed.

The overburn norite and leuconorite layers, situated below the core-loss zone at depths between 6 m and 11 m, are characterized by higher resistivities and P-wave seismic velocities of ~40 to 3,162 ohm.m and ~1,400 to 3,600 m/s, respectively (Fig. 12). These layers, i.e., the overburn, norite, and leuconorite layers, along with the top portion of the norite rock appearing at a depth of 11m and greater are interpreted to constitute the weathered bedrock zone. The layers situated below the weathered bedrock zone, starting with the norite layer at a depth of about 11 m and extending to greater depths, are characterised by much higher resistivities and seismic velocities of ~3,162 to 10,000 ohm.m and ~3,600 to 6,400 m/s, respectively. These high resistivity and seismic velocity zones are interpreted to represent fresh bedrock zones, fresh norite to anorthosite zones, that have been least affected by near-surface weathering processes (Fig 12b-c). The linear features on the GPR GL1 radargram are responses from structural features (joints and faults), which are correlatable with both the resistivity and seismic tomograms (Fig. 12b-d).

The resistivity, seismic inverted models and the GPR radargram for profile 3 (line with RL3, SL3, GL3 and RL3.1) are presented in Figure 13. In both the ERT and SRT depth sections,

horizons (i.e., saprolite clay, weathered bedrock and fresh bedrock) are inhomogeneous and present abrupt changes that can be attributed to fracture-related distortions (Fig. 13a-c). The ERT, SRT and GPR sections reveal that the lithology along profile 3 is highly disturbed (Fig. 13a-d). At a distance of about 145 m to 160 m, along RL3 and about ~0.5 – 1 m next to the line, exposed rocks (outcrops), likely corresponding to norite boulders, were observed. A high-resolution (1 m) electrical resistivity depth section of the area adjacent to the outcrops along RL3, RL3.1, is presented in Figure 13(b). Notably, the high-resolution resistivity depth section shows several high resistivity features (boulders) embedded in a zone of low resistivity along the eastern edge of the section. Some of these boulders were outcropping on surface (BO1, BO2 and BO3 in Fig. 13e), which provided confidence in our interpretation. Furthermore, the high-resolution section (RL3.1) details a central high resistivity zone (orange to dark red-colours), interpreted as fresh bedrock, embedded in a low resistivity zone (green to dark blue coloured), which corresponds to weathered/altered rock (Fig. 13b). The central high resistivity zone is suspected to be an underground extension of the norite bedrock, based on outcrops near where profile 3 was conducted. The presence of buried boulders is also seen in the GPR radargram as diffractions. The location and depth of the boulders match relatively well between the resistivity tomograms and GPR radargram (Fig. 13a-d).

The GPR radargram interpretation of grid GPR 3D (Fig. 3) are shown in Figure 14. The maximum depth of penetration of the electromagnetic wave is ~10 m. Figure 14(a-b) show the 3D view interpretation of GPR 3D grid lines along the North – South (X) and East – West (Y) directions, respectively. The steeply dipping linear features observed in the radargram sections likely correspond to reflections emanating from joints and fractures. These structural features have variable dips (~30 – 50°). The formation of these structures could be as a result of gradual mechanical/chemical weathering or recent mining activity (e.g., rock blasting). The linear features could also correspond to boulder interfaces within the saprolite clay horizon (e.g., Fig. 14b). The gentle dipping (~10 – 15^{o}) reflections in GPR 3D data likely correspond to responses emanating from the saprolite clay-boulder and weathered bedrock interface. Several diffractions on GPR data are interpreted as boulders, ranging between 2 – 4 m wide at ~1 – 7 m depth. In future, we plan to process the reflection seismic surveys acquired along these boulders to enhance the detection of these boulders and constrain their 3D geometry through diffraction imaging approaches (Moser and Howard, 2008). The results will be compared to diffraction patterns observed on the GPR data

to constrain their interpretation. Several authors (e.g., Khaidukov et al., 2004) have demonstrated the effectiveness of analysing seismic response of similar features through diffraction imaging. Diffraction analysis on the seismic data has the potential to detect even small boulders that are beyond the resolution of other geophysical methods used in this study (Moser and Howard, 2008).

Geological model

By overlying the electrical resistivity and seismic depth sections on Google Earth maps, we observe that there is strong correlation between the magnetic intensity, P-wave seismic velocity and resistivity variations (Fig. 15). Specifically, the magnetic intensity is higher in regions with a thin low seismic velocity and low resistivity zone. The opposite is also true, whereby magnetic intensity is lower in regions with a thick low seismic velocity or low resistivity zone (Fig. 15a-f). The thicker the low velocity or conductive zone, the less magnetic the area. Thus, there is a strong depth correlation between magnetic intensity, seismic velocity and resistivity (Fig. 15). The correlation is better observed on the TVDR projected images (Fig. 15b, d, f). This may imply that where magnetic highs are prominent, the ground is relatively less weathered, and the depth of the fresh bedrock is closer to the surface. In regions where the magnetic low is prominent, the thickness of the saprolite clay and weathered horizons is larger, and thus the depth to the fresh bedrock is greater (excluding regions where remanently magnetised bodies are present, e.g., above the IRUP). In areas where boulders were identified (i.e., Figs. 12 and 13a-d), a magnetic high anomaly in a magnetic low zone is observed, which is interpreted to be associated with the less-weathered nature of the boulders as compared to the host rock (Fig. 15c-f). These observations demonstrate that electrical resistivity and magnetic surveys can be successfully used to infer the presence of subterranean boulders in magnetic environments. The integrated geophysical data (Figs. 12, 13 and 14), combined with surface geological observations and borehole lithological data, were used to generate a 3D geological model of the study area (Fig. 16a-b).

The integration of the data are of significant interest for exploration and planning mining activities (e.g., blasting, extraction of ore, slope/ground stability). Interestingly, not all boulders found at Tharisa Mine are subterranean boulders, some are subaerial boulders caused by blasting activity (Fig. 2d). In open-pit mining, subaerial boulders are large rock fragments often formed during excavation and bench blasting, due to inefficient rock breakage. These types of boulders are a recognised by-product of the drill-and-blast techniques (Leng et al., 2020). The drill-and-

blasting technique is a cost-effective scheme often used in mines to quickly excavate large areas and break down benches. Oversized boulders are typically formed when the blasting energy is not enough to cause sufficient rock breakage.

The efficiency in rock breakage is affected by several factors, including: 1) uneven distribution of energy, 2) structural features (discontinuities), 3) intact rock properties, and 4) the type of blasting (design) used to break down the rock (Yang et al., 2018; Leng et al., 2020; Park and Kim, 2020). Often, the formation of subaerial boulders is an indication that the drill-and-blast technique used at a mine is not optimized to reduce the formation of boulders or produce sufficient rock breakage. Unoptimized blasting produces large fragments (boulders), which will require extra resources to remediate. Dealing with boulders might necessitate drilling and/or blasting again, which ultimately slows down production.

Additionally, when blasting is not optimised (designed) adequately, excessive throw and fly-rocks occur. Throw and fly-rock are a by-product of blasting that occur when blasting activity is not designed adequately and the blasting energy is misdirected (Monjezi et al., 2011; Raina et al., 2015). Fly-rocks pose a huge safety hazard, as they may cause property damage and injuries at mines. Thus, by using intact rock property and structural discontinuity information obtained from integrated geophysical survey results, one can be able to design optimised drill-and-blasting programs that result in more efficient rock breakage (less boulders), while also reducing throw and fly-rocks (which translates to a safer working environment), thus leading to increased productivity and reduced mining activity costs.

CONCLUSION

This study demonstrates that the integration of magnetic, electrical resistivity, refraction seismic and ground penetrating radar methods can be successfully used to gain a better understanding of the subsurface in order to increase efficient mining and enable sound engineering decisions. We propose the use of integrated geophysical techniques for mining and engineering site characterization to best identify geological features such as boulders, fractures and horizons (i.e., regolith to fresh bedrock). The results presented here demonstrate that by targeting weathering, structural and magnetization effects in subsurface rocks in magnetic environments, geological features that characterize and complicate mining processes can be successfully identified. By mapping the inherent loss of magnetization, presence of remanent magnetization, the degree of

weathering, the competence and structural features of subsurface rocks, we were able to successfully map boulders, fractures, undulating lithological horizons, and remanent igneous features (i.e., iron-rick ultramafic pegmatites). From these findings, it can be concluded that the integration of numerous geophysical methods can be used to improve mine blasting programs, reducing the formation of blasting related boulders, and assisting in making cost-effective decisions.

ACKNOWLEDGEMENTS

We would like to acknowledge Tharisa Mine for funding this project and giving us permission to publish this work. The authors also thank the NRF (National Research Foundation) and DSI-NRF CIMERA (Centre of Excellence for Integrated Mineral and Energy Resource Analysis) for funding this research project. Special thanks go to the post-graduate students from the School of Geosciences at the University of the Witwatersrand who assisted with the data collection and the Tharisa Mine staff, especially Hloniphani Hlongwa and Robey Labuschagne, for assisting us during the data acquisition. Special thanks to Nathi Mntungwa from Tharisa Mine for scientific discussions and support. The authors would also like to acknowledge the constructive comments from two anonymous reviewers which have greatly improved the readability of this manuscript. Chief Editor, Tijmen Jan Moser, and Associate Editor, Alireza Malehmir, are also greatly appreciated for the editorial handling.

DATA AVAILABILITY STATEMENT

The data were acquired by the Wits seismic research centre team and are available on request from the corresponding author, subject to the approval from the mine owners.

CONFLICT OF INTEREST

The authors declare no conflict of interest.

REFERENCES

Barnes, S.J., and Maier, W.D., (2002) Platinum-group element distribution in the Rustenberg Layered Suite of the Bushveld Complex, South Africa. In The Geology, Geochemistry, Mineralogy and Mineral Beneficiation of Platinum-Group Elements. Edited by L.J. Cabri, Canadian Institute of Mining, Metallurgy and Petroleum, Special Volume 54, p. 431-458.

Binley, A., and Kemna, A., (2005) DC resistivity and induced polarization methods. In: Rubin Y., Hubbard S.S. (eds) Hydrogeophysics, Water Science and Technology Library, 50, 129 – 156. Springer, Dordrecht, 50. https://doi.org/10.1007/1-4020-3102-5_5

Blanchy, G., Saneiyan, S., Boyd, J., McLachlan, P., and Binley, A., (2020) ResIPy, an intuitive open source software for complex geoelectrical inversion/modeling. Computers & Geosciences 137, p.104423.

Campbell, G., (2006) High resolution aeromagnetic mapping of "loss-of-ground" features at platinum and coal mines in South Africa. South African Journal of Geology 109, 439-458.

Cardarelli, E., Cercato, M., Cerreto, A., and Di Filippo, G., (2010) Electrical resistivity and seismic refraction tomography to detect buried cavities. Geophysical Prospecting, 58, 685-696. https://doi.org/10.1111/j.1365-2478.2009.00854.x.

Carollo, A., Capizzi, P., and Martorana, R., (2020) Joint interpretation of seismic refraction tomography by cluster analysis to detect buried cavities. Journal of Applied Geophysics, 178, 1-21. https://doi.org/10.1016/j.jappgeo.2020.104069.

Cawthorn, R.G., (2015) The Bushveld Complex, South Africa. In: Charlier B, Namur O, Latypov R, Tegner C (eds) Layered intrusions. Springer, Berlin, pp 517–587. https://doi.org/10. 1007/978-94-017-9652-1.

Cawthorn, R.G., and Webb, S.J., (2001) Connectivity between the western and eastern limbs of the Bushveld Complex. Tectonophysics 330, 195-209.

Cooper, G.R.J., and Cowan, D.R., (2008) Edge enhancement of potential-field data using normalized statistics. Geophysics, 73, H1-H4. https://doi.org/10.1190/1.2837309

5226 Dan, M.F.M., Mohamad., E.T., and Komoo, I., (2016) Characteristics of boulders formed in
5227 tropical weathered granite: A review. Jurnal Teknologi, 78, 23-30.
5228 https://doi.org/10.11113/jt.v78.9635

5229 Dunlop, D.J., Özdemir, Ö., and Alvarez, V.C., (2010) Magnetic properties of rocks of the
5230 Kapuskasing uplift (Ontario, Canada) and origin of long-wavelength magnetic anomalies.
5231 Geophysical Journal International, 183, 645-658. https://doi.org/10.1111/j.1365-
5232 246X.2010.04778.x

5233 Durgin, P.B., (1977) Landslides and the weathering of granitic rocks. Geological Society of
5234 America III, 127 – 131.

5235 Eales, H.V., Botha, W.J., Hattingh, P.J., De Klerk, W.J., Maier, W.D., and Odgers, A.T.R., (1993)
5236 The mafic rocks of the Bushveld Complex: a review of emplacement and crystallization
5237 history, and mineralization, in light of recent data. Journal of African Earth Sciences 16,
5238 121-142.

5239 Eales, H.V., and Cawthorn, R.G., (1996) The Bushveld Complex. Layered Intrusions, p. 181-229.

5240 Ettinger, S., Manville, V., Kruse, S., and Paris, R., (2014) GPR-derived architecture of a lahar-
5241 generated fan at Cotopaxi volcano, Ecuador. Geomorphology, 213, 225-239.
5242 https://doi.org/10.1016/j.geomorph.2014.01.013.

5243 Felletti, F., and Beretta, G.P., (2009) Expectation of boulder frequency when tunnelling in glacial
5244 till: A statistical approach based on transition probability. Engineering Geology, 108, 43-
5245 53. https://doi.org/10.1016/j.enggeo.2009.06.006.

5246 Fletcher, R.C., Buss, H.L., and Brantley, S.L., (2006) A spheroidal weathering model coupling
5247 porewater chemistry to soil thicknesses during steady-state denudation. Earth and Planetary
5248 Science Letters, 244, 44-457. https://doi.org/10.1016/j.epsl.2006.01.055

5249 Gomez, C., Lavigne, F., Hadmoko, D.S., and Wassmer, P., (2018) Insights into lahar deposition
5250 processes in the Curah lengkong (Semeru Volcano, Indonesia) using photogrammetry-
5251 based geospatial analysis, near-surface geophysics and CFD modelling. Journal of
5252 Volcanology and Geothermal Research, 353, 102-113.
5253 https://doi.org/10.1016/j.jvolgeores.2018.01.021.

Harding, K.A., Morris, W.A., Balch, S.J., Lapointe, P., and Latham, A.G., (1988) A comparison of magnetic character and alteration in the three granitic drill cores from Eastern Canada. Canadian Journal of Earth Sciences, 25, 1141-1150.

Hunt, E., Latypov, R., and Horvah P., (2018) The Merensky Cyclic Unit, Bushveld Complex, South Africa: Reality or Myth? Minetals, 8, 1-35.

Jee, W.W., and Ha, S., (2007) Feasible boulder treatment methods for soft ground shielded TBM. Underground Space – the 4th Dimension of Metropolises, 217-22.

Khaidukov, V., Landa, E. and Moser, T.J., (2004) Diffraction imaging by focusing-defocusing, an outlook on seismic superresolution. Geophysics, 69(6), 1478–1490.

Kruger, F.J., (2005) Filling the Bushveld Complex magma chamber: lateral expansion, roof and floor interaction, magmatic unconformities, and the formation of giant chromitite, PGE and Ti-V-magnetitite deposits. Mineralium Deposita, 40, 451-472. https://doi.org/10.1007/s00126-005-0016-8.

Lapointe, P., Morris, W.A., and Harding, K.L., (1986) Interpretation of magnetic susceptibility: A new approach to geophysical evaluation of the degree of rock alteration. Canadian Journal of Earth Sciences, 23, 393-401.

Leng, Z., Fan, Y., Gao, Q., and Hu, Y., (2020) Evaluation and optimization of blasting approaches to reducing oversize boulders and toes in open-pit mine. International Journal of Mining Science and Technology 30, 373-380. https://doi.org/10.1016/j.ijmst.2020.03.010.

Lu, S-G., Xue, Q-F, Zhu, L., and Yu, J-Y., (2008) Mineral magnetic properties of a weathering sequence of soils derived from basalt in Eastern China. Catena, 73, 23-33. https://doi.org/10.1016/j.catena.2007.08.004.

Malehmir, A., Durrheim, R., Bellefleur, G., Urosevic, M., Juhlin, C., White, D.J., Milkereit, B. and Campbell, G., (2012) Seismic methods in mineral exploration and mine planning: A general overview of past and present case histories and a look into the future. Geophysics 77, WC173-WC190, https://doi.org/10.1190/geo2012-0028.1.

Monjezi, M. Bahrami, A., and Varjani, A.Y., (2011) Prediction and controlling of flyrock in blasting operation using artificial neural network. Arabian Journal of Geosciences 4, 421-425. https://doi.org/10.1007/s12517-009-0091-8.

Moser, T.J. & Howard, C.B., (2008). Diffraction imaging in depth. Geophysical Prospecting, 56, 627–641.

Musil, M., Maurer, H., Green, A.G., Horstmeyer, H., Nitsche, F.O., Muhll, D.V., and Springman, S., (2002) Shallow seismic surveying of an Alpine rock glacier. Geophysics, 67, 1701-1710. https://doi.org/10.1190/1.1527071.

Onyebueke, E. O., Manzi, M. S. D., and Durrheim, R. J., (2018) High-resolution shallow reflection seismic integrated with other geophysical methods for hydrogeological prospecting in the Nylsvley Nature Reserve, South Africa. Journal of Geophysics and Engineering 15, 2658-2673. https://doi.org/10.1088/1742-2140/aadbe3.

Park, J., and Kim, K., (2020) Use of drilling performance to improve rock-breakage efficiencies: A part of mine-to-mill optimization studies in a hard-rock mine. International Journal of Mining Science and technology 30, 179-188. https://doi.org/10.1016/j.ijmst.2020.03.010.

Perritt, S., and Roberts, M., (2007) Flexural-slip structures in the Bushveld Complex, South Africa? Journal of Structural Geology 29, 1422-1429. https://doi.org/10.1016/j.jsg.2007.06.008.

Raina, A.K., Murthy, V.M.S.R., and Soni, A.K., (2015) Flyrock in surface mine blasting: understanding the basics to develop a predictive regime. Current Science 108, 660-665.

Reid, D.L., and Basson, I.J., (2002) Iron-rich ultramafic pegmatite replacement bodies within the Upper Critical Zone, Rustenburg Layered Suite, Northam Platinum Mine, South Africa. Mineralogical Magazine 66, 895-914. https://doi.org/10.1180/0026461026660066.

Roberts, M.K.C., and Clark-Mostert, V., (2010) Is there some commonality between the geological structures in the Bushveld Complex and the Great Dyke?. The 4th International Platinum Conference, Platinum in transition 'Boom or Bust', The Southern African Institute of Mining and Metallurgy.

Santana, G.P., Fabris, J.D., Goulart, A.T., and Santana, D.P., (2001) Magnetite and its transformation to hermatite in a soil derived from steatite. Revista Brasileira de Ci*ê*ncia do Solo, 25, 33-42.

Schoor, M.V., and Fourie, C.J.S., (2015) A guide for APPLYING GEOPHYSICS to COAL MINING PROBLEMS in South Africa. Struik Nature, South Africa.

Scoates, J.S., Wall, C.J, Friedman R.M., Weis, D., Mathez, E.A., and VanTongeren, J.A., (2021) Dating the Bushveld Complex: timing of crystallization, duration of magmatism, and cooling of the World's largest layered intrusions and related rocks. J Petrol 62:egaa107. https://doi.org/10.1093/petrology/egaa107.

Scoon, R.N., and Mitchell, A.A., (1994) Discordant iron-rich ultramafic pegmatites in the Bushveld Complex and their relationship to iron-rich intercumulus and residual liquids. Journal of Petrology, 35, 881-917.

Shao, J., Zhang, Q., Wu, X., Lei, Y., Wu, X., and Wang, Z., (2020) Investigation on the water flow evolution in filled fracture under seepage-induced erosion. Water 2020, 12, 3188. https://doi.org/10.3390/w12113188.

Sherrod, L., Schlosser, K., Kozlowski, A., Bird, B., Werkema Jr, D.D., and Swiontek, J., (2014) Geophysical Characterization of the Keene Valley Landslide in New York State. Journal of Environmental and Engineering Geophysics, 19, 139-155. https://doi.org/10.2113/JEEG19.3.139.

Soumya, G.S., Asanulla, R.M., and Radhakrishna, T., (2017). Rockmagnetism in relation to magnetic mineralogy of anorthosites in the southern granulite region of the Indian shield. Geophysical Journal International, 209, 1768-1778. https://doi.org/10.1093/gji/ggx134.

Taylor, C.D., Schulz, K.J., Doebrich, J.L., Orris, G.J., Denning, P.D., and Kirschbaum, M.J. (2009) Geology and nonfuel mineral deposit of Africa and the Middle East. U.S. Geological Survey Open-file Report 2005-1294-E, 1-246.

Twidale, C.R., and Romani, J.R.V., (2005) Landforms and geology of granite terrains. Taylor & Francis Group, London, United Kingdom.

Jinghong, W., Caineng, Z., and Rukai, Z., (2011) Characteristics and controlling factors of fractures in igneous rock reservoirs. Petroleum Exploration and Development 38, 708-715.

Udden, J.A., (1914) Mechanical composition of clastic sediments. Bulletin of the Geological Society of America 55, 655-744.

Wilson, A.H., Jermy, C.A., and Ridgeway, M., (2005) Rock strength and physical properties of Norites of the Merensky and Bastard Units, western Bushveld Complex. Geological Society of South Africa 108, 525-540.

van School, M., (2002) Detection of sinkholes using 2D electrical resistivity imaging. Journal of Applied Geophysics 50, 393-399.

Van School, M., and Fourie, C.J.S., (2015) A guide for APPLYING GEOPHYSICS to COAL MINING PROBLEMS in South Africa. Struik Nature, South Africa.

Vitale, S., and Isaia, R., (2014) Fractures and faults in volcanic rocks (Campi Flegrei, southern Italy): insight into volcano-tectonic processes. International Journal of Earth Science, 103, 801-819. https://doi.org/10.1007/s00531-013-0979-0.

von Dobeneck, T., Müller, M., Bosbach, B., and Klügel, A., (2021) Ground Magnetic Susceptibility and mapping across weathered basalt dikes reveal soil creep and pedoturbation. Frontiers in Earth Science, 8, 1-8. https://doi.org/10.3389/feart.2020.592986.

Yang, X., Zeng, X., Pu, C., and Xiao, D., (2018). Effects of the pre-existing fissures with different fillings in PMMA on blast-induced crack propagation. Advances in Materials Science and Engineering, 17, 1-17. https://doi.org/10.1155/2018/7378282.

Zhihui, W., Xiangmin, C., Jiayong, Y., Jiming, W., Yu, L., and Lei, Z., (2018) Using the integrated geophysical methods detecting active faults: a case study in Beijing, China. Journal of Applied Geophysics, 156, 82-91. https://doi.org/10.1016/j.jappgeo.2017.01.030.

List of Tables

Table 1: Weathered and fresh rock physical property measurements from samples collected in the study area. The resistivity measurements were taken from a study conducted by van Schoor and Fourier (2015) of rocks in South Africa.

Weathered norite rock measurements (Sample-X)			**Fresh norite rock measurements (Sample Y)**		
Number of measurements taken	Magnetic susceptibility (x10-3 SI)	P-wave seismic velocity (m/s)	Number of measurements taken	Magnetic susceptibility (x10-3 SI)	P-wave seismic velocity (m/s)
Sample-X 1	0.128	950	Sample-Y 1	5.84	5,710
Sample-X 2	0.137	1,090	Sample-Y 2	4.52	5,630
Sample-X 3	0.124	1,047	Sample-Y 3	5.09	5,610
Sample X Average	0.127	1,029	Sample Y Average	5.15	5,650
Weathered anorthosite resistivity			**Fresh anorthosite resistivity**		
Rock type		Resistivity (ohm.m)	Rock type		Resistivity (ohm.m)
Weathered anorthosite		~1,000 to 3,000	Fresh anorthosite		~5,000 to 10,000

Table 2: Seismic data processing parameters.

Step	**2D processing flow**
1.	Read SEG-Y data
2.	Edit traces, Add geometry (X, Y, Z)
3.	Pick first P-wave breaks

	Traveltime-distance curve Inversion
4.	Refraction and elevation corrections Survey lines 1, 2, 3 and 4: Datum 1,224 m above mean seal level (msl).

5370

5371 **Table 3**: GPR acquisition parameters.

Acquisition item	**3-D Grid/Line number parameters**	
	GPR 3D	GL1 and GL3
Instrument:	GSSI – SIR 4000 GPR system	
Grid size/line length:	12 m × 15 m (X, Y)	200 m
Grid and trace spacing:	1 m × 0.02 m	0.02 m
Survey direction:	N - S	W - E
Survey pattern:	Zigzag	Along the profile
Dielectric:	9 F/m	
Processing steps		
Energy Decay:	0 – 150 ns time window	
Bandpass filter:	80 – 400 MHz	
Subtract-mean (dewow):	1 – 2 ns time window	
Subtracting average/background removal:	10 – 20 average traces	
Diffraction stack:	Summation width (10 – 20 traces); velocity (0.1 – 0.2 ns)	
Time-depth conversion:	0.1 – 0.2 m/ns	

5372

5373

Figures and Captions

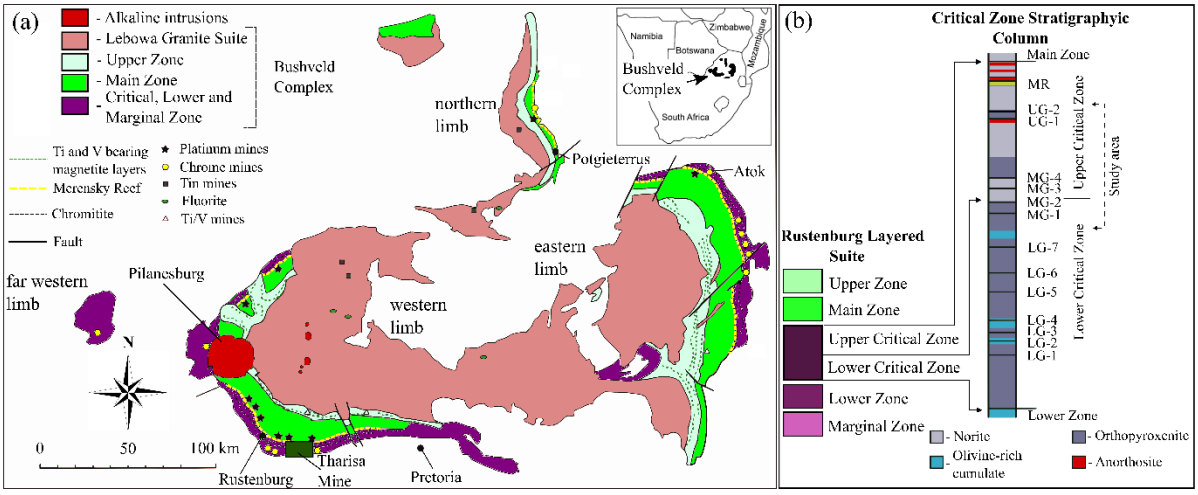


Figure 1: (a) Simplified geological map of the Bushveld Complex (modified from Taylor et al., 2009). (b) Simplified schematic stratigraphic column of the Critical Zone with its position within the Rustenburg Layered Suite. Included in the stratigraphic column is the location of Tharisa Mine, the Merensky Reef (MR), Upper Group (UP), Middle Group (MG) and Lower Group (LG) chromitite layers (modified from Hunt et al., 2018).

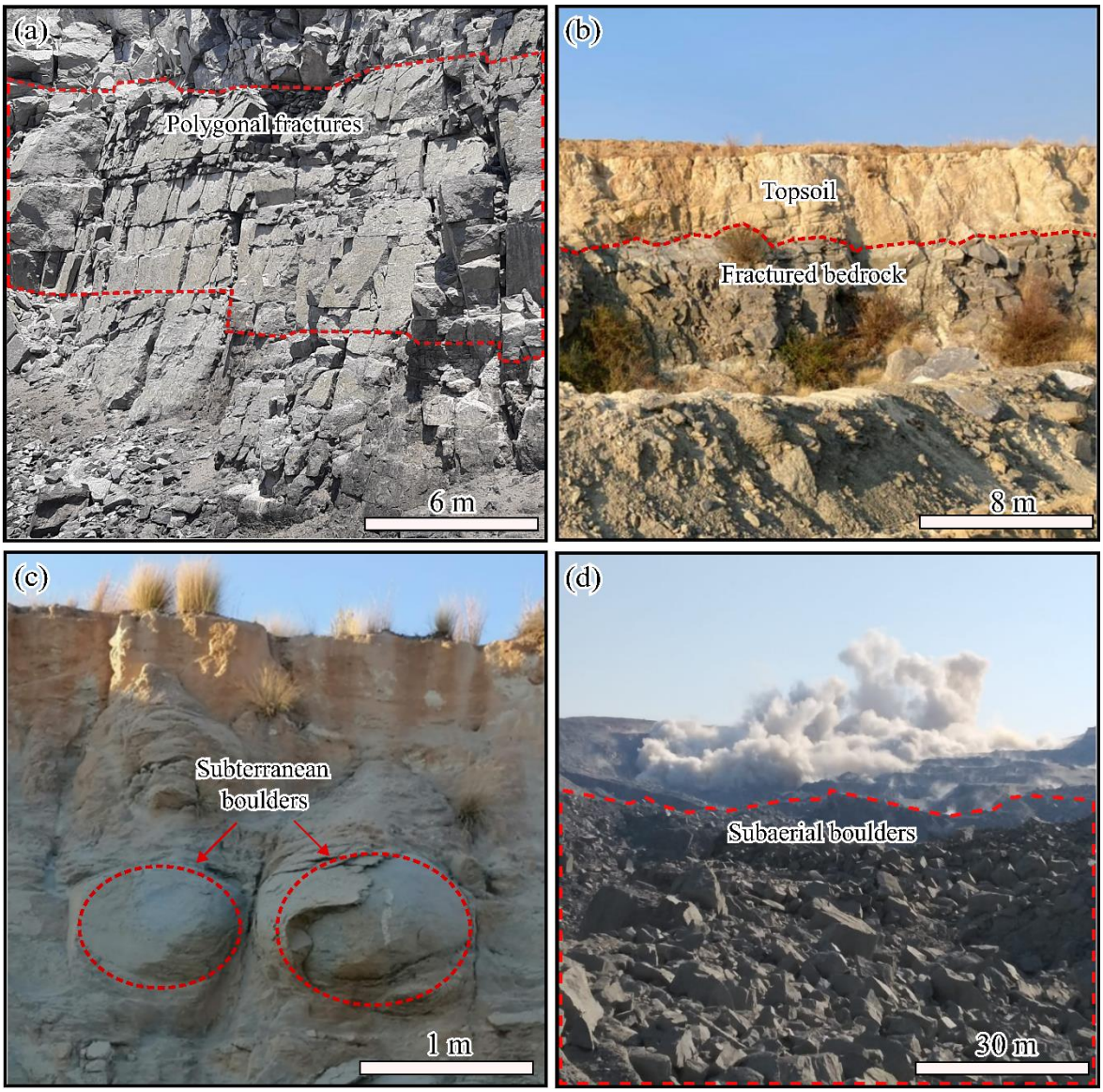


Figure 2: (a) Polygonal fractures in the norite and anorthosite rocks at Tharisa Mine, this image was taken inside the opencast mine pit. The red dotted line highlights a highly fractured zone. (b) Highwall face near the study area showing topsoil (highly weathered top zone) and fractured bedrock. (c) Subterranean boulders showing on the highwall face near the study area. (d) Subaerial boulders (blasting induced boulders) inside the pit, at Tharisa Mine. The red dotted line highlights the zone with the subaerial boulders. The presented photos were taken by Hloniphani Hlongwa (11/10/2021).

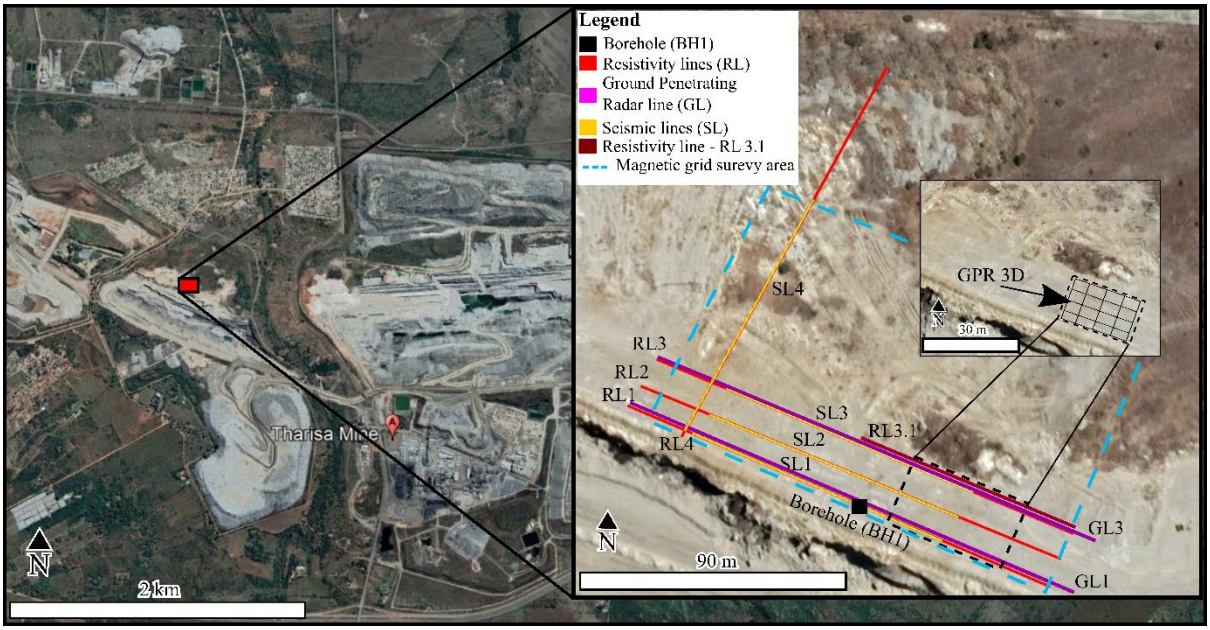


Figure 3: Google Earth image showing the location of the study area (marked with a red square) at Tharisa Mine and that of the magnetic, resistivity (RL), seismic (SL) and ground penetrating radar (GL and GPR 3D) grids collected over the study area (on the zoomed-in image of the study area).

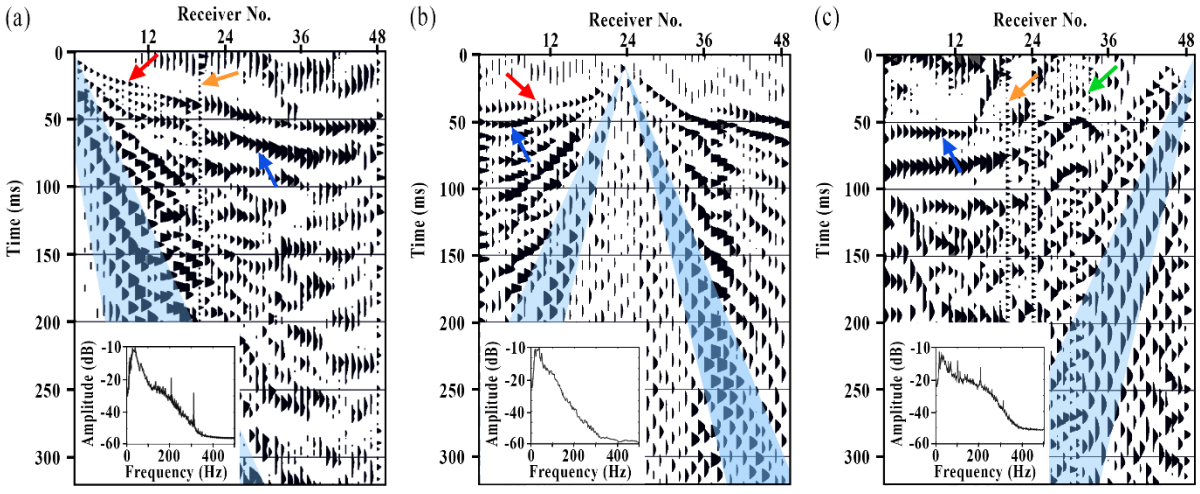


Figure 4: Raw seismic shot gathers (a-c) with corresponding frequency spectra. Bad traces (orange arrow) were removed from the shot gathers. The raw shot gathers show first arrivals (red arrows), reflections (blue arrow) that are masked by the surface waves and air waves (blue shaded areas).

The green arrow in (c) corresponds to noise introduced by a secondary source, while the blue shaded area highlights the groundroll (surface wave) zone.

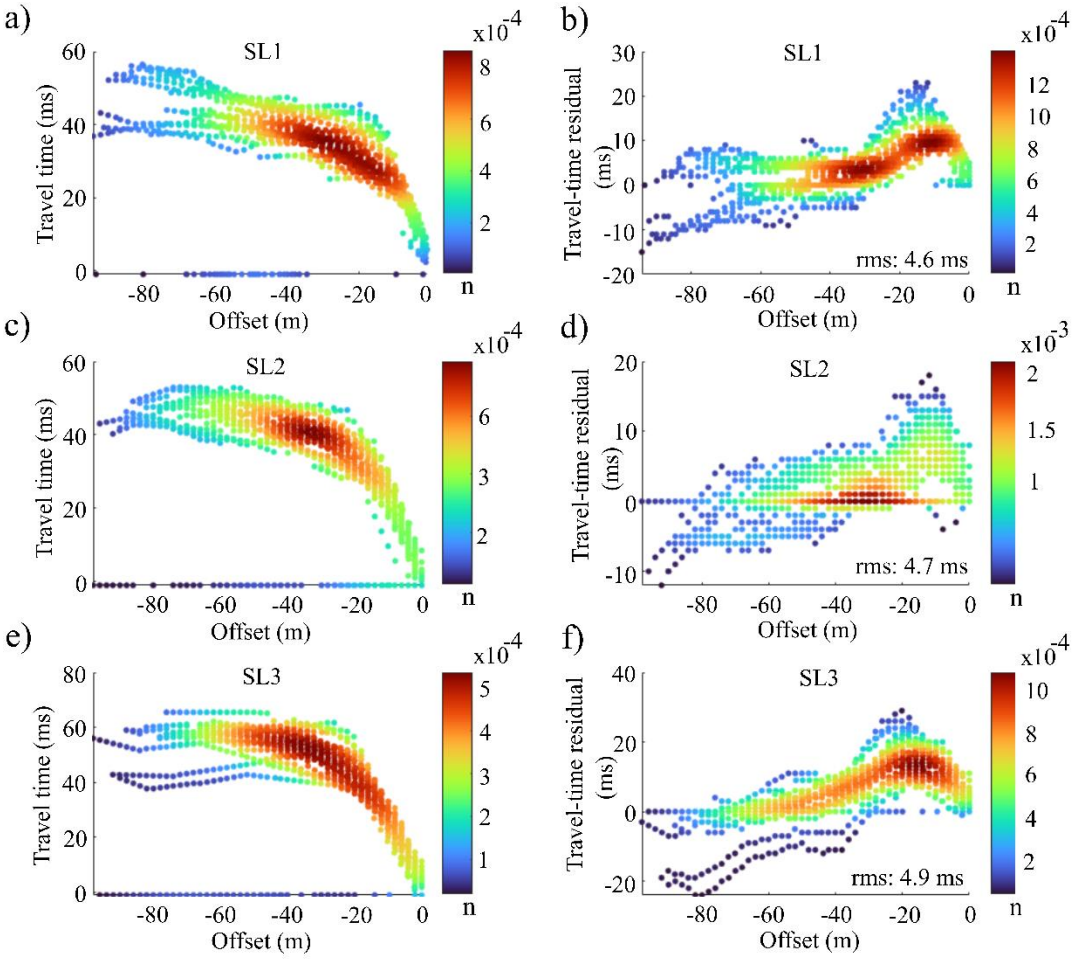


Figure 5: First break (a, c, e) and travel-time residuals (b, d, f) plots for seismic profiles SL1, SL2 and SL3. Both the first breaks and travel-time residuals are plotted as a function of offset, the colour scale used to illustrate the data represent the data density, where n – is the number of points within a range.

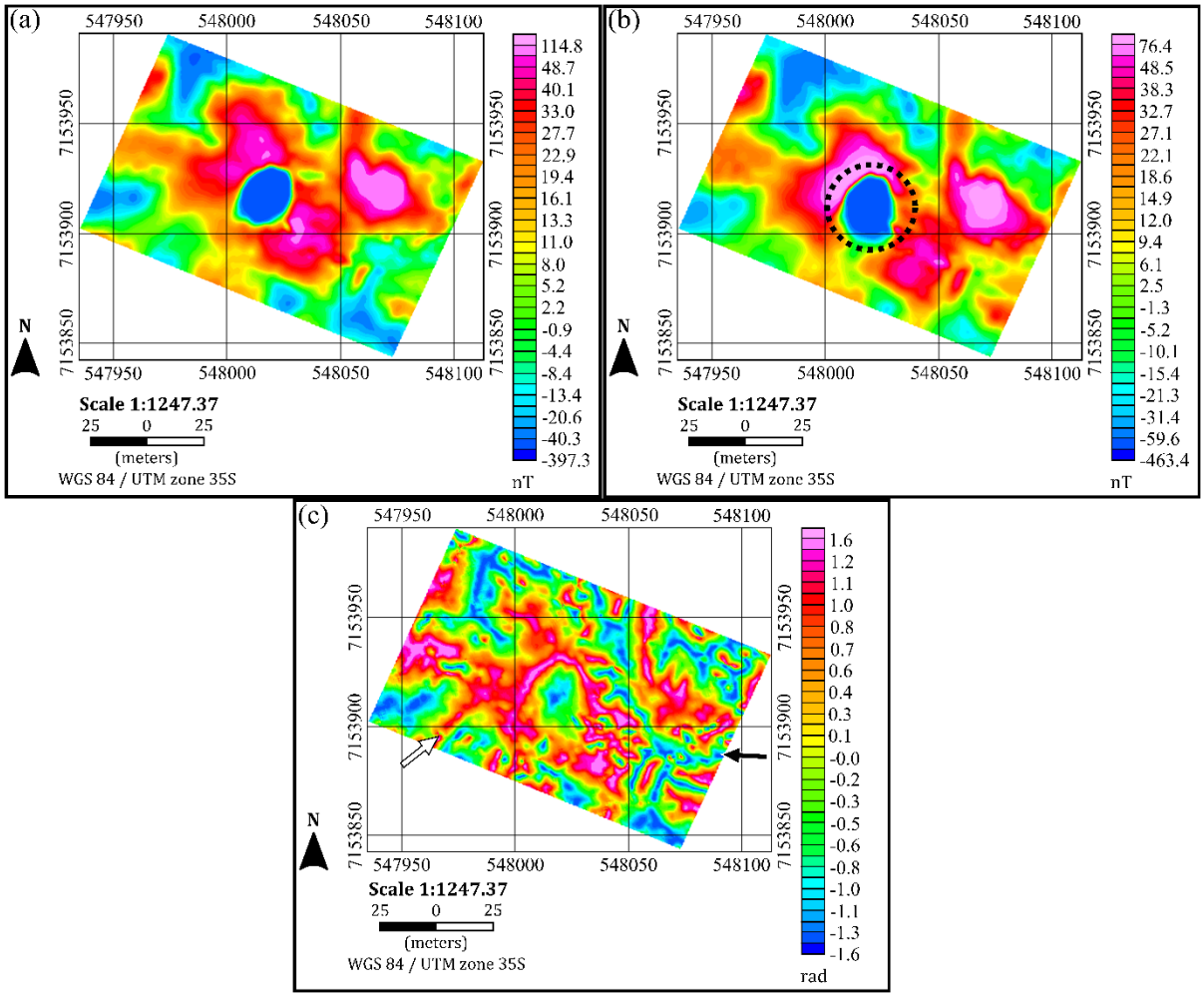
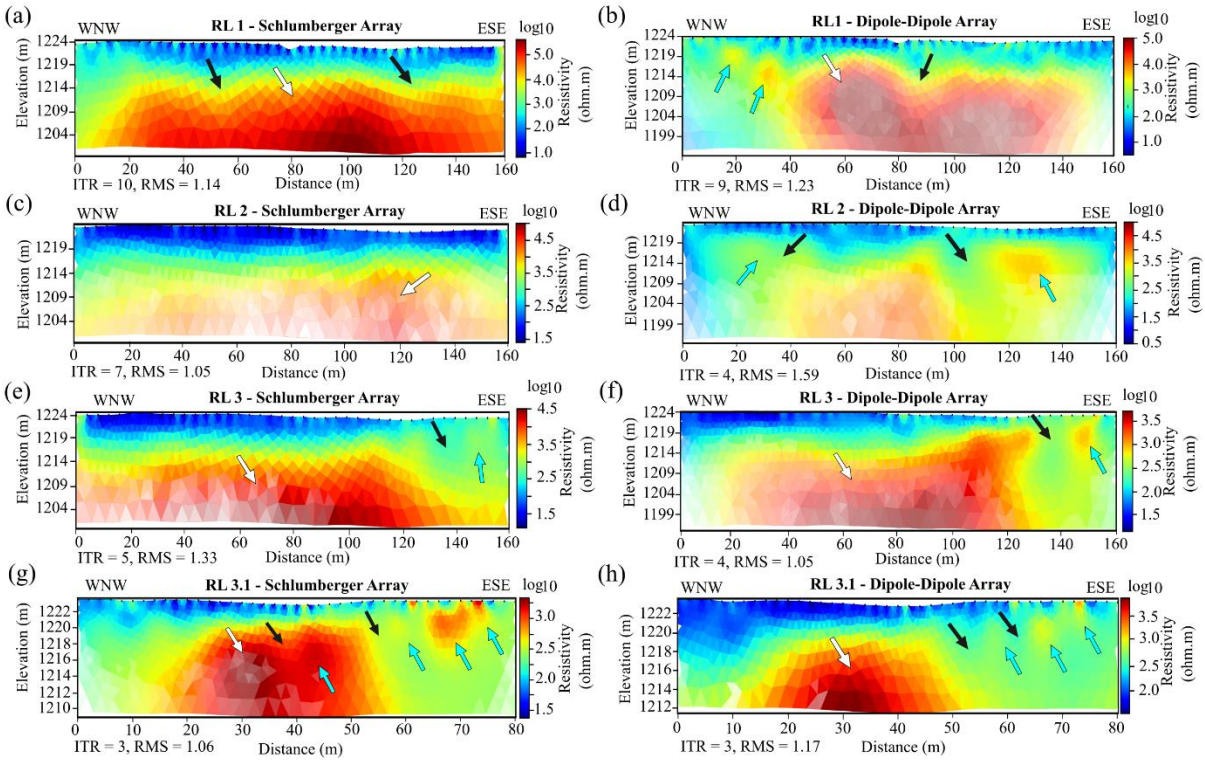


Figure 6: (a) Decultured, micro-levelled and detrended residual total magnetic intensity (TMI) map. (b) Reduced to magnetic pole (RTP) map, the black dotted circle shows the position of a body with remanent magnetisation found in the study area. (c) Vertical tilt angle of the RTP map. The black and white arrows show connected magnetic low zones and magnetic high zones,



5411

5412 **Figure 7**: Schlumberger (a, c, e, g) and dipole-dipole (b, d, f, h) resistivity inverse models for
5413 electrical resistivity tomography survey RL1 – RL3.1. The white, black and blue arrows in the
5414 plots indicate the high resistivity, low resistivity and potential boulders, respectively. The elevation
5415 used to produce the resistivity tomographs is the elevation above sea level, while the resistivity
5416 variation is measured in ohm.m.

5417

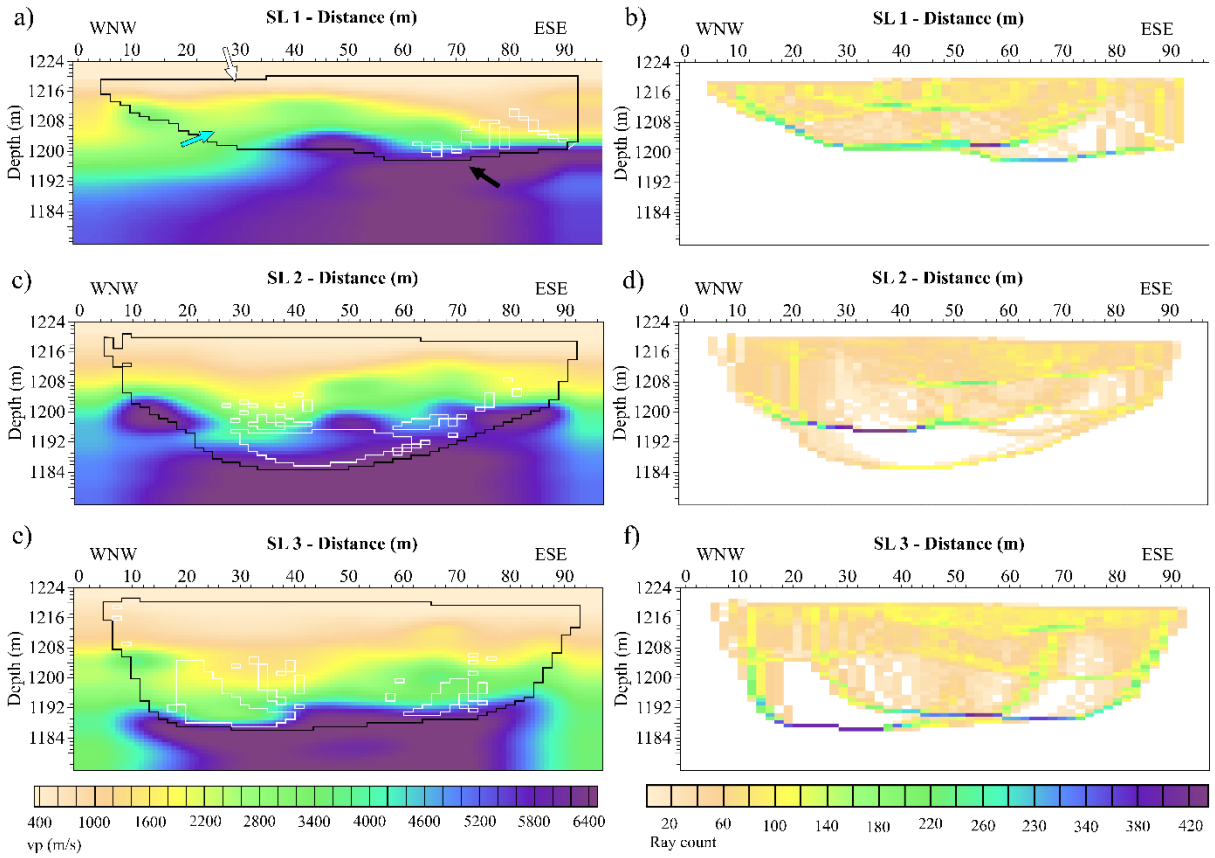


Figure 8: First break travel-time tomography model and their corresponding ray paths along profiles SL1 (a & b), SL2 (c & b), and SL3 (d & f). The outlines of the raypaths are drawn on the tomograms, the zones within the white borders are zones in which ray paths did not travel through. The tomograms display near-linear (top) to distorted (middle and bottom) seismic variations with increasing depth. The white, blue and black arrows show the three identified seismic velocity layers, starting from the layer characterised by the lowest velocities to the layer with the highest velocities, respectively.

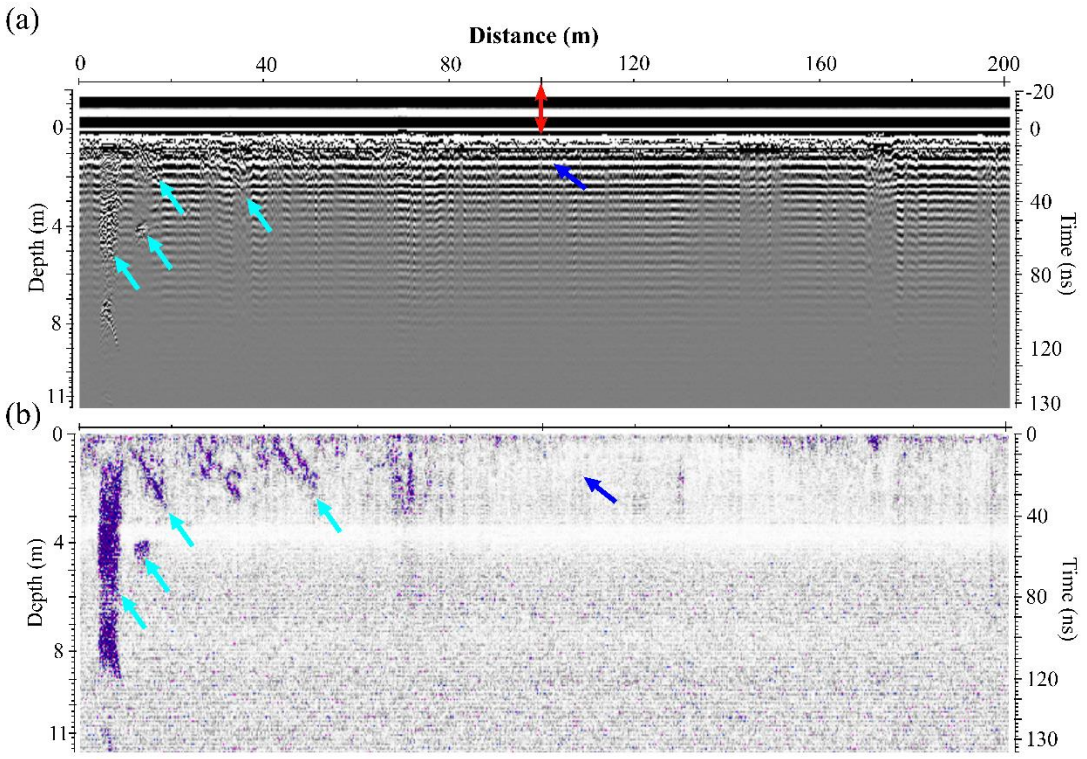


Figure 9: A sample of a raw (a) and processed 2D GPR sections (b) of profile GL1. The double headed red, light blue and dark blue arrows show the delay time, reflection and diffraction, and background noise, respectively. The observed reflection and diffraction events are possibly events originating from the contact of different lithologies and boulders.

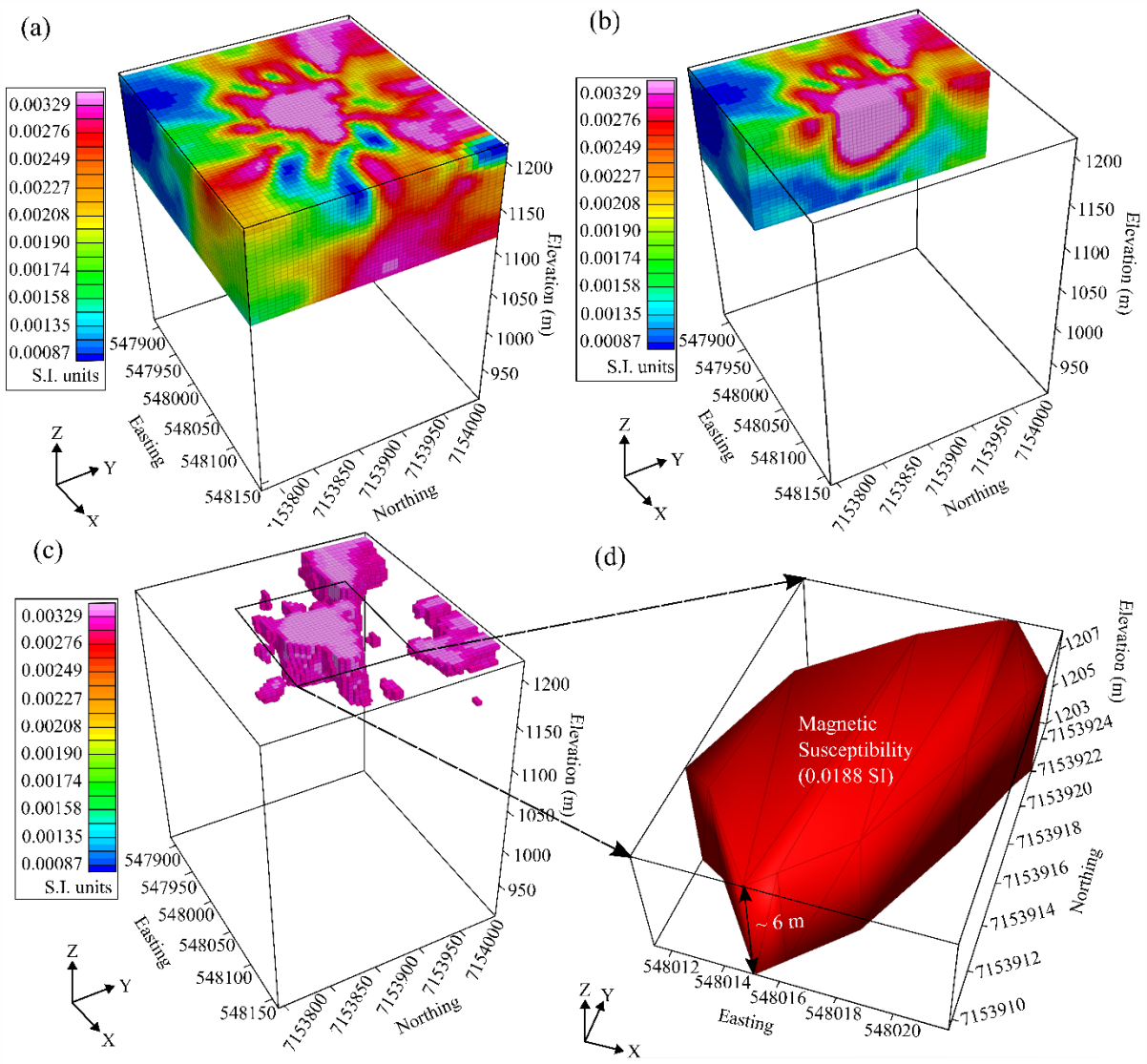


Figure 10: Susceptibility Magnetic Vector Inversion (MVI) model of the acquired TMI data in our study area. (a) Full MVI model of the magnetic data displaying the magnetic susceptibility of the rocks, including that of the IRUP (centre). (b) Clipped 3D susceptibility model showing the vertical nature of the IRUP. (c) Zones of high magnetic susceptibility around the IRUP are interpreted as potential boulders. (d) 3D best-fit ModelVision model of the IRUP.

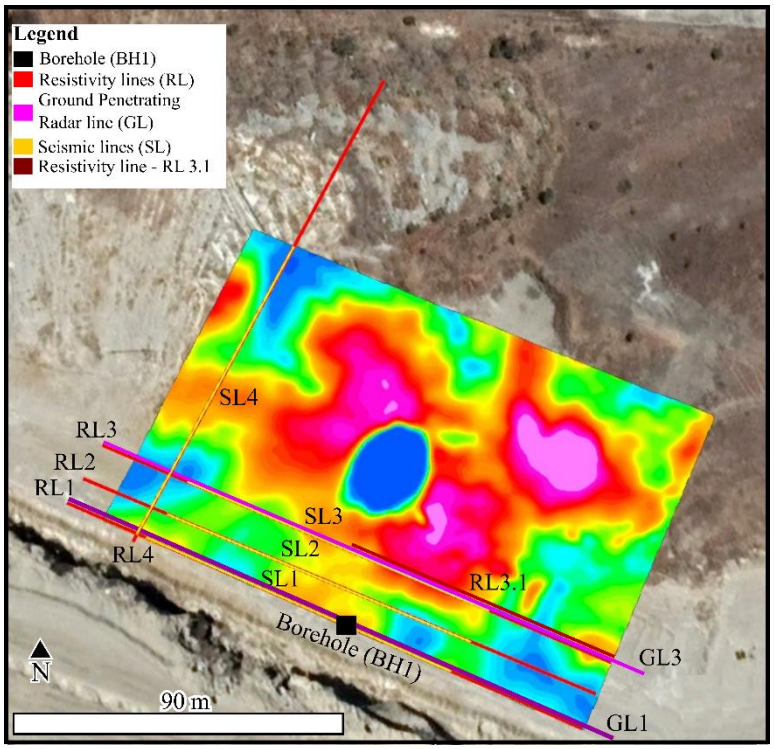
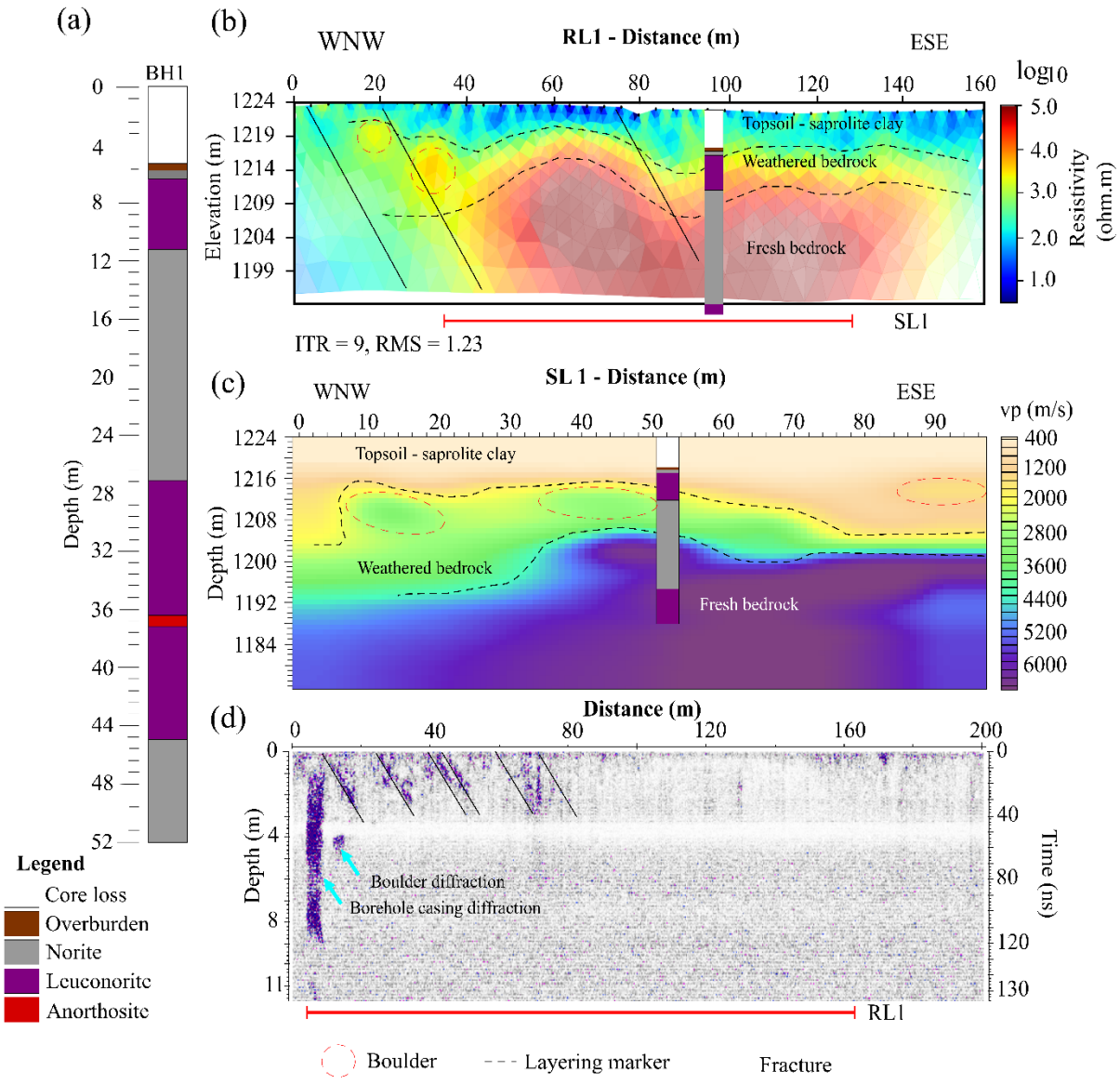


Figure 11: Seismic (SL), resistivity (RL) and ground penetrating radar (GL) 2D line locations overlain on the total magnetic intensity map of the study area. The seismic and resistivity profiles were placed on a zone with varying TMI to try map the observed magnetic variation in the subsurface rocks with depth.



5449

5450 **Figure 12**: Interpretation and integration of methods for profile 1 (profile where SL1, RL1 and
5451 GL1 were acquired) 1. (a) Borehole (BH1) lithology along profile 1. The lithological log has been
5452 correlated with RL1 and SL1. (b) BH1 overlain on the electrical resistivity tomogram of RL1. (c)
5453 BH1 overlain on the seismic refraction tomogram of SL1. (d) Ground penetrating radar section of
5454 profile GL1. The dotted lines show the lithological boundaries between saprolite clay, weathered
5455 bedrock and fresh bedrock. The solid black lines correspond to joints, fractures, or fault
5456 lineaments.

5457

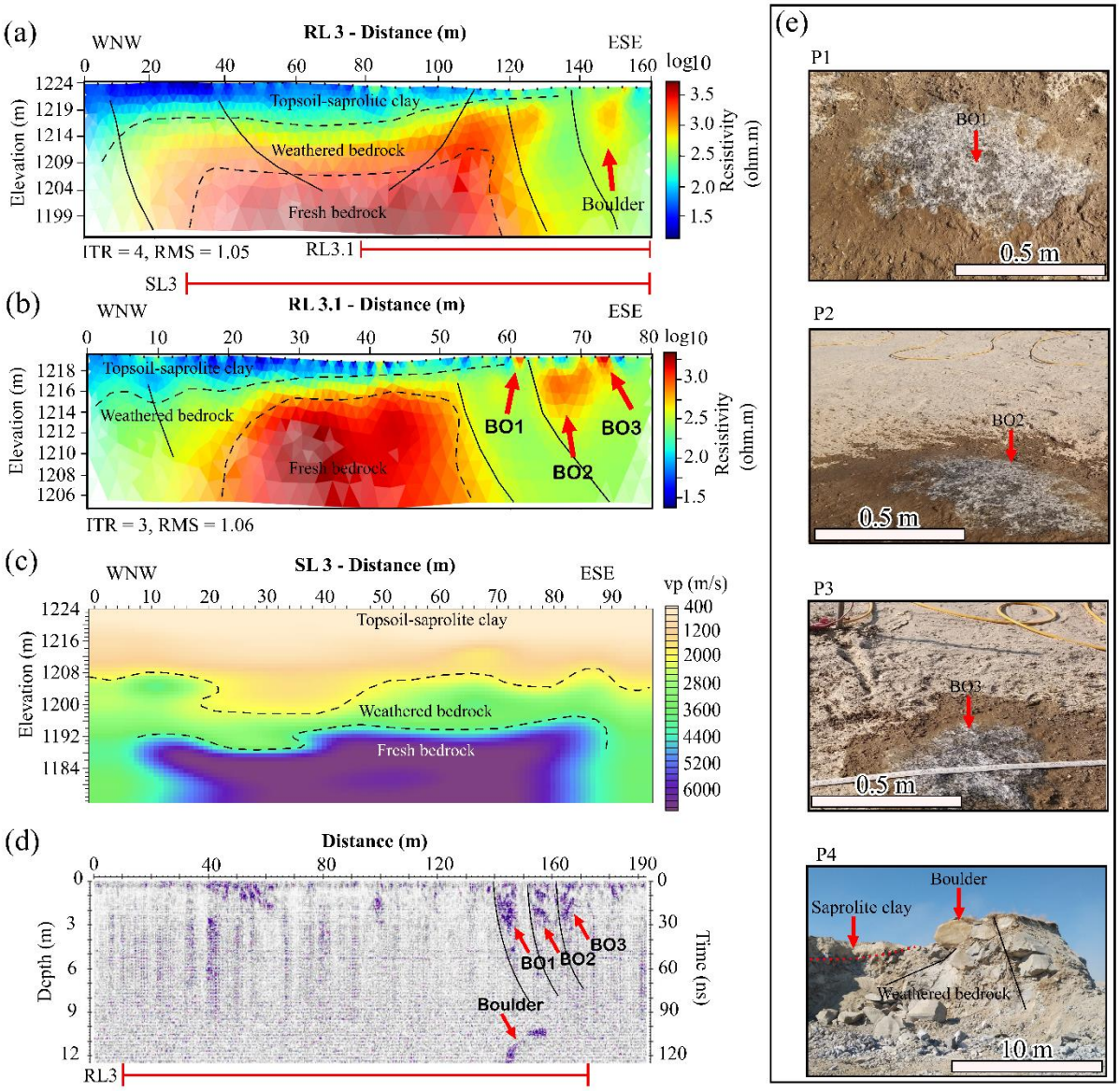


Figure 13: Interpretation and integration of methods for profile 3 (profile where SL3, GL3, RL3 and RL3.1 were acquired). (a) Electrical resistivity tomogram of profile RL3. (b) Electrical resistivity tomogram of profile RL3.1, high-resolution line mapping the outcropped region along RL3. (c) Seismic refraction tomogram for profile SL3. (d) Ground penetrating radar section of profile GL3. (e) Images of the outcropping rocks along profile 3 (pictures P1, P2, P3 and P4). The dotted lines show lithological boundaries between saprolite clay, weathered bedrock and fresh bedrock zones. The solid black lines show joints, fractures, or fault lineaments. BO – boulder outcrops.

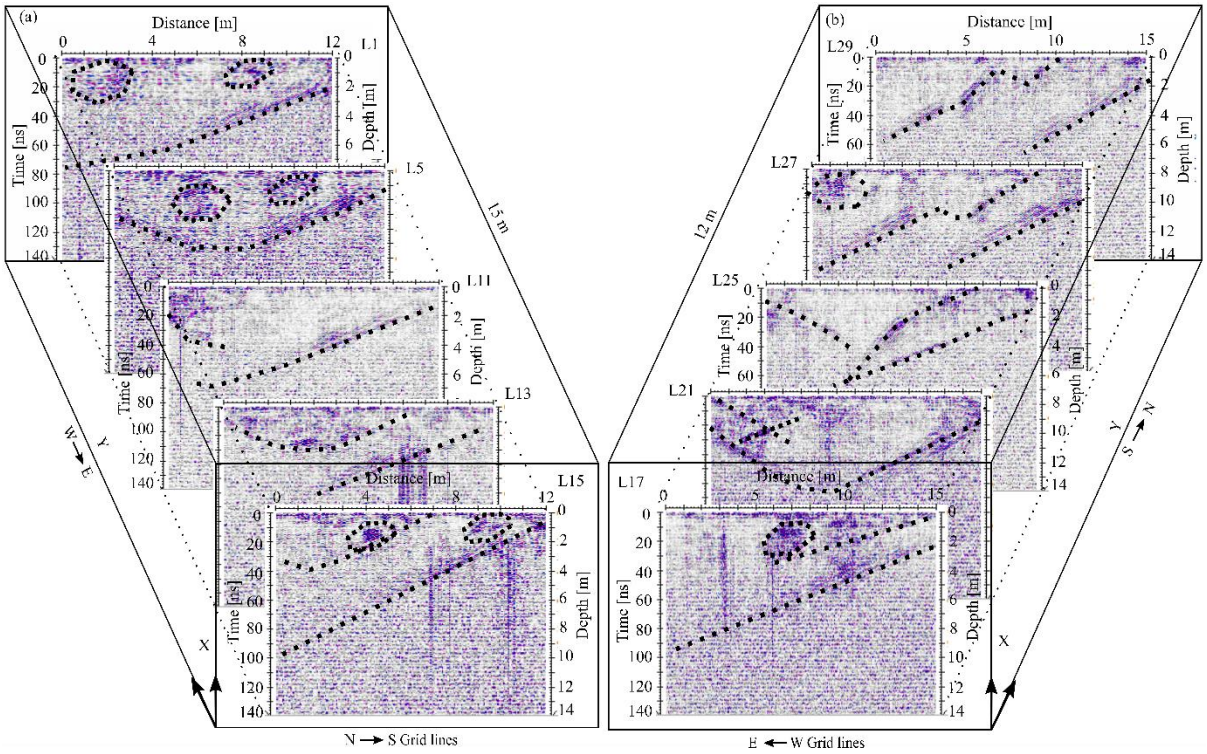


Figure 14: (a) and (b) 3D view interpretation of GPR 3D grid radargram lines along the north – south (X) and east – west (Y) directions, respectively. Note: Y-axes are not drawn to scale and the dotted black lines and circles in all sections correspond to different geological features.

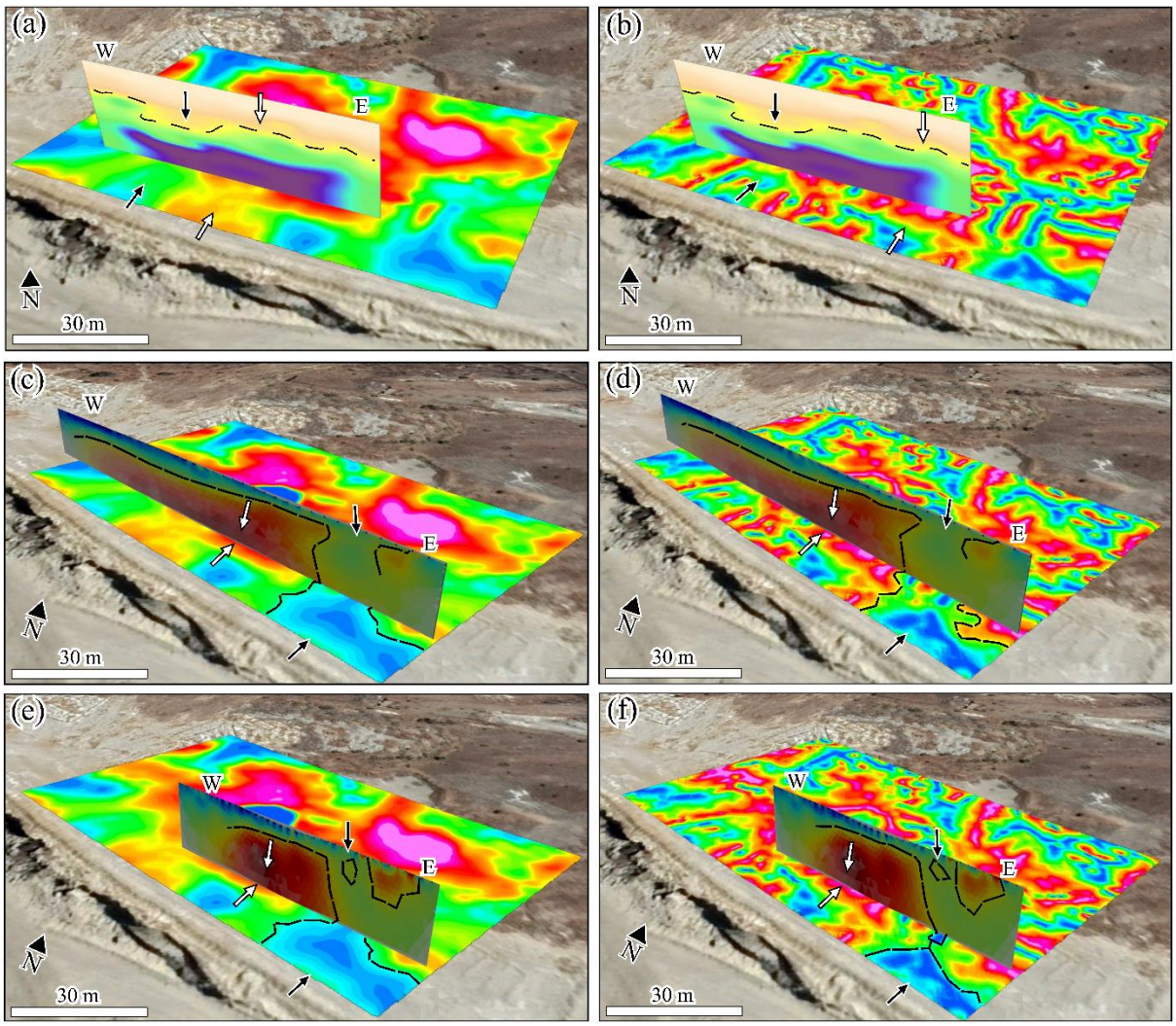


Figure 15: Profile SL3 seismic depth section projected on the TMI (a) and TVDR magnetic (b) maps. Profile RL3 resistivity depth section projected on the TMI (c) and TVDR (d) magnetic maps. Profile RL3.1 resistivity depth section projected on TMI (e) and TVDR (f) magnetic maps. The white and black arrow indicate areas where the is high and low correlation, respectively.

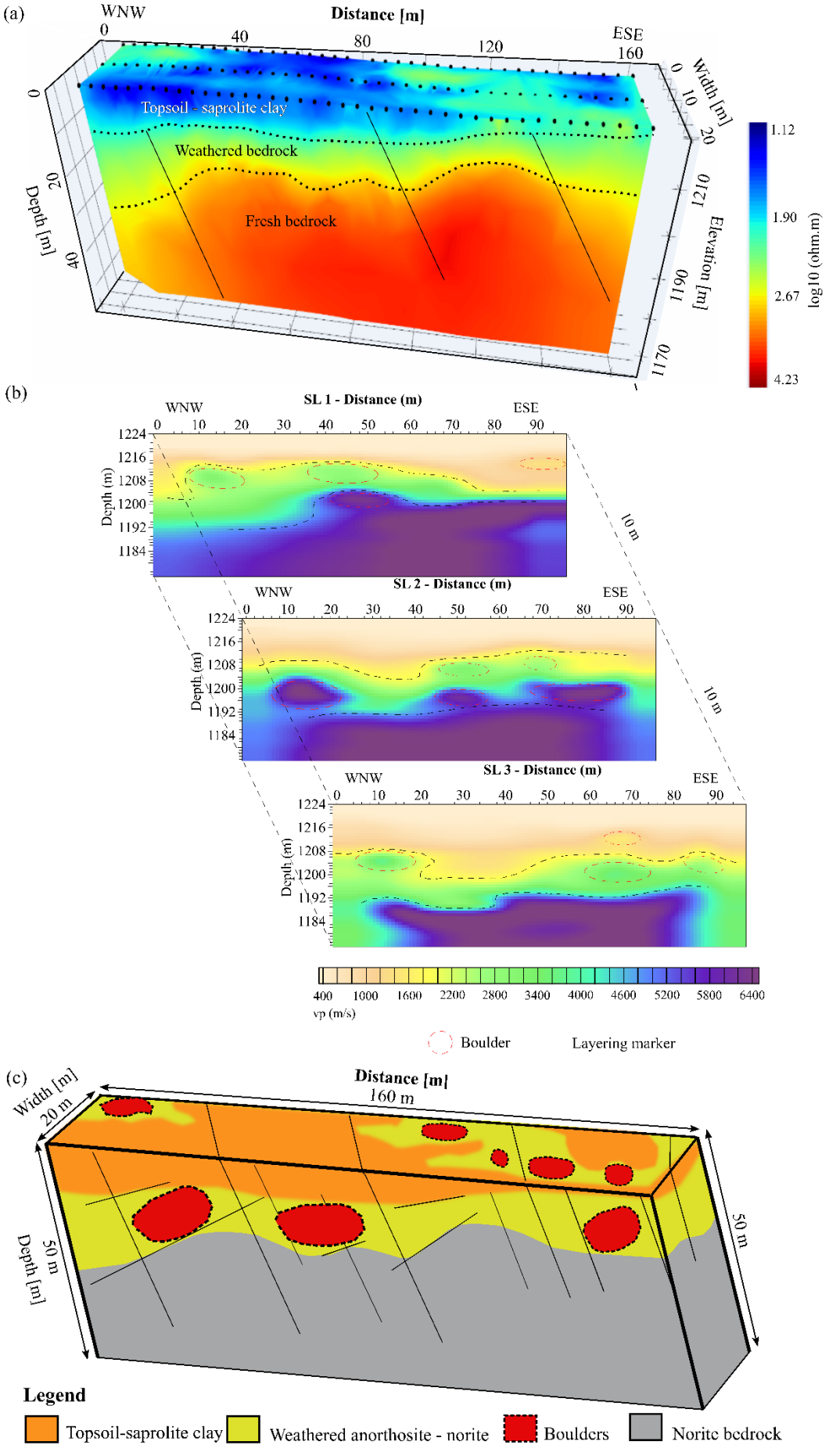

(a)
WNW
Distance [m]
ESE
Topsoil - saprolite clay
Weathered bedrock
Fresh bedrock
Depth [m]
Width [m]
Elevation [m]
log10 (ohm.m)
1.12
1.90
2.67
4.23
(b)
SL 1 - Distance (m)
SL 2 - Distance (m)
SL 3 - Distance (m)
Depth (m)
10 m
vp (m/s)
Boulder
Layering marker
(c)
Width [m]
Distance [m]
160 m
20 m
50 m
Depth [m]
Legend
Topsoil-saprolite clay
Weathered anorthosite - norite
Boulders
Norite bedrock

Figure 16: (a) 3D electrical resistivity model of survey lines RL1, RL2 and RL3. (b) 3D view of seismic refraction tomograms of survey line SL1, SL2 and SL3. (c) 3D geological model generated from the combined geophysical methods employed in this study.